

**KINEMATICS AND TIMING OF INTRA-ARC DEFORMATION  
AT THE SOUTHERN ANDES PLATE BOUNDARY ZONE**

by

José Cembrano

Submitted in partial fulfillment of the requirement for the degree of  
Doctor of Philosophy

at

Dalhousie University  
Halifax, Nova Scotia, Canada

December 1998

**DALHOUSIE UNIVERSITY**

**FACULTY OF GRADUATE STUDIES**

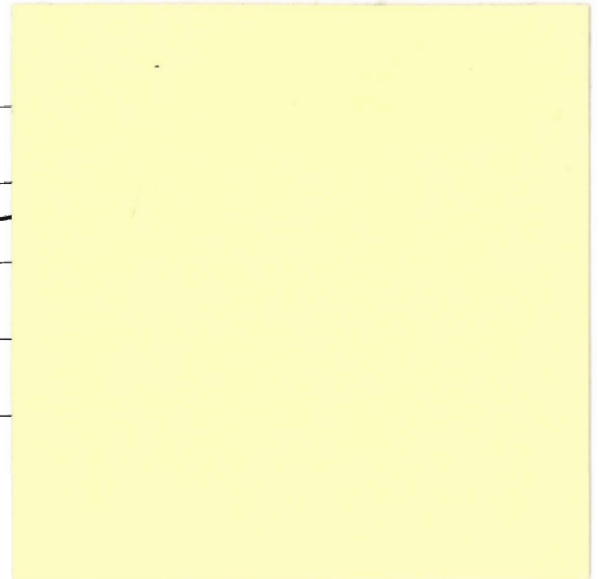
The undersigned hereby certify that they have read and recommend to the Faculty of Graduate Studies for acceptance a thesis entitled "Kinematics and Timing of Intra-Arc Deformation at the Southern Andes Plate Boundary Zone"

by José Cembrano

in partial fulfillment of the requirements for the degree of Doctor of Philosophy.

Dated: December 9, 1998

External Examiner \_\_\_\_\_  
Research Supervisor \_\_\_\_\_  
Examining Committee \_\_\_\_\_





DALHOUSIE UNIVERSITY

DATE: December 18, 1998

AUTHOR: Jose CEMBRANO

TITLE: Kinematics and timing of Intra Arc Deformation  
at the Southern Andes Plate Boundary Zone.

DEPARTMENT OR SCHOOL: Earth Sciences

DEGREE: Ph.D. CONVOCATION: \_\_\_\_\_ YEAR: 1999

Permission is herewith granted to Dalhousie University to circulate and to have copied for non-commercial purposes, at its discretion, the above title upon the request of individuals or institutions.



Signature of Author

The author reserves other publication rights, and neither the thesis nor extensive extracts from it may be printed or otherwise reproduced without the author's written permission.

The author attests that permission has been obtained for the use of any copyrighted material appearing in this thesis (other than brief excerpts requiring only proper acknowledgement in scholarly writing), and that all such use is clearly acknowledged.

## Distribution License

DalSpace requires agreement to this non-exclusive distribution license before your item can appear on DalSpace.

### NON-EXCLUSIVE DISTRIBUTION LICENSE

You (the author(s) or copyright owner) grant to Dalhousie University the non-exclusive right to reproduce and distribute your submission worldwide in any medium.

You agree that Dalhousie University may, without changing the content, reformat the submission for the purpose of preservation.

You also agree that Dalhousie University may keep more than one copy of this submission for purposes of security, back-up and preservation.

You agree that the submission is your original work, and that you have the right to grant the rights contained in this license. You also agree that your submission does not, to the best of your knowledge, infringe upon anyone's copyright.

If the submission contains material for which you do not hold copyright, you agree that you have obtained the unrestricted permission of the copyright owner to grant Dalhousie University the rights required by this license, and that such third-party owned material is clearly identified and acknowledged within the text or content of the submission.

If the submission is based upon work that has been sponsored or supported by an agency or organization other than Dalhousie University, you assert that you have fulfilled any right of review or other obligations required by such contract or agreement.

Dalhousie University will clearly identify your name(s) as the author(s) or owner(s) of the submission, and will not make any alteration to the content of the files that you have submitted.

If you have questions regarding this license please contact the repository manager at [dalspace@dal.ca](mailto:dalspace@dal.ca).

Grant the distribution license by signing and dating below.

---

Name of signatory

---

Date

## TABLE OF CONTENTS

List of figures.....	vi
List of Tables .....	.xi
Abstract.....	.xii
Acknowledgements.....	.xiii
<b>Chapter 1. Introduction.....</b>	<b>1</b>
1.1 Introductory Statement.....	1
1.2 Aims and purpose of this thesis.....	4
1.3 Kinematics of deformation at plate boundary zones: a review.....	9
1.4 Dating of absolute timing of deformation by the $^{40}\text{Ar}$ - $^{39}\text{Ar}$ method: summary of current knowledge.....	41
1.5. Previous geologic studies at the southern Andes plate boundary zone between 42 and 47°S.....	45
1.6 Organization of the thesis.....	48
<b>Chapter 2. Contrasting nature and timing of deformation along the northern part of the intra-arc Liquiñe-Ofqui fault zone, southern Chilean Andes .....</b>	<b>50</b>
2.1 Introduction.....	50
2.2 Tectonic setting of the Liquiñe-Ofqui fault zone.....	54
2.3. Regional geology of the Liquiñe-Ofqui fault zone.....	54
2.4. Structural transects.....	65
2.4.1 Liquiñe transect.....	70
2.4.2 Reloncaví transect.....	79
2.4.3 Hornopirén transect.....	83
2.5 Discussion.....	87
2.5.1 Nature and timing of deformation.....	87
2.5.2 Geodynamic significance of the Liquiñe-Ofqui fault zone.....	91
2.5.2.1 Oblique subduction.....	91
2.5.2.2 Indenter tectonics.....	93
2.6. Conclusions.....	94

<b>Chapter 3. Late Cenozoic transpressional ductile deformation north of the Nazca-South America-Antarctica triple junction.....</b>	<b>96</b>
3.1 Introduction.....	96
3.2 Geologic setting.....	100
3.3 Structural setting.....	105
3.4 Geometry and kinematics of ductile shear zones from the Puyuhuapi and Aysén transects.....	120
3.4.1 Puyuhuapi quarry shear zone.....	120
3.4.2 Queulat shear zone.....	121
3.4.3 Canal Jacaf shear zone.....	122
3.4.4 Río Cisnes shear zone.....	122
3.4.5 Islas Cinco Hermanas shear zone.....	123
3.4.6 Canal Costa shear zone.....	123
3.5. Age of deformation.....	129
3.5.1 Ar-Ar thermochronological data of the deformed rocks .....	135
3.6. Discussion.....	143
<b>Chapter 4. Dating deformation on heterogeneously deformed plutonic rocks: an example from ductile shear zones of the Patagonian Batholith.....</b>	<b>152</b>
4.1 Introduction.....	152
4.2 Microstructure and possible deformation mechanisms.....	163
4.3 Laser dating, techniques and targets.....	170
4.4 Results.....	171
4.5 Discussion.....	172
4.5.1 Limitations and advantages of the laser method in dating deformation of young plutonic rocks deformed under low greenschist facies conditions..	172
4.5.2 Significance of the ages for the tectonic evolution of the southern Andes.	172
<b>Chapter 5. General conclusions and discussion.....</b>	<b>174</b>
<b>Appendix 1. Ar-Ar analytical data from bulk mineral separates dated by furnace step heating and total laser fusion techniques.....</b>	<b>184</b>
<b>References.....</b>	<b>219</b>

## LIST OF FIGURES

<b>Figure 1.1</b> Geodynamic setting of the southern Andes plate boundary zone (modified from Herron, 1981, Cande and Leslie, 1986; Pardo-Casas and Molnar, 1987; Cembrano et al, 1996; Bourgois et al. 1996).....	2
<b>Figure 1.2</b> Regional scale geologic and tectonic setting of the Southern Andes plate boundary zone from 39 to 43 degrees south latitude (modified from SERNAGEOMIN, 1980; Cande and Leslie, 1986; Pardo-Casas and Molnar, 1987; Cembrano, 1996; Burgois, 1997).....	5
<b>Figure 1.3</b> Regional scale geologic and tectonic setting of the Southern Andes plate boundary zone from 44 to 48 degrees south latitude (modified from SERNAGEOMIN, 1980; Cande and Leslie, 1986; Pardo-Casas and Molnar, 1987; Cembrano, 1996; Burgois,1997).....	7
<b>Figure 1.4</b> Kinematics of plate boundary zones assuming monoclinic, constant-volume deformation. (simplified from Fossen et al.1994).....	10
<b>Figure 1.5</b> Kinematics of transpressional and transtensional plate boundary zones assuming monoclinic, constant-volume deformation (simplified from Sanderson and Marchini, 1984; Fossen et al. 1994, Tikoff and Greene, 1997).....	13
<b>Figure 1.6</b> Homogeneously distributed versus completely partitioned transpressional deformation (modified from Tikoff and Greene,1997).....	16
<b>Figure 1.7</b> Plan view of a constant-volume, monoclinic transpressional deformation zone (adapted from Teyssier et al. 1995). Homogeneously distributed and complete partitioned transpression are shown. ....	18
<b>Figure 1.8</b> High degree of strike-slip partitioning of transpressional deformation at the Pacific-North America plate boundary. (adapted from Fossen et al. 1994).....	22
<b>Figure 1.9</b> Geometry of foliation and stretching lineation for wrench dominated transpression. (from Tikoff and Greene, 1997).....	24
<b>Figure 1.10</b> Heterogeneous transpression is accommodated by discrete domains within which the components of pure shear and simple shear deformation are increased. S-C fabrics are a natural example of heterogeneous transpression at the sample scale (adapted from Tikoff and Greene, 1997).....	27
<b>Figure 1.11</b> Partitioning of bulk transpressional deformation for the upper, brittle crust and for the mid- to lower ductile crust. The simple shear component of transpression is accommodated by slip on a single fault in the upper crust. This fault grades downward into a wider zone of distributed ductile simple shear.....	29

<b>Figure 1.12</b> Cartoon showing the case of general triclinic heterogeneous transpressional deformation as commonly observed in nature.....	31
<b>Figure 1.13</b> Geometry and boundary conditions for a dynamic numerical model of obliquely convergent plate-boundary zones (Braun and Beaumont, 1995). .....	34
<b>Figure 1.14.</b> Triclinic deformation is characterized by the existence of a vertical simple shear component of motion. The component of simple shear is not necessarily horizontal but oblique with respect to the horizontal plane (adapted from Lin et al. 1998).....	39
<b>Figure 2.1</b> Regional scale geometry of the Liquiñe-Ofqui fault zone and geotectonic setting of the southern Chilean Andes (modified from Cifuentes, 1989; Cembrano et al. 1996). Transect location is shown by boxes across the Liquiñe-Ofqui fault zone. ....	52
<b>Figure 2.2</b> Regional geology and local structure of the Liquiñe-Ofqui fault zone for the Liquiñe region. Simplified from Moreno and Parada (1976) and Hervé (1977). Locations of available radiometric age determinations (Hervé, 1977; Munizaga et al. 1988) are shown with symbols. Triangle: K-Ar dates on biotite, inverted triangle: K-Ar whole rock dates.....	59
<b>Figure 2.3</b> Regional geologic map of the Liquiñe-Ofqui fault zone for the Reloncaví area. Simplified from Thiele et al. (1986), Parada et al. (1987) and Carrasco (1991). Locations of available radiometric age determinations (Drake et al. 1990; Drake et al. 1991; Carrasco, 1991) are shown with symbols. Solid square: total fusion Ar-Ar dates on biotite; half-filled square: total fusion Ar-Ar dates on hornblende; triangle: K-Ar dates on biotite, inverted triangle: K-Ar whole rock dates.. .....	61
<b>Figure 2.4</b> Regional geology and local structure of the Liquiñe-Ofqui fault zone for the Hornopirén region. Simplified from Hervé et al. (1979) and Cembrano (1990). Locations of available radiometric age determinations (Hervé et al. 1979; Drake et al. 1990; Drake et al. 1991; Schermer et al. 1996) are indicated with symbols. Solid square: total fusion Ar-Ar dates on biotite; half-filled square: total fusion Ar-Ar dates on hornblende; diamond: Rb-Sr whole rock isochron; triangle: K-Ar dates on biotite, inverted triangle: K-Ar whole rock dates; filled circle: U-Pb dates on zircon.....	63
<b>Figure 2.5</b> Summary of microstructural criteria used to determine:	
<b>(a)</b> Shear sense on mylonites(Berthé et al. 1979; Passchier and Simpson, 1986; Lister and Snoke, 1984; Simpson and Schmid, 1983).....	65
<b>(b)</b> Physical conditions of deformation (simplified from Simpson,1985; Tullis and Yund, 1987).....	66
<b>Figure 2.6</b> <sup>40</sup> Ar- <sup>39</sup> Ar apparent age spectra for the Liquiñe transect crosscutting dyke (Amphibole bulk mineral separate).....	72

<b>Figure 2.7</b> Lower hemisphere, equal area projections showing the orientation of ductile fabrics from deformed rocks within the Liquiñe-Ofqui fault zone. Poles to schistosity for Liquiñe (a) and Hornopirén (b) (crosses) ; Stretching and mineral lineation plots for Liquiñe (c) and Hornopirén (d) (dots). .....	75
<b>Figure 2.8</b> Photomicrographs of shear sense indicators from XZ sections of deformed rocks occurring within the Liquiñe-Ofqui fault zone. ....	77
<b>Figure 2.9</b> Lower hemisphere, equal angle projections, showing orientation and kinematic data for mesoscopic faults at Reloncaví (a,b) and Hornopirén (c) computed to obtain the local stress tensor. From method of Carey and Brunier (1974).....	81
<b>Figure 3.1</b> Regional-scale tectonic setting of the Southern Andes. Northeast-trending, trench-parallel lineaments, correspond to the Liquiñe-Ofqui fault zone. Current position of the Nazca-South America-Antarctica triple junction is shown. Series of small arrows represent convergence vectors between the Nazca and South American plates for the last 48 Ma. (Modified from Pardo-Casas and Molnar, 1987, Cembrano et al., 1996, Burgois et al. 1996).....	98
<b>Figure 3.2.</b> Regional-scale geologic map of the southern Chilean Andes between 44° and 47°S. (modified from SERNAGEOMIN, 1980; Bobenrieth et al. 1983; Pankhurst and Hervé, 1994, Hervé et al. 1995). ....	101
<b>Figure 3.3</b> Regional geology and structure of the Puyuhuapi transect showing the location of major ductile shear zones.....	106
<b>Figure 3.4</b> Regional geologic map of the Puyuhuapi transect showing location of samples selected for $^{40}\text{Ar}$ - $^{39}\text{Ar}$ analysis.....	108
<b>Figure 3.5</b> New $^{40}\text{Ar}$ - $^{39}\text{Ar}$ , mean ages, for undeformed rocks and mylonites of the Puyuhuapi transect (Spectra shown in figure 9). Previously published Rb-Sr ages are indicated (Pankhurst and Hervé, 1994; Hervé et al. 1995) .....	110
<b>Figure 3.6</b> Lower hemisphere, stereographic projections of poles to foliations (crosses) and stretching lineations (dots) for ductile shear zones of the Puyuhuapi and Aysén transects.....	112
<b>Figure 3.7</b> Regional geology and structure of the Aysén transect. Location of major shear zones is shown.....	114
<b>Figure 3.8</b> Regional geologic map of the Aysen transect showing location of samples selected for $^{40}\text{Ar}$ - $^{39}\text{Ar}$ analysis.....	116
<b>Figure 3.9</b> New $^{40}\text{Ar}$ - $^{39}\text{Ar}$ ages for undeformed rocks and mylonites of the Aysén transect (Spectra shown in figure 9). Previously published Rb-Sr ages are indicated (Pankhurst and Hervé, 1994; Hervé et al. 1995).....	118

<b>Figure 3.10</b> Photomicrographs of high strain rocks from the Puyuhuapi Quarry shear zone (a) and Rio Cisnes shear zone (b). Sections cut perpendicular to the foliation and parallel to the stretching lineation. Scale and shear sense are indicated.....	124
<b>Figure 3.11</b> $^{40}\text{Ar}$ - $^{39}\text{Ar}$ apparent age spectra for samples of the shear zones. Puyuhuapi Quarry (a,b,c,d,e); Rio Cisnes (f) and Islas Cinco Hermanas (g).....	126
<b>Figure 3.12</b> (a) Polished rock slab of sample 95GA19 showing numbered targets selected for laser spot analysis. (b) Plot of apparent $^{40}\text{Ar}$ - $^{39}\text{Ar}$ age data for the selected targets..	137
<b>Figure 3.13</b> (a) Polished rock slab of sample 95GA17 showing numbered targets selected for laser spot analysis. (b) Plot of apparent $^{40}\text{Ar}$ - $^{39}\text{Ar}$ age data for the selected targets..	140
<b>Figure 3.14</b> Migration of the Chile Ridge and fracture zones with respect to the plate boundary during the last 6 Ma (Bourgeois et al. 1996).....	145
<b>Figure 3.15</b> Current models for the tectonic consequences of ridge collision (a), and oblique subduction(b), in the tectonics of plate boundaries. (Tapponier and Molnar, 1976; Nelson and Arit, 1994; Beck, 1991).....	147
<b>Figure 3.16</b> Cartoon of the Nazca-South America plate boundary zone showing how overall heterogeneous transpressional deformation arising from oblique convergence and ridge subduction has been accommodated during the last 6 Ma.....	150
<b>Figure 4.1</b> Regional-scale tectonic setting of the Southern Andes. Northeast-trending, trench-parallel lineaments, correspond to the Liquiñe-Ofqui fault zone. Current position of the Nazca-South America-Antarctica triple junction is shown by a triangle. Series of small arrows represent convergence vectors between the Nazca and South American plates for the last 48 Ma. (Modified from Cembrano et al., 1996, Bourgeois et al. 1997; Pardo-Casas and Molnar, 1987).....	156
<b>Figure 4.2</b> Regional geology and local structure of the Liquiñe-Ofqui fault zone for the Hornopirén region. Simplified from Hervé et al. (1979) and Cembrano (1990). Locations of available radiometric age determinations (Hervé et al. 1979; Drake et al. 1990; Drake et al. 1991; Schermer et al. 1996) are indicated with symbols. Solid square: total fusion Ar-Ar dates on biotite; half-filled square: total fusion Ar-Ar dates on hornblende; diamond: Rb-Sr whole rock isochron; triangle: K-Ar dates on biotite, inverted triangle: K-Ar whole rock dates; filled circle: U-Pb dates on zircon. Sample location is shown.....	158
<b>Figure 4.3</b> Migration of the Chile Ridge and fracture zones with respect to the plate boundary during the last 6 Ma (Bourgeois et al. 1996).....	161



**Figure 4.4** (a) Polished slab (~10 by 5 cm) of the heterogeneously deformed granodiorite. Target numbers are labeled on the polished thick section.....164

**Figure 4.5** Photomicrograph of S-C fabrics.....166

**Figure 4.6** Plot of the  $^{37}\text{Ar}/^{39}\text{Ar}$  ratio against apparent age of the different spots selected for laser dating. ....168

**Figure 5.1** Comparison between the geometry and kinematics of transpressional shear zones in experiments and nature. (a) Geometry and kinematics obtained from recent analog models of transpression (Schreurs and Coletta, 1998); (b) Geometry and kinematics of ductile shear zones in the Cenozoic magmatic arc of the southern Andes (Liquiñe-Ofqui fault zone).....178

## LIST OF TABLES

**Table 2.1.** Previously published geochronological data from the three geological transects.

**Table 3.1.** Summary of new  $^{40}\text{Ar}$ - $^{39}\text{Ar}$  age data for the Puyuhuapi and Aysen transects.

## Abstract

The southern Andes plate boundary zone records a protracted history of bulk transpressional deformation during the Cenozoic. Transpression has been related to both oblique subduction and ridge collision. However, few structural and chronological studies of regional deformation are available to support one hypothesis or the other. The present thesis addresses along and across-strike variations in the nature and timing of plate-boundary deformation to better understand the Cenozoic tectonics of the southern Andes. A general objective was to gain insights into the nature of transpressional deformation at obliquely convergent plate margins. Five transects were mapped along the southern Andes, from 39°S to 46°S. The northernmost, Liquiñe transect (39°S), documents ductile deformation of pre-Late Cretaceous age. Brittle deformation is represented by a regional, high angle, northeast-trending reverse fault that places greenschist facies mylonites against an undeformed Miocene granitoid. In contrast, Late Cenozoic brittle faulting of Cretaceous and Miocene plutons is well developed farther south at Reloncaví (41°S), where contractional and strike-slip kinematics are documented. At Hornopirén (42°S), Late Cenozoic ductile to brittle dextral strike-slip deformation along northeast striking shear zones was continuous from syntectonic pluton emplacement at 10 Ma, to low temperature, solid-state deformation at ca. 4.3 Ma. Brittle faults indicate that dextral strike-slip deformation remained active after 3 Ma. Puyuhuapi and Aysén transects (44-46°S), document a remarkable increase in the contractional component of ductile and brittle deformation. At Puyuhuapi (44°S), north-south trending, high-angle contractional ductile shear zones that developed from plutons, coexist with moderately dipping dextral-oblique shear zones in the wallrocks. In Aysén (45-46°), top to the southeast, oblique thrusting predominates to the west of the Cenozoic magmatic arc, whereas dextral strike-slip shear zones develop within it. New  $^{40}\text{Ar}$ - $^{39}\text{Ar}$  data from mylonites and undeformed rocks from the five transects suggest that dextral strike-slip and contractional deformation occurred at nearly the same time but within different structural domains along and across the orogen. For instance,  $^{40}\text{Ar}$ - $^{39}\text{Ar}$  laser dating on highly strained synkinematic biotite from plutonic rocks with S-C fabrics at 42°S documents dextral ductile shear at  $4.3 \pm 0.3$  Ma. Similar ages were obtained on both high strain pelitic schists with dextral strike-slip kinematics ( $4.4 \pm 0.3$  Ma, laser on muscovite-biotite aggregates, Aysén transect, 45°S) and on mylonitic plutonic rocks with contractional deformation ( $3.8 \pm 0.2$  to  $4.2 \pm 0.2$  Ma, fine-grained, recrystallized biotite, Puyuhuapi transect). Oblique-slip, dextral reverse kinematics of uncertain age is documented at the Canal Costa shear zone (45°S) and at the Queulat shear zone at 44°S. Published dates for the undeformed protholiths suggest both shear zones are likely Late Miocene or Pliocene, coeval with contractional and strike-slip shear zones farther north. Coeval strike-slip, oblique-slip and contractional deformation on ductile shear zones of the southern Andes suggest different degrees of along- and across-strike deformation partitioning of bulk transpressional deformation. The long-term dextral transpressional regime appears to be driven by oblique subduction. The short-term deformation is in turn controlled by ridge collision from 6 Ma to present day. This is indicated by most deformation ages and by a southward increase in the contractional component of deformation. Oblique-slip to contractional shear zones at both western and eastern margins of the Miocene belt of the Patagonian batholith define a large-scale flower structure by which deeper levels of the crust have been differentially exhumed since the Pliocene.

## ACKNOWLEDGEMENTS

This thesis is the result of the generosity and enthusiasm of many people and institutions devoted to education and science. Dalhousie University granted me a Walton Killam Doctoral Fellowship, which funded my stay in Canada and paid for my tuition fees. The University of Chile kept my job and salary while I was away. The Chilean National Science Foundation (Fondo de Desarrollo Científico y Tecnológico, FONDECYT) granted me two consecutive research projects for structural work in southern Chilean Andes during the last 5 years through projects 1931096 and 1950497.

I thank my advisor Prof. Marcos Zentilli for staying optimistic throughout the development of my thesis project. He firmly believed that the chances of married with children foreigners to pursue graduate students in Canada were good. Marcos remained convinced of the relevance of my scientific project and that was fundamental in the initiation and final conclusion of this thesis.

Professors Peter Reynolds, Becky Jamieson and Nick Culshaw made a significant contribution to the definition and development of the main subject of this thesis. Their constructive criticism during the thesis defense is greatly appreciated. Dr. David Prior (University of Liverpool), external examiner of the present thesis, contributed to improve the text and clarify some of the ideas regarding the significance of microstructural analysis, Ar dating and current tectonic models of Andean evolution.

Special thanks to Keith Taylor for his assistance during the different stages of sample preparation for Ar-Ar analysis and final dating. His patience and care when dealing with my unusually young rocks is greatly appreciated. Keith did a great job with the laserprobe on tiny, young and highly deformed minerals.

Professors and friends Francisco Hervé (University of Chile) and Myrl Beck (Western Washington University, USA) taught me the fundamentals of scientific research and are somewhat responsible for my initiation in science. Their permanent interest and enthusiasm throughout the development of this thesis is greatly appreciated.

Liz Schermer (Western Washington University, U.S.A.), Alain Lavenu (ORSTOM, France) and Alejandro Sanhueza (University of Chile) have been coworkers in my research projects during the last years. In particular, I thank Liz for my first lessons on kinematic analysis of mylonites. Alain taught me the tricks and shortcomings of brittle fault-slip data analysis with patience and interest. Alejandro Sanhueza (El Flaco) was the first student I got interested in kinematic analysis, and now he is doing a PhD thesis of his own. Liz, Alain and Alejandro made important suggestions and corrections to Chapter 2 of this thesis, which hopefully will become a collective journal publication.

Chilean graduate students Gloria Arancibia, Gloria López, Jorge Clavero and Luis Lara participated in several field trips to southern Chile from 1994 to 1998 and contributed with many good ideas. I thank them for their time and effort, which now concludes with my thesis and publications in common with some of them. Cristina Maureira helped with manuscript preparation and final checking of the whole thesis draft.

My wife Connie, my son Josecito and my daughter Carla supported me all this time with their love and company. I dedicate this thesis to them, because everything I have done in the last years has been the result of a collective family effort.

Finally, I thank my parents, Stelio and Mariolina who have shown me with their lifetime of care and commitment that only with love and perseverance it is possible to reach one's personal goals.

# Chapter 1. Introduction

## 1.1 Introductory Statement

The nature and style of regional-scale deformation at plate boundary zones is primarily controlled by the magnitude and angle of the relative plate motion vector (e.g. Dewey, 1980, McKenzie and Jackson, 1983; Braun and Beaumont, 1995; Teyssier et al. 1995). Bulk transpressional deformation is expected at obliquely convergent plate-boundary zones (e.g. Sanderson and Marchini, 1984; Fossen et al. 1994). However, the exact manner in which long-term transpressional deformation is accommodated along and across long-lived convergent plate boundaries varies significantly from one orogen to another. This appears to depend upon specific kinematic and geological constraints that are not yet fully understood (e.g. Dewey et al. 1998). Systematic geometric and kinematic studies in the field, along with detailed  $^{40}\text{Ar}$ - $^{39}\text{Ar}$  dating of deformed rocks at long-lived convergent plate-boundaries with protracted deformation histories, can provide significant information on the nature of transpressional deformation.

The southern Chilean Andes is a natural laboratory to investigate the nature of long-term and short-term transpressional deformation across an obliquely convergent continental margin. An active ridge, the Chile Ridge, is currently subducting under southwestern South America and a trench-parallel fault system has developed along the Cenozoic magmatic arc (Figure 1.1). The Cenozoic geodynamic setting of the southern Chilean Andes is well constrained, showing relatively steady right-oblique subduction of the Farallon (Nazca) plate beneath South America since 48 Ma with the exception of orthogonal convergence from 26 to 20 Ma (Pardo-Casas and Molnar, 1987) (Figure 1.1).

**Figure 1.1** Geodynamic setting of the southern Andes plate boundary zone (modified from Herron, 1981; Cande and Leslie, 1986; Pardo-Casas and Molnar, 1987; Cembrano et al. 1996; Bourgois et al. 1996).

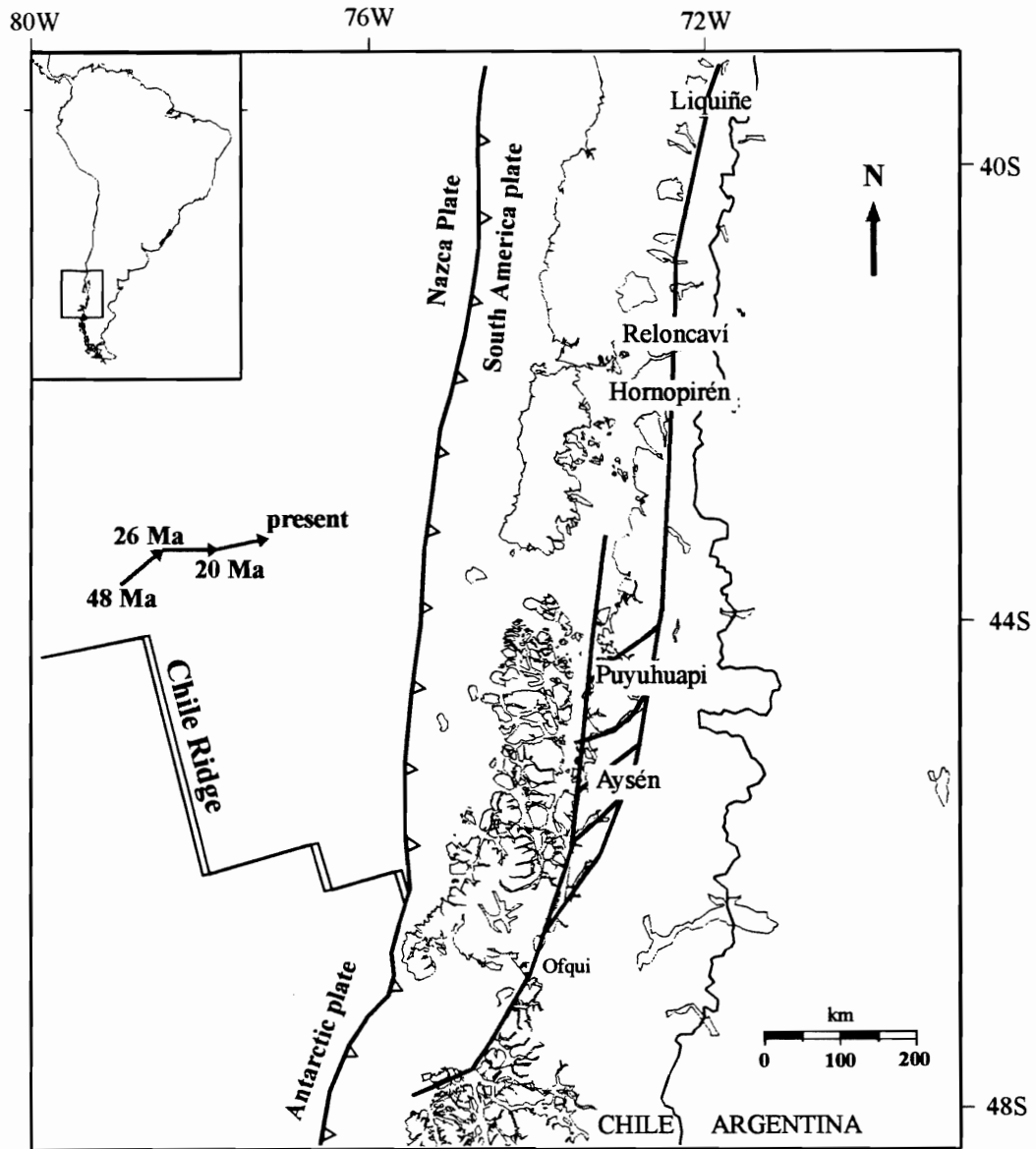


Figure 1.1



This thesis documents structural and  $^{40}\text{Ar}$ - $^{39}\text{Ar}$  thermochronological data from five transects across the Cenozoic magmatic arc of the southern Andes. These transects, named according to geographic localities, are from north to south: Liquiñe, Reloncaví, Hornopirén, Puyuhuapi and Aysén. These transects are distributed along the main lineaments of the Liquiñe-Ofqui fault zone (Figures 1.1; 1.2; 1.3). Based on field and thermochronological data from the transects, I present a tectonic model for the southern Andes plate boundary zone, which accounts for the complex combination of partly coeval dip-slip, oblique-slip and strike-slip deformational structures observed in the field.

## **1.2 Aims and Purpose of this Thesis**

The main purpose of this thesis is to better understand the nature and style of regional-scale deformation at transpressional plate boundaries and its causal relation with plate kinematics and other factors such as ridge subduction. Specific aims are: (1) to better constrain the geometry, kinematics and timing of deformation along and across a ca. 800 km-long segment of the southern Andes; and (2) to assess the relative importance of oblique subduction and ridge collision in the tectonics of the southern Andes, north of the Nazca - South America - Antarctica triple junction. Previous studies have attempted to answer some of these questions (e.g. Forsythe and Nelson, 1985; Pankhurst et al. 1992; Nelson et al. 1994). However, most of these studies lack the detailed structural and chronological data needed to support tectonic models. This thesis represents the first systematic study of the tectonics of the southern Andes magmatic arc using current modern techniques of structural, kinematic and thermochronological analysis of deformed rocks.

**Figure 1.2** Regional scale geologic and tectonic setting of the Southern Andes plate boundary zone from 39 to 43 degrees south latitude (modified from SERNAGEOMIN, 1980; Cande and Leslie, 1986; Pardo-Casas and Molnar, 1987; Cembrano, 1996; Burgois, 1997).

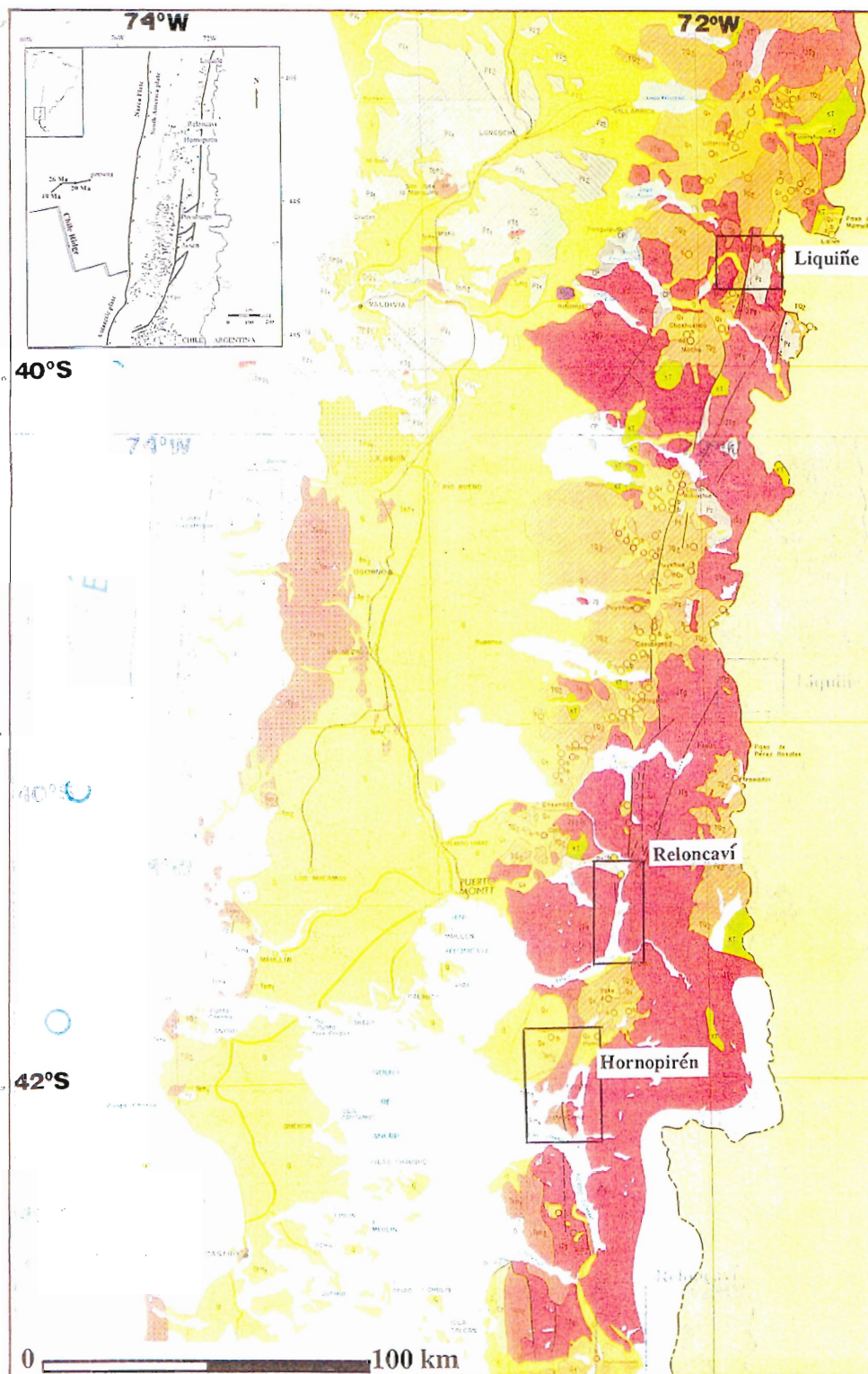


Figure 1.2

**Figure 1.3** Regional scale geologic and tectonic setting of the Southern Andes plate boundary zone from 44 to 48 degrees south latitude (modified from SERNAGEOMIN, 1980; Cande and Leslie, 1986; Pardo-Casas and Molnar, 1987; Cembrano, 1996; Burgois, 1997).

Partial Legend: Gray (Pz): Paleozoic basement metamorphic rocks; yellow (Q): Quaternary sediments; green (Ki): Lower Cretaceous (?) volcanosedimentary rocks; light brown (TQ<sub>2</sub>) Pliocene-Quaternary volcanic rocks; circles: Recent volcanic centers (Q<sub>v</sub>); red (Jg, JTg, Tg): North Patagonian Batholith; dark green and blue (K, J): Jurassic-Cretaceous volcano-sedimentary rocks.



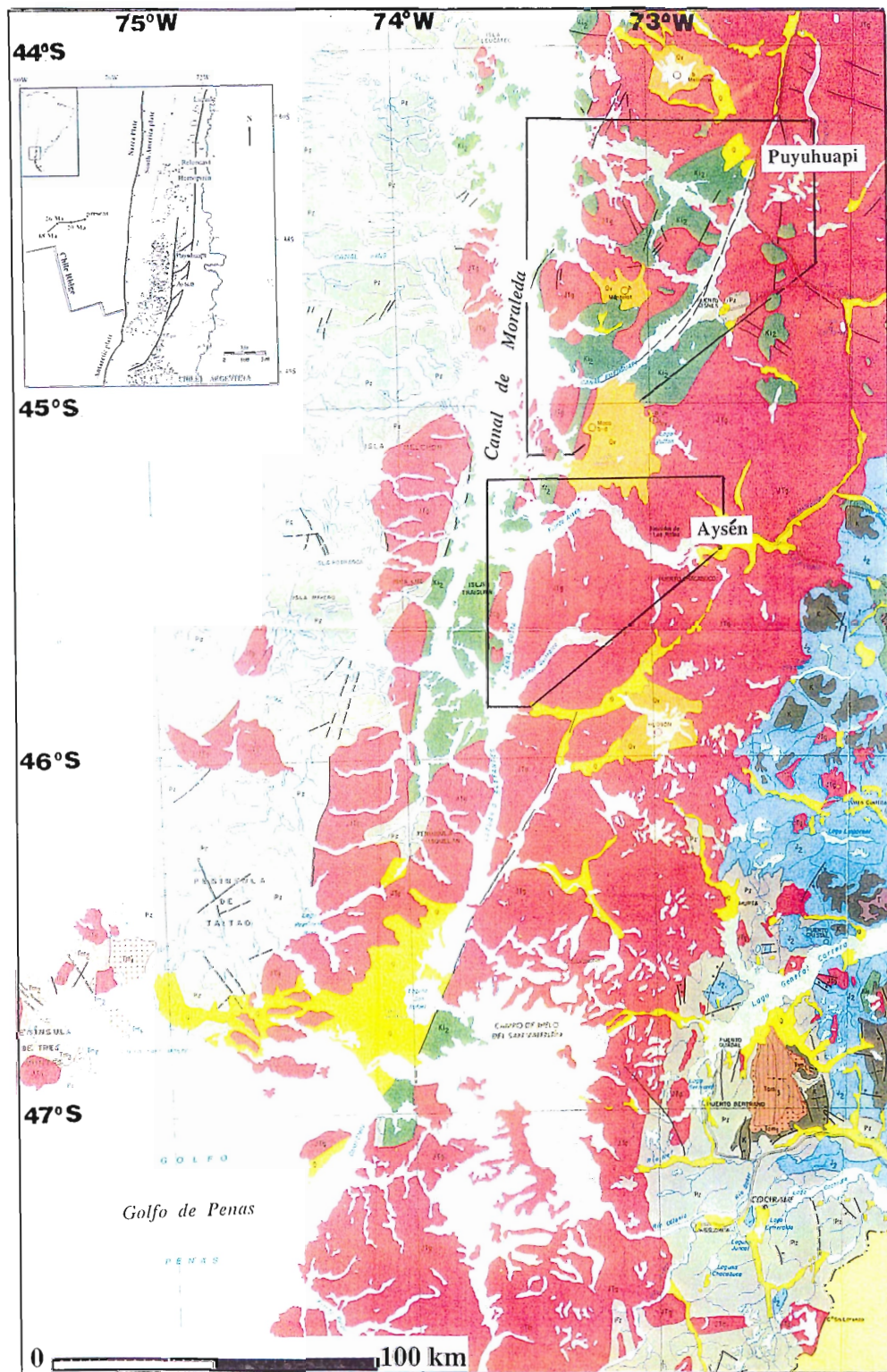


Figure 1.3

### **1.3 Kinematics of deformation at plate boundary zones: a review**

The kinematics of deformation at plate boundaries is primarily controlled by the direction and magnitude of the relative slip vector with respect to the trend of the plate boundary zone (e.g. McKenzie and Jackson, 1983, Tikoff and Teyssier, 1994; Braun and Beaumont, 1995).

End-member cases of volume-constant, monoclinic deformation, are strike-slip, contractional and extensional plane strain deformations (e.g. Fossen et al. 1994, Figure 1.4a,b, c). Monoclinic deformation implies that the rotation axis remains vertical and parallel to one of the incremental axis of the strain ellipsoid during progressive deformation.

Pure strike-slip kinematics results from a slip vector that is parallel to the plate boundary zone (Figure 1.4a). The deforming zone undergoes simple shearing; the maximum instantaneous shortening axis is horizontal and lies at 45 degrees with respect to the plate boundary zone. Progressive simple shearing produces both stretching and rotation of material lines with respect to the boundary zone on a horizontal plane (e.g. Means, 1990). This implies that the finite deformation ellipsoid is non-coaxial with the incremental deformation ellipsoid leading to a non-coaxial progressive deformation. Foliation is vertical and oblique with respect to the boundary. Stretching lineation remains horizontal during progressive deformation. Pure contractional deformation results from a convergence vector perpendicular to the plate boundary zone (Figure 1.4b). The deforming zone undergoes pure shearing; the maximum instantaneous shortening axis lies at 90 degrees with respect to the plate boundary zone.

**Figure 1.4** Kinematics of plate boundary zones assuming monoclinic, constant-volume deformation. Block A is allowed to move, block B remains fixed (simplified from Fossen et al. 1994).

(a) Simple shearing results from a slip vector parallel to the plate boundary zone; schistosity is vertical and oblique to the plate boundary, stretching lineation is horizontal.

(b) Contractional deformation derives from plate-orthogonal convergence, foliation is vertical and boundary-parallel, stretching lineation is vertical as material extrudes vertically to accommodate shortening.

(c) Pure extensional deformation results from plate-orthogonal divergence, foliation and stretching lineations are horizontal.

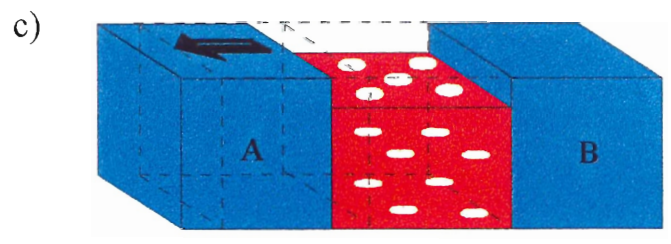
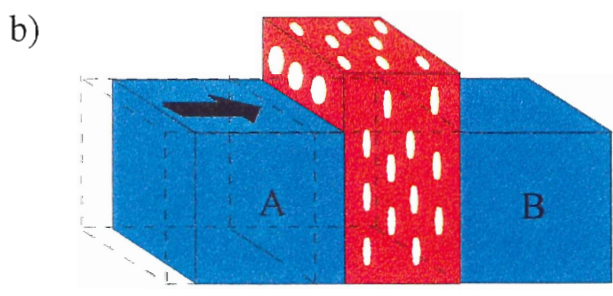
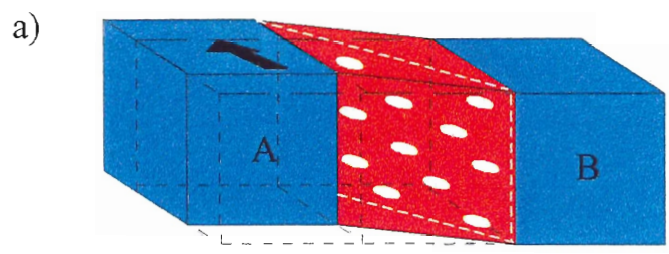
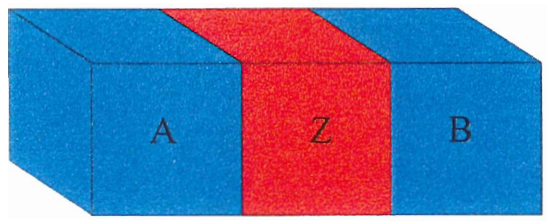


Figure 1.4

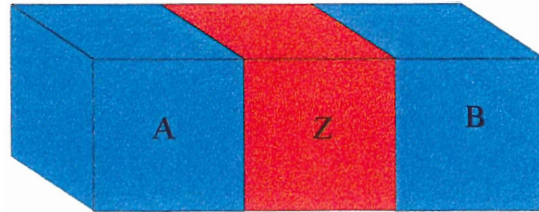


Progressive pure shearing produces stretching of material lines within the deforming zone with no bulk rotation. Since pure contractional deformation is a plane-strain deformation, during natural contraction material extrudes vertically with progressive pure shearing (i.e. the long axis of the finite strain ellipsoid is vertical). Thus, the finite and instantaneous deformation ellipsoids remain coaxial during progressive deformation. This effect is called a coaxial progressive deformation (e.g. Means, 1990). Foliation is vertical and parallel to the plate boundary. Stretching lineations are vertical.

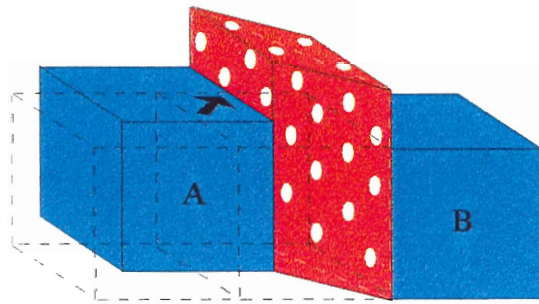
Pure extensional deformation results from a divergence vector perpendicular to the plate boundary zone (Figure 1.4c). As in contractional deformation, the deforming zone undergoes pure shearing, however in this case both instantaneous and finite stretching axes are horizontal; plane strain extension is accomplished via vertical shortening and lateral extrusion. Foliations and lineations are horizontal.

Consequently, the general case of monoclinic deformation will result from different combinations of pure contractional and strike-slip deformation or between pure extensional and strike-slip deformation. Concomitant contractional and strike-slip kinematics is called transpression (e.g. Harland, 1971; Sanderson and Marchini, 1984) whereas transtension corresponds to the combination of extensional and strike-slip components (Figure 1.5a,b). At convergent plate margins the velocity vector lies somewhere between 0 and 90 degrees with respect to the plate boundary zone. Therefore, the general case is that of oblique convergence and transpressional kinematics will be expected to dominate across and along the plate boundary zone (Figures 1.5a, 1.6)

**Figure 1.5** Kinematics of transpressional and transtensional plate boundary zones assuming monoclinic, constant-volume deformation. Expected geometry of foliation and stretching lineation are shown (simplified from Sanderson and Marchini, 1984; Fossen et al. 1994; Tikoff and Greene, 1997).



a)



b)

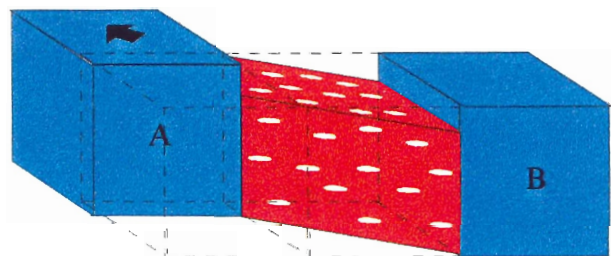


Figure 1.5

In recent years, several workers have obtained quantitative relationships between the angle of convergence and the geometry of incremental and finite deformation ellipsoids. Consequences for the orientation and nature of geological structures such as stretching lineations, foliations and folds have also been assessed (e.g. Sanderson and Marchini, 1984; Tikoff and Teyssier, 1994; Jones and Tanner, 1995; Krantz, 1995).

Tikoff and Teyssier (1994) obtained exact relationships between the angle of plate convergence and the direction of the maximum incremental shortening and stretching axes assuming constant-volume monoclinic deformation. They defined two important parameters:  $\alpha$ : angle between the plate boundary and the convergence vector;  $\theta$ : angle between the maximum instantaneous shortening axis and the plate boundary (Figure 1.7). From tensor analysis they obtain different absolute values of  $\theta$  according to known values of  $\alpha$  in the range of 0 and 90 degrees (from pure strike-slip to pure contraction). One simple but important consequence of Tikoff's and Teyssier's model of transpression is that the convergence vector is in no case parallel to the maximum instantaneous shortening direction in the plate margin, with the sole exception of orthogonal convergence. Furthermore, by introducing different degrees of deformation partitioning of transpressional deformation (Figure 1.6), the geometric relationship between the convergence vector and shortening direction within the deforming zone can be established. They introduced partitioning as a variable based on the fact that most convergent plate boundaries show plate-boundary-parallel crustal faults that have long been thought to localize the pure strike-slip component of deformation (e.g. Fitch, 1972; Beck, 1983; McCaffrey, 1992). Deformation partitioning of transpression is a critical concept in structural geology. It simply means that strike-slip and contractional

**Figure 1.6** Homogeneously distributed versus completely partitioned transpressional deformation. Stretching lineation switches from horizontal to vertical for high strain transpressional deformation (modified from Tikoff and Greene, 1997).

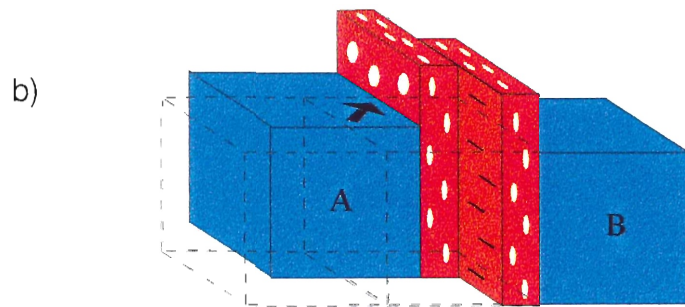
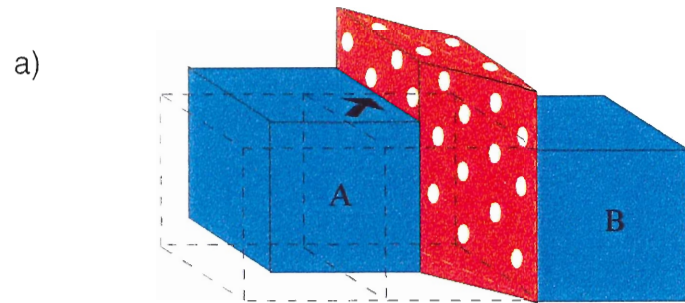
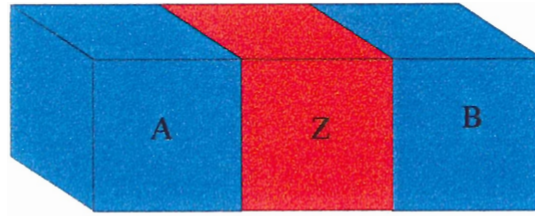
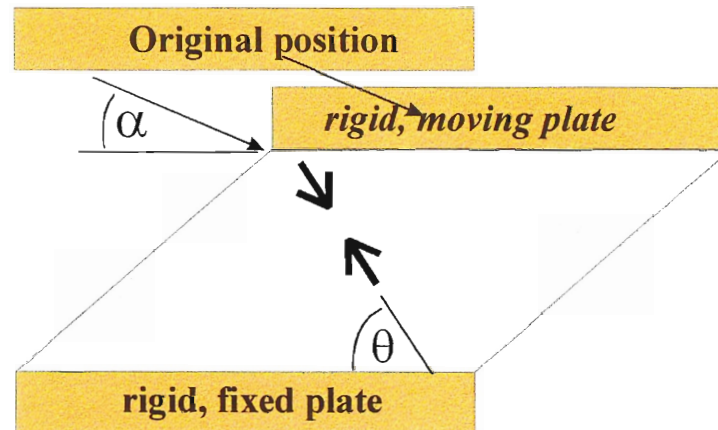


Figure 1.6

**Figure 1.7** Plan view of a constant-volume, monoclinic transpressional deformation zone (adapted from Teyssier et al. 1995). Homogeneously distributed and completely partitioned transpression are shown. Parameter  $\alpha$  is defined as the angle between the convergence vector and the plate boundary, parameter  $\theta$  is the angle between the maximum instantaneous shortening direction and the plate boundary. A large, thick arrow represents the convergence vector. The maximum instantaneous shortening axis is indicated with a small, thin arrow.

## HOMOGENEOUS VS PARTITIONED TRANSPRESSION

HOMOGENEOUS



$\alpha$  = angle between the convergence vector and the plate boundary

$\theta$  = angle between the maximum instantaneous shortening axis and the plate boundary

PARTITIONED

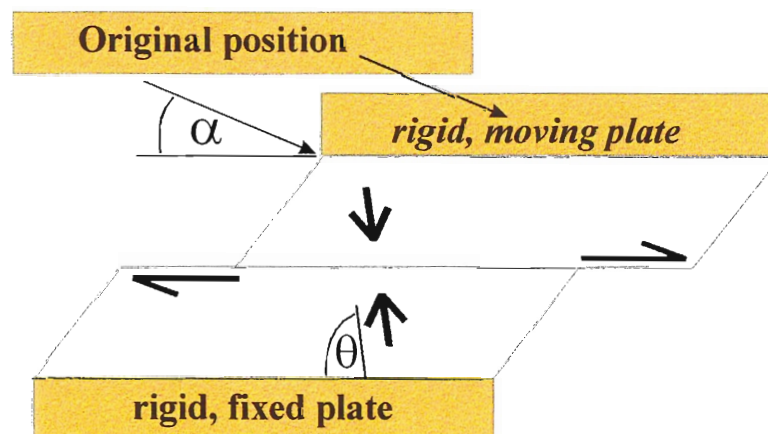


Figure 1.7



components of the overall bulk transpressional deformation are accommodated in different discrete domains across the deforming zone, i.e. transpression is not distributed homogeneously across the deforming zone but is compartmentalized (Figures 1.7a,b).

The most important contribution of Tikkoff's and Teyssier's model is that it predicts the orientation of the long and short axes of the incremental strain ellipsoids across transpressional plate boundary zones for different angles of convergence and different degrees of strike-slip partitioning. One important consequence of this is that the nature and orientation of field structures such as foliations and stretching lineations can be related back to the bulk deformation regime. For instance, their model can predict the orientation of thrust faults and strike-slip faults for non-partitioned to completely partitioned case studies for the brittle and ductile fields.

The most spectacular case of nearly complete partitioning of transpressional deformation occurs at the Pacific-North America plate boundary. The deforming zone is several hundred kilometers wide and, surprisingly, displays subparallel traces of regional thrusts and strike-slip faults, the most important of which is the San Andreas Fault (Figure 1.8). If overall transpression was homogeneously distributed across the deforming zone, the trace of thrust faults should be significantly different than that of strike-slip faults. This was a common belief in the seventies and early eighties following classical clay box experiments (Tchalenko, 1970) and distributed simple shear and transpressional models (e.g. Harding, 1974; Ramsay, 1980) (Figure 1.4). Seismic, geodetic and geologic studies along the Pacific-North American plate boundary strongly suggest that the San Andreas Fault takes up almost the entire strike-slip component of bulk transpression by dextral slip along the fault. The other kinematic component of

transpression, plate-boundary orthogonal contraction, is accommodated by a series of thrust faults and folds whose trends are almost parallel to the main trend of the San Andreas Fault (Figure 1.8).

In other papers (Fossen et al. 1994; Tikoff and Greene, 1997) the orientation and shape of instantaneous and finite deformation ellipsoids are predicted for different angles of convergence. The term pure-shear dominated transpression is used for those cases in which  $\alpha$  is greater than 20 degrees, whereas wrench-dominated transpression is used in those cases in which  $\alpha$  is smaller than 20 degrees. These analyses are of great importance for the structural and kinematic analysis of deformed rocks since the orientation of the finite deformation ellipsoid is believed to be closely related to observed features such as stretching lineations and fold axes.

During pure-shear dominated transpression the long axis of the strain ellipsoid is always vertical, therefore stretching lineations will be vertical for the low and high strain cases. Additionally, the strike-slip component of the overall pure-shear dominated transpression will be absorbed through lateral displacement concomitant with vertical stretching (Tikoff and Greene, 1997). Therefore, the direction of instantaneous and finite stretching for pure shear dominated transpression is never parallel to the direction of lateral shear as assumed by traditional kinematic analyses (e.g. Berthe et al. 1979; Simpson and Schmid, 1983). For instance, in a pure-shear dominated dextral transpressional regime, stretching lineations are vertical but kinematic indicators of dextral shear can be found on horizontal planes (e.g. Hudleston et al. 1998; Robin and Cruden, 1994; Tikoff and Greene, 1997)

**Figure 1.8** High degree of strike-slip partitioning of transpressional deformation at the Pacific-North America plate boundary. The San Andreas fault takes up most of the simple shear component, bounding blocks accommodate margin-orthogonal contraction through a series of thrusts and fold axes that are nearly parallel to the San Andreas Fault (adapted from Fossen et al. 1994).

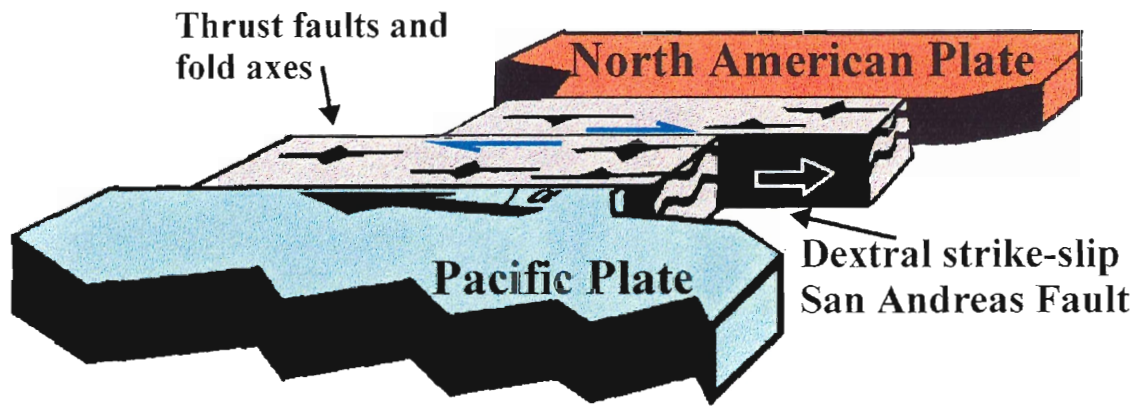


Figure 1.8

**Figure 1.9** Geometry of foliation and stretching lineation for wrench dominated transpression. Stretching lineation switches from horizontal at low strains to vertical at high strains, passing through an intermediate stage of a poorly developed lineation. (from Tikoff and Greene, 1997).

## Wrench-dominated transpression

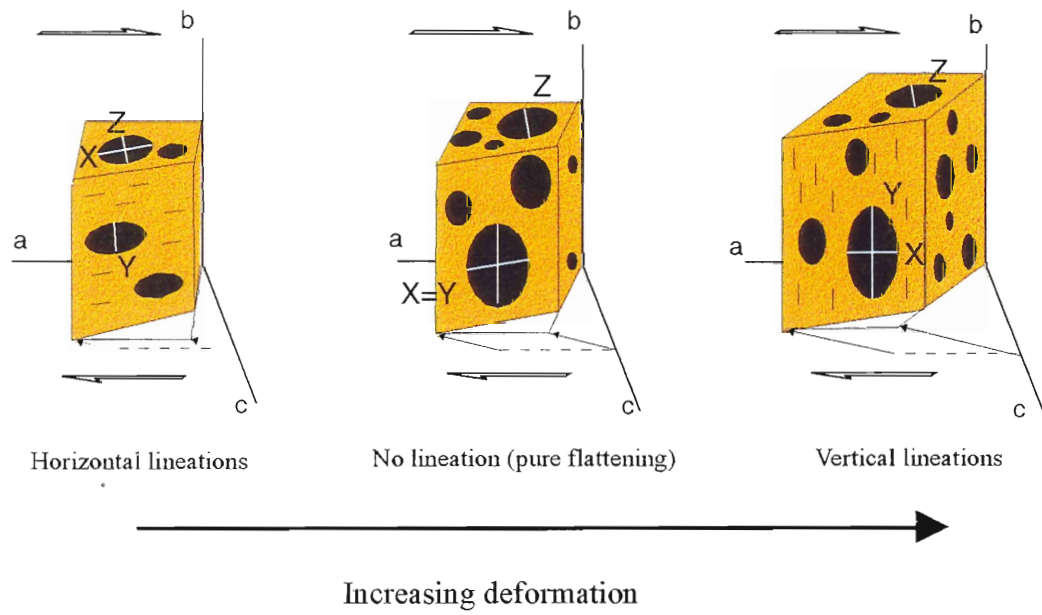


Figure 1.9

During wrench-dominated transpression, the long axis of the finite strain ellipsoid switches from horizontal at low strains to vertical at high strains, passing through an intermediate stage of a poorly-developed stretching lineation, which are typical of flattening-type strains (Figure 1.9).

If deformation partitioning is added as another variable to the model of constant-volume, monoclinic transpression, one may expect a complex coexistence of subhorizontal and subvertical stretching lineations across a transpressional shear zone at all scales, from the hand sample to the plate margin. In fact, subhorizontal stretching lineations may dominate within discrete domains or surfaces, whereas subvertical lineations will prevail in other intercalated structural domains. A classical simple case of deformation partitioning at the sample scale is that of S-C fabrics. It is common that S-C mylonites show no stretching lineation on the schistosity surface (flattening-type strain prevails) while showing subhorizontal lineations (streaky lineations similar to slickensides) on C surfaces. These are interpreted to take up a significant part of the strike-slip component of the transpressional deformation (e.g. Lin and Williams, 1992) (Figure 1.10). Whatever the nature of the combination of strike-slip and contractional components, and the degree of deformation partitioning, all domains will show vertical lineations on high-strain transpressional shear zones.

**Figure 1.10** Heterogeneous transpression is accommodated by discrete domains within which the components of pure shear and simple shear deformation are increased. S-C fabrics are a natural example of heterogeneous transpression at the sample scale (adapted from Tikoff and Greene, 1997).



## Heterogeneous transpression

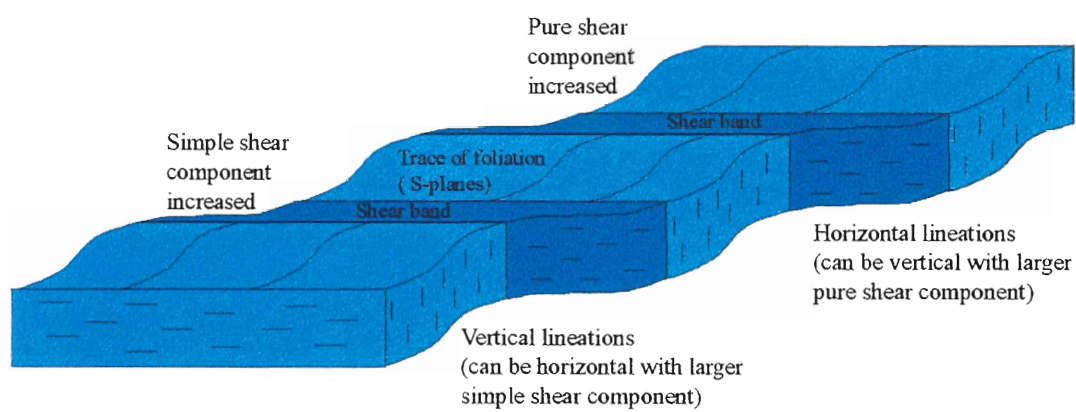
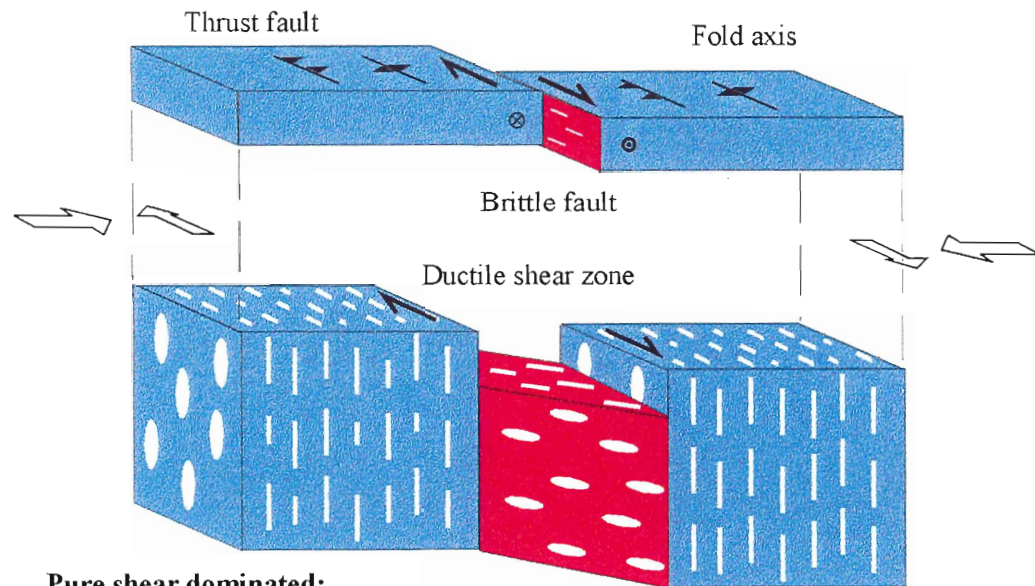


Figure 1.10

**Figure 1.11** Partitioning of bulk transpressional deformation for the upper, brittle crust and for the mid- to lower ductile crust. The simple shear component of transpression is accommodated by slip on a single fault in the upper crust. This fault grades downward into a wider zone of distributed ductile simple shear (modified from Fossen et al. 1994).



**Pure shear dominated:**  
Vertical stretching lineation  
and vertical foliation sub-parallel  
to deformation zone.

**Wrench dominated:**  
Horizontal lineation and  
vertical foliation oblique  
to deformation zone

Figure 1.11

**Figure 1.12** Cartoon showing the case of general triclinic heterogeneous transpressional deformation as commonly observed in nature. Discrete high-strain zones of predominant horizontal simple shear coexist with other zones in which the pure shear component predominates. Boundary orthogonal contraction is not only accommodated by vertical extrusion in the pure shear domains but also through a significant dip-slip component of motion within moderately dipping reverse shear zones. Large intervening domains of non-deformed rocks separate the narrower, high-strain domains

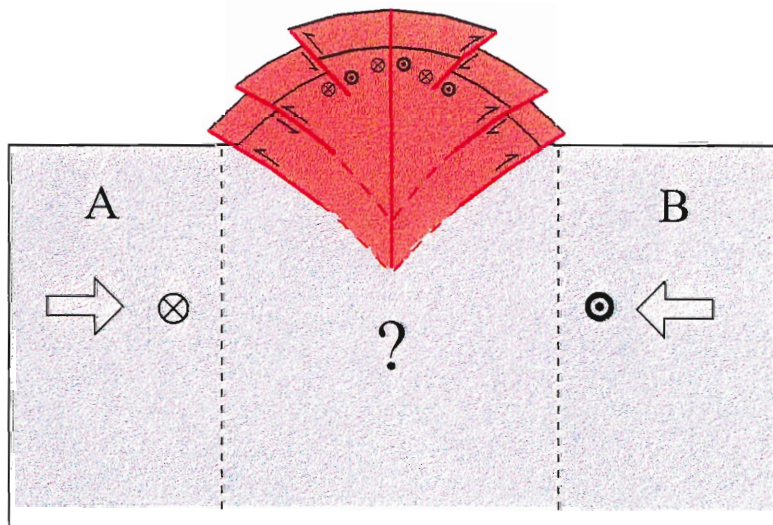
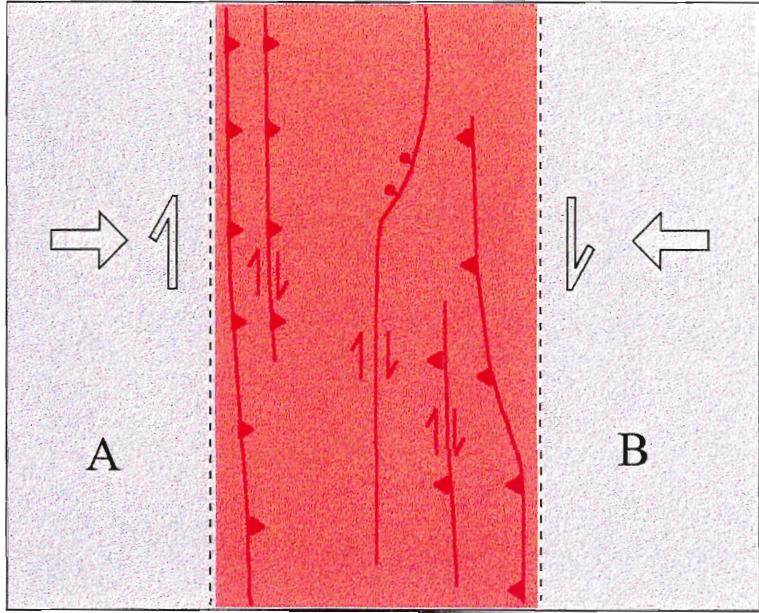


Figure 1.12

It is important to emphasize that Tikoff's and Teyssier's (1995) model of deformation and deformation partitioning for transpressional plate boundaries is strictly valid only for the upper brittle crust. In such environments, a single major fault accommodates the strike-slip component of motion, whereas the pure shear component is absorbed across contiguous volumes of rock (Figure 1.11). However, for the ductile mid- to lower crust, which is the case for exhumed ancient shear zones, one may expect a more complex deformation-partitioning pattern. This includes broader zones accommodating the simple shear component and adjacent zones absorbing the pure shear component (Figure 1.11). Furthermore, an overall transpressional deformation zone in nature may contain a complex combination of coexisting domains of wrench-dominated and pure shear dominated transpressional shear zones, with large intervening volumes of virtually undeformed rock (Figure 1.12). The geometry and kinematics of such crustal-scale deforming zones developed at obliquely convergent plate boundaries can be predicted by dynamic models of deformation (e.g. Braun and Beaumont, 1995; figure 1.13). Through a series of numerical experiments, Braun and Beaumont (1995) obtained the nature and the three-dimensional geometry of regional-scale shear zones at transpressional plate boundaries for a whole range of kinematic boundary conditions ranging from pure convergence to pure transcurrent motion of the two plates. In models dominated by convergence, both contractional and simple shear components are accommodated by oblique slip across a single pair of V-shaped structures (deformation is not partitioned at the crustal scale). In contrast, models dominated by transcurrent boundary conditions predict two separate sets of coexisting structures. Shallowly-dipping thrust zones

**Figure 1.13** Geometry and boundary conditions for a dynamic numerical model of obliquely convergent plate-boundary zones (Braun and Beaumont, 1995). The model assumes oblique convergence between two near-rigid lithospheric mantles, one of which detaches at S and is subducted beneath the other. Overlying crust undergoes shortening and plate boundary-parallel shearing concentrated in the region above S. The continental-scale style of deformation and partitioning of bulk transpression depends on the ratio ( $r$ ) of the normal component with respect to the normal plus lateral component of motion. For compression-dominated cases ( $r$  close to 1), both contraction and strike-slip components are accommodated within a pair of v-shaped moderately-dipping oblique-slip thrust zones. In contrast, for increased wrenching component ( $r$  close to 0), bulk transpressional deformation is partitioned into thrust shear zones and strike-slip shear zones

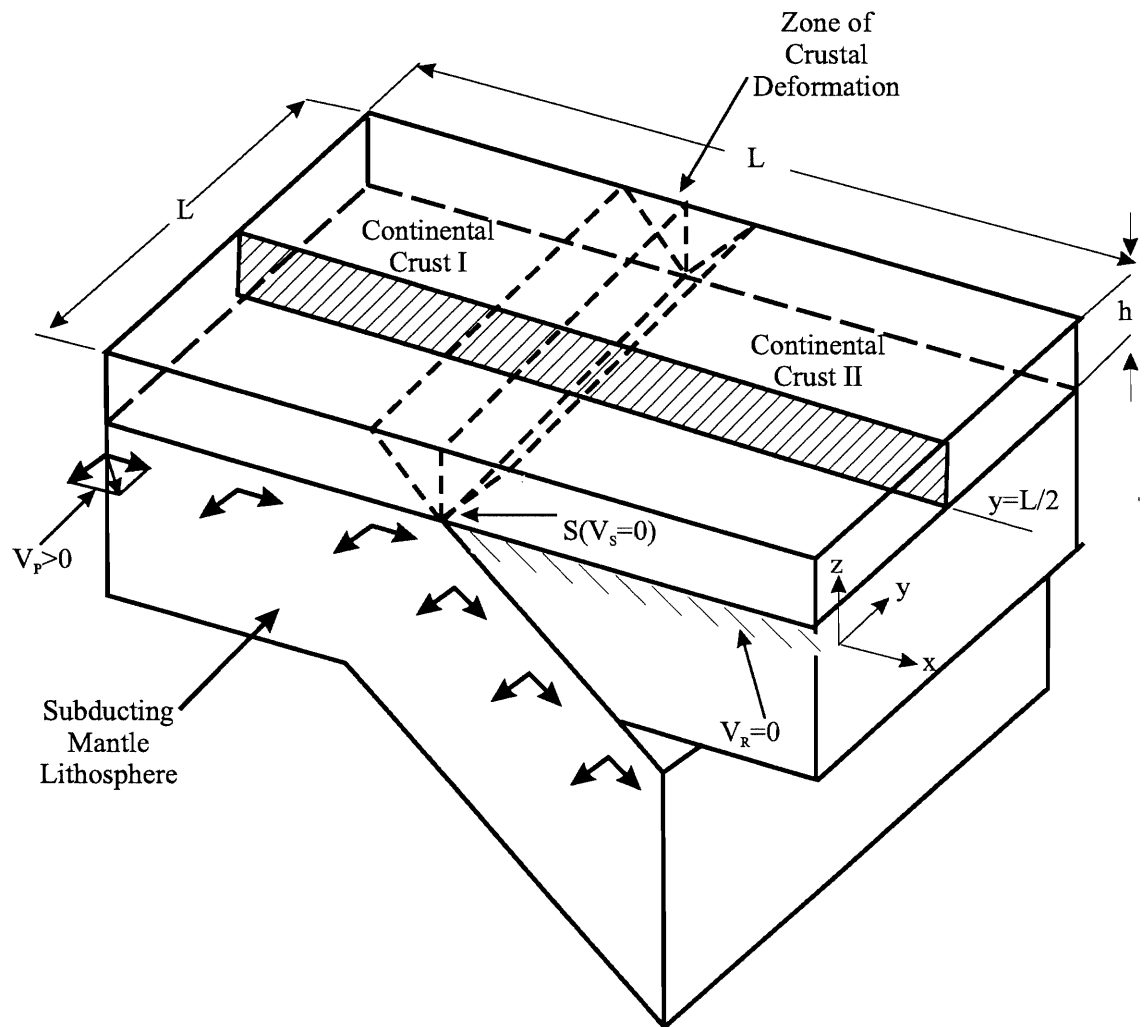


Figure 1.13



accommodate the contractional component of deformation whereas steeply-dipping shear zones absorb the strike-slip component of oblique convergence (bulk transpressional deformation is partitioned). The predictions of this dynamic model are in good agreement with those of Teyssier et al. (1995)'s kinematic model in the sense that partitioning of bulk transpressional deformation is expected for wrench-dominated plate boundaries, whereas no partition is expected for contraction-dominated convergent zones. However, Braun and Beaumont (1995) find that the contractional component is accommodated through slip along shallowly-dipping reverse shear zones. In contrast, Teyssier et al (1995) propose that plate boundary orthogonal shortening is accommodated through vertical extrusion with no component of dip-slip.

So far, I have described currently accepted models for constant-volume, monoclinic deformation and their consequences in the predicted orientations of geological structures at all scales. However several authors state that monoclinic, constant-volume deformation models only account for a small part of all possible cases of natural deformation (e.g. Lin et al. 1998; Jones and Holdsworth, 1998). By documenting the geometry of foliations and stretching lineations of natural shear zones, they have recently challenged the model of monoclinic deformation. They propose, instead, that natural deformation has a triclinic symmetry. To discuss the consequences of these new models, it is important to recall two key assumptions made by previous models of monoclinic deformation, which may not hold true for natural cases: (1) the simple shear component is horizontal, i.e. no component of vertical simple shear is considered; and (2) the pure shear component of deformation is accomplished via vertical extrusion, i.e.

no lateral extrusion is allowed. As I will show below, both assumptions have strong consequences for the predicted geometry of stretching lineations in deformed rocks.

First of all, because simple shearing is assumed to be horizontal, the stretching component induced by it during progressive deformation will remain horizontal. So the contribution of the simple shearing component of transpression to the overall bulk deformation will be that of horizontal stretching. Likewise, as the pure-shear component is accomplished by vertical extrusion only, the contribution of pure-shear to bulk transpression will be that of vertical stretching. A competition will then take place between the horizontal stretching induced by simple shearing and the vertical stretching induced by pure shearing. Because pure shearing is more efficient in accumulating finite strain (e.g. Fossen et al. 1994), the stretching lineation will *switch* from horizontal at low strain to vertical at high strain, passing through an intermediate stage of no lineation or flattening strain (Figure 1.9). In consequence, monoclinic models do not account for stretching lineations that vary from *strike-parallel* to *dip-parallel* (i.e. oblique lineations). Oblique lineations are, however, common features in ancient shear zones (e.g. Robin and Cruden, 1994; Lin et al. 1998). The existence of oblique lineations in nature can be explained theoretically when a vertical component of simple shear is introduced as a variable in mathematical models of deformation (Figure 1.14). These models (e.g. Jones and Holdsworth, 1998; Lin et al. 1998) are then triclinic in symmetry and show significant differences with the more simplistic monoclinic models of previous authors (e.g. Teyssier et al. 1995, Tikoff and Greene, 1997). Although the complexity of the new triclinic models could be somewhat discouraging for the field structural geologists, it seems reasonable to be extremely careful when relating geological structures to a

particular kinematic framework without a full, rigorous field description. Only by careful and systematic mapping and dating of field structures such as foliations, stretching lineations and kinematic indicators across high strain zones, it will be possible to better understand their significance into a broad kinematic context.

**Figure 1.14.** Triclinic deformation is characterized by the existence of a vertical simple shear component of motion. The component of simple shear is then not necessarily horizontal but may be oblique with respect to the horizontal plane. Resulting deformation is no longer monoclinic but triclinic, allowing for a more general orientation of foliations and stretching lineations (adapted from Lin et al. 1998).

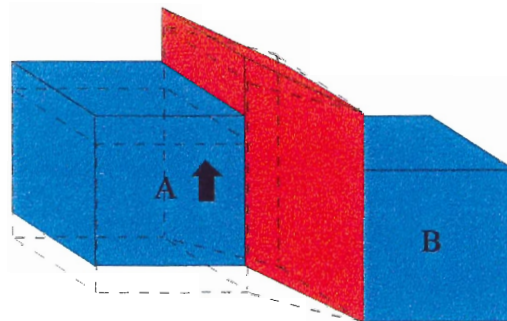
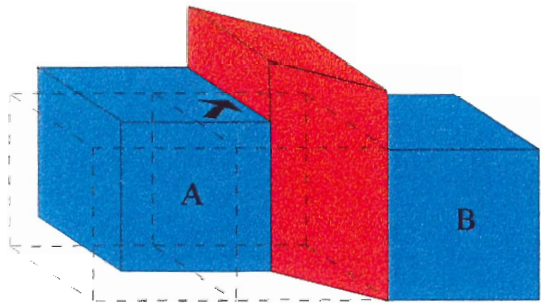
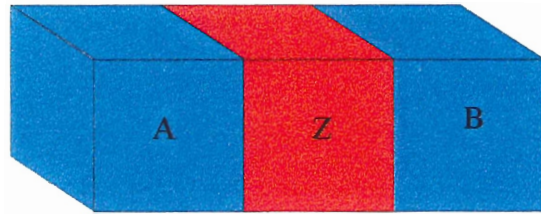


Figure 1.14

## **1.4 $^{40}\text{Ar}$ - $^{39}\text{Ar}$ dating of absolute timing of deformation: Summary of current knowledge**

The  $^{40}\text{Ar}$ - $^{39}\text{Ar}$  radiometric dating technique is one of the most widely used methods to constrain the thermal history of crustal rocks. The method is based on the radioactive decay of  $^{40}\text{K}$  to  $^{40}\text{Ar}$  and is useful for dating K-bearing minerals with sufficient potassium content to yield measurable amounts of daughter Ar (e.g. micas, K-feldspar, hornblende).

The  $^{40}\text{Ar}$ - $^{39}\text{Ar}$  method provides information on the time at which a particular mineral passes through its closure temperature during slow cooling. Ranges of closure temperatures for different minerals have been estimated from both experimental and empirical means (e.g. Dodson, 1973; Dodson, 1976; Harrison and Mc Dougall, 1988). Estimated closure temperatures for hornblende are in the range of 450-500°C, depending upon chemical composition. Biotite and muscovite show closure temperatures in the range of 300-350°C, whereas K-feldspar shows closure temperatures between 250-300°C. Therefore,  $^{40}\text{Ar}$ - $^{39}\text{Ar}$  dating of muscovite and biotite may provide important information on the time at which greenschist facies deformation takes place. However, true closure temperatures may vary dramatically for the same mineral in rocks that have undergone different thermal histories. Closure temperatures are strongly dependent on the prevailing intragranular and intergranular mechanisms of Ar diffusion. Traditional analysis of  $^{40}\text{Ar}$ - $^{39}\text{Ar}$  data assumes that Ar transport in the crystal lattice occurs mainly by volume diffusion (e.g. Dodson, 1973, Dodson, 1976; McDougall and Harrison, 1988). However, recent studies (e.g. Lee, 1995; Reddy et al. 1997) show that other transport mechanisms may play a critical role in Ar diffusion through crystals. In particular, Lee

(1995) emphasized the importance of crystal defects such as dislocations and microfractures in providing efficient pathways for Ar transport in and out of the crystal lattice. Furthermore, big atoms such as naturally produced radiogenic  $^{40}\text{Ar}$  will tend to migrate toward lower-energy sites of the crystal lattice such as dislocations within grains and/or to grain boundaries. As a result, effective closure temperatures of minerals can be much lower than those predicted assuming only a volume diffusion mechanism. This concept is particularly relevant to dating deformed minerals, which usually develop a high-density network of internal dislocations and microfractures in response to the applied high strain conditions.

Constraining the absolute age of deformational events has been a major problem for structural geologists for decades (e.g. Kligfield et al. 1986; Dunlap et al. 1991; Reddy et al. 1996). Commonly used minerals to date deformation are muscovite and biotite, mainly because of their ubiquity in crustal rocks. As stated before, although Ar volume diffusion is relatively well understood for minerals undergoing slow cooling under tectonically quiet conditions, the consequences of high strain solid-state deformation on Ar transport within the crystal lattice of silicates remain poorly known. However, it is now widely recognized that Ar loss during deformation occurs not only by volume diffusion as commonly assumed for the static cooling model. A series of other processes, such as dislocation motion through the crystal lattice, even at temperatures below the closure temperature of a specific mineral also are important (e.g. Scheuber et al. 1995; Lee, 1995; Reddy et al. 1996). Moreover, the rate of Ar loss from crystal lattices through dislocation motion and subsequent dislocation accumulation at newly created grain

boundaries during the strain-driven process of dynamic recrystallization may be several orders of magnitude higher than volume diffusion.

It is well known that high strain rocks commonly contain a complex mix of relic grains (porphyroclasts) and a matrix of dynamically recrystallized minerals. Moreover, the relic grains are usually partly recrystallized around their margins (core and mantle structure) whereas the so-called “recrystallized grains” often contain domains in which dynamic recrystallization has not been fully accomplished as revealed by detailed SEM studies (e.g. Trimby et al. 1998). Therefore, even in those cases in which relic or recrystallized minerals can be physically separated from the rock neither the relic grains or the “recrystallized” ones fully represent the deformational event. In the simplest case, this means that bulk separates of a specific mineral species will almost certainly contain a mix of relic and new grains. Therefore, the isotopic signature will very likely be a geologically meaningless average of the two unless a methodology is developed to recognize the presence of two different generations of the same mineral species with distinctive Ar retentive properties in the same bulk sample. West and Lux (1993) analyzed Ar behavior of muscovite in a high-strain shear zone. Through step-heating of bulk mineral separates they were able to discriminate between the isotopic signature of old relic grains and that of a new generation of recrystallized grains by a careful interpretation of staircase muscovite release patterns. These patterns are otherwise commonly interpreted in two ways: (1) as partial diffusive radiogenic Ar loss during a thermal event subsequent to initial cooling (e.g. Harrison, 1983); or (2) loss of radiogenic Ar from the porphyroclasts along grain boundaries in response to intra-granular deformation during mylonitization (e.g. Kelley, 1988). Another way to date deformation



by Ar-Ar step heating of bulk mineral separates was proposed by Scheuber et al. (1995). These authors dated a continuous series of rocks from the undeformed protholith to a high strain mylonite in the middle of a kilometer-wide ductile shear zone in northern Chile. They found that  $^{40}\text{Ar}$ - $^{39}\text{Ar}$  ages are fully reset by deformation-induced recrystallization in the high strain mylonites while mixed ages in the form of staircase patterns were obtained in the low strain varieties in which both relic and recrystallized minerals coexist.

The Ar-Ar laser technique is one way to solve the problem of selecting a meaningful target by choosing those minerals (or parts thereof) which are interpreted to be dynamically recrystallized at or below the closure temperature of the mineral. There comes the second problem: the methodology used to select the material to be dated prior to its preparation for dating. Most microstructural features of deformed minerals are usually described and interpreted using an optical microscope. While this might not represent a problem for relatively coarse-grained rocks, it involves a serious limitation for fine-grained mineral aggregates in which more than one mineral phase may be present in a single grain and cannot be optically identified. This is particularly relevant in those cases in which a low-K bearing mineral is contaminated by a high-K bearing mineral. In fact, Wartho (1995) has demonstrated that very small amounts of biotite within hornblende crystals can significantly affect the isotopic signature of the sample; once again the age will be geologically meaningless. Although it is possible to identify the presence of biotite traces once the Ar release pattern of hornblende is known, the actual time at which the hornblende system closed will remain uncertain.

Besides spatial resolution, another advantage of using the laser probe on specific targets instead of traditional furnace heating of bulk mineral separates is avoiding homogenization of argon isotopic variations within grains due to structural breakdown and chemical reaction of hydrous phases such as hornblende, biotite and muscovite. In fact, homogenization of natural argon isotope variations within step-heated grains may yield misleadingly flat plateau spectra which are geologically meaningless (e.g. Lee et al. 1991; Wartho, 1995).

### **1.5 Previous geological studies at the Southern Andes plate boundary zone between 42° and 47°S.**

The geology of the Southern Andes is only known at the regional scale. Most geological studies of this vast and remote region have been carried out during the last two decades. During the seventies and eighties, the studies mainly dealt with regional geology, geochemistry, and geochronology at the reconnaissance level (e.g. Fuenzalida and Etchart, 1975; Bobenrieth et al. 1983; Bartholomew, 1984, Godoy et al. 1984). These early studies provided important information regarding the general spatial distribution of major geological units and the local nature of their regional contacts at approximately 1:1.000.000 scale (Figures 1.2, 1.3). The Patagonian Batholith, the metamorphic basement, and a patchy cover of metasedimentary and metavolcanic rocks have been studied in further detail in the last ten years (e.g. Bartholomew and Tarney, 1984; Parada et al. 1987; Cembrano et al. 1992; Pankhurst et al. 1992; Pankhurst and Hervé, 1994; Hervé et al. 1995; Parada et al. 1996).

Bartholomew and Tarney (1984) addressed a possible causal relationship between oceanic-floored Tertiary basins and extensional/transensional magmatic arc tectonics by studying a geological transect at around 45°S. This work encouraged other scientists to undertake the study of the general geometry and kinematics of deformation related to initiation and inversion of such basins and their relation to the Patagonian Batholith (e.g. Hervé et al. 1993, Hervé et al. 1995).

Hervé et al (1993) conducted a combined geological and chronological study of the Patagonian Batholith at 44°S to address the causal relationship between the locus of plutonism and tectonic activity along the Liquiñe-Ofqui fault zone (LOFZ). They proposed a model by which rapid exhumation along the LOFZ between 10 and 5 Ma enhanced melting at high crustal levels giving rise to garnet-bearing two-mica granites, a peculiar facies within the mostly granodioritic-dioritic Patagonian Batholith.

However, detailed structural and geochronological data for the region are still lacking, although a few efforts have been made during the last few years to better understand the nature and timing of deformation in the southern Andes. Collaborative projects between US, French and Chilean scientists, undertaken during the last 5 years, have addressed the general problem of intra-arc deformation (e.g. Schermer et al. 1995, Schermer et al. 1996; Cembrano et al. 1996). The present thesis arises as the main product of two such projects. The first project (1993-1995) was called “Structural study of the Liquiñe-Ofqui fault zone between 39° and 43°S” and was granted to the author of this thesis by the Chilean National Science Foundation (FONDECYT). Co-investigators Elizabeth Schermer (Western Washington University), Alain Lavenu (ORSTOM) and Alejandro Sanhueza (graduate student, University of Chile) participated in the field trips

and discussion of the data. The second project called “Long-term and short-term kinematics of the Liquiñe-Ofqui fault zone between 44° and 46°S, southern Chilean Andes” (1995-1998) was also granted to the author of this thesis by FONDECYT. It involved the participation of the same collaborators as in the first project. Prof. Francisco Hervé (University of Chile), Gloria Arancibia (who did her undergraduate thesis under the guidance of the author in 1996-97) and Gloria Lopez (who is currently pursuing a Master degree at the University of Chile) were also part of the project. All participants were involved in one or more of the field trips during the austral summers of 1996, 1997, and 1998. The collection, organization and interpretation of the field data have always been in the charge of the author of this thesis.

Lastly, the southernmost Andes has been the focus of a few, regional-scale tectonic studies. Forsythe and Nelson (1985) proposed that the collision of the Chile Ridge at the southern termination of the Liquiñe-Ofqui fault zone was responsible for the detachment and northward transport of an outboard crustal sliver, the Chiloé Block, during Cenozoic times. The Chiloé block was thought to be bounded to the east by the dextral-strike slip Liquiñe-Ofqui fault zone. However, they provided no field structural or chronological data to support their hypothesis.

A region which has received much attention during the last decade is the Nazca-South America triple junction, where the Chile Ridge is currently subducting (e.g. Forsythe and Nelson, 1985; Cande and Leslie, 1986; Murdie et al. 1993, Bourgois et al. 1996). Most studies are based on geophysical data and on sample cores obtained during ODP projects. They are mostly concerned with the nature of offshore and onshore volcanic and sedimentary rocks located close to the triple junction. The analysis of

seismic reflection profiles of the offshore region close to Península de Taitao and in the Golfo de Penas have provided important data regarding the current geometry and topography of the different ridge segments and the trench (e.g. Cande and Leslie, 1986). However, only a few studies provide data on the geometry and kinematics of forearc deformation related to ridge collision and/or oblique subduction (e.g. Behrmann et al, 1992; Murdie et al. 1993). Murdie et al. (1993), based on seismic data, suggested that oblique convergence is completely partitioned into orthogonal shortening in the forearc and dextral strike-slip along the Liquiñe-Ofqui fault zone, for hundreds of kilometers north of the triple junction. In contrast, close to trench, just north of the triple junction, oriented cores from the forearc show evidence of distributed dextral transpression (e.g. Behrmann et al. 1992).

## **1.6 Organization of the thesis**

This thesis is organized into four, self-contained chapters. The scientific problem to be addressed, and the theoretical and geologic background are presented in Chapter 1. Chapter 2 documents the nature and timing of intra-arc deformation in the Southern Andes between latitudes 39°S and 43°S, along the part of the 1000 km-long Liquiñe-Ofqui fault zone. Emphasis is placed on the marked contrasts in the style and age of ductile and brittle deformation in three transects of the northern section of the Liquiñe-Ofqui fault zone. A tectonic model explains such variations in time and space in the context of plate motion reconstruction and available ridge subduction models.

Chapter 3 addresses the way bulk transpressional deformation is accommodated along and across the southern Andes plate boundary zone. Structural and thermochronological studies of several ductile shear zones along two transects provide the first modern systematic study of the kinematics and timing of deformation for this part of the Andes. The contribution of oblique subduction and ridge collision to bulk transpression at the plate boundary is further discussed by using newly acquired high-precision  $^{40}\text{Ar}$ - $^{39}\text{Ar}$  thermochronological data.

Chapter 4 assesses the problem of dating deformation in heterogeneously deformed granitic rocks with the  $^{40}\text{Ar}$ - $^{39}\text{Ar}$  technique through a representative case study. The advantages and shortcomings of total fusion laserprobe dating of deformation are critically evaluated and suggestions are made for future studies on similar rocks. A well-constrained deformation age is obtained for the selected sample by assuming complete resetting of the Ar isotopic system by high strain deformation along discrete shear bands.

Chapter 5 presents a discussion and the general conclusions of this thesis.

## **Chapter 2. Contrasting nature and timing of deformation along the northern section of the Liquiñe-Ofqui fault zone, Southern Chilean Andes.**

### **2.1 Introduction**

Regional-scale fault zones spatially associated with ancient and present-day magmatic arcs provide a unique opportunity to address both tectonic and magmatic phenomena at a crustal scale (e.g. Beck et al. 1983; Saint Blanquat et al. 1998). Studying the nature and timing of both ductile and brittle deformation along intra-arc fault zones may give valuable insights into deformation partitioning along and across convergent margins. Many examples of ancient and active intra-arc faults have been reported (see Fitch, 1972; Dewey, 1980; Beck, 1983; Jarrard, 1986; Busby-Spera and Saleeby, 1990; Beck, 1991; McCaffrey, 1992). However, well-documented cases are surprisingly rare (e.g. Scheuber and Reutter, 1992; Tikoff and Teyssier, 1992; Brown et al, 1993; Tikoff and Greene, 1997). One reason for this scarcity may be that most available evidence for intra-arc faulting come from earthquake fault plane solutions (e.g. McCaffrey, 1992), while field studies of long-lived intra-arc shear zones have been complicated by plutonic and volcanic activity which partially obliterate evidence for phases of faulting. One way to address the complexity of the deformation is to study along-strike variations in the nature and timing of the deformation using systematic field and microstructural studies and geochronological data.

In this chapter, I present structural and geochronological data from three transects across the Liquiñe-Ofqui fault zone of the southern Chilean Andes. These data constrain part of the long-term kinematic history of the fault zone and indicate the variation in

timing and style of deformation in different transects. The Liquiñe-Ofqui fault zone is marked by a set of north-northeast-trending lineaments, faults and ductile shear zones that cut through the magmatic arc from near the Nazca - South America - Antarctica triple junction northward for ca. 1000 km (Figure 2.1) (Hervé, 1977; Hervé and Thiele, 1987; Cembrano et al. 1996). Several workers have claimed that the Liquiñe-Ofqui fault zone has played a major role in deformation and location of the magmatic activity during the Cenozoic (Parada et al. 1987; Pankhurst et al. 1992; Dewey and Lamb, 1992). Recently, speculative models for the Liquiñe-Ofqui fault zone kinematics have been proposed on the basis of paleomagnetic data (García et al. 1988; Cembrano et al. 1992; Beck et al. 1993; Rojas et al. 1994), and upon regional considerations of the Liquiñe-Ofqui fault zone geometry and geology (Hervé, 1994; Cembrano et al, 1996). However, until now, few structural and geochronologic data were available to constrain the nature and timing of deformation along the fault zone. Thus its significance in partitioning oblique subduction of the Nazca plate has been poorly understood.



**Figure 2.1** Regional scale geometry of the Liquiñe-Ofqui fault zone and geotectonic setting of the southern Chilean Andes (modified from Cifuentes, 1989; Cembrano et al. 1996). Transect locations are shown by small boxes across the Liquiñe-Ofqui fault zone.

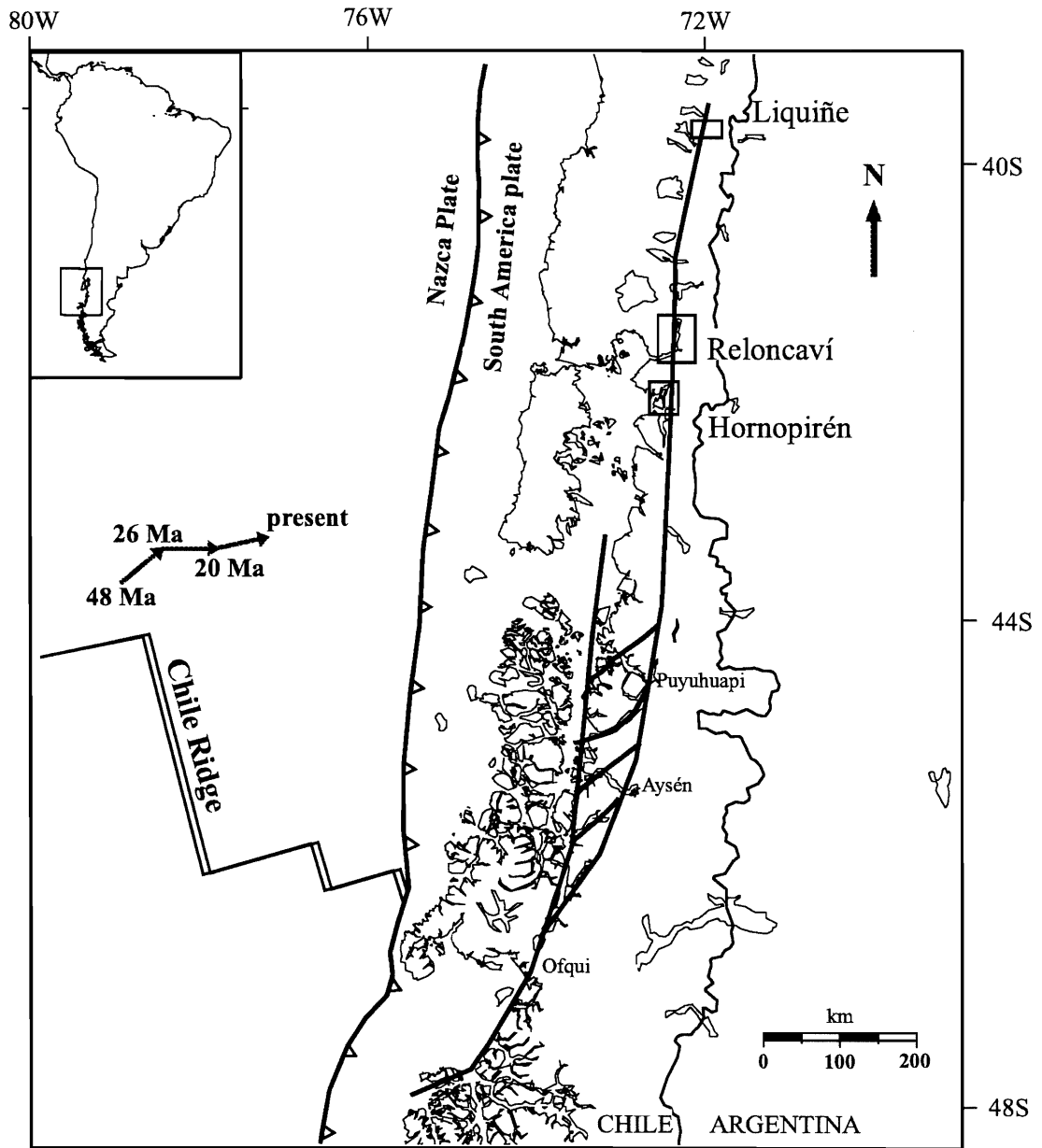


Figure 2.1

## **2.2 Tectonic setting of the Liquiñe-Ofqui fault zone**

The Cenozoic geodynamic setting of the southern Chilean Andes is well constrained, showing relatively steady right-oblique subduction of the Farallon (Nazca) plate beneath South America since 48 Ma with the exception of nearly orthogonal convergence from 26-20 Ma (Pardo-Casas and Molnar, 1987). At present, the angle of obliquity of the Nazca - South America plate convergence vector with respect to the orthogonal to the trench is  $\sim 26^\circ$  for southern Chile (Jarrard, 1986). The slab dip is approximately  $16^\circ$  (Jarrard, 1986) and the age of the subducting Nazca plate decreases from  $\sim 25$  Ma at  $38^\circ\text{S}$  to virtually 0 Ma at  $46^\circ\text{S}$ , where the Chile Ridge is currently subducting (Herron et al. 1981). The limited seismic data available suggest that the Chilean forearc between  $39^\circ$  and  $46^\circ\text{S}$  is currently undergoing trench-orthogonal shortening; the volcanic arc is absorbing a small trench-parallel component (Chinn and Isacks, 1983; Cifuentes, 1989; Barrientos and Acevedo, 1992; Dewey and Lamb, 1992; Murdie, 1994). Thus, oblique subduction has been considered to be a driving mechanism for the long-term right-lateral shear deformation along the Liquiñe-Ofqui fault zone (Hervé, 1977; Beck, 1988; Cembrano et al. 1996). Other authors have emphasized the indenter effect arising from subduction of the Chile Ridge at the southern termination of the Liquiñe-Ofqui fault zone (Forsythe and Nelson, 1985; Nelson et al. 1994).

## **2.3 Regional geology of the Liquiñe-Ofqui fault zone**

The Meso-Cenozoic North Patagonian Batholith forms most of the southern Chilean Andes and consists of heterogeneously deformed granodioritic to tonalitic plutonic rocks and minor undeformed two-mica granite and leucogranite (Parada et al.

1987; Hervé et al. 1993a). The batholith is made up of a Late Jurassic-Early Cretaceous belt to the west, a central relatively narrow (30 km-wide) Mio-Pliocene belt, and an eastern mid-Cretaceous belt (Pankhurst and Hervé, 1994). Available K-Ar, Ar-Ar, and Rb-Sr radiometric ages of plutonic rocks in the study area are shown in Table 2.1 and in Figures 2.2, 2.3, 2.4 (Cembrano, 1990; Carrasco, 1995; Cembrano et al. 1996). The plutonic rocks intrude low-to medium-grade metamorphic rocks making up an upper Paleozoic accretionary prism (Munizaga et al. 1988; Hervé, 1988; Pankhurst et al. 1992). Recent studies show that at least some of the low-grade wallrocks, particularly some deformed metabasites and dike swarms, may be much younger than previously thought and spatially associated with transtension during mid-Tertiary times (Hervé et al. 1993b; Hervé et al. 1995).

The regional-scale geometry of the Liquiñe-Ofqui fault zone is characterized by two major north-northeast-trending segments joined by a series of *en échelon* northeast-trending lineaments at a right step (Hervé and Thiele, 1987; Hervé, 1994). The resulting arrangement has been interpreted as a strike-slip duplex (Cembrano et al. 1996) similar to those described in Woodcock and Fisher (1986) (Figure 2.1). Along the LOFZ, both the North Patagonian Batholith and metamorphic wallrocks have centimeter to meter-wide high strain zones showing penetrative foliations and a poor to moderately well defined stretching lineation. Superposed on the ductile fabric, an anastomosing network of fractures and faults occurs along conspicuous north-trending lineaments. Quaternary volcanoes are aligned along the fault zone, as well as in northeast and northwest-trending groups oblique to the fault zone (Cembrano and Moreno, 1994; Lopez-Escobar et al. 1995).

Table 2.1. Previously published geochronological data from the three geological transects

Location	Rock type	Material	Method	Age (Ma)	Observations	Source
Liquiñe	dacytic dyke	whole rock	K-Ar	29 ± 1	crosscuts mylonites	Hervé, 1979
Liquiñe	dacytic dyke	biotite	Ar-Ar, steps	48	crosscuts low strain mylonites	Schermer et al. 1997
Liquiñe	granodiorite	biotite	Ar-Ar, total fusion	15	non-deformed, faulted	Munizaga et al. 1988
Reloncaví	tonalite	biotite	Ar-Ar, total fusion	124	non-deformed, faulted	Carrasco, 1995
Reloncaví	diorite	biotite	Ar-Ar, total fusion	119	non-deformed, faulted	Carrasco, 1995
Reloncaví	diorite	biotite	Ar-Ar, total fusion	113	non-deformed, faulted	Carrasco, 1995
Reloncaví	tonalite	biotite	Ar-Ar, total fusion	121 ± 0.3	non-deformed, faulted	Carrasco, 1995
Reloncaví	tonalite	biotite	Ar-Ar, total fusion	115 ± 0.7	non-deformed, faulted	Carrasco, 1995
Reloncaví	tonalite	biotite	Ar-Ar, total fusion	114 ± 0.5	non-deformed, faulted	Carrasco, 1995
Reloncaví	tonalite	biotite	Ar-Ar, total fusion	115 ± 0.5	non-deformed, faulted	Carrasco, 1995
Reloncaví	granodiorite	biotite	K-Ar	10.7	non-deformed, faulted	Carrasco, 1995
Reloncaví	granodiorite	biotite	K-Ar	11.5	non-deformed, faulted	Carrasco, 1995
Hornopirén	granodiorite	biotite	Ar-Ar, total fusion	6.6 ± 0.3	low strain	Cembrano, 1990
Hornopirén	granodiorite	biotite	Ar-Ar, total fusion	3.6 ± 0.3	low strain	Cembrano, 1990
Hornopirén	granodiorite	hornblende	Ar-Ar, total fusion	8.7 ± 0.7	low strain	Cembrano, 1990
Hornopirén	tonalite	biotite	Ar-Ar, total fusion	6.4 ± 1.7	low strain, S-C fabrics	Cembrano, 1990
Hornopirén	tonalite	hornblende	Ar-Ar, total fusion	13.1 ± 0.1	low strain, S-C fabrics	Cembrano, 1990
Hornopirén	tonalite	whole rock	Rb-Sr	4.7 ± 0.6	low strain, S-C fabrics	Pankhurst et al. 1992
Hornopirén	tonalite	zircon	U-Pb	9.9 ± 0.2	low strain, S-C fabrics	Schermer et al. 1997
Hornopirén	diorite	biotite	Ar-Ar, total fusion	8.8 ± 1.7	non-deformed	Cembrano, 1990

Location	Rock type	Material	Method	Age (Ma)	Observations	Source
Hornopirén	diorite	hornblende	Ar-Ar, total fusion	$8.6 \pm 0.6$	non-deformed	Cembrano, 1990
Hornopirén	granodiorite	biotite	Ar-Ar, steps	$3.59 \pm 0.01$	high strain mylonite	Schermer et al. 1996
Hornopirén	tonalite	biotite	Ar-Ar, steps	$3.78 \pm 0.01$	high strain mylonite	Schermer et al. 1996
Hornopirén	mica schist	biotite	Ar-Ar, total fusion	$7.2 \pm 0.7$	high strain	Cembrano, 1990
Hornopirén	mica schist	muscovite	Ar-Ar, total fusion	$10.6 \pm 0.1$	high strain	Cembrano, 1990
Hornopirén	tonalite	biotite	Ar-Ar, total fusion	$3.4 \pm 0.5$	no strain	Cembrano, 1990
Hornopirén	diorite	hornblende	Ar-Ar, total fusion	$114.3 \pm 3$	no strain	Cembrano, 1990

**Figure 2.2** Regional geology and local structure of the Liquiñe-Ofqui fault zone for the Liquiñe region. Simplified from Moreno and Parada (1976) and Hervé (1977). Locations of available radiometric age determinations (Hervé, 1977; Munizaga et al. 1988) are shown with symbols. Triangle: K-Ar dates on biotite, inverted triangle: K-Ar whole rock dates.



Figure 2.2

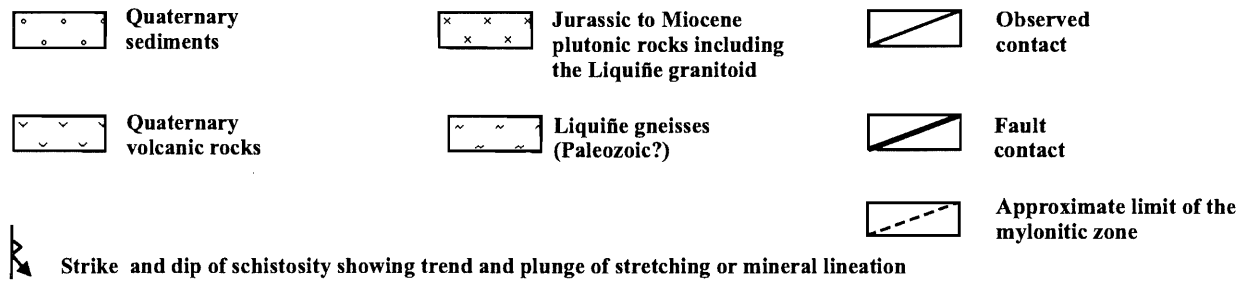
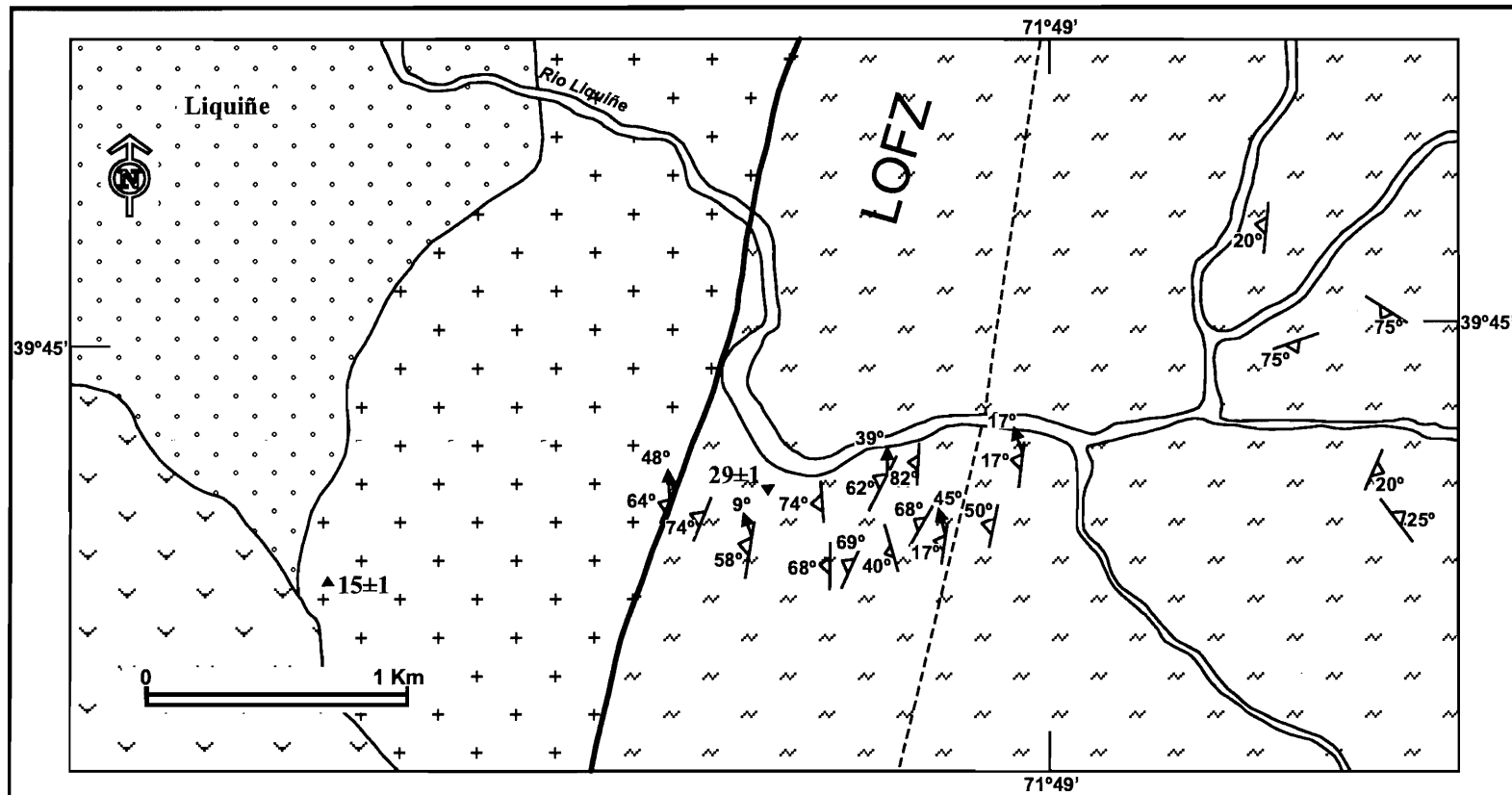


**Figure 2.3** Regional geologic map of the Liquiñe-Ofqui fault zone for the Reloncaví area. Simplified from Thiele et al. (1986), Parada et al. (1987) and Carrasco (1991). Locations of available radiometric age determinations (Drake et al. 1990; Drake et al. 1991; Carrasco, 1991) are shown with symbols. Solid square: total fusion Ar-Ar dates on biotite; half-filled square: total fusion Ar-Ar dates on hornblende; triangle: K-Ar dates on biotite, inverted triangle: K-Ar whole rock dates.

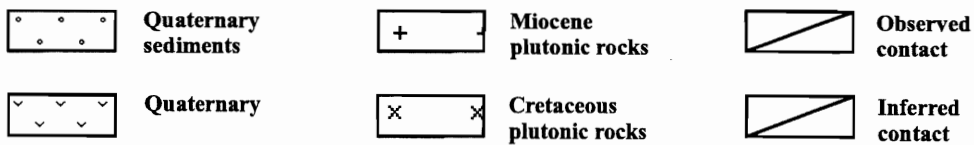
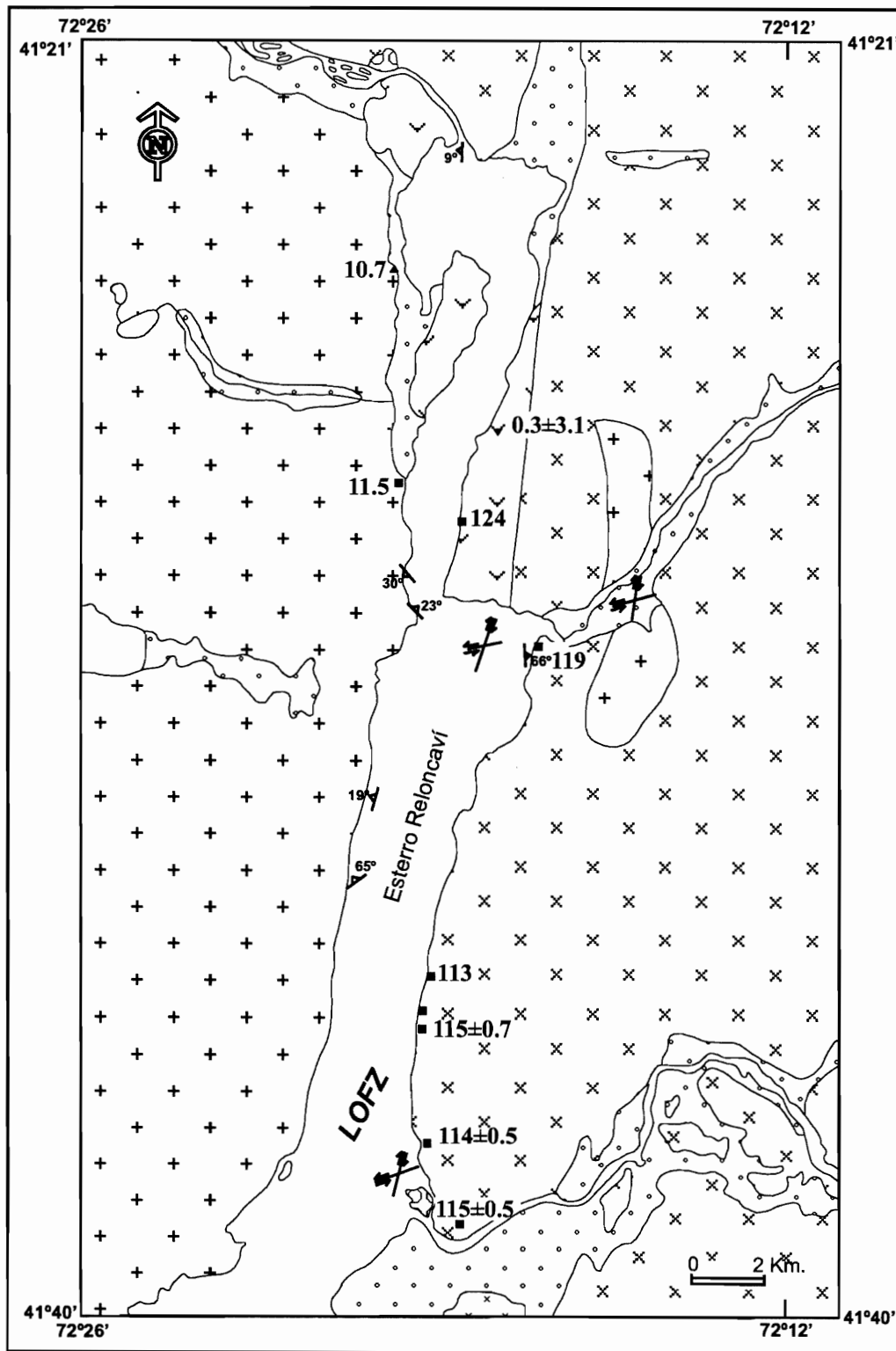


Figure 2.3

**Figure 2.4** Regional geology and local structure of the Liquiñe-Ofqui fault zone for the Hornopirén region. Simplified from Hervé et al. (1979) and Cembrano (1990). Locations of available radiometric age determinations (Hervé et al. 1979; Drake et al. 1990; Drake et al. 1991; Schermer et al. 1996) are indicated with symbols. Solid square: total fusion Ar-Ar dates on biotite; half-filled square: total fusion Ar-Ar dates on hornblende; diamond: Rb-Sr whole rock isochron; triangle: K-Ar dates on biotite, inverted triangle: K-Ar whole rock dates; filled circle: U-Pb dates on zircon.

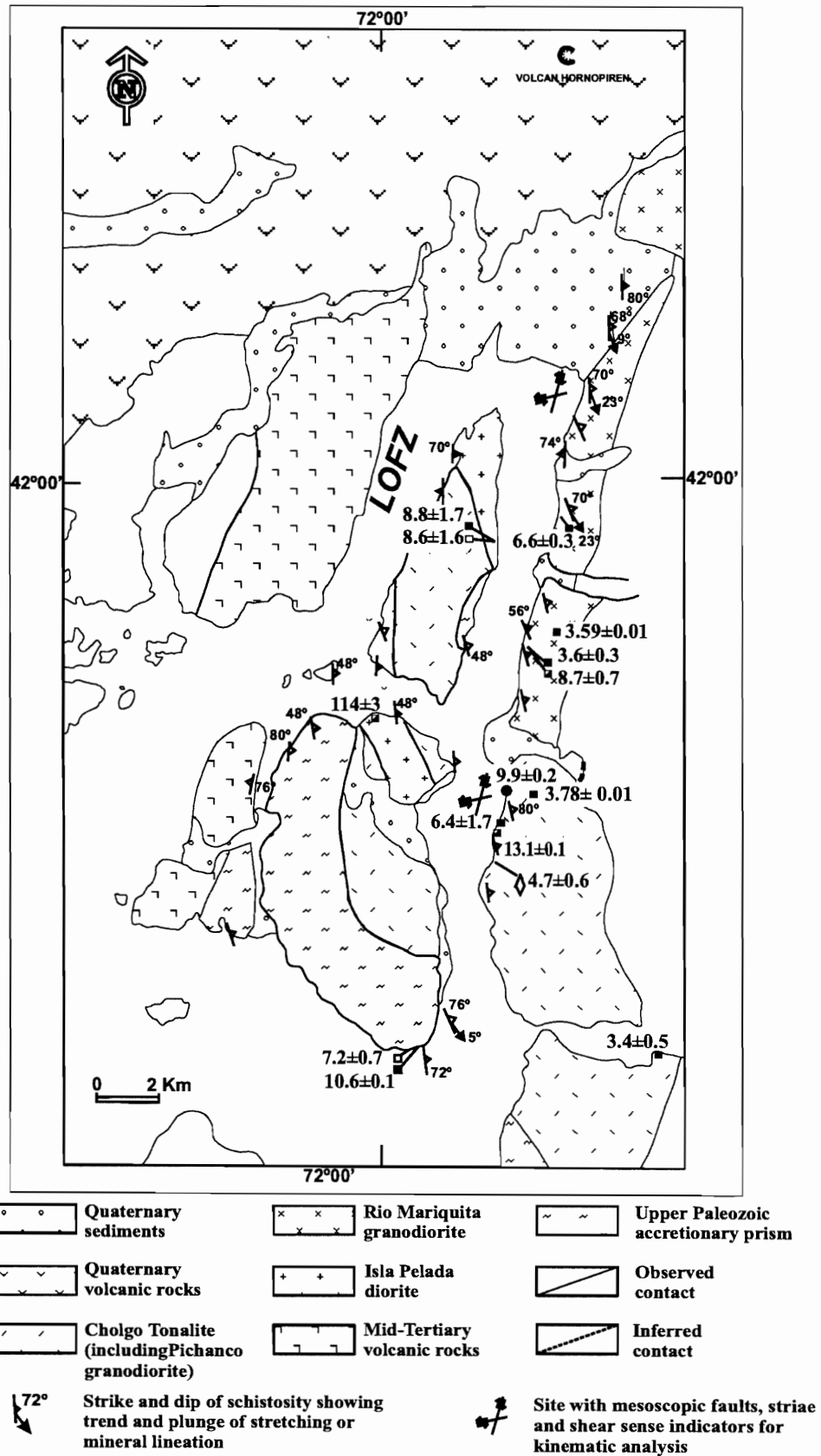


Figure 2.4

## 2.4 Structural transects

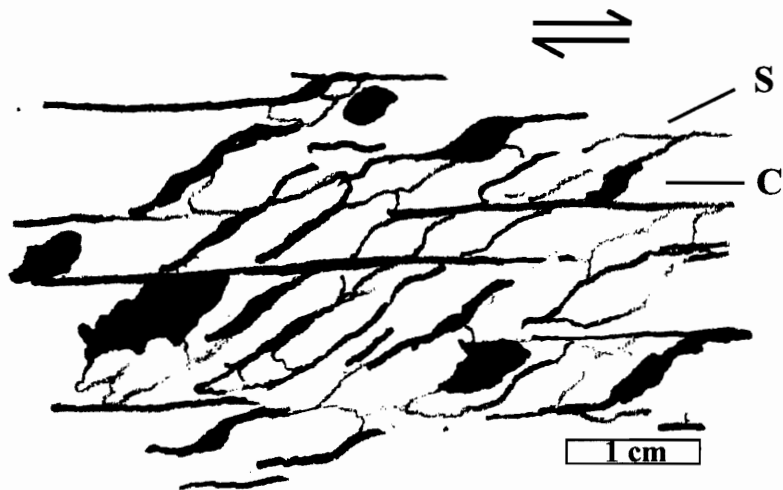
Three transects were mapped across the LOFZ at Liquiñe, Reloncaví, and Hornopirén (Figure 2.1). Geologic maps of these areas are shown in Figures 2.2, 2.3 and 2.4, respectively. Earlier workers (M. Hervé, 1977; F. Hervé et al. 1979) identified and characterized, at the regional scale, the main lineaments comprising the fault zone, but little detailed structural or geochronological work was done to document the kinematics, timing and style of deformation. Dense forest cover prevents detailed mapping of large areas, however the good coastal and roadside exposures analyzed during this study provide the first detailed kinematic analysis of the LOFZ. I analyzed ductile structures in mylonitic rocks on the mesoscopic and microscopic scales to determine the kinematics and approximate conditions of deformation. Kinematic indicators include S-C fabrics (Berthé et al. 1979; White et al. 1980; Platt, 1984; Shimamoto, 1988), asymmetric porphyroclast systems (Passchier and Simpson, 1986), mica fish (Lister and Snoke, 1984), and domino structures (Simpson and Schmid, 1983). Quartz ribbon microstructure (types 1,2,3 of Boullier and Bouchez, 1978, Simpson, 1985) and feldspar microstructure (White, 1975; Simpson, 1985, Tullis and Yund, 1987; Fitz-Gerald and Stunitz, 1993) were documented to provide a rough estimate of P-T conditions of deformation. A summary of the microstructural criteria used to determine kinematics and physical conditions of deformation is illustrated in Figure 2.5.

Brittle structures were analyzed using the criteria of Petit (1987). Stress inversion analysis using the methods of Carey and Brunier (1974) and Carey (1979) was conducted for the areas where numerous faults contained unambiguous kinematic

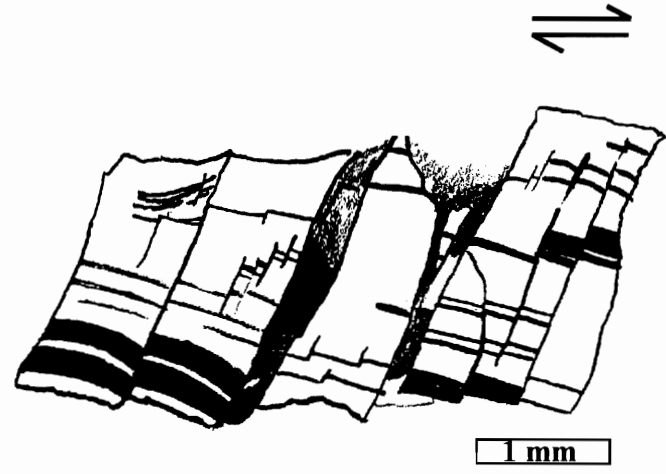
**Figure 2.5** Summary of microstructural criteria used to determine:

- (a)** shear sense on mylonites. (1) S-C fabrics; (2) domino structures; (3) asymmetric porphyroclast systems; (4) mica fish. (Berthé et al. 1979; Passchier and Simpson, 1986; Lister and Snoke, 1984; Simpson and Schmid, 1983).
- (b)** Physical conditions of deformation. (1) Different types of quartz-ribbons according to metamorphic facies conditions as defined by Bouchez and Boullier (1978) and Simpson (1985). (2) Typical microstructures of plagioclase, orthoclase and quartz in granitic rocks deformed at low greenschist facies (2.1); mid-to-upper greenschist facies conditions (2.2), epidote-amphibolite facies (2.3) and amphibolite facies conditions (4) (simplified from Simpson, 1985; Tullis and Yund, 1987).

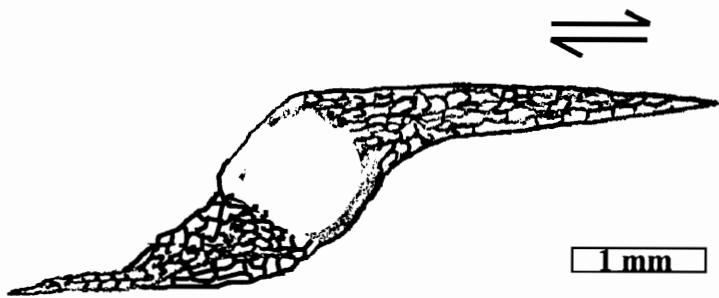
Figure 2.5a



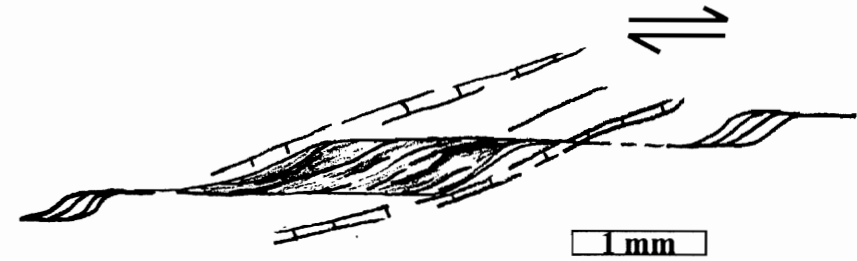
a.1 S-C fabric (e.g. Berthé et al. 1979; Lin and Williams, 1991)



a.2 Domino structure, microfaulted plagioclase (e.g. Simpson and Schmid, 1983)



a.3 Asymmetric porphyroblast system (e.g. Passchier and Simpson, 1986)

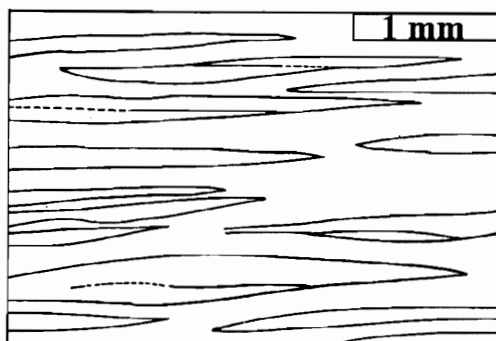


a.4 Mica fish (e.g. Lister and Snoke, 1984)

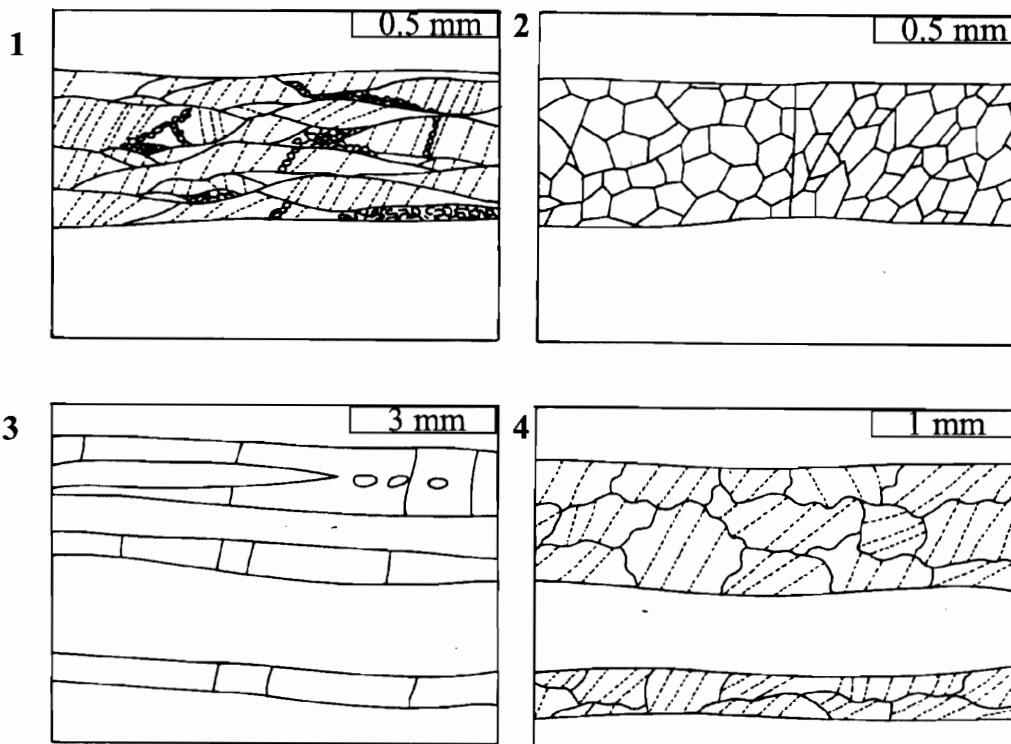


### Monocrystalline ribbons

Low-greenschist facies conditions



### Polycrystalline ribbons



**b.1 Different types of monocrystalline and polycrystalline quartz ribbons according to Boullier and Bouchez (1978)**

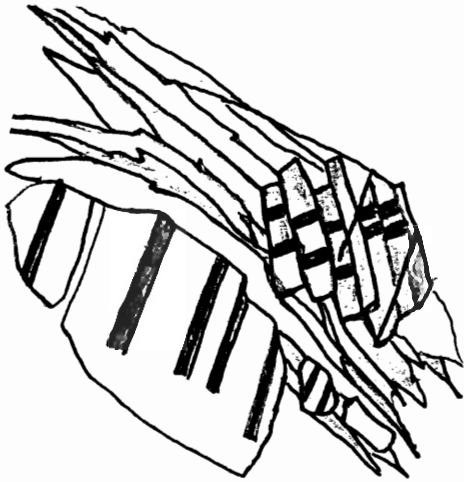
**Type 1:** Low- to mid-greenschist facies conditions

**Type 2:** Mid- to upper-greenschist facies conditions

**Type 3:** Amphibolite facies conditions

**Type 4:** Mid- to upper-greenschist facies conditions

**Figure 2.5b**

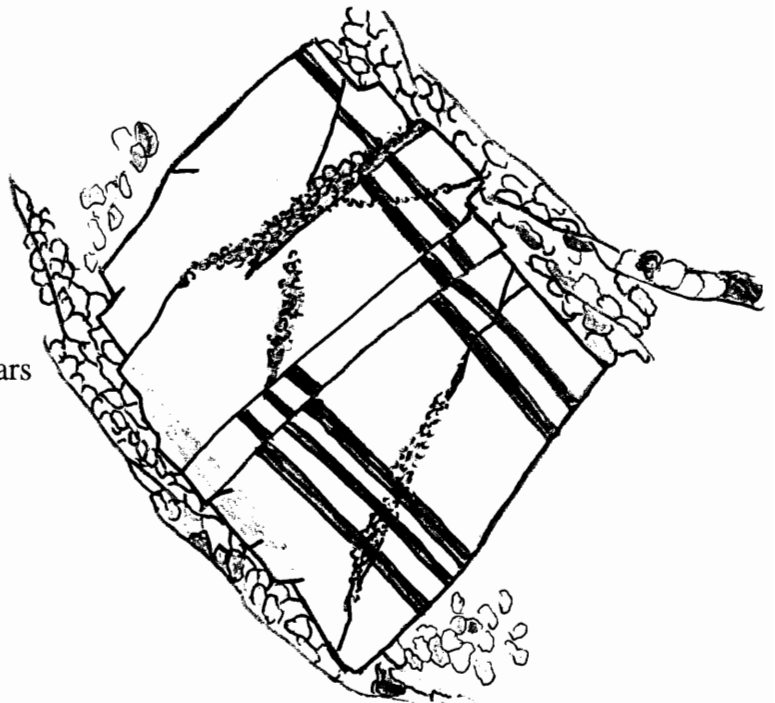


**Low-greenschist facies conditions:**

Fractured plagioclase and orthoclase, microfaulting leading to domino structures is common. Quartz ribbons are generally monocrystalline and show serrated grain boundaries. This overall microstructure indicates brittle behavior of feldspars and incipient dynamic recrystallization of quartz by grain boundary migration (e.g. Simpson, 1985).

**Mid-to-upper greenschist facies conditions:**

Plagioclase shows fine-grained aggregates located along internal fractures and grain boundaries. This is interpreted to result from dynamic recrystallization of feldspars restricted to high strain sites. Quartz occurs as a matrix of a fine-grained aggregate made of strain-free recrystallized grains (e.g. Simpson, 1985).



**Amphibolite facies conditions:**

Quartz occurs in ribbons showing straight grain boundaries at high angles with respect to ribbon edge. This microstructure may result from continuous grain growth of quartz at high temperatures; sideways grain growth is usually inhibited by mica grains. Plagioclase and/or orthoclase form bands made of polygonal aggregates of strain-free grains. Feldspar microstructure is interpreted to result from full dynamic recrystallization of feldspars at amphibolite facies and above (e.g. Simpson, 1985).

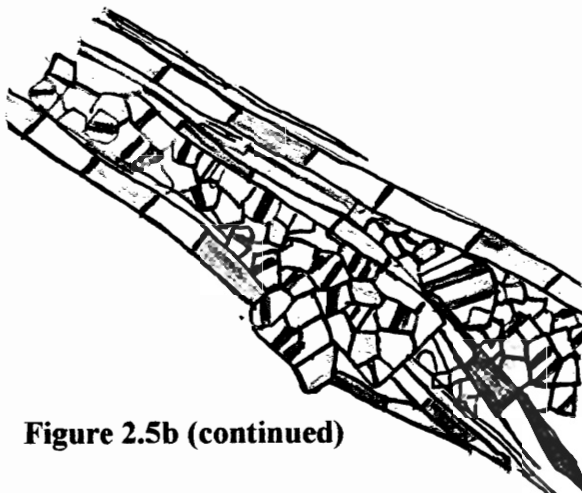


Figure 2.5b (continued)

indicators. In this technique, homogeneous populations of faults (faults which are kinematically consistent, with striations compatible with a single stress tensor) were identified by iteration tests based on the following steps: (i) faults having similar trends, dips, and pitches are grouped together; then comparison of these different groups is done qualitatively with the purpose of evaluating their kinematic compatibility (e.g. dextral and sinistral faults having similar strikes are not compatible); (ii) consistent faults sets are regrouped and a mean stress tensor is calculated, then this stress tensor is applied to the entire population of faults collected on a given site; (iii) according to the distribution of the angular deviation ( $\tau_s$ ) taken lesser or equal to  $30^\circ$  between theoretical striae ( $\tau$ ) derived from the computed stress tensor and the measured striae ( $s$ ), a homogeneous population of faults can be identified (for a complete description of the method and underlying rationale, see Bott, 1959; Sébrier et al. 1985; Lavenu et al. 1995).

#### **2.4.1 Liquiñe transect**

Previous reconnaissance mapping (Hervé et al. 1974; Moreno and Parada, 1976; Hervé, 1977) shows that the Liquiñe region is characterized by two main, north-trending geologic units: the "Liquiñe granitoid" and the "Liquiñe gneisses" (Figure 2.2). The Liquiñe granitoid was originally assigned to the Jurassic (Hervé, 1977), although recent K-Ar dating (biotite) suggests a Miocene emplacement age (Munizaga et al. 1988). The Liquiñe gneisses have been dated as upper Paleozoic on the basis of a poorly constrained Rb-Sr errorchron (Hervé, 1977). The Liquiñe granitoid and the Liquiñe gneisses are juxtaposed by the Liquiñe-Reloncaví fault (Moreno and Parada, 1976; Hervé, 1977). According to Hervé (1977), a 1 km-wide zone of cataclasites developed in the granitoid is exposed west of the fault while a 1 km-wide mylonitic zone occurs east of it developed

from the Paleozoic gneisses. An undeformed dacitic porphyry dated as 29 Ma (K-Ar, whole rock), cut the mylonites. We obtained a new  $^{40}\text{Ar}$ - $^{39}\text{Ar}$  step-heating date of bulk hornblende separates from the crosscutting dyke. This gives a well-constrained mean age of  $100 \pm 2$  Ma (Figure 2.6). We interpret this age as the minimum age of deformation for the mylonites of the Liquiñe transect. Another dyke, which crosscuts a low-strain variety of the mylonites has recently been dated at 48 Ma (Ar-Ar, biotite) (Schermer et al. 1996).

A mesoscopic-scale "conjugate system" of north-trending right-separation and east-northeast-trending left-separation mesoscopic faults was identified within and to the east of the mylonitic zone. This observation plus a predominant steeply dipping mylonitic foliation were used to interpret the shear zone as a pre-Oligocene dextral fault zone (Hervé, 1977). No stretching lineations or fault striae were reported in these early studies. Our own mapping along the Liquiñe transect partly agrees with that of Hervé (1977) and indicates there is a sharp contact between a brittlely deformed granitoid and high strain mylonitic rocks formed from the gneisses (Figure 2.2). However, in contrast with previous mapping, I found that deformation in the granitoid is weak and only locally developed within a few tens of meters of the contact with the mylonites. Since there is no thermal aureole developed in the mylonites close to the granitoid, the contact between the granitoid and the mylonitized gneisses very likely corresponds to a brittle fault with a significant east-side-up component of motion as early recognized by Hervé (1977).

Detailed structural study carried out within the mylonitic zone of the Liquiñe area, east of the main lineament of the Liquiñe-Ofqui fault (Figure 2.2), shows that a meter-wide dark green mylonitic strip gives way eastward to distinctive meter-wide domains of dark gray porphyroclast-free mylonite.

**Figure 2.6**  $^{40}\text{Ar}$ - $^{39}\text{Ar}$  apparent age spectra for the Liquiñe transect crosscutting dyke (hornblende bulk mineral separate).

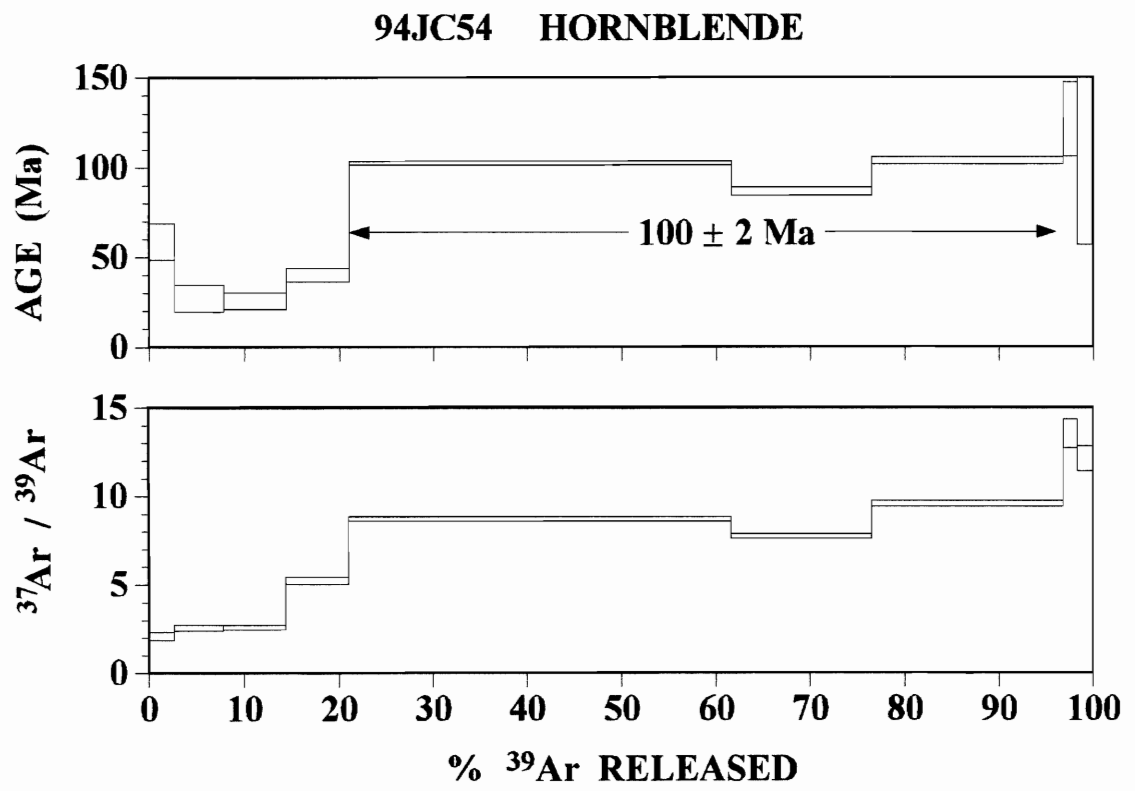


Figure 2.6

These alternate with domains of porphyroclastic quartz-feldspar-mica-bearing, strongly foliated and poorly lineated mylonite. The penetrative schistosity strikes approximately north and dips steeply to the west (Figure 2.2, 2.7a); stretching lineations, defined by slightly elongated quartz-feldspar and mica aggregates, plunge shallowly to moderately to the north (Figure 2.2, 2.7c).

Three types of deformed rocks can be distinguished across the Liquiñe transect: widely distributed quartz-feldspar-mica mylonites, which include quartz-rich and quartz-poor varieties, and chlorite-bearing S-C mylonites, which are only locally observed.

The quartz-feldspar rocks show distinctive microstructures depending upon quartz abundance. Quartz-rich mylonites display a penetrative schistosity resulting from the parallel alignment of type 2 quartz-ribbons and muscovite-biotite foliae which wrap around isolated feldspar porphyroclasts showing both symmetrical and asymmetrical tails. Among the latter,  $\sigma$  and  $\delta$  porphyroclast systems are present and exhibit a sinistral shear-sense geometry (Figure 2.8a). This sense of shear is consistent with discrete shear bands defined by fine-grained mica aggregates that are oblique to the schistosity.

Quartz-poor mylonites show a less well-developed schistosity as quartz-ribbons are scarce and globular aggregates of nearly equant quartz grains are more common. Porphyroclasts of feldspar are more widespread than in the quartz-rich mylonites and are locally surrounded by conjugate sets of microshear bands along which fine-grained biotite occurs (Figure 2.8b). The overall fabric of these rocks is markedly symmetric in character (sensu Choukroune et al. 1987).

**Figure 2.7** Lower hemisphere, equal area projections showing the orientation of ductile fabrics from deformed rocks within the Liquiñe-Ofqui fault zone. Poles to schistosity for Liquiñe (**a**) and Hornopirén (**b**) (crosses) ; Stretching and mineral lineation plots for Liquiñe (**c**) and Hornopirén (**d**) (dots).



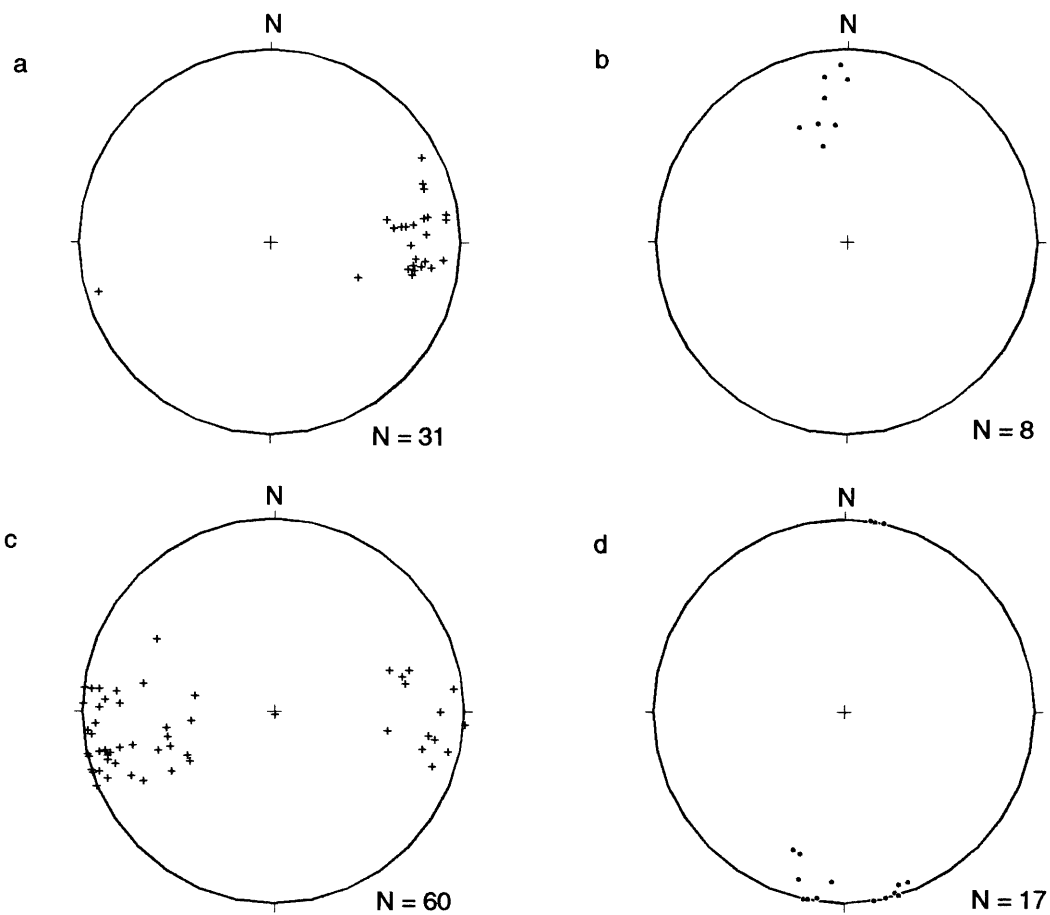
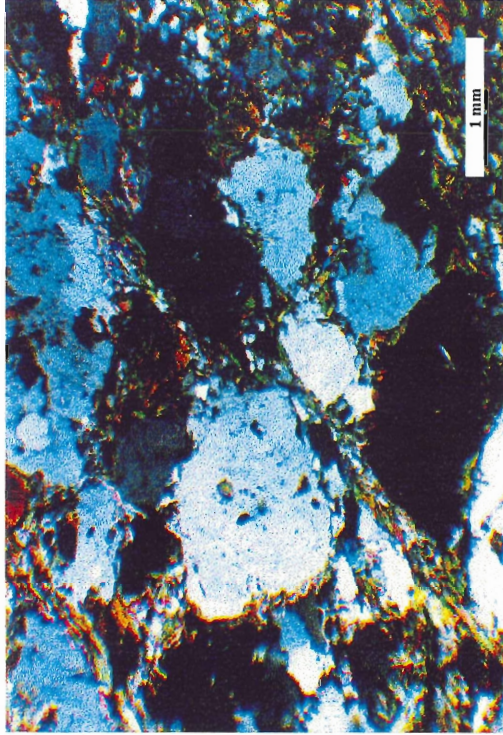


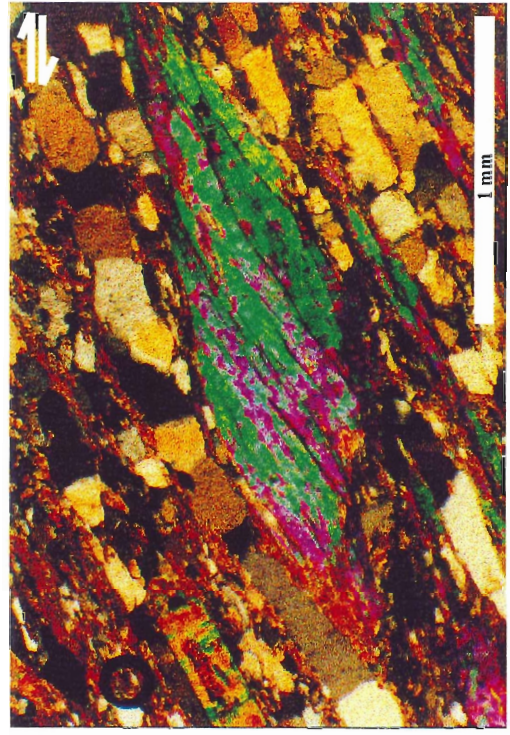
Figure 2.7

**Figure 2.8** Photomicrographs of shear sense indicators from XZ sections of deformed rocks occurring within the Liquiñe-Ofqui fault zone.

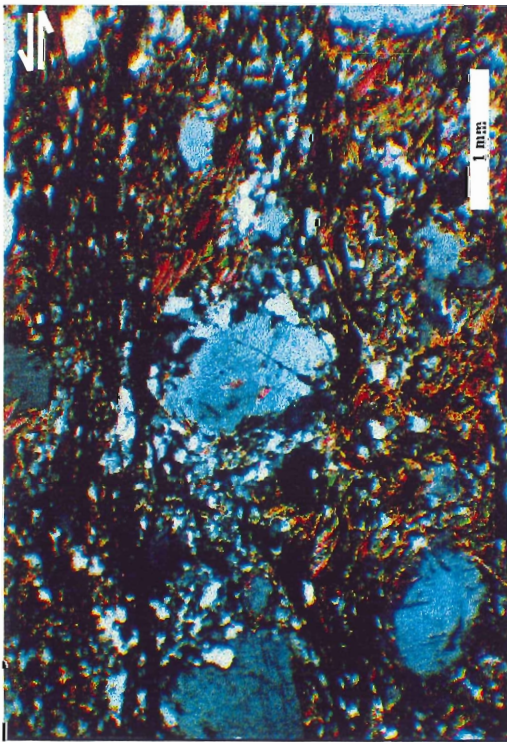
- (a)  $\sigma$ -type porphyroclast system of feldspar and coexisting shear bands oblique to the schistosity from mylonites of the Liquiñe transect. Sense of shear is sinistral.
- (b) conjugate shear bands and symmetric porphyroclasts from low strain mylonites of the Liquiñe transect.
- (c) microfaulted plagioclase from deformed plutonic rocks of the Hornopirén transect. Domino structure indicates dextral shear.
- (d) mica-fish from wallrock pelitic schists of the Hornopirén section indicate dextral shear sense.



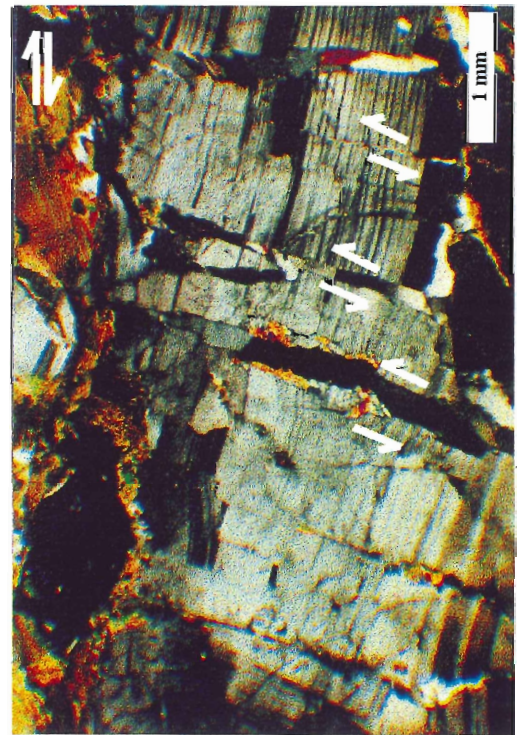
b



d



a



c

Figure 2.8

The chlorite-bearing mylonites show isolated altered plagioclase porphyroclasts in a very fine-grained matrix of chlorite-calcite-sericite and residual mafic minerals. Well-developed S-C fabrics indicate sinistral shear sense.

The most prominent brittle fabrics in the Liquiñe area occur in the Liquiñe granitoid and correspond to a meter-spaced set of fractures and faults striking north-northeast. Some of the faults are high-angle reverse; others show evidence of left or right-lateral motion as indicated by kinematic indicators present on the fault surfaces. However, the limited number and erratic nature of the mesoscopic faults in the Liquiñe region prevents a detailed kinematic analysis. Within a few tens of meters west of the Liquiñe-Ofqui fault zone main lineament (Figure 2.2), the Liquiñe granitoid displays spaced centimeter-scale fractures which locally coalesce to define a roughly defined north-striking cataclastic foliation.

#### **2.4.2 Reloncaví Transect**

Previous studies (Thiele et al. 1986; Parada et al. 1987; Carrasco, 1995) have shown that northeast trending granodioritic and tonalitic plutonic units are only slightly ductilely deformed along the continuation of the major lineaments trending south from Liquiñe. The plutonic rocks have yielded Ar-Ar ages which are concentrated in Early Cretaceous and Miocene times (Drake et al. 1991; Carrasco, 1995) (Table 2.1, Figure 2.3). Carrasco (1995) interpreted the slightly ductilely deformed Miocene rocks as being the result of high-temperature deformation during plutonic emplacement, with only minor, late emplacement sub-solidus deformation. Our observations that most plutonic units show little evidence of high strain ductile deformation, with the exception of

meter-wide septa of annealed mylonitic rock within largely undeformed plutonic rocks, agree with those of previous authors (Thiele et al. 1986; Carrasco, 1995).

On both sides of Estuario Reloncaví centimeter- to decameter-scale striated fault planes cut all the plutonic units ranging in age from Cretaceous to Miocene; Quaternary sediments and volcanic rocks do not show evidence of faulting. Most faults are steeply dipping ( $>60^\circ$ ); striae range in pitch from subhorizontal to subvertical.

Using the procedure described in the methodology section, two distinct homogeneous populations of faults were recognized in the Reloncaví region. The first one is represented in Figure 2.9a, which includes faults with a predominant strike-slip component, and a few with predominant dip-slip component. Faults whose strike range between  $337^\circ$  and  $040^\circ$  (average  $010^\circ$ ) show right lateral slip-sense; faults striking between  $060^\circ$ - $106^\circ$  (average around  $080^\circ$ ) are left-lateral; faults striking west-northwest are reverse-slip. A second diagram (Figure 2.9b) shows the second homogeneous population of faults identified; most of them have a significant down-dip component, although some strike-slip faults also are included. Faults striking  $010^\circ$ - $080^\circ$  (mainly  $60^\circ$  to  $80^\circ$ ) are dextral-reverse slip. Faults striking  $115^\circ$ - $144^\circ$  (mostly  $120^\circ$ - $130^\circ$ ) show sinistral reverse slip-sense.

The kinematic analysis of the mesoscopic faults using E.C.G-Geoldynsoft software (Carey and Brunier, 1974; Carey, 1979) yields a dextral strike-slip deformation regime for the first population of faults:  $\sigma_1=219^\circ, 05^\circ$ ;  $\sigma_2=110^\circ, 75^\circ$ ;  $\sigma_3=310^\circ, 14^\circ$  (Figure 2.9a). In contrast, a compressional regime is suggested by the second fault population:  $\sigma_1=275^\circ, 05^\circ$ ;  $\sigma_2=184^\circ, 12^\circ$ ;  $\sigma_3=25^\circ, 77^\circ$  (Figure 2.9b).

**Figure 2.9** Lower hemisphere, equal angle projections, showing orientation and kinematic data for mesoscopic faults at Reloncaví (a,b) and Hornopirén (c) computed to obtain the local stress tensor. Arrows attached to the fault traces correspond to the measured slip vectors. Thick segments on the fault traces show deviations between measured (s) and predicted (t) slip vector on each plane. Corresponding histograms show the number of faults (n) as a function of the difference in pitch between t and s. Convergent large arrows give azimuths of the computed maximum principal stress direction ( $\sigma_1$ ). From method of Carey and Brunier (1974).



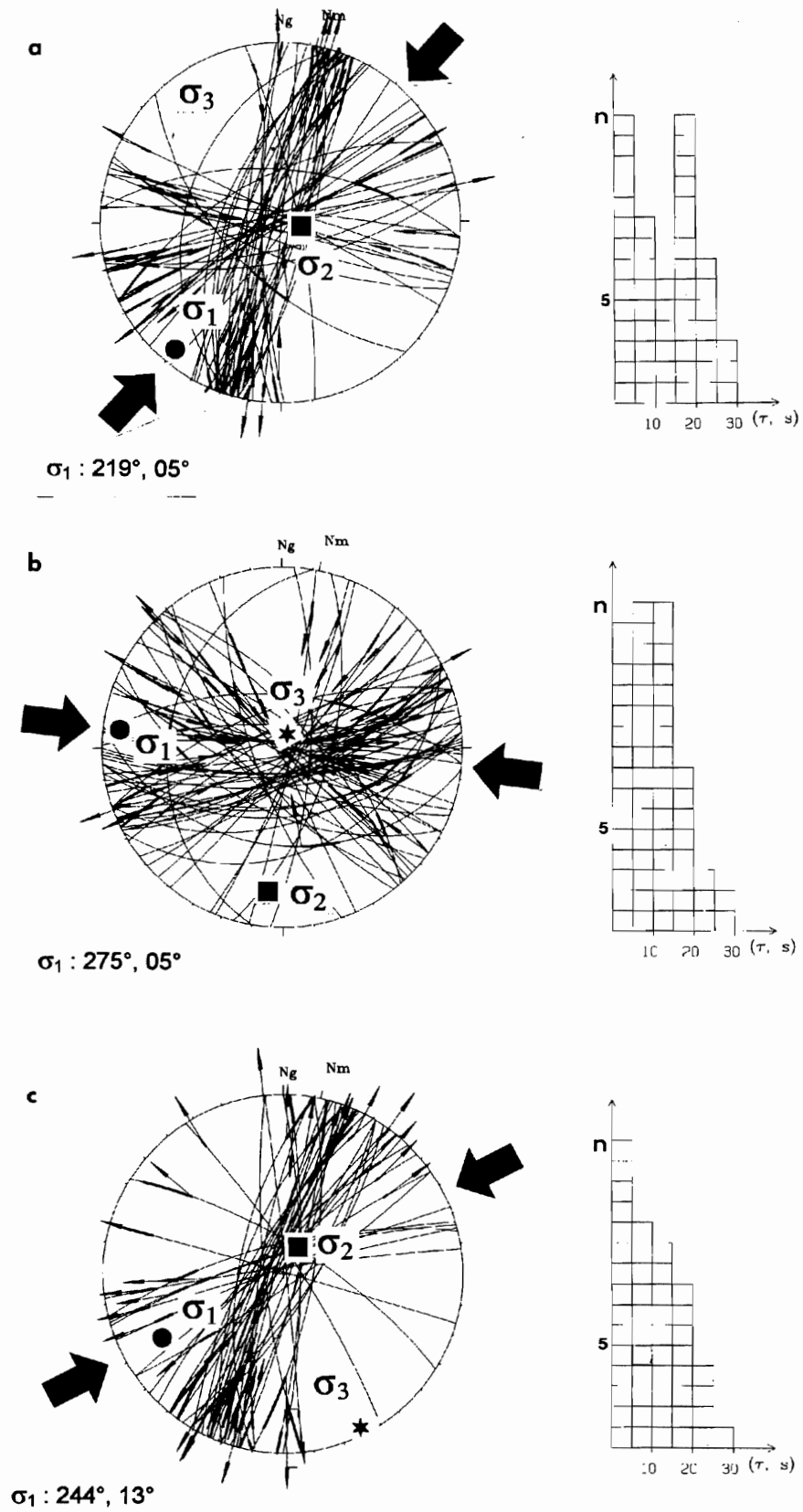


Figure 2.9

### 2.4.3 Hornopirén Transect

In the Hornopirén Region, the Liquiñe-Ofqui fault zone is represented by a 4-5 km wide zone of heterogeneously deformed granitoids and by low-to medium-grade metamorphic wallrock (Figure 2.4). The plutonic rocks, mainly hornblende-biotite tonalite and granodiorite, have been grouped into informal units on the basis of petrography and poorly mapped field relations (Figure 2.4). The largely inferred contacts between the plutonic units and wallrocks trend roughly northwest (Cembrano, 1990).

Plutonic rocks of the Hornopirén region appear to be mainly Cretaceous and Miocene in age. Granodiorite dated by U-Pb zircon at 135 Ma (Schermer et al. 1996) occurs along the northeast flank of the canal and diorite with an Ar-Ar total fusion age of 114 Ma occurs on Isla Llancahue. The diorite is undeformed, in contrast to other plutonic rocks of the region, possibly due to its low quartz content. A Miocene (9.9 Ma) U-Pb age was obtained on the Cholgo pluton (Schermer et al. 1996) (Figure 2.4) but the emplacement ages of other plutons are uncertain. A Rb-Sr isochron of  $4.7 \pm 0.6$  Ma has been considered the age of emplacement of a partly gneissic tonalite located within and to the east of the LOFZ (Pankhurst et al. 1992) (Figure 2.4). However, the fact that the isochron is largely constrained by the aplitic end-members suggests that it combines unrelated plutonic units. Further mapping and dating by the authors support this hypothesis. Abundant Miocene Ar-Ar and whole rock K-Ar dates have been obtained from the Hornopirén region (Figure 2.4). The ages on plutonic rocks have been interpreted as emplacement ages related to the migration of intrusive foci toward the LOFZ from Jurassic to Neogene, or alternatively, as the result of differential uplift and static cooling of granitoids in the vicinity of the LOFZ during the Neogene (Hervé et al.



1979). A third interpretation is that the ages are reset ages resulting from shear heating along the LOFZ (Hervé et al. 1979). More recent laser total fusion Ar-Ar dates of biotite and hornblende (Cembrano., 1990; Drake et al. 1991) have been interpreted to reflect Late Miocene to Pliocene (6 to 3 Ma) solid-state recrystallization of these minerals during ductile dextral shear deformation (Cembrano, 1992). Two recently obtained Ar-Ar step-heating dates on recrystallized biotite from mylonitic samples of the Río Mariquita and Cholgo units are in the range of 3.6 to 3.8 Ma. These were interpreted by Schermer et al (1995) as the age of a greenschist facies ductile deformation event.

The metamorphic wallrocks in the Hornopirén region consist of metapelite and metabasite belonging to a Late Paleozoic accretionary prism of regional distribution (Hervé, 1988; Pankhurst et al. 1992). These rocks record a progressive west to east change in metamorphic grade from greenschist to amphibolite facies as the contact with intrusive rocks is approached (Cembrano, 1992). Pelitic rocks near the contact have yielded a laser total fusion Ar-Ar age of  $7.2 \pm 0.7$  Ma on biotite (Drake et al. 1991).

The plutonic bodies display a north-northwest striking, poorly to well developed subvertical schistosity (Figure 2.4, 2.6b) defined by the preferred alignment of plagioclase crystals, hornblende-biotite aggregates, and by flattened interstitial quartz grains. Whereas in the Cholgo Unit a mesoscopic set of cm-spaced north-northeast-striking shear bands occurs at an angle of  $15^\circ$  to  $25^\circ$  to the schistosity (Figure 2.7c), in the Río Mariquita Unit there are spaced meter-wide mylonite zones. Lineations are typically absent in the granitoids, although isolated meter-wide ultra-mylonitic zones show subhorizontal stretching lineations (Figure 2.6d). More common are subhorizontal

striae of biotite flakes lying in the shear bands, similar to those described by Lin and Williams (1992) for granitoids deformed in the brittle-ductile transition zone.

Typical solid-state microstructures exhibited in the plutonic rocks include deformation bands and core and mantle structure in quartz, which locally occurs as type 1 and type 2 ribbons (Boullier and Bouchez, 1978; Simpson, 1985). Plagioclase crystals, which in places show a strong alignment, are generally microfaulted, bent, and less commonly recrystallized to a fine-grained aggregate along edges and internal fractures. Hornblende occurs as porphyroclasts surrounded by biotite, which in turn is extensively recrystallized to a finer-grained aggregate. A conspicuous pattern of north-northeast-striking dextral and east-northeast-striking sinistral microfaults is observed in oriented thin sections. Localized high strain zones exhibit a mylonitic fabric characterized by  $\sigma$ -type porphyroclasts of feldspar floating in a matrix of fine-grained recrystallized quartz-muscovite-epidote. Kinematic indicators, such as asymmetrical tails and domino structures, indicate dextral shear (Figure 2.8d).

Metamorphic wallrocks exhibit a more penetrative foliation than the plutonic rocks. Foliation in the metapelites strikes north-northwest and dips moderately to steeply to both west and east (Figure 2.4, 2.7b). Quartz-feldspar-rich layers and micaceous foliae define the schistosity. Subhorizontal stretching and mineral lineations are present on the schistosity. Spaced vertical shear bands that strike north-northeast and cut the schistosity occur locally. The metabasites show an anastomosing subvertical foliation, which locally wraps around mesoscopic-scale pods of virtually undeformed rock. Linear fabrics have not been recognized in the metabasic rocks.

Pelitic schists exhibit a penetrative foliation defined by discontinuous alternating layers of type-3 quartz ribbons (Boullier and Bouchez, 1978) and biotite + muscovite foliae. Well-preserved mica-fish (Lister and Snoke, 1984) define C-surfaces along interconnecting trails that are oblique to the quartz ribbon-schistosity, indicating dextral shear (Figure 2.9d). The geometry of asymmetrical tails on feldspar porphyroclasts also indicates dextral shear.

In the Hornopirén section both ductile and brittle deformation are well expressed. Ductile dextral shear deformation is recorded within plutonic units and metamorphic wallrocks. Core and mantle microstructure in quartz aggregates, type 1 and 2 quartz ribbons (Boullier and Bouchez, 1978), and fracturing and bending of plagioclase all indicate low-to mid-greenschist facies conditions for the latest solid-state deformation of the plutonic rocks. Metamorphic wallrocks exhibit synkinematic amphibolite facies metamorphic mineral assemblages (quartz-cordierite-biotite-sillimanite) and microstructures (type 3 quartz ribbons, Figure 2.5) (Boullier and Bouchez, 1978; Simpson, 1985) but do not show evidence of retrogression, suggesting deformation of the wallrocks ended earlier than in the plutonic rocks.

The Rb-Sr whole rock isochron age of  $4.7 \pm 0.6$  Ma has been interpreted as an emplacement age for adjacent coarse-grained tonalite and granodiorite (Pankhurst et al. 1992). However, the locally intense solid-state deformation of these rocks (Figure 2.7c), the difference in deformation between the tonalite (foliated) and granodiorite hosting aplite (relatively undeformed), and single-crystal total fusion ages on hornblende and biotite from the tonalite of 13-6 Ma (Figure 2.4) suggest there may be two distinct plutons, an older tonalite and younger granodiorite.

Detailed studies carried out along the main lineament flanking Hornopirén Canal reveal the existence of sharp faults that cut the ductile fabric of the plutonic rocks. Most faults are vertical to subvertical, have prominent subhorizontal striae and vary in length from decimeters to decameters. The majority of these faults group into a single homogeneous population including two families: the most abundant strikes  $000^{\circ}$ - $030^{\circ}$ ; the other shows variable strikes between  $060^{\circ}$ - $080^{\circ}$ . Both sets of faults display well-developed kinematic indicators on the fault surfaces, which indicate dextral slip for the north-northeast-striking set and sinistral slip for the east-northeast-striking set (Figure 2.7c). A dextral strike-slip deformation regime is obtained when applying the E.C.G.-Geodynsoft to these fault sets, giving stress axes of  $\sigma_1 = 244^{\circ}, 13^{\circ}$ ;  $\sigma_2 = 57^{\circ}, 77^{\circ}$ ;  $\sigma_3 = 154^{\circ}, 02^{\circ}$  (Figure 2.7c).

## **2.5 Discussion**

### **2.5.1 Nature and timing of deformation**

Heterogeneously deformed rock units exposed in three traverses mapped along the LOFZ document a complex history of episodic ductile deformation followed by brittle deformation. In comparing the three transects, we emphasized the similarities and differences in our detailed observations, which are separated by kilometers of poorly exposed and poorly studied terrain or areas covered by Quaternary volcanic units. However, reconnaissance observations between the transects indicate the structural style is similar for tens of kilometers north and south of each transect. Regardless of the detailed reasons for along strike continuity (or lack thereof) in kinematics, style and timing of deformation, our new data indicate that important new distinctions can be made

between the different parts of the LOFZ. Detailed consideration of timing of deformation must await further geochronologic and thermochronologic study.

The 2 km-wide mylonitic belt occurring in the northernmost end of the Liquiñe-Ofqui fault zone records an important episode of ductile deformation which affected Paleozoic gneisses. Our recently obtained Ar-Ar date of  $100 \pm 2$  Ma in amphibole phenocrysts from an undeformed dyke which crosscuts the mylonites in the center of the Liquiñe shear zone suggest that deformation in this region is pre-late Cretaceous. Kinematic indicators suggest sinistral-reverse shear in most domains. Coexisting symmetric fabrics, such as globular quartz porphyroclasts and conjugate shears suggest that at least part of the deformation was coaxial within discrete domains (*sensu* Choukroune et al. 1987). The coexistence of sinistral-reverse shear and shortening across-strike in the rocks from Liquiñe may be the result of a bulk sinistral transpressional deformation that was partitioned into orogen-parallel oblique-slip and across-strike shortening in the anastomosing fashion described by Bell (1981) and Bell et al. (1986). Alternatively, two discrete episodes of deformation may have occurred, however no evidence of crosscutting structures was observed.

Diagnostic microstructures such as type-2 quartz ribbons (Boullier and Bouchez, 1978; Simpson, 1985) and plagioclase crystals with internal fractures and partly recrystallized rims in the rocks of the Liquiñe region suggest that deformation occurred under mid-to upper-greenschist metamorphic facies conditions (i.e. temperatures in the range of 300°-350°C; Simpson, 1985). The metamorphic mineral assemblage present in these rocks (quartz-biotite-muscovite) is compatible with the metamorphic conditions suggested from the microstructures.

Brittle overprinting on the early ductile fabric is poorly developed in Liquiñe and does not show the consistent geometry and kinematics necessary to obtain a local stress tensor.

Some two hundred kilometers south of Liquiñe, in the Reloncaví region, ductile deformation is nearly absent, while brittle deformation is very conspicuous along north-trending lineaments. Faults cut isotropic plutonic rock ranging in age from mid-Cretaceous to Miocene. North-northeast-striking dextral and east-northeast-striking sinistral faults along with west-northwest-striking reverse faults are consistent with a horizontal maximum compressional stress direction trending northeast associated with an overall dextral strike-slip tectonics. Another fault population of east-northeast-striking dextral-reverse and west northwest striking sinistral reverse faults appears to have been the result of east-west compression. The time relationship between these two brittle deformational events is not clear, as crosscutting relations of distinctive striae are not observed on single fault surfaces. However, the absolute timing of the E-W compressional event is likely Upper Miocene or later as similar faults are observed in both Cretaceous and Miocene rocks. However, the strike-slip stress tensor identified in Reloncaví is very similar to that obtained in Hornopirén, which may indicate that both regions record the same post -3 Ma deformational event.

The presence of parallel magmatic and subsolidus fabrics in the Cholgo Unit suggests dextral shear started during emplacement or early cooling of the plutonic rocks and continued during cooling and unroofing of the batholith. Single crystal total fusion Ar-Ar ages of biotite from plutonic rock ranging from 8.7 to 3.6 Ma (Drake et al. 1991; Cembrano et al. 1996; Schermer et al. 1996) may reflect recrystallization of these

minerals during solid-state deformation and/or cooling following deformation. The 7.2 Ma Ar-Ar biotite age from synkinematic biotite in wallrock schist represents cooling following wallrock deformation and appears to be coeval with intrusion and/or subsequent cooling and deformation of the plutonic rocks. The predominance of hornblende ages from 9-13 Ma and biotite ages from 3-6 Ma suggest that ductile deformation began in late Miocene time, shortly after synkinematic emplacement of the Cholgo Unit at 9.9 Ma, and progressed during cooling from 500°-300°C during late Miocene-Pliocene time.

The brittle deformation in the Hornopirén region overprints the ductile fabric, forming a population of north-northeast-striking subvertical dextral faults and less common east-northeast-striking sinistral faults. As observed in the Reloncaví area, the geometry and kinematics are consistent with a dextral strike-slip deformation regime. In contrast to the Reloncaví transect, however, the east-west compressional event is not represented, showing that this event may have been local in character or, possibly older and not recorded in the younger plutonic rocks of Hornopirén. The brittle deformation in the Hornopirén region certainly took place after the mid-Pliocene since the faults cut rocks with Ar-Ar ages as young as 3.3 Ma. In fact, this fixes a maximum age for the brittle deformation of the rock as the closure temperature for biotite is around 325°C (Harrison et al. 1985), which is slightly higher than the temperature at which quartz begins to exhibit ductile behavior. The absence of ductile deformation in the Reloncaví segment may reflect a different level of exposure due to differential uplift along the fault zone, or the lack of widespread pluton emplacement and concomitant thermal weakening during deformation.

## **2.5.2 Geodynamic significance of the Liquiñe-Ofqui fault zone**

The Liquiñe-Ofqui fault zone has been regarded as an intra-arc strike-slip fault zone resulting either from oblique subduction (Hervé, 1977; Beck, 1988) or from the indenter effect of the Chile Rise at the southern termination of the fault system (Forsythe and Nelson, 1985; Nelson et al. 1994). Although both models seem plausible, previous workers had limited structural data to relate plate motions to the actual deformation of the overriding plate. Kinematic data from the Liquiñe-Ofqui fault zone obtained in this study can be used to assess the influence of these parameters in the tectonics of an active continental margin.

### **2.5.2.1 Oblique subduction**

Most authors studying margin-parallel faulting along oblique subduction zones (Fitch, 1972; Beck, 1983; Jarrard, 1986; Beck, 1991; McCaffrey, 1992; Beck et al. 1993) agree that there are several factors controlling the formation of a forearc sliver. These include the nature of the overriding plate (continental versus oceanic), angle of obliquity, convergence rate, and interplate coupling. The importance of these factors can be assessed for the LOFZ. The best-constrained period of ductile deformation reported here occurred during Late Miocene to Pliocene time, when dextral shear appears to have dominated the tectonic setting of the magmatic arc. Plate reconstructions show a slightly right oblique convergence at a high rate for that time period (Pardo-Casas and Molnar, 1987; Engebretson, written communication, 1995). Although the sense of obliquity is consistent with the documented sense of shear, the angle between the convergence vector and the orthogonal to the trench seems to have been too small ( $\sim 25^\circ$ ) to account by itself for the strike-slip tectonics within the magmatic arc. In fact, McCaffrey (1992) has



shown that, for present-day oblique convergent margins, slip on the intra-arc strike-slip fault does not occur for obliquities less than  $30^\circ$ . For the southern Chilean Andes, we propose that strong intraplate coupling resulting from the subduction of young and buoyant oceanic lithosphere north of the Nazca - South America - Antarctica triple junction plus a weak continental crust appear to be the key factors for intra-arc faulting.

U-Pb dating on plutons and Ar-Ar data on mylonites suggest that cooling from ductile to near-brittle dextral shear occurred from 9-3 Ma and may have been continuous into the post-3 Ma brittle dextral fault regime. Since plate motions have not changed substantially after the Pliocene (Pardo-Casas and Molnar, 1987), deformation partitioning of the Nazca-South America slip vector into forearc shortening and intra-arc dextral strike-slip displacement may have been continuous for several million years.

In contrast to Miocene-Pliocene dextral shear, pre-Late Cretaceous sinistral-reverse shear documented in Liquiñe is too poorly constrained in time to allow a meaningful correlation with plate kinematics. In any case, plate motion reconstructions are not reliable for the South American plate margin before the Early Cenozoic (Engelbreton, pers. com. 1995). However, Early Cretaceous sinistral shear deformation has been found along the intra-arc Atacama Fault System in northern Chile (Scheuber and Andriessen, 1990; Brown et al. 1993), raising the possibility of activity along the Liquiñe-Ofqui Fault zone extending back into the Mesozoic. If that is the case, the fault zone would be a long-lived structure reactivated at different times in response to an evolving plate kinematic framework (e.g. White et al. 1986). The short-term instantaneous deformation regime at the Liquiñe-Ofqui fault zone has been obtained from the dextral strike-slip fault plane solution of two crustal earthquakes at both extremes of

the fault system (Chinn and Isacks, 1983; Barrientos and Acevedo, 1992). Although sparse and insufficient, these data suggest that the fault zone is currently active as a dextral strike-slip fault absorbing the margin-parallel component of the convergence slip vector (Dewey and Lamb, 1992). More seismic data are needed to better constrain the present-day nature of motion of the Liquiñe-Ofqui fault zone.

#### **2.5.2.2 Indenter tectonics**

Forsythe et al. (1985) proposed that some motion on the Liquiñe-Ofqui fault zone has been the result of the impingement of the Chile Ridge on the southern Andes continental margin during the last 14 Ma. According to their model, the Chile ridge has acted as an indenter causing an outboard sliver, the "Chiloé block", to move northward and become detached from the continent along the Liquiñe-Ofqui fault zone. More recently, Nelson et al. (1994) have assessed the effect of ridge subduction and oblique subduction at the Peru-Chile trench through numerical modeling. Their model predicts the trajectory of maximum horizontal stress ( $\sigma_{Hmax}$ ) and the distribution of vertical strain along and across the continental margin as a result of the collision of the Chile ridge at its present-day position. According to Nelson et al. (1994), the current geometry and sense of motion of the southern termination of the Liquiñe-Ofqui fault zone seems to be compatible with the predicted orientation of  $\sigma_{Hmax}$ . On the other hand, modeled strain patterns also are consistent with limited available short-term seismic and geodetic data for the southern Andes forearc (Plafker and Savage, 1970; Barrientos and Ward, 1990). However, field evidence on the nature and timing of long-term and short-term deformation along the entire length of the Liquiñe-Ofqui fault zone is not discussed in

detail by Nelson et al. (1994) to test compatibility of their ridge subduction model with the long-term evolution of the LOFZ. Therefore, although fairly consistent with the short-term deformation, Nelson et al.'s model does not address the effect of long-term ridge subduction on deformation along the Liquiñe-Ofqui fault zone, particularly at its northern half which is some 500-1000 km away from the present-day triple junction, and may have been unaffected by ridge subduction. Nonetheless, the oblique subduction component of their model does explain recent dextral motion along the length of the LOFZ. Consequently, the long-term and steady nature of oblique subduction makes this driving mechanism more likely to explain the overall tectonics of the Liquiñe-Ofqui fault zone rather than the indenter effect of the Chile ridge, which we see as a second-order mechanism enhancing the Pliocene-Recent dextral strike-slip motion along the Liquiñe-Ofqui fault zone.

## **2.6 Conclusions**

Structural and geochronological data presented in this chapter document a long and complex history of intra-arc deformation in the southern Chilean Andes. The northern half of the Liquiñe-Ofqui fault zone appears to exhibit different styles and times of deformation in three transects. The northernmost, Liquiñe region, experienced sinistral ductile shear prior to 100 Ma, and later faulting of uncertain kinematics. The central, Reloncaví segment, shows no clear evidence of ductile shear from Cretaceous to Miocene time, but brittle fault fabrics are well developed in plutons of both mid-Cretaceous and late Miocene ages. Inversion of fault slip data for the stress tensor suggests dextral strike-slip and compressional deformation regimes. The southern,

Hornopirén segment, exhibits evidence for both ductile and brittle deformations. Kinematic data from both brittle and ductile structures suggest dextral shear; published radiometric dating suggests ductile shear during late Miocene-Pliocene time (13-3 Ma), with brittle shear occurring after 3 Ma. The older sinistral deformation seen in the northernmost segment is of uncertain significance but may be related to a period of margin parallel sinistral shear in the Early Cretaceous coeval with that of the Atacama fault system. The dextral structures appear to be related to oblique subduction of the Nazca plate and partitioning of deformation in the thermally weakened crust of the continental margin. The dextral system appears to characterize the long and short-term kinematics of the Liquiñe-Ofqui fault zone, as evidenced by both the structural data presented herein and limited earthquake data.

## **Chapter 3. Late Cenozoic transpressional ductile deformation north of the Nazca-South America-Antarctica triple junction.**

### **3.1 Introduction**

Overall transpressional deformation is expected at continental margins where the convergence vector is oblique with respect to the plate-boundary zone (e.g. Sanderson and Marchini, 1984; Tikoff and Teyssier, 1997). Other first-order factors controlling the tectonics of convergent margins are the age of the subducting plate, the nature and thermal structure of the overriding plate, the existence of major trench-parallel faults and ridge subduction (e.g. Jordan et al. 1983; Jarrard, 1986; Beck, 1991; Nelson et al. 1994).

Transpressional deformation arising from oblique convergence is accomplished by distinctive structural styles along and across different plate boundaries, mostly depending on the angle of obliquity, defined as the angle between the convergence vector and the plate boundary (Teyssier et al. 1995). Transpression may be homogeneously distributed, as in the case of the Australian-Pacific plate boundary in New Zealand (low obliquity), or completely partitioned as in the Pacific-North America plate boundary of the western US (high obliquity). The general case, however, will be that of heterogeneous transpression in which discrete domains across the plate boundary accommodate wrench-dominated or pure-shear dominated transpression (e.g. Fossen et al. 1994; Tikoff and Greene, 1997). This is the case for ancient ductile shear zones, in which the strike-slip component of transpression is not taken up by slip on a single fault but within zones of distributed shear (e.g. Fossen et al. 1994; Jones and Tanner, 1995).

Thus, the nature and degree of deformation partitioning will not only depend on the angle of obliquity. The existence of major plate boundary-parallel shear zones that can accommodate a significant part of the strike-slip component of overall convergence, either by slip on discrete faults in the upper crust or by distributed shear at mid-to low-crustal levels, will also be important.

The southern Chilean Andes provides a natural laboratory to investigate the nature of long-term and short-term transpressional deformation across an obliquely convergent continental margin. An active ridge, the Chile Ridge, is currently subducting under western South America and a trench-parallel fault system has developed along the Cenozoic magmatic arc (Figure 3.1). The Cenozoic geodynamic setting of the southern Chilean Andes is well constrained, showing relatively steady right-oblique subduction of the Farallon (Nazca) plate beneath South America since 48 Ma with the exception of nearly orthogonal convergence from 26 to 20 Ma (Pardo-Casas and Molnar, 1987). At present, the angle of obliquity of Nazca - South America plate convergence vector with respect to the orthogonal to the trench is  $\sim 26^\circ$  for southern Chile (Jarrard, 1986). The slab dip is approximately  $16^\circ$  (Jarrard, 1986) and the age of the subducting Nazca plate decreases from  $\sim 25$  Ma at  $38^\circ\text{S}$  to virtually 0 Ma at  $46^\circ\text{S}$ , where the Chile Ridge is currently subducting (Herron et al. 1981; Burgois et al. 1997). The limited seismic data available suggest that the Chilean forearc between  $39^\circ$  and  $46^\circ\text{S}$  is currently undergoing trench-orthogonal shortening; the volcanic arc is absorbing a small trench-parallel component (Chinn and Isacks, 1983; Cifuentes, 1989; Barrientos and Acevedo, 1992; Dewey and Lamb, 1992; Murdie, 1994). One major problem when trying to establish the relationship between the tectonics of the overriding South American plate and the

**Figure 3.1** Regional-scale tectonic setting of the Southern Andes. Northeast-trending, trench-parallel lineaments, correspond to the Liquiñe-Ofqui fault zone. Current position of the Nazca-South America-Antarctica triple junction is shown. Series of small arrows represent convergence vectors between the Nazca and South American plates for the last 48 Ma. (Modified from Pardo-Casas and Molnar, 1987, Cembrano et al. 1996, Burgois et al. 1997).

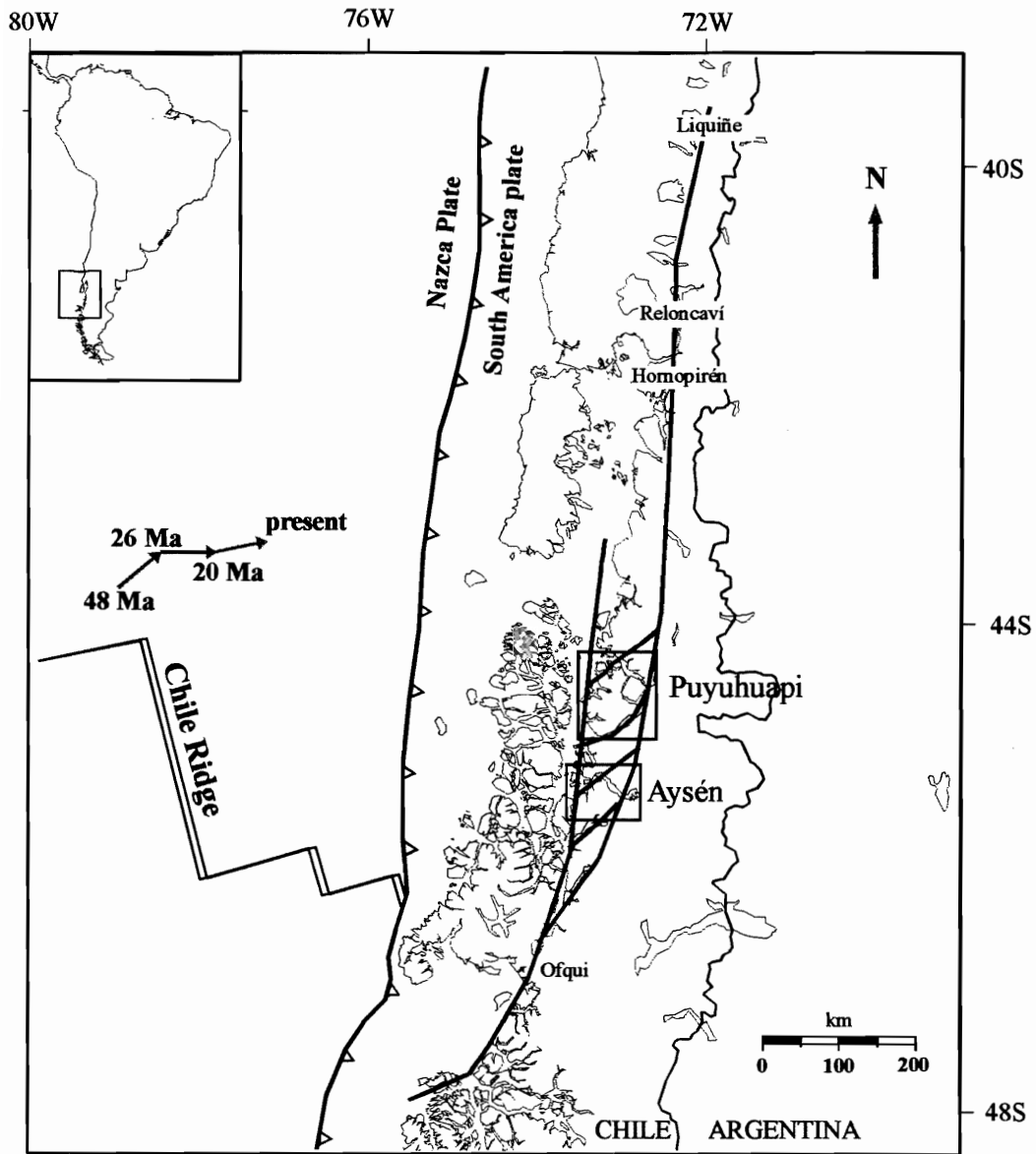


Figure 3.1



Cenozoic plate kinematic framework has been the almost complete lack of detailed structural and thermochronological studies in the Patagonian region. With the exception of regional geology and petrology-oriented work (e.g. Bobenrieth et al. 1983, Bartholomew and Tarney, 1984; Hervé et al. 1995) there has been no systematic study of the tectonic evolution of this important segment of the Andes from the structural point of view. The regional geology and structure of the foreland, however, has been recently studied by Chilean and British scientists (Flint et al. 1994, Suarez et al. 1996). One important feature of this segment of the Andes is the absence of a Meso-Cenozoic regional fold and thrust belt inland of a 1000 km long Cenozoic intra-arc fault zone which has been assumed to accommodate much of the convergence deformation.

On the other hand, field studies have been difficult to carry out in the western slope of the Patagonian Cordillera because of dense vegetation and generally poor weather conditions. However, a large network of valleys and fjords allows most of the area to be reached by boat. Furthermore, it is possible to study several east-west transects across the orogen. In this chapter, I present and discuss field, structural and thermochronological data from two transects across the southern Andes, at latitudes 44° and 46°, the Puyuhuapi and Aysén transect, respectively (Figure 3.1, 3.2). In the previous chapter, I presented a summary of along-strike contrasts in the nature and timing of deformation along the segment immediately north, from 39° to 43°S.

### **3.2 Geologic Setting**

The North Patagonian Batholith (NPB) occupies a central belt, ca. 1000 long and 200 km wide, along the Patagonian Cordillera. It is flanked to the west by a basement

**Figure 3.2.** Regional-scale geologic map of the southern Chilean Andes between 44° and 47°S. (modified from SERNAGEOMIN, 1980; Bobenrieth et al. 1983; Pankhurst and Hervé, 1994, Hervé et al. 1995). The Paleozoic Basement is represented with gray color. It is exposed in the Archipiélagos and also to the east of the main outcrop of the Patagonian Batholith. This Patagonian Batholith is represented with red color. The star pattern corresponds to the Late Jurassic to Early Cretaceous western belt whereas the cross pattern indicates the main outcrop of the eastern mid-Cretaceous granitoid belt. The Central Miocene belt is pattern free. A few, small plutons of Eocene age (x pattern), crop out in between the Paleozoic basement and the Miocene plutonic belt. Outcrops of the mid-Tertiary Traiguén Formation are represented by isolated, light green-colored spotty areas, distributed along a narrow strip, immediately to the west of Canal de Moraleda and at Isla Magdalena. Mesozoic foreland undeformed volcanosedimentary rocks are blue- and dark green-colored and crop out extensively in the Patagonian region of Aysén.

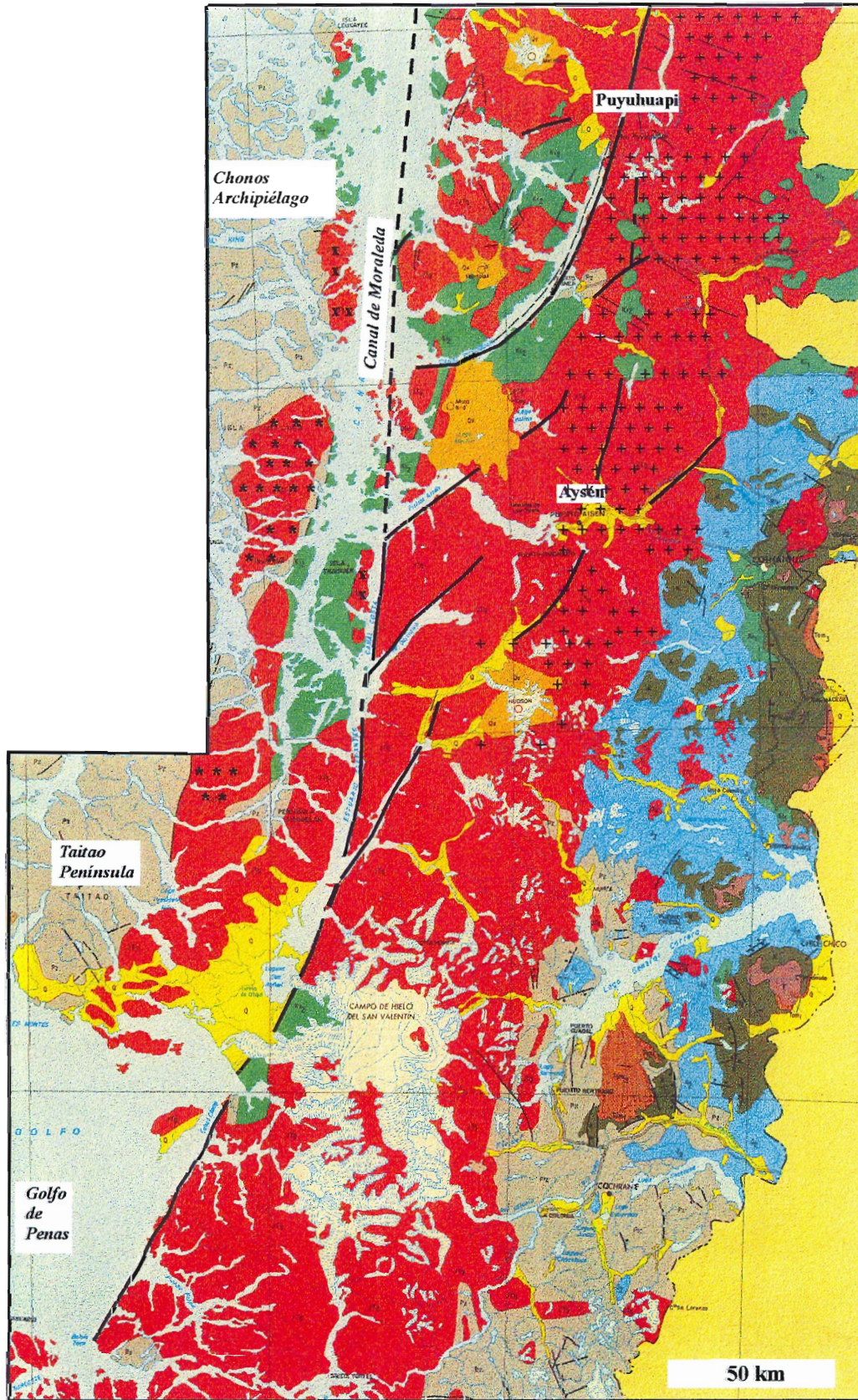


Figure 3.2

composed of polyphase metamorphic rocks and to the east by a weakly deformed volcano-sedimentary cover. A thin, discontinuous strip of metasediments and pillow metabasalts crops out between the metamorphic basement and the NPB. Such rocks are generally flat-lying west of a major north-south-trending lineament (Canal de Moraleda) and highly deformed at and to the east of the channel where they are very scarce (Figure 3.1, 3.2).

The basement is mostly composed of metasedimentary rocks and less-well-exposed greenstone and chert. Godoy et al. (1984) suggested that the basement was Late Paleozoic in age based upon field and geochronological reconnaissance. Hervé (1988) interpreted the metamorphic basement as an accretionary prism, deposited and deformed in situ during Late Paleozoic times. Basement rocks are locally reactivated along northeast-trending ductile shear zones, meters to hundreds of meters in width. In places, it is difficult to discriminate between high strain metapelitic rocks and metabasites developed from the basement and those developed from the Tertiary Traiguén Formation. This problem can be partially solved by a close look at the surrounding less-deformed protolith. While basement rocks are usually folded and show clear evidence of polyphase deformation, Traiguén Formation rocks are only slightly deformed away from the shear zones.

Based upon regional mapping and basic geochronologic dating, the North Patagonian Batholith has been divided into three orogen-parallel belts: A western Jurassic to Cretaceous granodioritic belt, a central Miocene belt of granodiorite-diorite with few granites, and an eastern mid-Cretaceous belt constituted by monzogranites and



granites (Pankhurst et al. 1992, Hervé et al. 1993, Pankhurst and Hervé, 1994), (Figure 3.2).

Bartholomew and Tarney (1984) proposed that the north-south trending strip of volcanoclastic and sedimentary rock located between the Paleozoic basement and the main outcrop of the Patagonian Batholith represented a Late-Cretaceous-Tertiary intra-arc basin. According to their model, crustal thinning arising from east-west extension was sufficient for true oceanic floor to develop. Their model is supported mainly by the geochemical signature of the volcanic rocks: tholeiitic rather than calc-alkaline in character. Field evidence documenting the geometric and kinematic relationship between the intra-arc basin deposits and the batholith is very limited. They proposed that, during a Miocene compressional event, the basin was inverted and underthrust below the plutonic complex. Easterly-dipping shear zones outcropping along the margins of the basin were presented as evidence for underthrusting. The fact that plutonic and metamorphic rocks representing lower crustal levels crop out to the east of Canal de Moraleda was used as evidence for west-verging regional thrust faults.

Hervé et al. (1995) proposed an alternative model for the origin of the pillow basalts and associated metasediments. Based on geologic mapping of the Traiguén Formation at Isla Magdalena, they suggested that a strike-slip basin nucleated along a leaky transform fault, represented now by the LOFZ. However, as in the former model, little structural and chronological evidence was provided to relate coeval dextral-strike-slip motion on the fault to basin formation and sedimentation. A major difficulty has been to date the metabasalts and metasediments, which for the most part, have yielded poorly constrained Miocene ages (Hervé et al. 1995).

### **3.3 Structural Setting**

Cenozoic continental margin deformation along the southern Andes is mostly restricted to the magmatic arc, where a major fault-system, the Liquiñe-Ofqui fault zone (LOFZ) runs for more than a 1000 km in a north-south direction (e.g. Forsythe and Nelson, 1985; Dewey and Lamb, 1992; Hervé, 1994; Cembrano et al. 1996). The forearc and foreland regions show very little evidence of regional-scale deformation. The region under study does not have a foreland fold-and-thrust belt as do the Andean regions immediately south and north (e.g. Ramos et al. 1989; Ramos and Kay, 1992). The development of the Patagonian foreland fold-and-thrust belt south of 47°S is attributed to the northward migration of the subducting Chile-Ridge over the last 14 Ma. According to Hervé (1994) the absence of foreland deformation north of 47°S has resulted from the accommodation of a significant part of the bulk convergent deformation along the Liquiñe-Ofqui fault zone.

### **3.4 Geometry and kinematics of discrete ductile shear zones of the Puyuhuapi and Aysén transects.**

Detailed structural work was performed in several high strain zones developed from rocks of different nature and age along and across the magmatic arc in the two studied transects. Some of these shear zones are located along the eastern lineament of the LOFZ, whereas others occur along the western lineament. Other, less-well developed shear zones occur between the two main crustal lineaments (Figures 3.2, 3.3, 3.4, 3.5, 3.6, 3.7, 3.8, 3.9). Bartholomew (1984) had previously identified some of these shear zones at the regional scale, during reconnaissance work. However, he provided no data on the

**Figure 3.3** Regional geology and structure of the Puyuhuapi transect showing the location of major ductile shear zones.

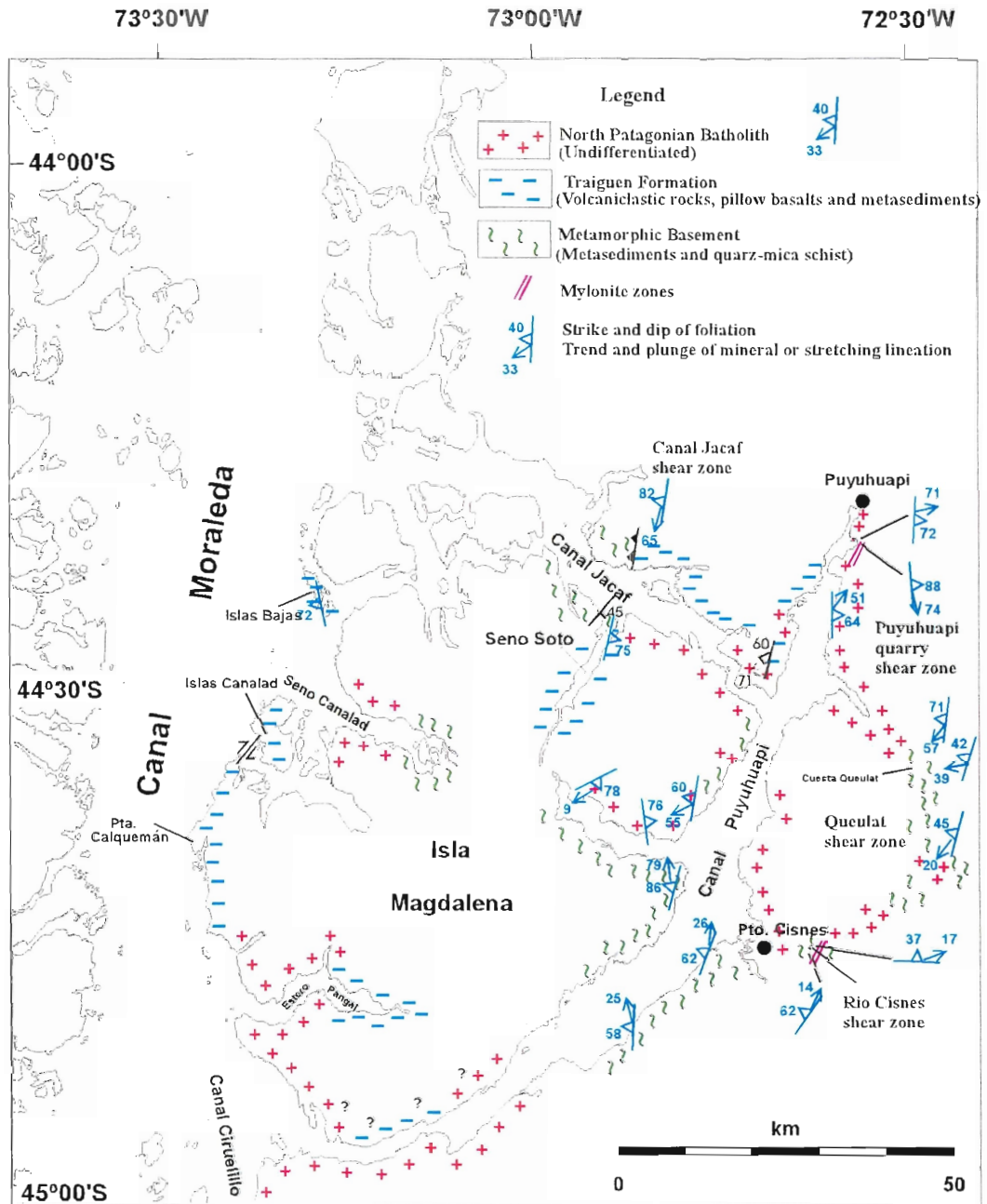


Figure 3.3



**Figure 3.4** Regional geologic map of the Puyuhuapi transect showing location of samples selected for  $^{40}\text{Ar}$ - $^{39}\text{Ar}$  analysis.

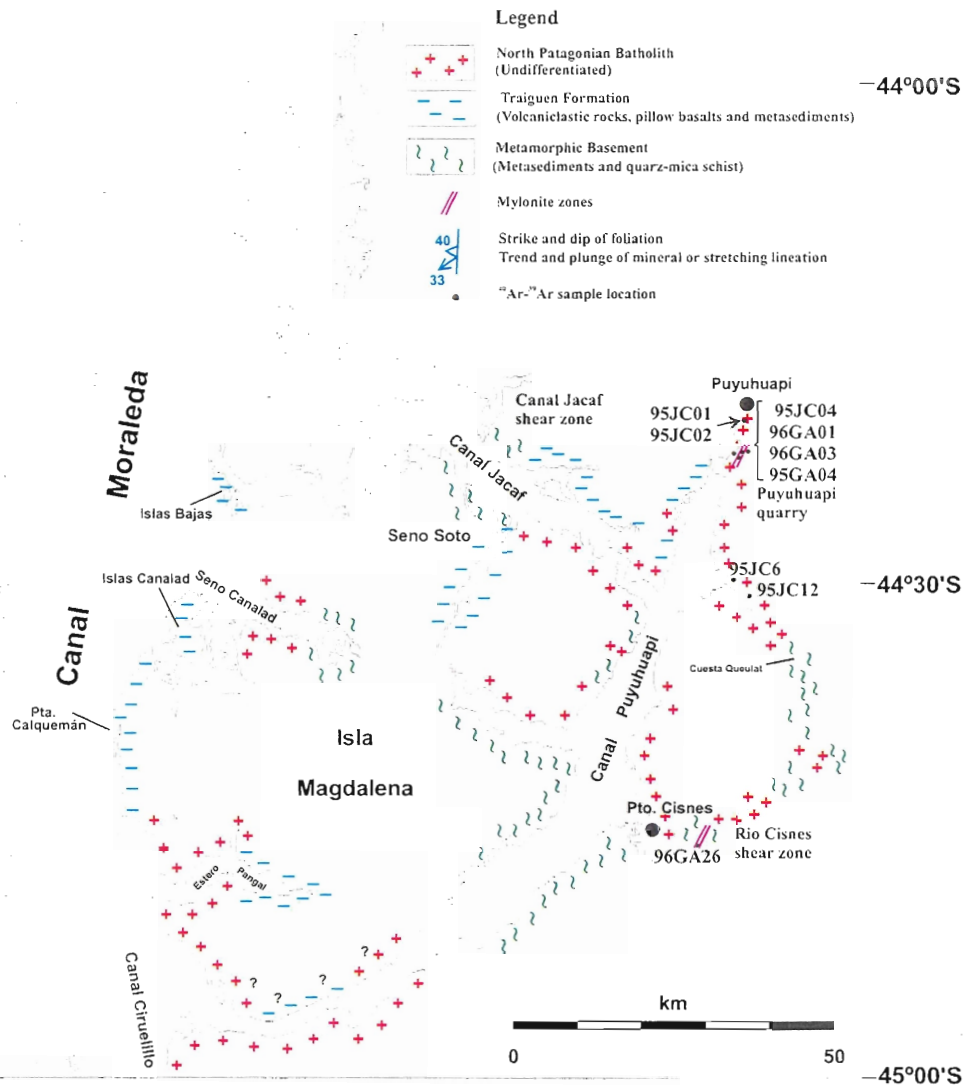


Figure 3.4

**Figure 3.5** New  $^{40}\text{Ar}$ - $^{39}\text{Ar}$ , mean ages, for undeformed rocks and mylonites of the Puyuhuapi transect (Spectra shown in figure 9). Previously published Rb-Sr ages are indicated (Pankhurst and Hervé, 1994; Hervé et al. 1995).

73°30'W

73°00'W

72°30'W

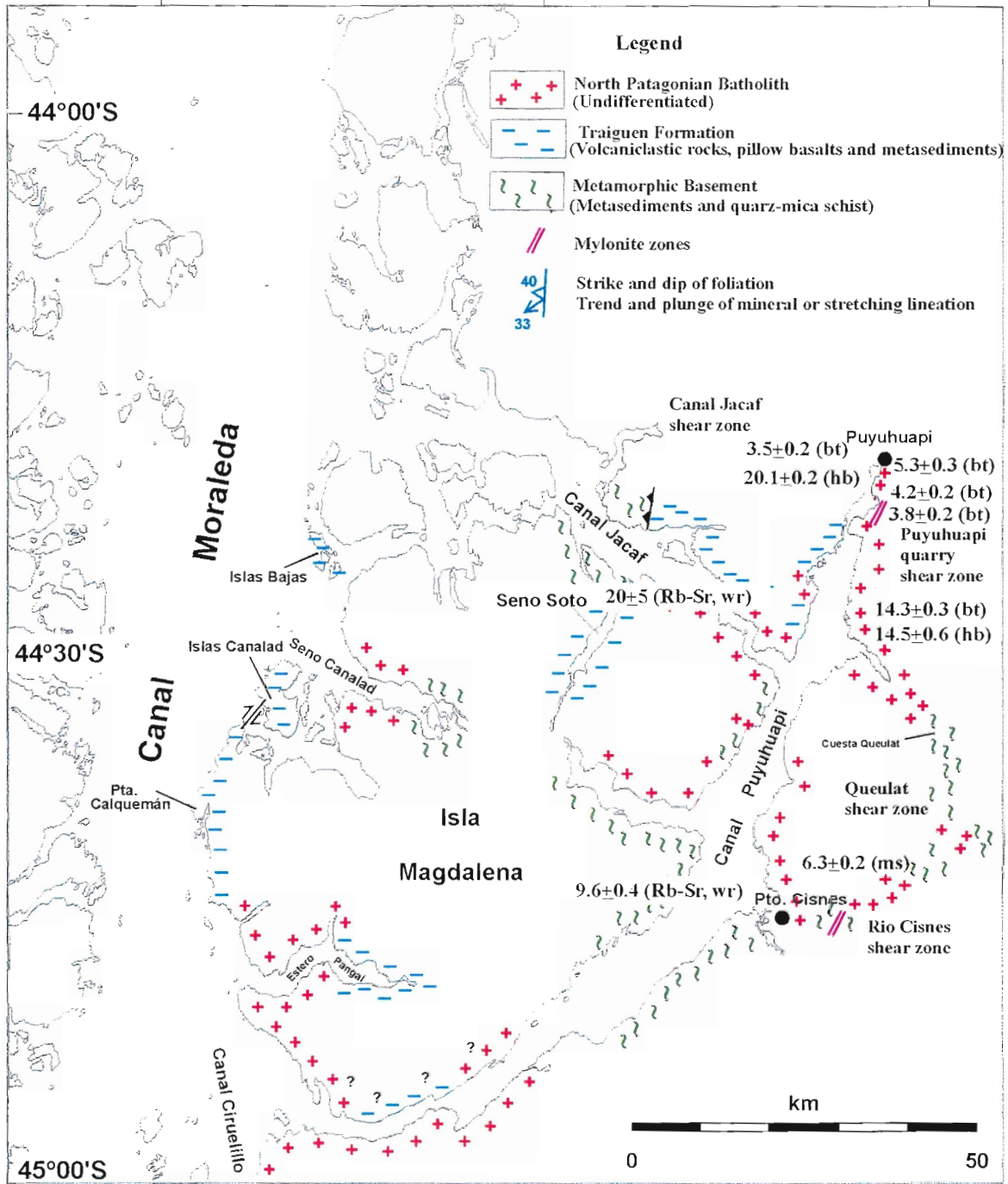
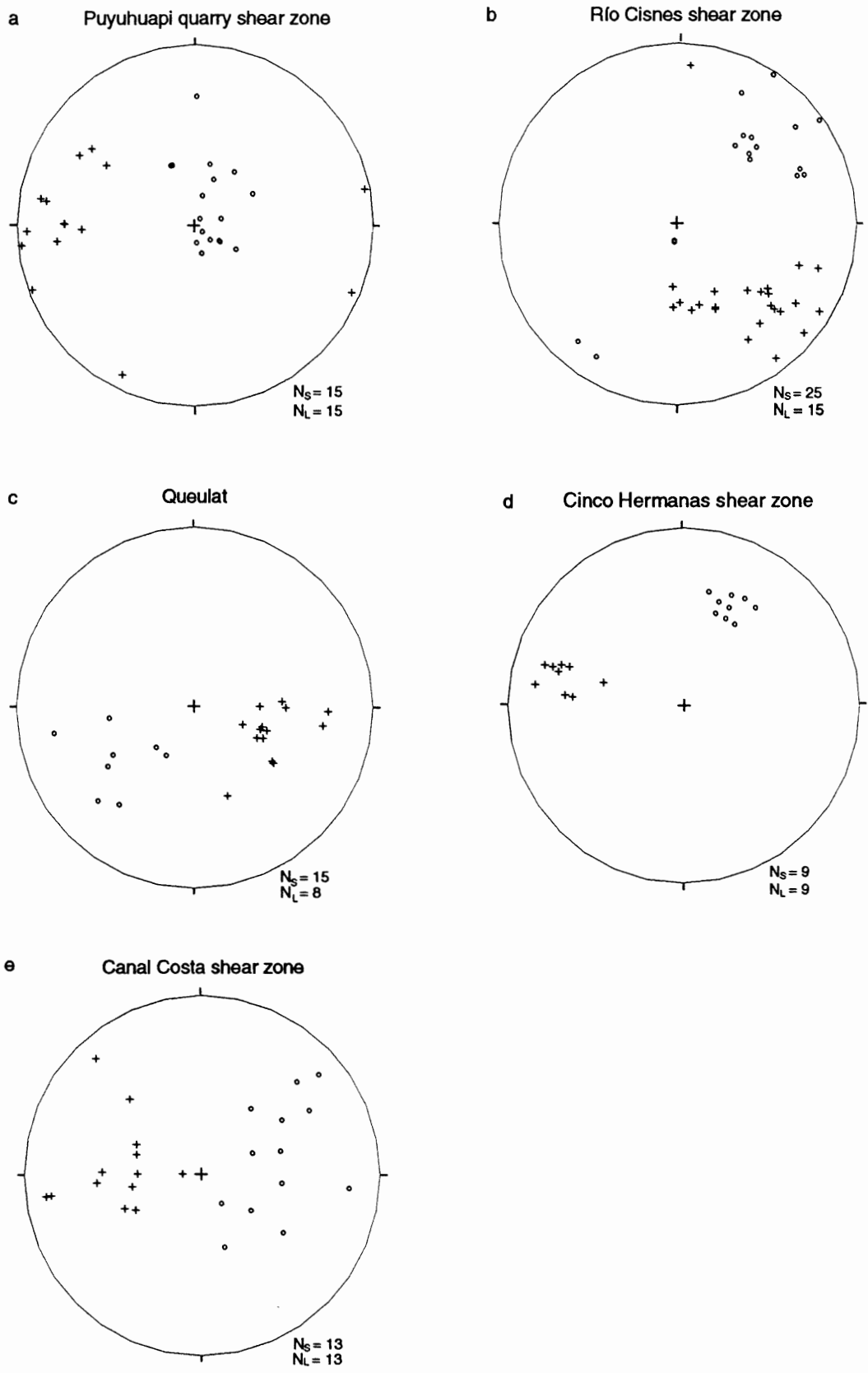


Figure 3.5

**Figure 3.6.** Lower hemisphere, stereographic projections of poles to foliations (crosses) and stretching lineations (dots) for ductile shear zones of the Puyuhuapi and Aysén transects



**Figure 3.6**

**Figure 3.7** Regional geology and structure of the Aysén transect. Location of major shear zones is shown.

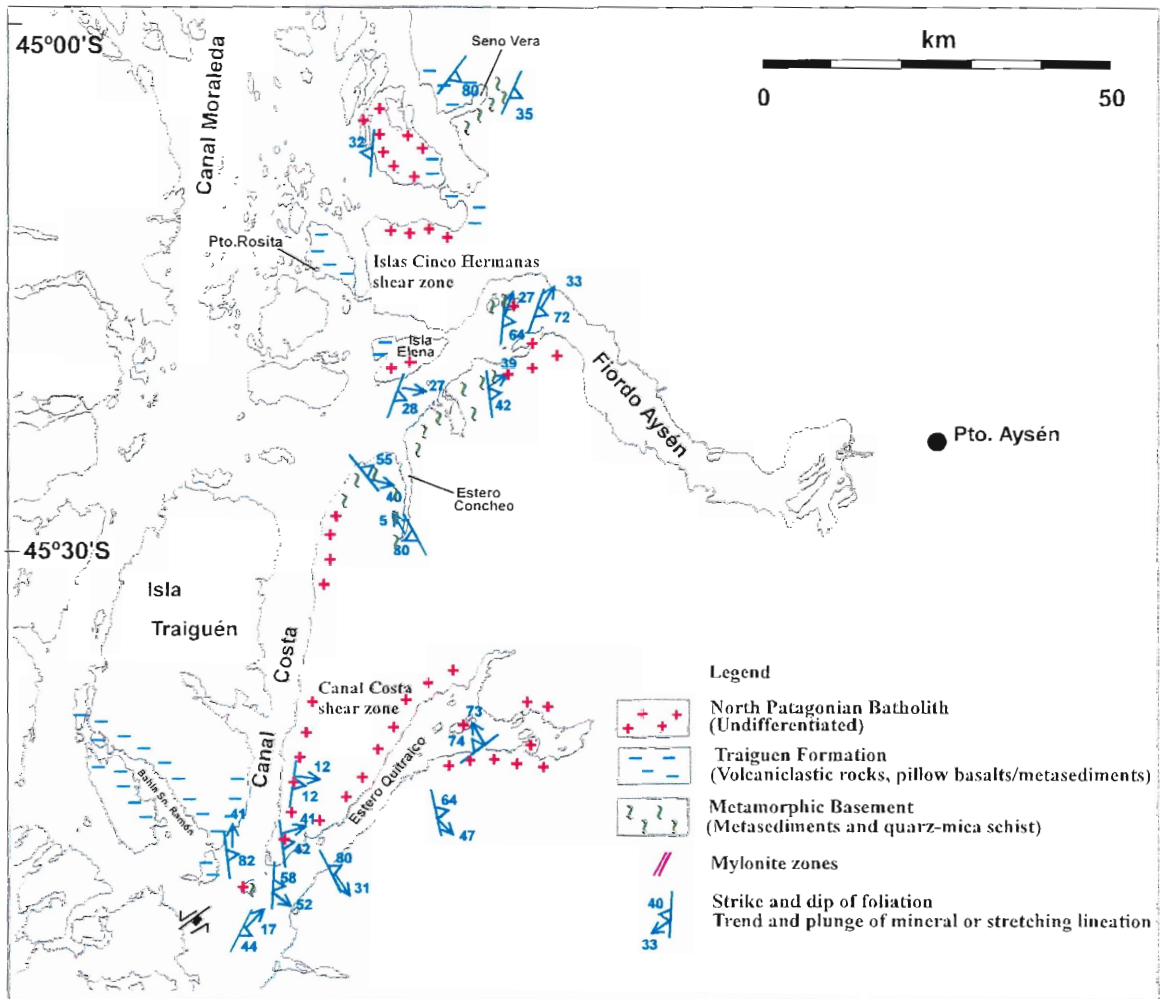


Figure 3.7



**Figure 3.8** Regional geologic map of the Aysen transect showing location of samples selected for  $^{40}\text{Ar}$ - $^{39}\text{Ar}$  analysis.

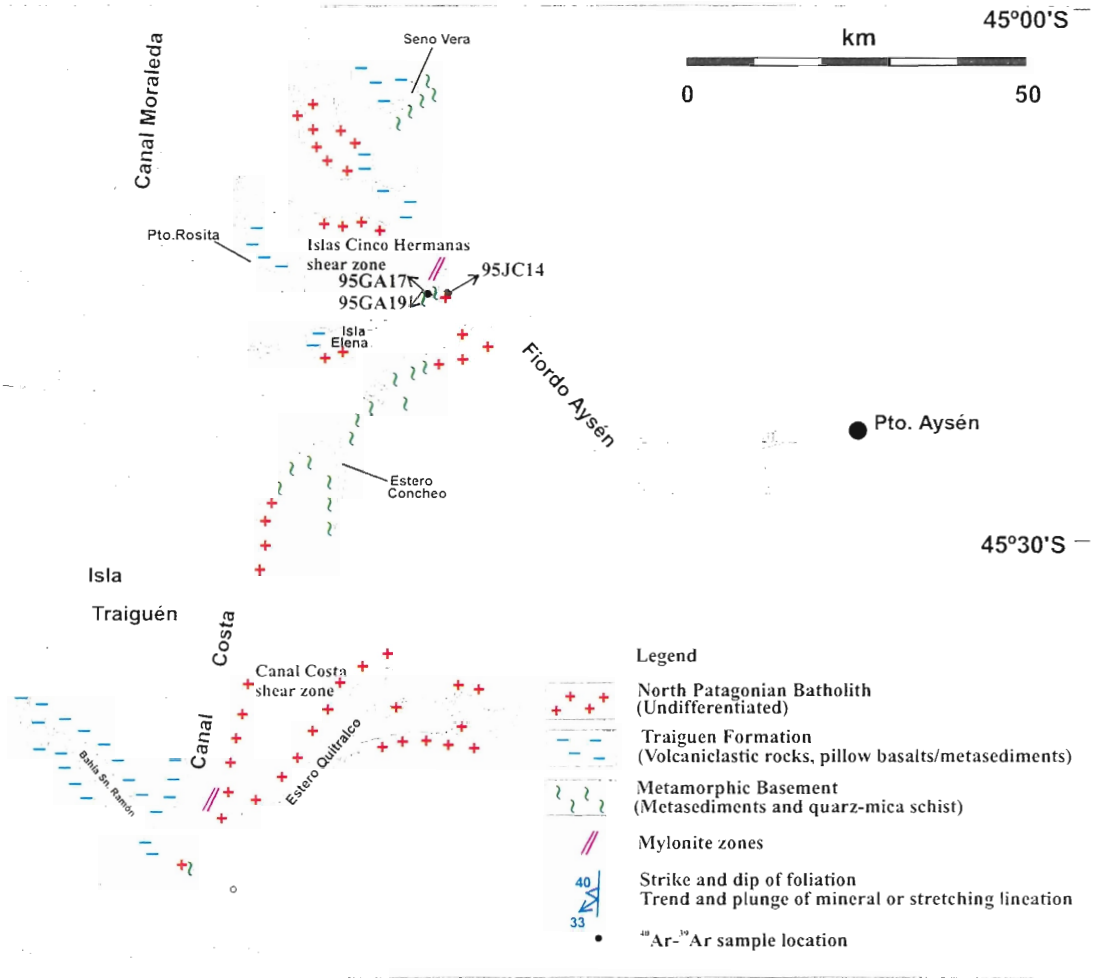


Figure 3.8

**Figure 3.9** New  $^{40}\text{Ar}$ - $^{39}\text{Ar}$  ages for undeformed rocks and mylonites of the Aysén transect (Spectra shown in figure 9). Previously published Rb-Sr ages are indicated (Pankhurst and Hervé, 1994; Hervé et al. 1995).

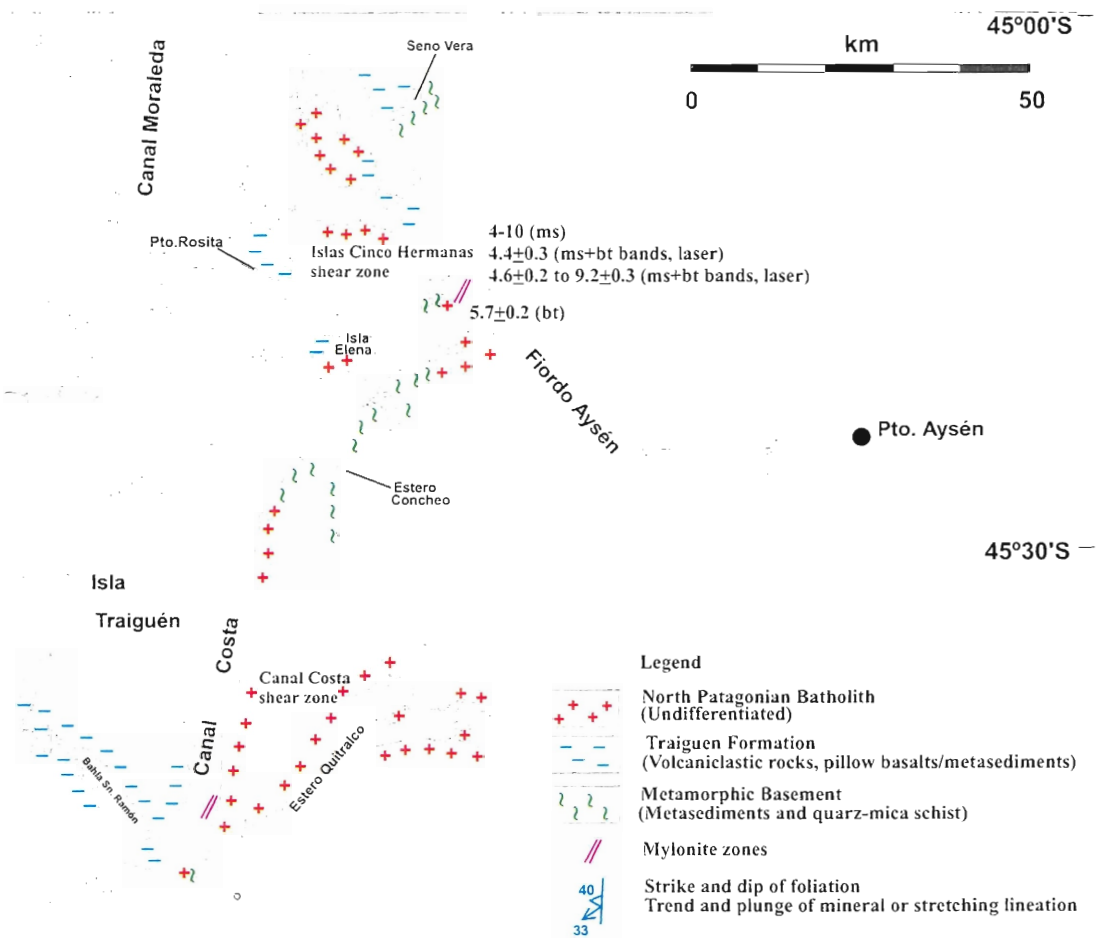


Figure 3.9

geometry of stretching lineations and on the kinematics of deformation, as he was mainly concerned with the geochemistry of the plutonic rocks.

Figures 3.3 and 3.7 show the spatial distribution and geometry of solid-state fabrics of the Andean region between 44 and 46 degrees south. Stereoplots of foliations and lineations are shown in Figure 3.6. The regional structural map and the stereoplots show variable dips of foliations and shallowly to steeply plunging lineations throughout. Most foliations dip to the east along the western margin of the Miocene plutonic belt of the North Patagonian Batholith whereas they dip to west along its eastern margin. This pattern of foliations and lineations suggests a large-scale transpressional flower-like structure. Kinematic indicators in east-dipping mylonitic zones of the Canal Costa shear zone (see below) document top-to-the-west thrusting of the plutonic complex onto the Traiguén Formation. At the eastern side (Puyuhuapi and Queulat shear zones), kinematic indicators of ductile thrusting and dextral transpressional deformation predominate.

#### **3.4.1 Puyuhuapi quarry shear zone**

This shear zone consists of mingled diorite and granodiorite belonging to a 16.7 Ma unit (Rb-Sr, whole rock; Pankhurst and Hervé, 1994) (Figures 3.3, 3.6). The plutonic rock is heterogeneously deformed across a 50 meter-wide, well-exposed, quarry wall located along the eastern lineament of the LOFZ. Centimeter- to meter-wide high strain zones occurs within the plutonic rocks (Figure 3.3). The mylonites are green-colored and extremely fine-grained, only a few porphyroclasts remain visible with the naked eye. The plutonic rocks show a northeast-trending, steeply-dipping magmatic foliation and down-dip mineral lineation given by euhedral amphibole crystals. The solid-state fabric is subparallel to the magmatic fabric at the outcrop scale. Steeply-plunging stretching

lineations are defined by quartz ribbons and elongate porphyroclast systems. Outcrop-scale kinematic indicators such as S-C fabrics and asymmetric porphyroclasts suggest top-to-the-west dextral-oblique ductile thrusting. Consistent kinematic indicators, such as amphibole fish, were found at the microscopic scale (Figure 3.10a). Diagnostic microstructures such as recrystallized aggregates of quartz and highly strained, fractured plagioclase crystals indicate greenschist facies conditions for the mylonitic deformation. Actinolite occurs around the edges of amphibole porphyroclasts and within the foliated matrix where it coexists with fine-grained biotite. This mineral association is consistent with greenschist facies conditions of metamorphism, as indicated by the microstructure.

Samples for microstructural and thermochronological analyses were taken from the center and edges of the mylonite zones as well as from one km to the east of the shear zone in the same plutonic unit (Figure 3.3, 3.6, Table 3.1).

### **3.4.2 Queulat shear zone**

This shear zone, hundreds of meters wide, is defined by a poorly exposed unit composed of weakly to moderately deformed metasediments and metavolcanics that probably belong to the Traiguén Formation (Bobenrieth et al. 1983) (Figures 3.2, 3.3). The Queulat shear zone roughly coincides with the eastern limit of the Miocene plutonic belt of the Patagonian batholith in the Puyuhuapi transect. Foliations, defined by flattened conglomerate pebbles and layers of mica and chlorite, strike north and dip moderately to steeply to the west. Stretching and mineral lineations show variable pitches but consistently plunge to the southeast (Figure 3.6). Good quality kinematic indicators are scarce but, for the most part, are consistent with northeast contraction.

Shear sense, where observed, is consistently dextral-reverse (top to the northeast) along north-south trending, moderately dipping, ductile shear zones.

### **3.4.3 Canal Jacaf shear zone.**

This deformation zone, several tens of meters wide, juxtaposes the metamorphic basement to the west and the Traiguén Formation to the east (Figure 3.3). The zone is characterized by both a penetrative west-dipping subvertical foliation and poorly defined down-dip lineation. Kinematic indicators at the outcrop-scale suggest top to the east dextral oblique thrusting of the metamorphic basement over the Traiguén Formation (Figure 3.3).

### **3.4.4 Rio Cisnes shear zone**

This shear zone is oriented ~N 60°E and is represented in aerial photographs and satellite images as a ~30 km long lineament following the length of Rio Cisnes (Figures 3.2, 3.3). In the field, the shear zones affect both the 10 Ma Puyuhuapi granite (Rb-Sr, whole rock, Hervé et al. 1993) and metamorphic basement wallrocks of possible Paleozoic age (Figure 3.3). High strain shear zones in the pluton and wallrock are tabular in shape, centimeter to hundreds of meters in width, strike east-northeast and dip moderately to the northwest. The stretching lineation, defined by quartz-ribbons and streaks of muscovite and biotite, plunges shallowly to moderately to the southwest. Mesoscopic-scale kinematic indicators, such as S-C fabrics and asymmetric porphyroclast systems, document dextral-oblique shear with a dip-slip, normal component of motion. Extensional crenulation cleavage, foliation fish, and spectacular mica fish (Figure 3.10b) also indicate dextral shear with a normal, dip-slip component of motion. Recrystallized quartz aggregates, and the development of S-C fabrics suggest

that deformation took place under mid-greenschist facies conditions (e.g. Shimamoto, 1988; Lister and Snoke, 1984).

#### **3.4.5 Islas Cinco Hermanas shear zone**

A high strain shear zone developed from polyphase metamorphic rocks of the metamorphic basement at Islas Cinco Hermanas (Figure 3.7). A north-northeast-striking subvertical foliation is defined by flattened and stretched quartz ribbons and mica foliae. A subhorizontal stretching lineation is very well developed. S-C fabrics, z-shaped folds and sigmoidal porphyroclasts are seen on horizontal surfaces parallel to the lineation and perpendicular to the foliation. Shear sense is consistently dextral (Figure 3.10c). Metamorphic conditions of mylonitization were probably greenschist facies, as documented by very fine-grained aggregates of recrystallized quartz and mica.

Bulk mineral separates of muscovite were dated by the  $^{40}\text{Ar}$ - $^{39}\text{Ar}$  step-heating technique. Total fusion laser dating was performed on schistosity-parallel bands of recrystallized mica (Figures 3.8, 3.9).

#### **3.4.6 Canal Costa shear zone**

This major shear zone follows the north-south trend of the Canal Costa and affects granitic rocks of the Patagonian Batholith and volcanic and sedimentary rocks of the Traiguén Formation (Figures 3.2, 3.7). At a regional scale, the Canal Costa represents a morphologic boundary between the so-called Central Depression to the west and the Main Range to the east, dominated by outcrops of the Traiguén Formation and the Patagonian Batholith, respectively. Moreover, west of the channel, volcanic and sedimentary rocks are almost flat-lying whereas they are highly deformed at the Canal Costa shear zone and do not occur extensively to the east of the channel (Figures 3.2, 3.7)



**Figure 3.10** Photomicrographs of high strain rocks from the Puyuhuapi Quarry shear zone (a); Islas Cinco Hermanas shear zone (b) and Rio Cisnes shear zone (c). Sections cut perpendicular to the foliation and parallel to the stretching lineation. Scale and shear sense are indicated.

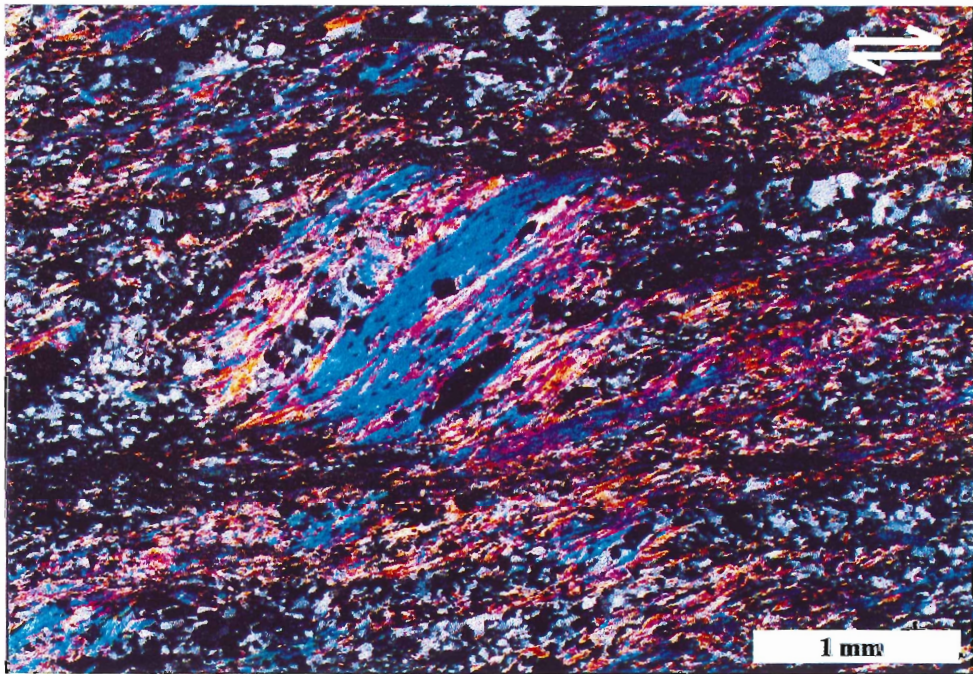
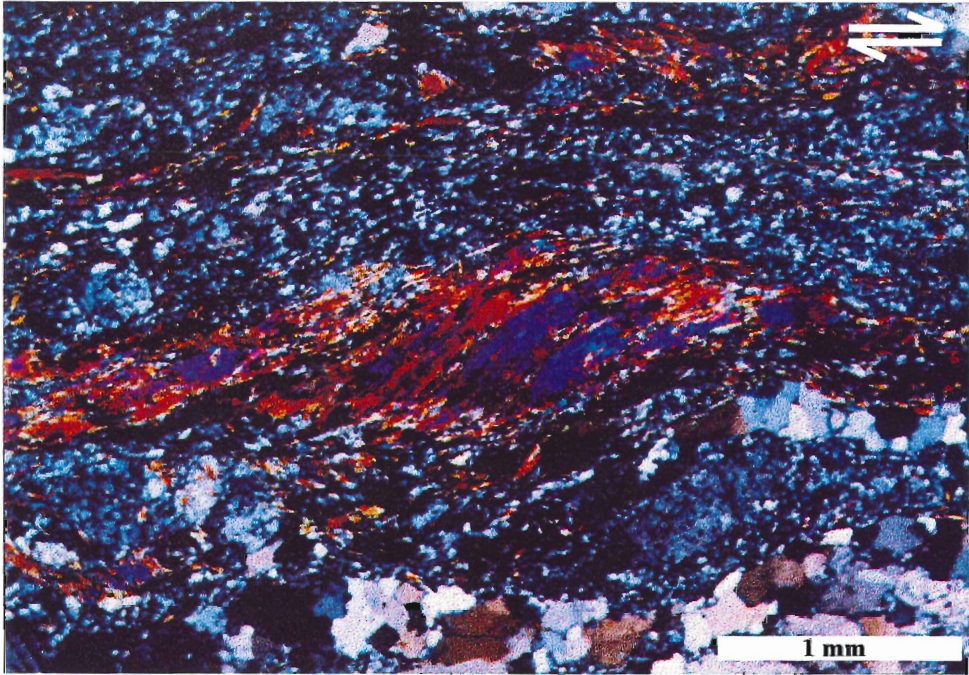


Figure 3.10

**Figure 3.11**  $^{40}\text{Ar}$ - $^{39}\text{Ar}$  apparent age spectra for samples of the shear zones. Puyuhuapi Quarry (a,b,c,d,e); Rio Cisnes (f) and Islas Cinco Hermanas (g, h).

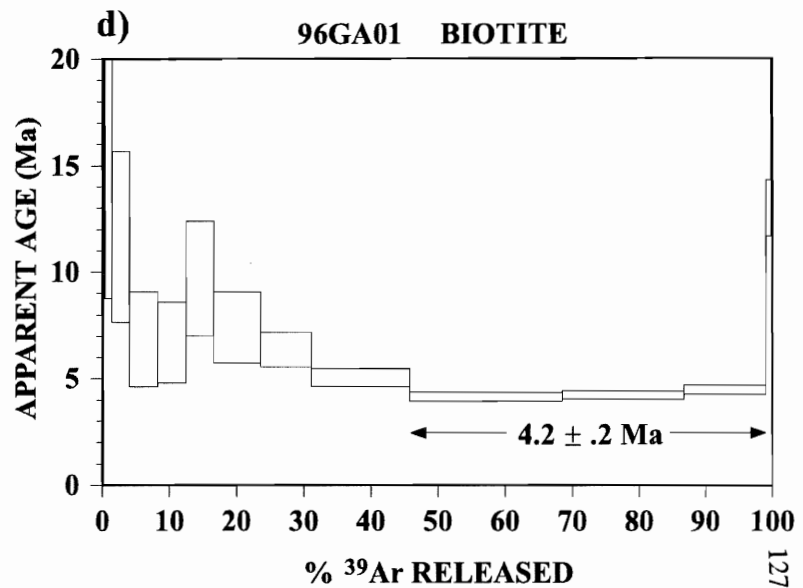
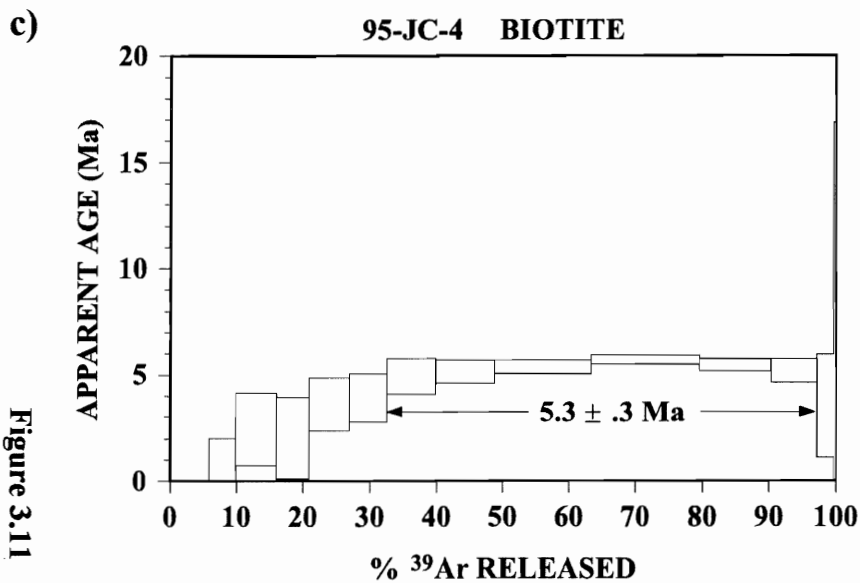
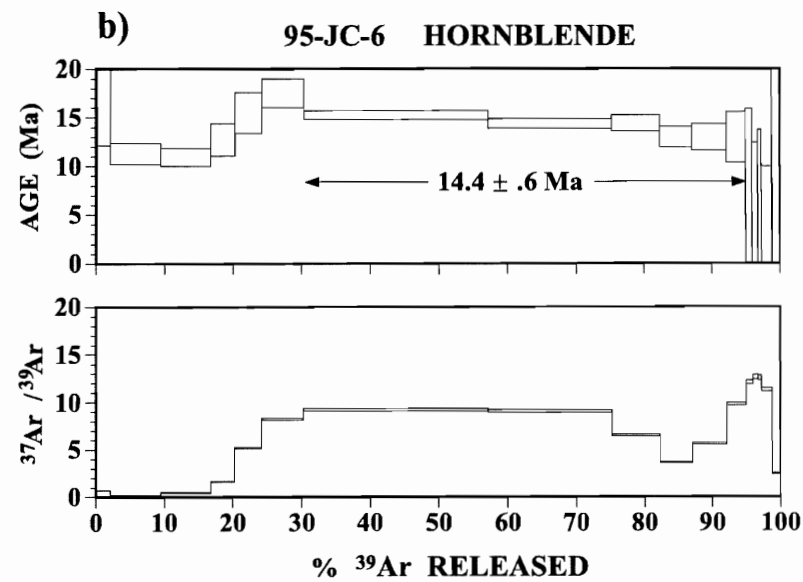
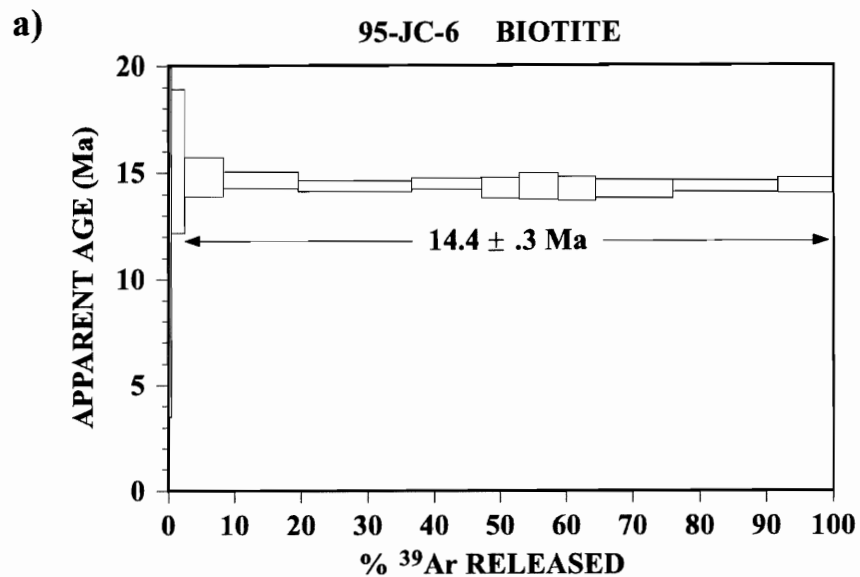


Figure 3.11

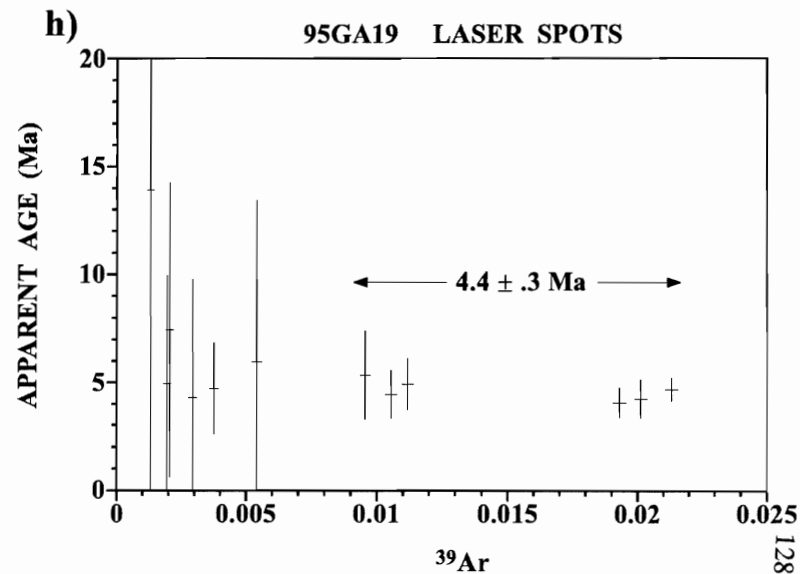
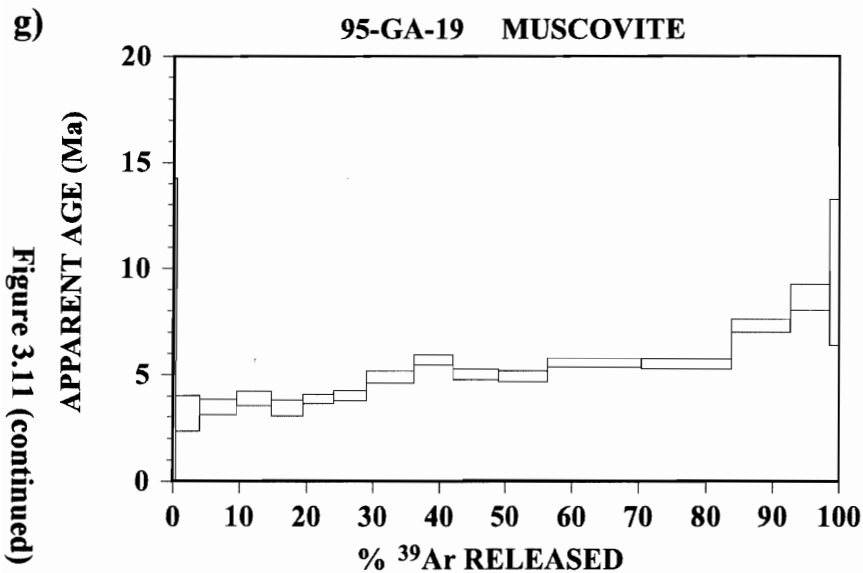
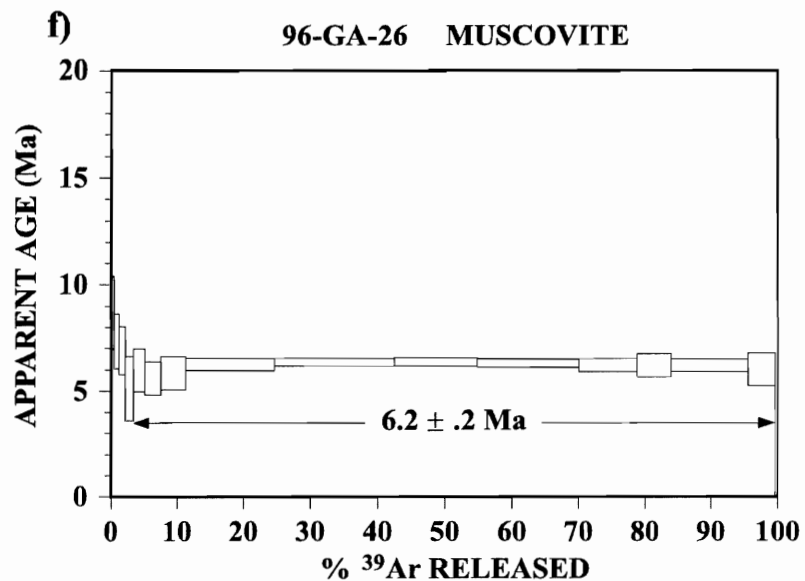
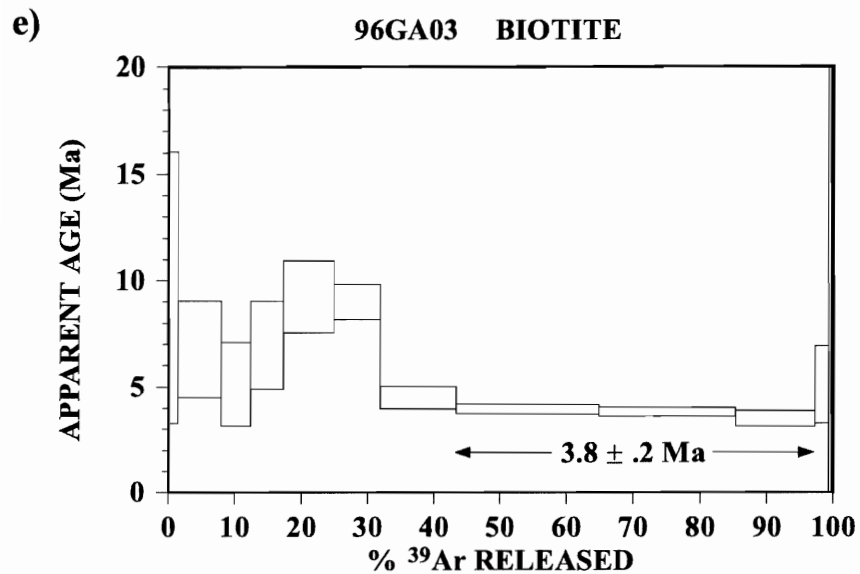


Figure 3.11 (continued)

High strain cataclastic and mylonitic rocks occur as a discontinuous strip along the eastern side of the channel. Most of them show north-south-trending foliations dipping steeply to the east. Stretching lineations in the mylonites plunge moderately to the north, although other directions of plunge are observed (Figure 3.6). Kinematic indicators document top to the southwest dextral-reverse ductile shearing; a few kinematic indicators showing dip-slip normal motions are locally found.

### **3.5 Age of deformation**

The  $^{40}\text{Ar}$ - $^{39}\text{Ar}$  radiometric dating technique is one of the most widely used methods to constrain the thermal history of crustal rocks. The method is based on the radioactive decay of  $^{40}\text{K}$  to  $^{40}\text{Ar}$  and is useful for dating K-bearing minerals with sufficient potassium content to yield measurable amounts of daughter Ar (e.g. micas, K-feldspar, hornblende). The  $^{40}\text{Ar}$ - $^{39}\text{Ar}$  method provides information on the time at which a particular mineral passes through its closure temperature during cooling. Ranges of closure temperatures for different minerals have been estimated from both experimental and empirical means (e.g. Mc Dougall and Harrison, 1988). Estimated closure temperatures for hornblende are in the range of 450-500°C, depending upon chemical composition. Biotite and muscovite show closure temperatures in the range of 300-350°C, whereas K-feldspar shows closure temperatures between 250-300°C. Therefore,  $^{40}\text{Ar}$ - $^{39}\text{Ar}$  dating of muscovite and biotite may provide important information on the age at which greenschist facies deformation takes place. However, true closure temperatures may vary dramatically for the same mineral in rocks that have undergone different metamorphic histories.

Constraining the absolute age of deformational events has been a major problem for structural geologists for decades (e.g. Kligfield et al. 1986; Dunlap et al. 1991; Reddy et al. 1996). Commonly used minerals to date deformation are muscovite and biotite, mainly because of their ubiquity in crustal rocks. However, the consequences of high strain solid-state deformation on Ar transport within the crystal lattice of silicates remain poorly understood. Ar loss during deformation occurs not only by volume diffusion, as commonly assumed for static cooling, but also through a series of other crystal-plastic processes. Dislocation motion through the crystal lattice, even at temperatures below the closure temperature of a specific mineral, can transport Ar away from the lattice (e.g. Scheuber et al. 1994; Lee 1995; Reddy et al. 1996).

High strain rocks commonly contain a complex mix of relic grains (porphyroclasts) in a matrix of dynamically recrystallized minerals. Moreover, the relic grains are usually partly recrystallized around their margins (core and mantle structure) whereas the so-called "recrystallized grains" often contain domains in which dynamic recrystallization has not been fully accomplished as revealed by detailed SEM studies (e.g. Trimby et al. 1998). Therefore, even in those cases in which relic or recrystallized minerals can be physically separated from the rock, neither the relic grains nor the "recrystallized" ones may fully represent the deformational event. In the general case, this means that bulk separates of a specific mineral species will almost certainly contain a mix of relic and new grains. Therefore, the isotopic signature will very likely be a geologically meaningless average of the two, unless a methodology is developed to recognize the presence of two different generations of the same mineral species with distinctive Ar retention properties in the same bulk sample (e.g. West and Lux, 1993).

Another way to date deformation by  $^{40}\text{Ar}$ - $^{39}\text{Ar}$  step heating of bulk mineral separates was proposed by Scheuber et al. (1995). The authors dated a continuous series of rocks from the undeformed protholith to a high strain mylonite in the middle of a kilometer-wide ductile shear zone in northern Chile. They found that  $^{40}\text{Ar}$ - $^{39}\text{Ar}$  ages are fully reset by deformation-induced recrystallization in the high strain mylonites while mixed ages in the form of staircase patterns were obtained in the low strain varieties in which both relic and recrystallized minerals coexist. This last approach was used here for the high-strain rocks that appear to be fully recrystallized during mylonitic deformation.

For those samples in which both pre- and synkinematic grains of the same mineral species coexist at the sample scale, the  $^{40}\text{Ar}$ - $^{39}\text{Ar}$ -laser technique is one way to solve the problem of selecting a meaningful target to date deformation. It is possible to do so by choosing those minerals (or parts thereof) which are interpreted as dynamically recrystallized at or below the closure temperature of the mineral. Thus, proper identification of individual mineral species to be dated is critical, particularly in those cases in which a low-K bearing mineral is contaminated by a high-K bearing mineral. In fact, Wartho (1995) has demonstrated that very small amounts of biotite within hornblende crystals can significantly affect the isotopic signature of the sample. The problem of identifying a contaminating phase can be partially solved with the aid of the  $^{37}\text{Ar}$ - $^{39}\text{Ar}$  ratio, which is available for the  $^{40}\text{Ar}$ - $^{39}\text{Ar}$  dating technique.

Besides spatial resolution, another advantage of using the laser probe on specific targets instead of traditional furnace heating of bulk mineral separates is avoiding homogenization of argon isotopic variations within grains due to structural breakdown and chemical reaction of hydrous phases such as hornblende, biotite and muscovite. In



fact, homogenization of natural argon isotopes within step-heated grains may yield misleadingly flat plateau spectra which are geologically meaningless (e.g. Lee et al. 1991; Wartho, 1995). Correlation diagrams are needed to assess the excess argon component and then isolate meaningful ages (e.g. Reddy et al. 1997).

With the above criteria in mind, a total of twelve representative samples with good structural and kinematic control were selected for  $^{40}\text{Ar}$ - $^{39}\text{Ar}$  dating by furnace step-heating and/or by total fusion using an infrared laser. Sample lithology, location, material dated, and intensity of sample deformation are all listed in Table 3.1. Stepwise  $^{40}\text{Ar}$ - $^{39}\text{Ar}$  furnace heating was performed on bulk mineral separates of hornblende and biotite from undeformed and high strain varieties of the plutonic rocks, in an attempt to obtain and compare apparent ages of undeformed and dynamically recrystallized mineral species. Because mylonitic deformation was shown to have taken place at low to medium greenschist facies conditions, apparent ages from biotite and/or muscovite are likely to represent the age of deformation as the closure temperatures for micas are in the range of 300-350°C. Bulk mineral separates of synkinematic biotite and muscovite were obtained from high strain pelitic schist (wallrock) deformed under greenschist facies conditions. Two samples (samples GA 17 and GA19) were dated by total fusion using the high-resolution infrared laser on selected microstructural targets, which were previously selected as representing recrystallized single minerals or mineral aggregates.

Table 3.1. Summary of new  $^{40}\text{Ar}$ - $^{39}\text{Ar}$  age data for the Puyuhuapi and Aysen transects.

Sample	Location	Transect	Rock type	Strain	Material	Age (Ma) $\pm 1\sigma$
95JC1	puyuhuapi	puyuhuapi	mingled gd-diorite	low	bt	3.5 $\pm$ 0.2
95JC1	puyuhuapi	puyuhuapi	mingled gd-diorite	low	amp	20.2 $\pm$ 0.2
95JC2	puyuhuapi	puyuhuapi	mingled gd-diorite	low	bt	1.6 $\pm$ 0.2
95JC4	quarry	puyuhuapi	mingled gd-diorite	low	amp	37.4 $\pm$ 3
95JC4	quarry	puyuhuapi	mingled gd-diorite	low	bt	5.3 $\pm$ 0.3
95JC6	seno queulat	puyuhuapi	granodiorite	no	amp	14.4 $\pm$ 0.6
95JC6	seno queulat	puyuhuapi	granodiorite	no	bt	14.4 $\pm$ 0.3
95JC12	seno queulat	puyuhuapi	granodiorite	no	amp	discordant
95JC12	seno queulat	puyuhuapi	granodiorite	no	bt	13.3 $\pm$ 0.2
96GA01	quarry	puyuhuapi	mylonite	high	bt (bulk)	4.2 $\pm$ 0.2
96GA03	quarry	puyuhuapi	mylonite	high	bt (bulk)	3.8 $\pm$ 0.2
95GA04	quarry	puyuhuapi	mingled gd-diorite	low	bt (bulk)	4.2 $\pm$ 0.1
96GA26	pto cisnes	puyuhuapi	bt-ms schist	high	ms	6.2 $\pm$ 0.2
95JC14	isla 5 hermanas	aysen	bt granite	no	bt	5.7 $\pm$ 0.2
95GA17	fiordo aysen	aysen	schist	very high	ms (bulk)	no result
95GA17	fiordo aysen	aysen	schist	very high	ms+bt bands (laser spots)	4.6-9.4Ma
95GA19	fiordo aysen	aysen	schist	very high	ms (bulk)	4-10Ma, 5.1 $\pm$ 0.2(tga)
95GA19	fiordo aysen	aysen	schist	very high	ms+bt bands (laser spots)	4.4 $\pm$ 0.3

### 3.5.1 $^{40}\text{Ar}$ - $^{39}\text{Ar}$ thermochronological data

$^{40}\text{Ar}$ - $^{39}\text{Ar}$  apparent age spectra for samples of undeformed and high strain rocks are shown in figures 3.11, 3.12b and 3.13b. Mean ages are displayed on corresponding geologic maps of transects (Figures 3.5, 3.8).

Samples 95JC6, 95JC4, 96GA01 and 96GA03 (Table 3.1, Figure 3.4) represent undeformed and several varieties of low to high strain mylonites from the Queulat plutonic unit at the Puyuhuapi Quarry (Figures 3.3, 3.4, 3.5). Sample 95JC6 (undeformed diorite) yielded well-defined plateau ages of  $14.5\pm 0.6$  and  $14.3\pm 0.3$  in hornblende and biotite, respectively (Figures 3.9a, b). These ages are interpreted as cooling ages of the pluton immediately following emplacement at about 16.3 Ma (Rb-Sr whole rock age, Pankhurst and Hervé, 1994). Sample 95JC4, a low strain variety of the mylonitic granodiorite-diorite, yielded a mean age of  $5.3\pm 0.3$ , which we interpret as partial resetting during solid-state deformation (Figure 3.11c). Samples GA-01 and GA-03, corresponding to high strain mylonites, gave mean ages of  $4.2\pm 0.2$  and  $3.8\pm 0.2$ , respectively, after removal of a low-temperature, disturbed  $^{39}\text{Ar}$  component (Figure 3.11 d,e). These ages are interpreted as ages of high strain solid-state contractional ductile deformation that affected the Queulat plutonic unit during Pliocene times.

Sample 96GA26 corresponds to a high strain pelitic schist taken from the Rio Cisnes shear zone (Table 3.1, Figures 3.3, 3.9f). A bulk mineral separate of muscovite gave a plateau age of  $6.3\pm 0.2$  Ma. This age may have two different meanings: (1) static cooling of wallrock along with the intruding Puerto Cisnes pluton from 10 Ma to 6 Ma during exhumation, (2) solid-state deformation and recrystallization of muscovite during

a dextral transtensional event at around 6 Ma. Supporting the latter hypothesis is the fact that the rock was deformed under greenschist facies conditions, and that muscovite grains define the extensional crenulation cleavage indicating dextral transtensional deformation.

Samples 95GA17 and 95GA19 correspond to high strain quartz-mica schists collected from Islas Cinco Hermanas in the Aysén fjord (Figure 3.4). Fine-grained bulk mineral separates of muscovite from sample 95GA19 yielded a staircase  $^{39}\text{Ar}$  release pattern (Figure 3.11g). This spectrum may indicate: (1) discrete events of Ar loss produced by two distinctive thermal events at 10 Ma and ~4 Ma; (2) partial resetting of “old” muscovite grains by high strain deformation at around 5 to 6 Ma; or (3) a mix of two families of grains, a relic fraction represented by the higher ages and a recrystallized fraction represented by the younger ages. High-resolution laser dating of muscovite-biotite fine-grain aggregates in sigmoidal lenses parallel to the foliation in sample 95GA19, gave total fusion ages in the range of 4 to 5 Ma (Figures 3.12a,b). These ages are here interpreted as the timing of recrystallization of mica to a finer grained aggregate during high strain deformation. High-resolution laser spot dating performed on similar fine-grained mica layers from sample 95GA17 yielded total fusion apparent ages in the range of 4.6 to 9.2 Ma. Figure 3.13b shows the apparent age data of twelve laser spots plotted against  $\text{Ar}^{39}$ . The laser spots are labeled on the analyzed rock slab (Figure 3.13a). Although ages range from 4.6 to 9.2 Ma, the better constrained data indicate ages between 4.6 and 5.9 Ma. I interpret the older ages as dominated by the isotopic signature of relic muscovite-biotite grains, whereas the younger ages would be dominated by newly crystallized mica grains. This hypothesis is supported by the staircase Ar release spectra from companion sample 95GA19, which starts at ca. 4 Ma for low temperature releases

**Figure 3.12 (a)** Polished rock slab of sample 95GA19 showing numbered targets selected for laser spot analysis. **(b)** Plot of apparent  $^{40}\text{Ar}$ - $^{39}\text{Ar}$  age data for the selected targets. Field of view is 40 by 20 millimeters.



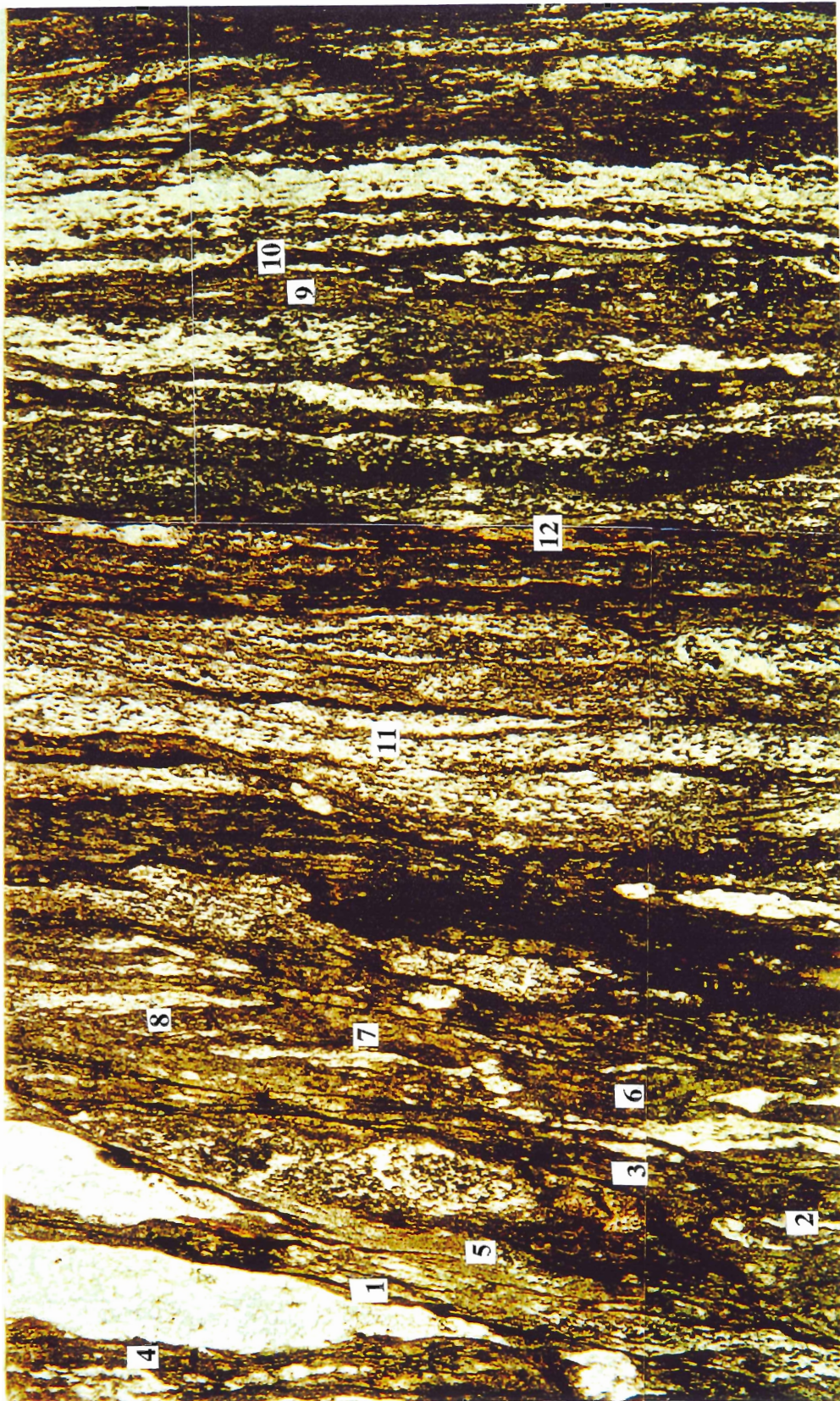


Figure 3.12a

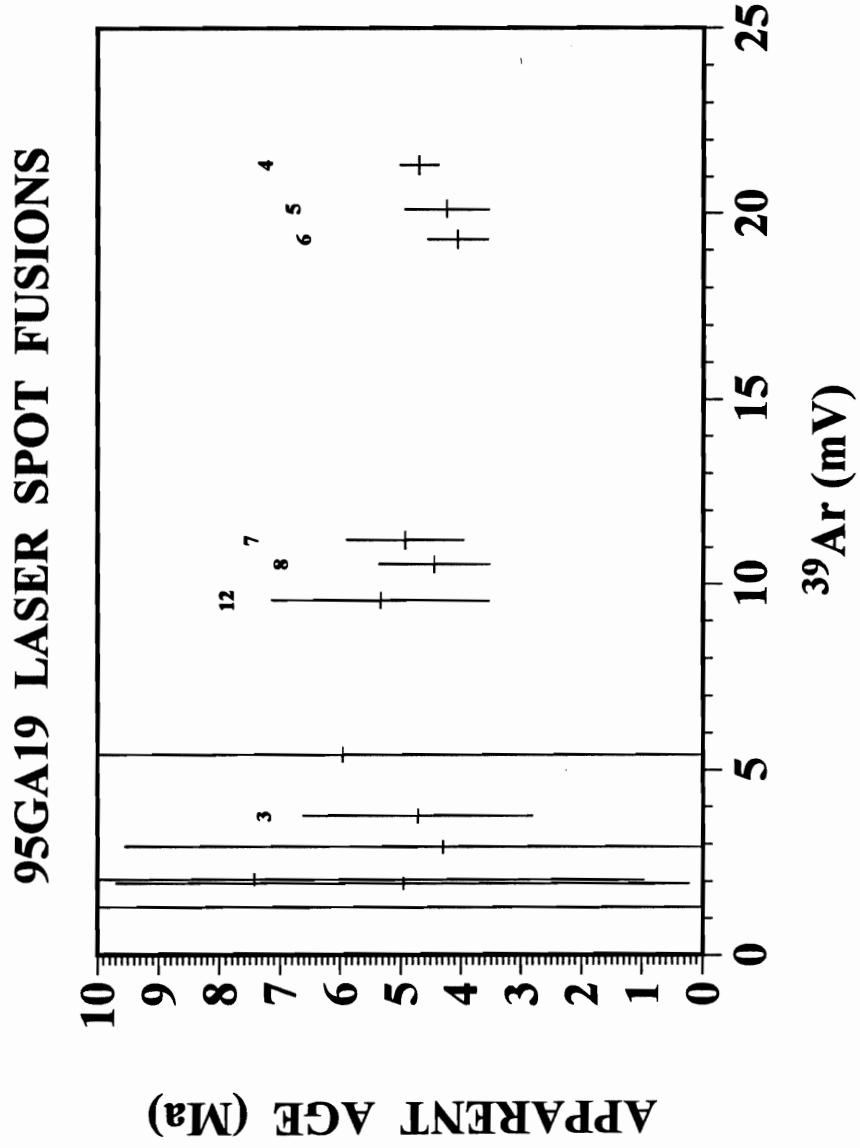


Figure 3.12b



**Figure 3.13 (a)** Polished rock slab of sample 95GA17 showing numbered targets selected for laser spot analysis. **(b)** Plot of apparent  $^{40}\text{Ar}$ - $^{39}\text{Ar}$  age data for the selected targets. Field of view is 40 by 20 millimeters.

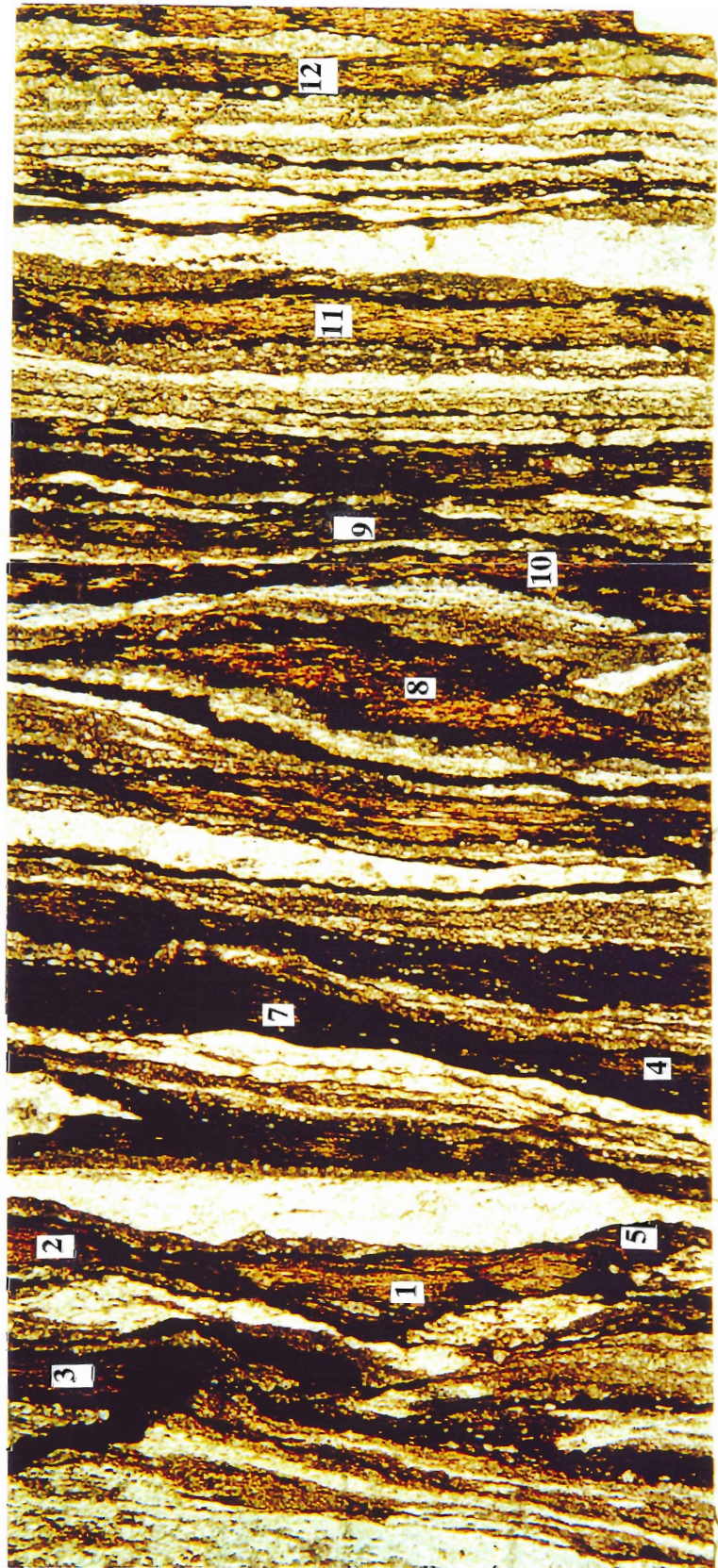


Figure 3.13a

### 95GA17 LASER SPOT FUSIONS

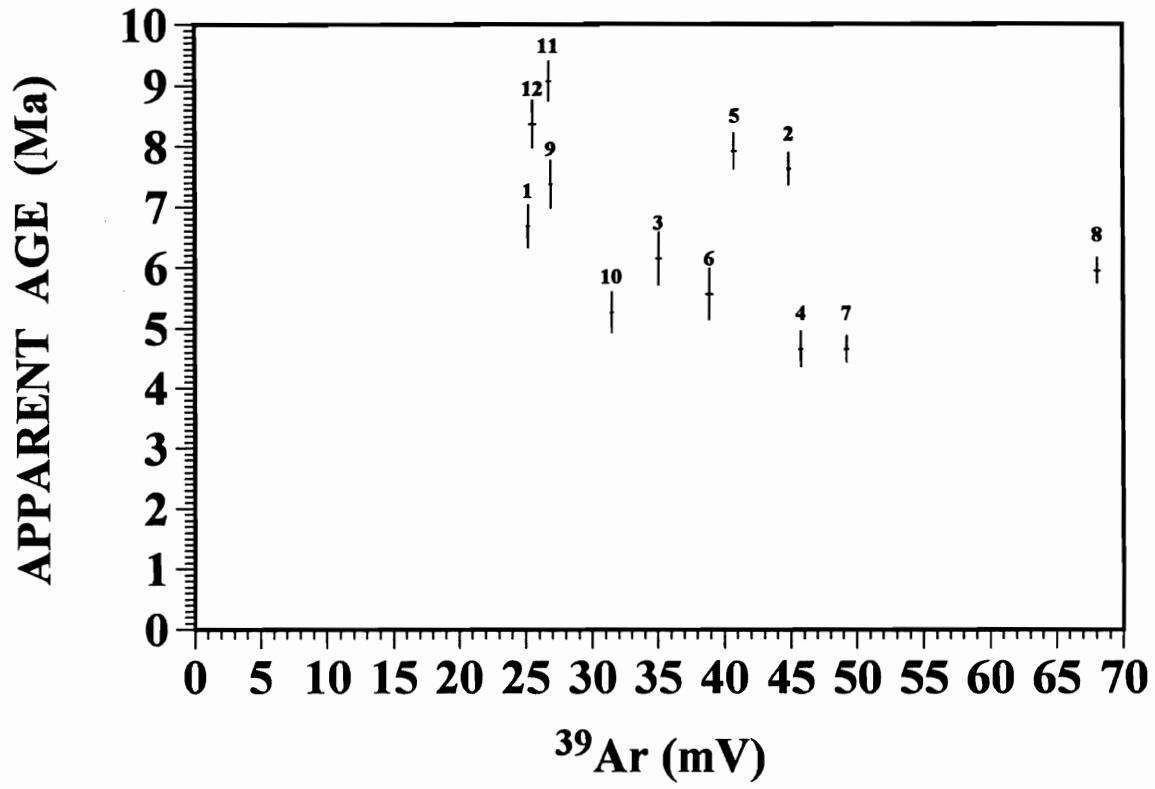


Figure 3.13b

and ends at ca. 10 Ma at the high temperature part of the spectra. As it was indicated above, this staircase spectra suggests a mixed yield from old relic mica grains and recrystallized new mica grains by a high strain deformation event at around 4.6 Ma..

### **3.6 Discussion**

I undertook a geometric, kinematic and thermochronological study on selected ductile shear zones in the Patagonian Batholith and deformed wallrocks. These shear zones are located along major north- and northeast-trending lineaments of the Liquiñe-Ofqui fault zone and represent well the different styles and nature of deformation along and across the southern Andes between 44 and 46°S. Although much more work needs to be done to better constrain the nature and timing of deformational events, this first effort has provided the first general kinematic framework for the region of the southern Andes immediately north of the Nazca-South America-Antarctica triple junction.


Geometric and kinematic data presented here document the existence of dextral strike-slip and contractional to oblique-slip ductile deformation zones in the magmatic arc of the Southern Andes. The bulk of the transpressional deformation took place at around 4 Ma as documented by  $^{40}\text{Ar}$ - $^{39}\text{Ar}$  dating on recrystallized biotite and muscovite from several greenschist facies shear zones of contractional oblique-slip and strike-slip kinematics within plutonic and metamorphic wallrocks. A slightly older dextral transtensional event may have taken place in the region at about 6 Ma.

Ridge collision and oblique subduction have been proposed as alternative driving mechanisms of transpressional deformation at the leading edge of the South American plate. Collision of successive segments of the Chile Ridge took place between 6 and

3Ma, close to the present position of the triple junction (Figure 3.1, 3.14). Dextral right-oblique subduction, in turn, has prevailed during most of the Cenozoic (Figure 3.1). Theoretically, ridge subduction favors margin-orthogonal contraction close to the indenter and oblique-slip to strike-slip deformation a few hundred kilometers away from it (Tapponier and Molnar, 1976; Nelson et al. 1994) (Figure 3.15a). On the other hand, oblique subduction is thought to produce overall transpressional deformation along ancient and present-day plate boundaries (e.g. Jarrard, 1986; Beck, 1991; McCaffrey, 1992; Teyssier et al. 1995), (Figure 3.15b).

I envisage oblique subduction as the long-term driving mechanism of dextral transpression in the southern Andes. From previous studies, we know that dextral transtension occurred locally along the magmatic arc during early Tertiary times when subduction was highly dextral-oblique and intraplate basin formation may have occurred in a “leaky transform environment” (e.g. Hervé et al. 1995). The basin was later inverted in Miocene-Pliocene (?) times when less oblique convergence took place. Less oblique convergence could have led to contraction and overthrusting of the Patagonian Batholith over the basinal deposits.

During the Pliocene, subduction of the Chile Ridge must have played a more significant role in the tectonics of the southern Andes than previously recognized. The series of ridge segments that have collided with the continent at about the same latitude from 6 Ma have probably enhanced the contractional component of dextral-oblique transpressional deformation, close to the indenter. Dextral-strike slip deformation found a few hundred kilometers to the north at 42°S (Cembrano et al. 1996) and dextral



**Figure 3.14** Migration of the Chile Ridge and fracture zones with respect to the plate boundary during the last 6 Ma (Bourgeois et al. 1996). Several north-northwest-trending short segments of the ridge were consecutively subducted from around 6 Ma to present-day close to the Taitao Peninsula.

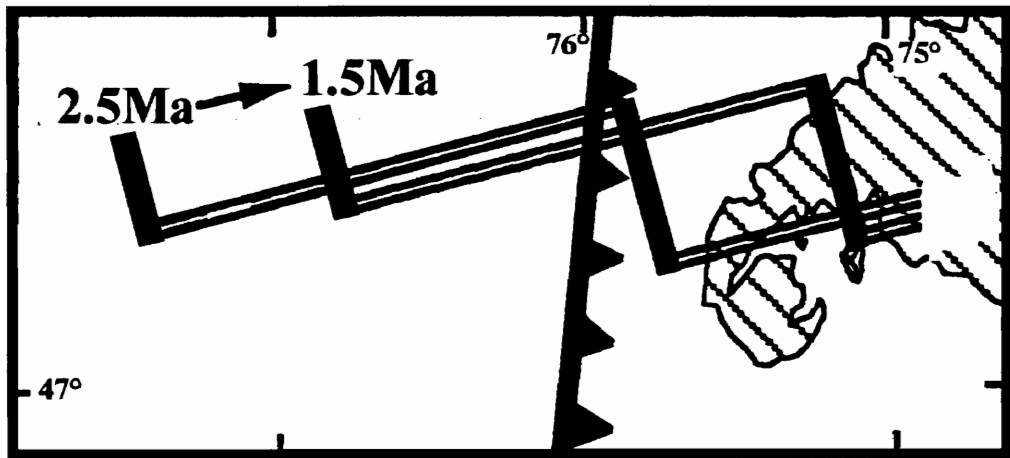
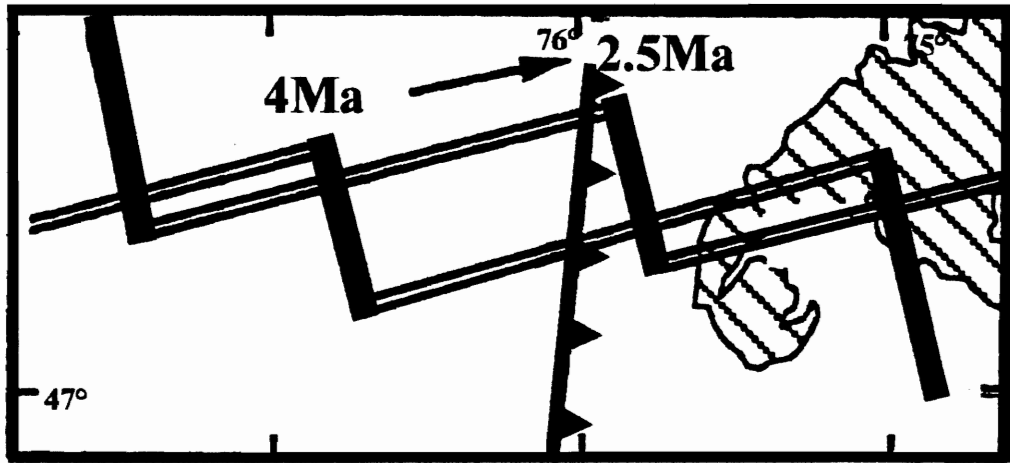
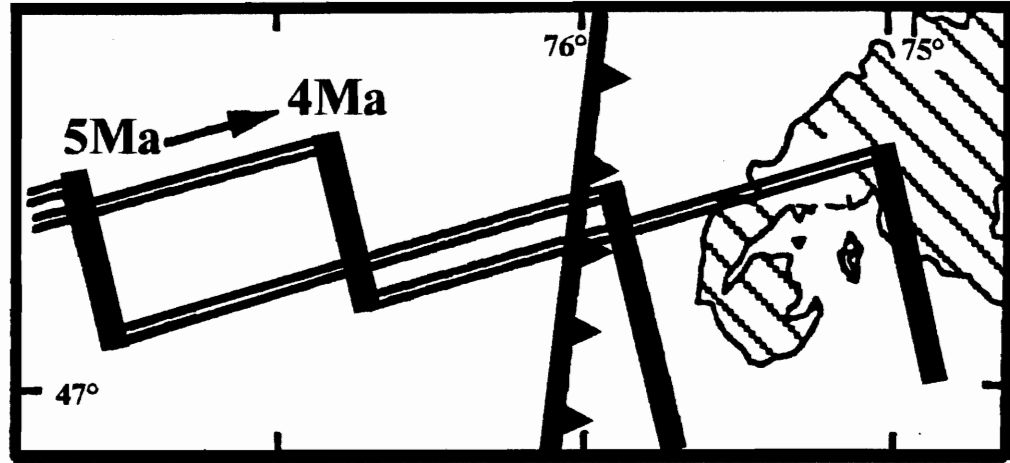
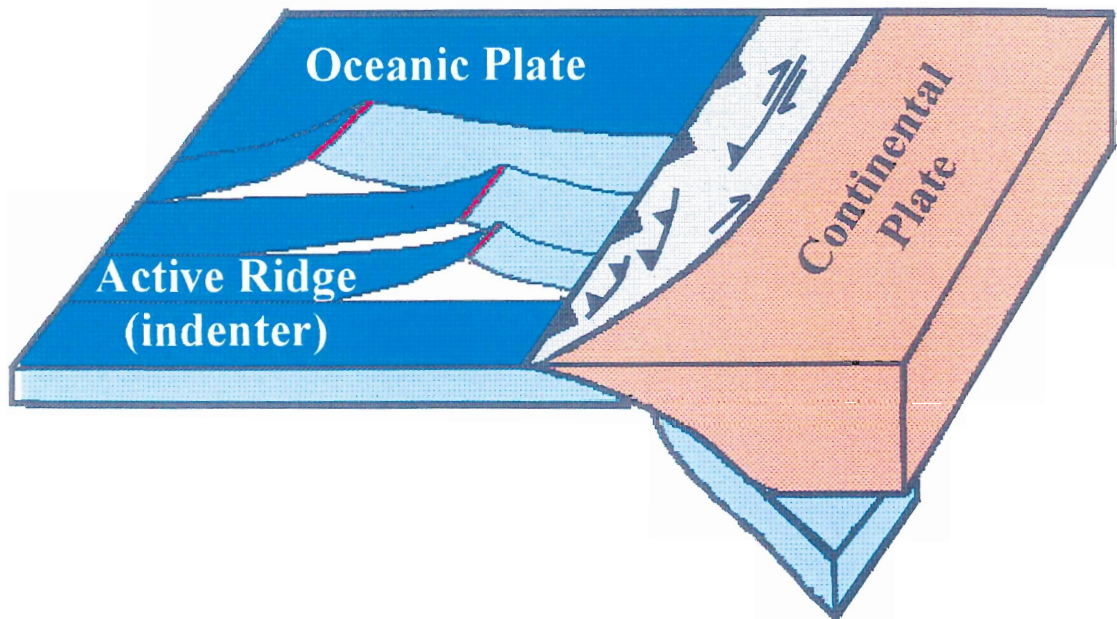


Figure 3.14

**Figure 3.15** Models for the tectonic consequences of ridge collision (a), and oblique subduction(b), in the tectonics of plate boundaries. (Tapponier and Molnar, 1976; Nelson and Arit, 1994; Beck, 1991).



a)



b)

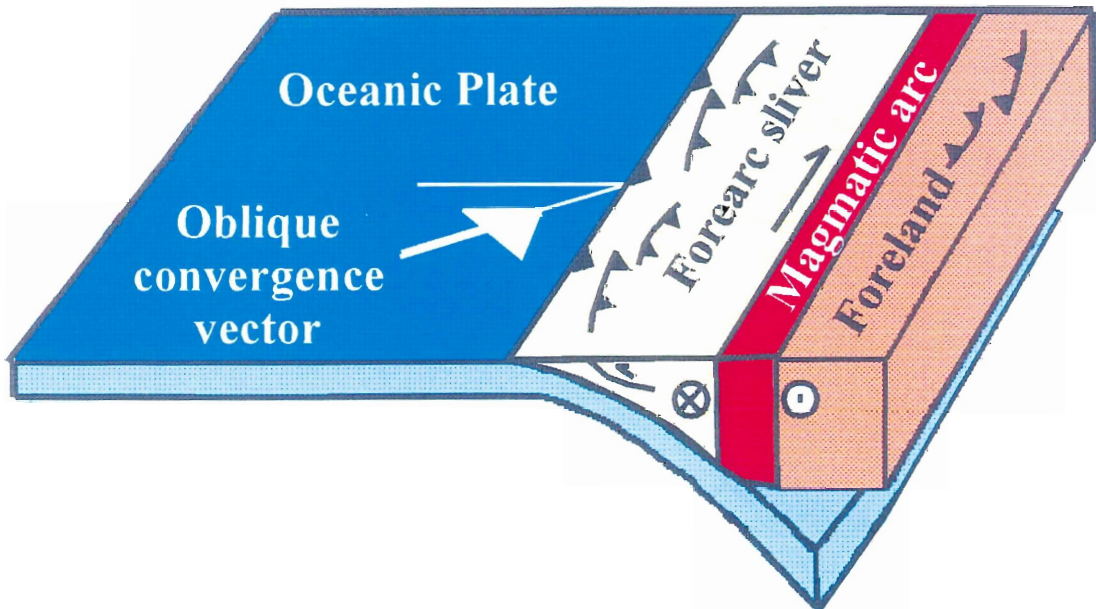


Figure 3.15

transensional deformation recorded at 6 Ma along east-northeast-trending shear zones at 44°S, are kinematically compatible with bulk dextral transpressional deformation induced by the indenter effect of the Chile Ridge. Furthermore, coeval oblique-reverse slip and strike-slip ductile deformation zones of similar orientation between 42 and 47°S, suggest that overall dextral transpression at the Nazca-South America plate boundary zone has been accommodated heterogeneously into zones of contraction-dominated and strike-slip dominated kinematics within the magmatic arc. In contrast, the forearc and foreland regions have remained nearly undeformed (Figure 3.16).

Concomitant contraction and strike-slip ductile deformation has been documented for ancient orogens such as the Sierra Nevada and the Archean provinces of Canada (e.g. Tikoff and San Blaquadt, 1997; Hudleston et al. 1988). Some authors emphasize that transpression is accomplished by concomitant vertical stretching and lateral shear in the same volume of rock (e.g. Tikoff and Greene, 1997). Others, instead, suggest that transpressional orogens record a more complex history in which there is a gradual change in time and space from pure contractional to strike-slip kinematics (Tobisch et al. 1995).

The southern Andes could well be a Late Cenozoic analog for ancient transpressional orogens, although structural levels may be deeper, as in most Archean examples. Further regional geologic mapping in southern Chile along with detailed U-Pb and Ar-Ar dating will allow better understanding of transpressional deformation at obliquely convergent plate boundaries and its interaction with other processes such as ridge subduction.

**Figure 3.16** Cartoon of the Nazca-South America plate boundary zone showing how overall heterogeneous transpressional deformation arising from oblique convergence and ridge subduction has been accommodated during the last 6 Ma. Discrete zones of dextral-reverse shear, dextral strike-slip and margin-orthogonal contraction are found along and across the plate boundary, concentrated in the magmatic arc. The component of plate-boundary contraction is enhanced close to the Chile Ridge collision zone. Dextral strike-slip deformation is favored as the distance from the collision zone increases to the north.

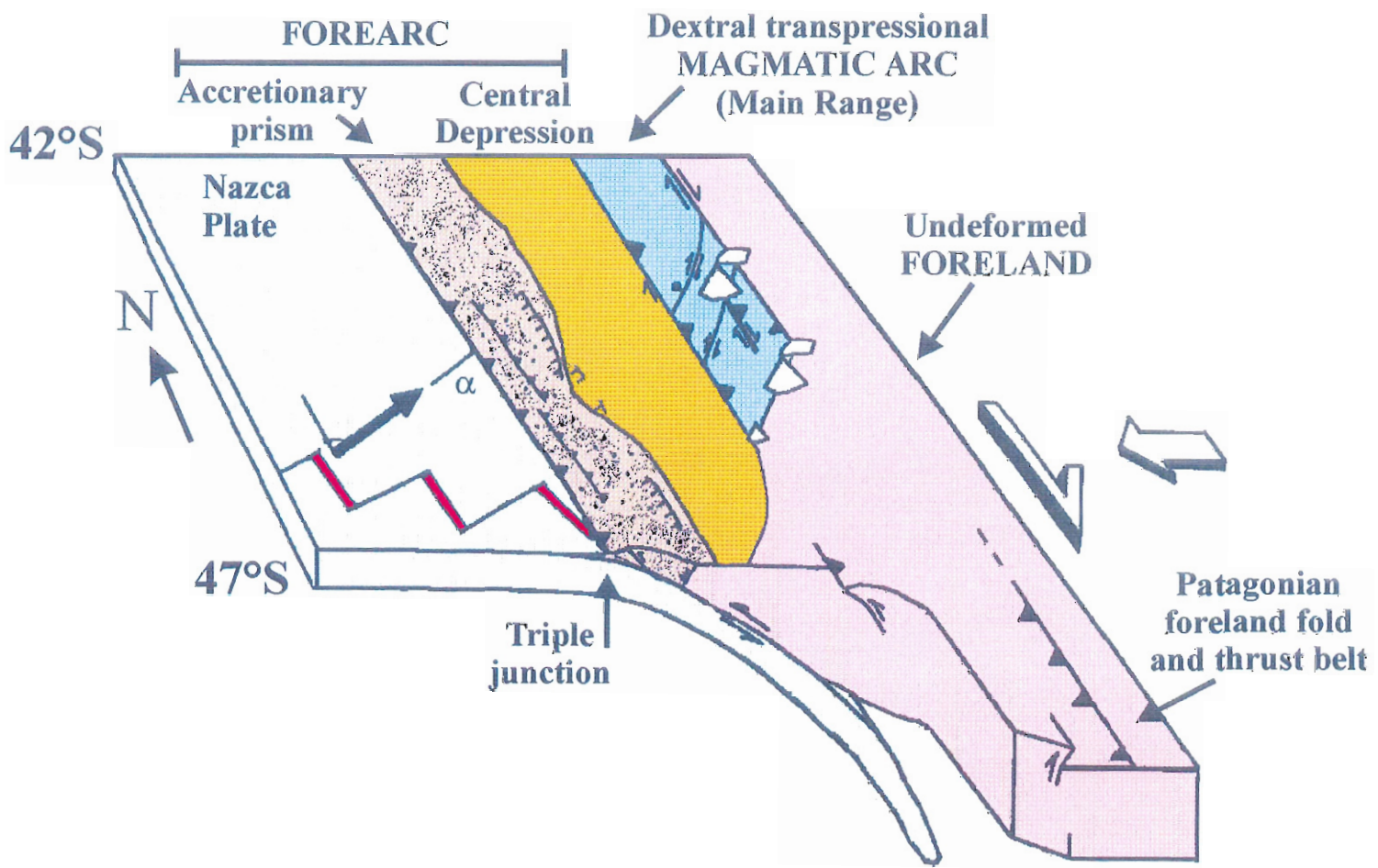


Figure 3.15

# **Chapter 4. Dating deformation on heterogeneously deformed plutonic rocks: an example from ductile shear zones of the Patagonian Batholith**

## **4.1 Introduction**

The  $^{40}\text{Ar}$ - $^{39}\text{Ar}$  radiometric dating technique is one of the most widely used methods to constrain the thermal history of crustal rocks. The method is based on the radioactive decay of  $^{40}\text{K}$  to  $^{40}\text{Ar}$  and is useful for dating K-bearing minerals with sufficient potassium content to yield measurable amounts of daughter Ar (e.g. micas, K-feldspar, hornblende).

The  $^{40}\text{Ar}$ - $^{39}\text{Ar}$  method provides information on the time at which a particular mineral passes through its closure temperature during cooling. Ranges of closure temperatures for different minerals have been estimated from both experimental and empirical means (e.g. Mc Dougall and Harrison, 1988). Estimated closure temperatures for hornblende are in the range of 450-500°C, depending upon chemical composition. Biotite and muscovite show closure temperatures in the range of 300-350°C, whereas K-feldspar shows closure temperatures between 250-300°C. Therefore,  $^{40}\text{Ar}$ - $^{39}\text{Ar}$  dating of muscovite and biotite may provide important information on the age at which greenschist facies deformation takes place. Closure temperatures, however, are strongly dependent on the prevailing intragranular and intergranular mechanisms of Ar diffusion. Traditional analysis of  $^{40}\text{Ar}$ - $^{39}\text{Ar}$  data assumes that Ar transport in the crystal lattice occurs mainly by volume diffusion (e.g. McDougall and Harrison, 1988). However, recent studies (e.g.

Lee, 1995; Reddy et al, 1997) show that other transport mechanisms may play a critical role in Ar diffusion through crystals. In particular, Lee (1995) emphasizes the importance of crystal defects such as dislocations and microfractures in providing efficient pathways for Ar transport in and out of the crystal lattice. Large atoms, such as naturally produced radiogenic  $^{40}\text{Ar}$ , will tend to migrate toward lower-energy sites of the crystal lattice such as dislocations within grains and/or to grain boundaries. As a result, effective closure temperatures of minerals can be much lower than those predicted assuming only a volume diffusion mechanism. This is particularly important for deformed minerals that usually develop a high-density network of internal dislocations and microfractures in response to the applied high strain conditions.

Constraining the absolute age of deformational events has been a major problem for structural geologists during decades (e.g. Kligfield et al. 1986; Dunlap et al. 1991; Reddy et al. 1996). Commonly used minerals to date deformation are muscovite and biotite mainly because of their ubiquity in crustal rocks. However, as stated before, Ar loss during deformation occurs not only by volume diffusion, as commonly assumed for the static cooling model, but also through a series of other processes. Dislocation motion through the crystal lattice is one of such processes, and can transport Ar out of the crystal lattice even at temperatures below the closure temperature of a specific mineral (e.g. Scheuber et al. 1995, Lee 1995; Reddy et al. 1996).

High strain rocks commonly contain a complex mix of relic grains (porphyroclasts) and a matrix of dynamically recrystallized minerals. Moreover, the relic grains are usually partly recrystallized around their margins (core and mantle structure) whereas the so-called "recrystallized grains" often contain domains in which dynamic

recrystallization has not been fully accomplished as revealed by detailed SEM studies (e.g. Trimby et al. 1998). Therefore, even in those cases in which relic or recrystallized minerals can be physically separated from the rock, neither the relic grains nor the "recrystallized" ones fully represent the deformational event. In the simplest case, this means that bulk separates of a specific mineral species will almost certainly contain a mix of relic and new grains. Therefore, the isotopic signature will very likely be geologically meaningless average of the two, unless a methodology is developed to recognize the presence of two different generations of the same mineral species with distinctive Ar retentive properties in the same bulk sample (e.g. West and Lux, 1993). Another way to date deformation by  $^{40}\text{Ar}$ - $^{39}\text{Ar}$  step heating of bulk mineral separates was proposed by Scheuber et al. (1995). The authors dated a continuous series of rocks from the undeformed protholith to a high strain mylonite in the middle of a kilometer-wide ductile shear zone in northern Chile. They found that  $^{40}\text{Ar}$ - $^{39}\text{Ar}$  ages are fully reset by deformation-induced recrystallization in the high strain mylonites while mixed ages in the form of staircase patterns were obtained in the low strain varieties in which both relic and recrystallized minerals coexist.

The  $^{40}\text{Ar}$ - $^{39}\text{Ar}$ -laser technique is one way to solve the problem of selecting a meaningful target by choosing those minerals (or parts thereof) which are interpreted as dynamically recrystallized at or below the closure temperature of the mineral. Thus, proper identification of individual mineral species to be dated is critical, particularly in those cases in which a low-K bearing mineral is contaminated by a high-K bearing mineral. In fact, Wartho (1995) have demonstrated that very small amounts of biotite within hornblende crystals can significantly affect the isotopic signature of the sample.

The problem of identifying a contaminating facies can be partially solved with the aid of the  $^{37}\text{Ar}$ - $^{39}\text{Ar}$  ratio, which is available for the  $^{40}\text{Ar}$ - $^{39}\text{Ar}$  dating technique.

Besides spatial resolution, another advantage of using the laser probe on specific targets instead of traditional furnace heating of bulk mineral separates is avoiding homogenization of argon isotopic variations within grains due to structural breakdown and chemical reaction of hydrous phases such as hornblende, biotite and muscovite. In fact, homogenization of natural argon isotope variations within step-heated grains may yield misleadingly flat plateau spectra which are geologically meaningless (e.g. Lee et al. 1991; Wartho, 1995).

In this chapter we present and discuss the results of detailed, spot fusion  $^{40}\text{Ar}$ - $^{39}\text{Ar}$  laser dating, on one heterogeneously deformed granodiorite from the Patagonian batholith, southern Chile, for which the emplacement age is well constrained by a previously published U-Pb zircon date (Schermer et al. 1996). The sample comes from a plutonic unit located along one of the main north-northeast-trending lineaments of the Liquiñe-Ofqui fault zone in southern Chile (Figures 4.1, 4.2). The southern Chilean Andes provides a natural laboratory to investigate the nature of the spatial and temporal relationships between plate kinematics and styles of deformation on the overriding plate, as well as the tectonic consequences of ridge subduction on a plate margin. Plate motion reconstructions for the Southern Andes plate boundary zone are very well constrained for the last 48 Ma, showing relatively steady right-oblique subduction of the Nazca plate beneath South America (e.g. Pardo-Casas and Molnar, 1987, Figure 4.1). On the other hand, the geometry and timing of ridge subduction underneath the leading edge of South America during the last 14 Ma is also well known (e.g. Cande and Leslie, 1986; Bourgois



**Figure 4.1** Regional-scale tectonic setting of the Southern Andes. Northeast-trending, trench-parallel lineaments, correspond to the Liquiñe-Ofqui fault zone. Current position of the Nazca-South America-Antarctica triple junction is shown by a triangle. Series of small arrows represent convergence vectors between the Nazca and South American plates for the last 48 Ma. (Modified from Cembrano et al. 1996, Burgois et al. 1996; Pardo-Casas and Molnar, 1987).

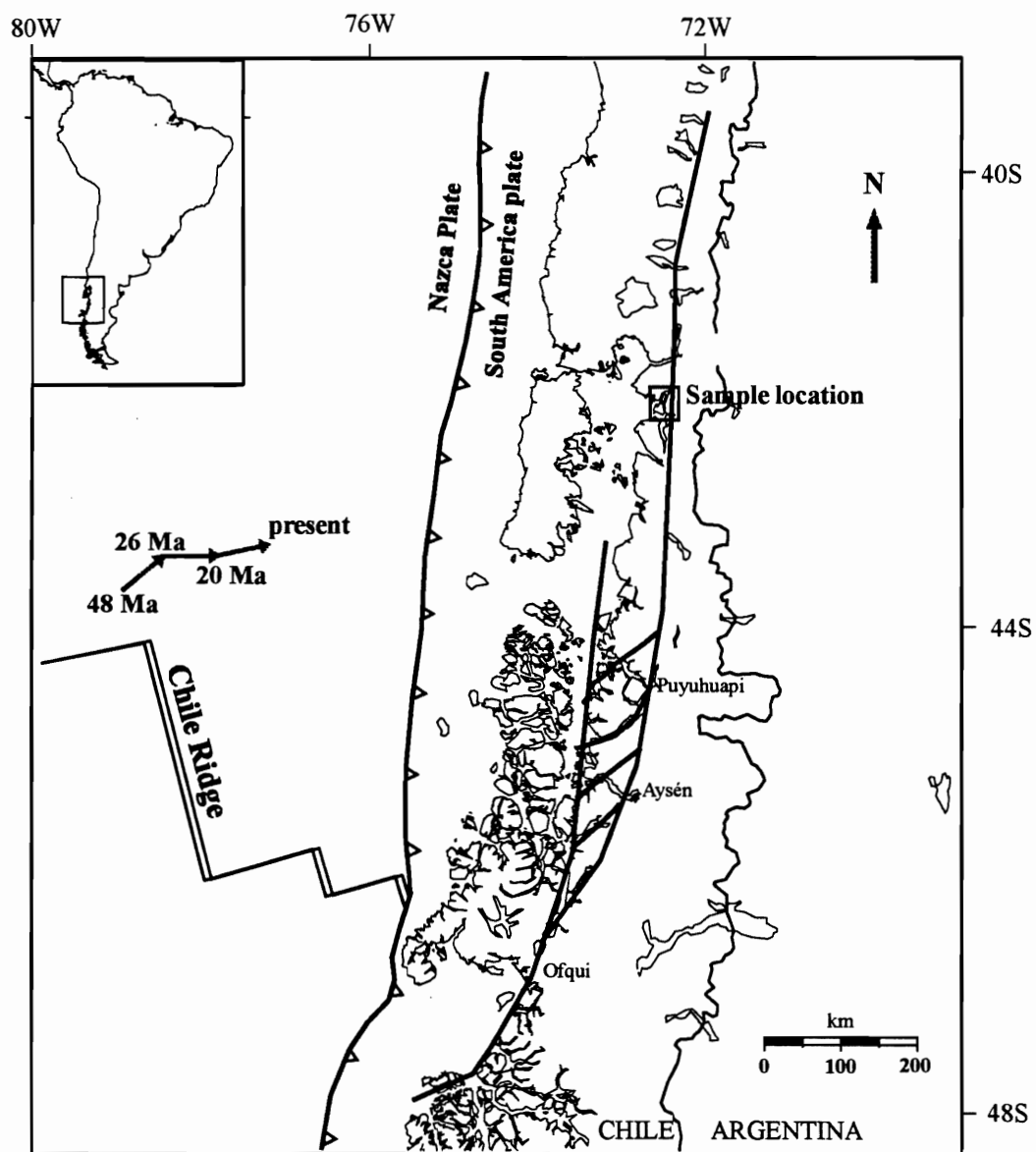


Figure 4.1

**Figure 4.2** Regional geology and local structure of the Liquiñe-Ofqui fault zone for the Hornopirén region. Simplified from Hervé et al. (1979) and Cembrano (1990). Locations of available radiometric age determinations (Hervé et al. 1979; Drake et al. 1990; Drake et al. 1991; Schermer et al. 1996) are indicated with symbols. Solid square: total fusion Ar-Ar dates on biotite; half-filled square: total fusion Ar-Ar dates on hornblende; diamond: Rb-Sr whole rock isochron; triangle: K-Ar dates on biotite, inverted triangle: K-Ar whole rock dates; filled circle: U-Pb dates on zircon. Sample location is shown.

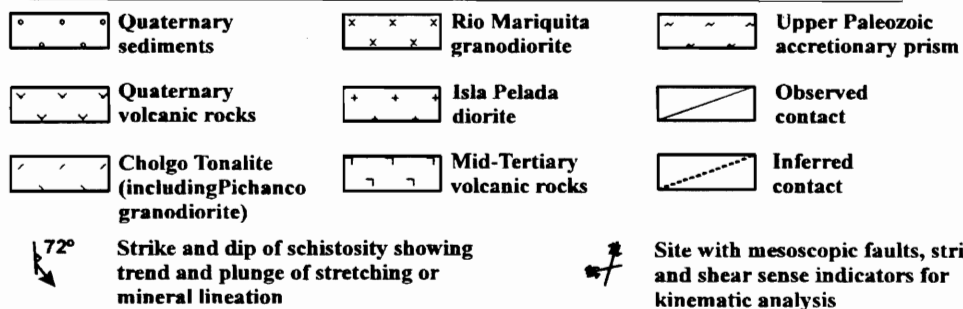
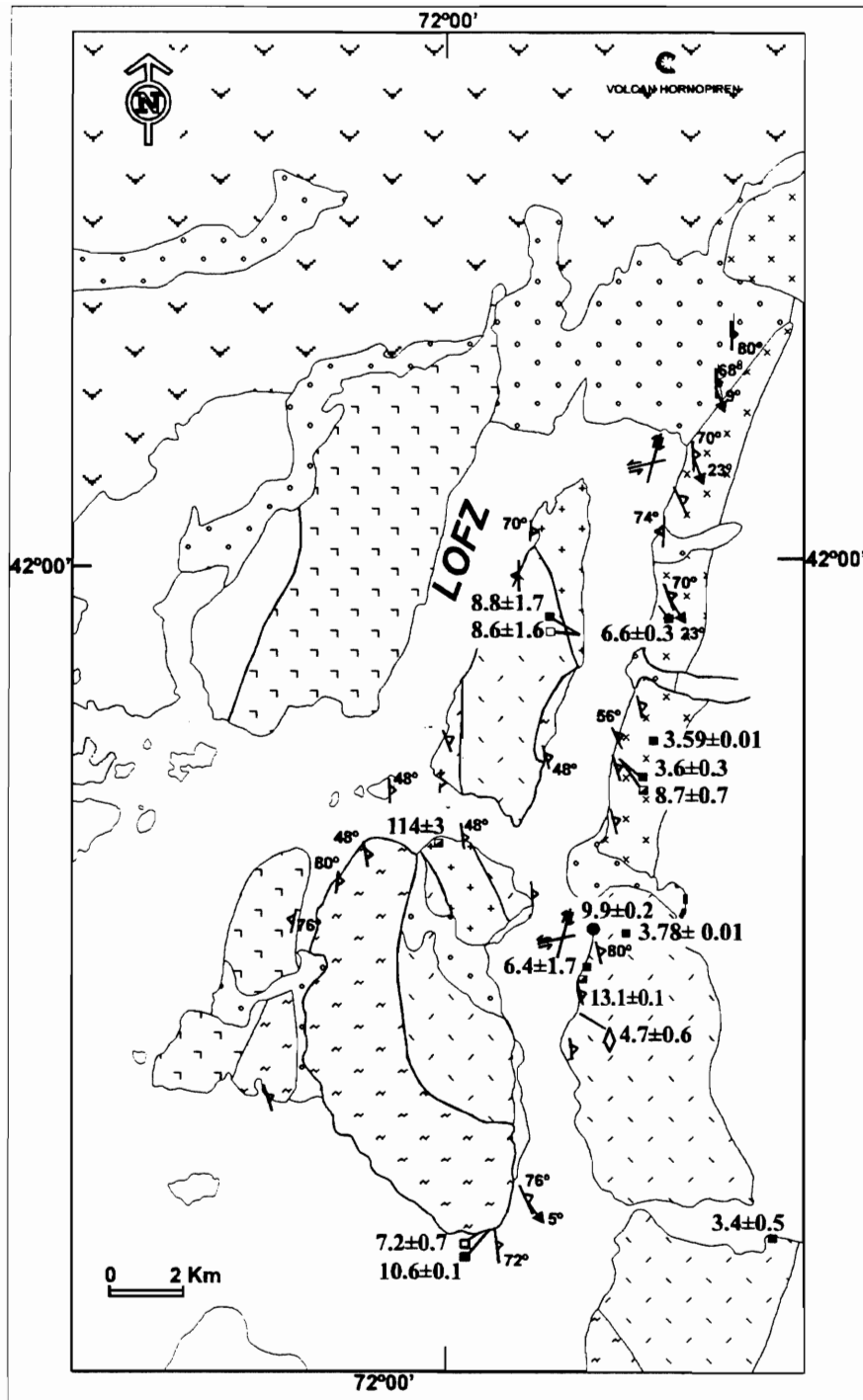


Figure 4.2

et al. 1996). A very long segment of the ridge subducted between 14 Ma and 6 Ma, starting at Tierra del Fuego and continuing northwards. From 6 Ma to the present-day, a series of short segments have impinged close to the present position of the Nazca-South America triple junction (Figure 4.3).

Cenozoic dextral transpressional deformation in the southern Andes plate boundary zone has been attributed to either oblique subduction (e.g. Beck, 1988; Cembrano et al. 1996) or ridge collision (e.g. Forsythe and Nelson, 1985; Nelson et al. 1994). However, few structural chronological data have been presented to support one model or the other. Only by detailed kinematic and thermochronological analyses of the deformed rocks along the plate boundary, will it be possible to assess the actual role of oblique subduction and ridge collision to the deformation of the overriding plate during the Cenozoic.

The sample we have chosen for detailed microstructural and  $^{40}\text{Ar}$ - $^{39}\text{Ar}$  analysis is representative of the kinematic and physical conditions of deformation found along much of the trend of the Cenozoic magmatic arc, represented now by the Patagonian Batholith. On the basis of previous field and microstructural studies, the plutonic unit from which the sample was obtained was interpreted to be emplaced syntectonically with dextral-slip motion during the late Cenozoic (Cembrano et al. 1996). Low temperature solid-state fabrics overprint magmatic fabrics and are well developed in the pluton. The sample seems suitable for  $^{40}\text{Ar}$ - $^{39}\text{Ar}$  dating on biotite since it represents well the general case of bulk ductile deformation at low greenschist facies conditions of granitic rocks. The sample shows a well-developed schistosity formed by monocrystalline and polycrystalline quartz ribbons wrapped around subhedral phenocrysts of plagioclase and

**Figure 4.3** Migration of the Chile Ridge and fracture zones with respect to the plate boundary during the last 6 Ma (Bourgeois et al. 1996).

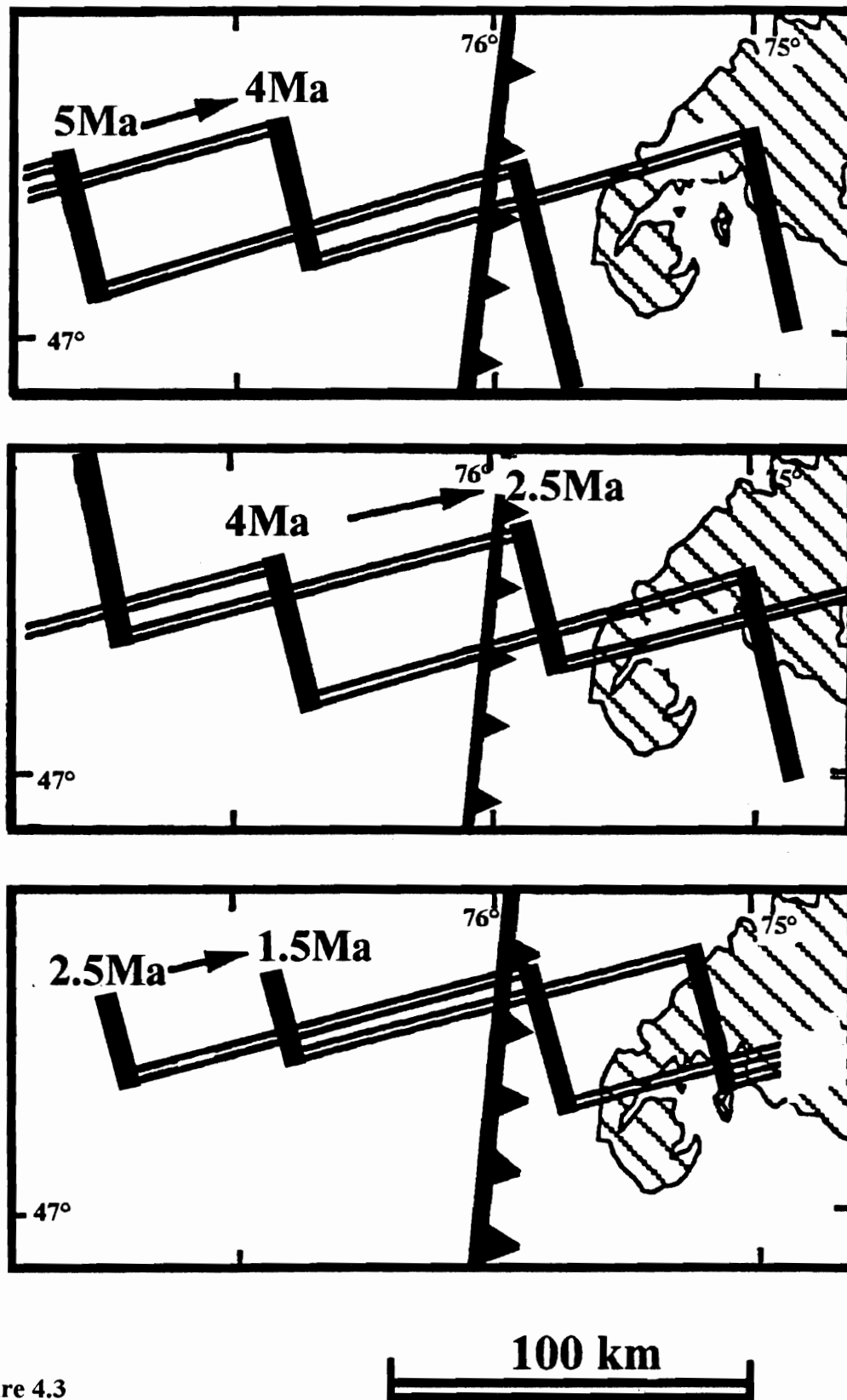


Figure 4.3

amphibole. Fish-shaped biotite grains and polycrystalline hornblende-biotite aggregates are common along discontinuous shear bands (Figure 4.4). The rock has no well-defined stretching lineation but shows conspicuous striae-like subhorizontal lineations on the shear bands (e.g. Lin and Williams, 1992). The shear bands make a 25 to 30 degree angle with the schistosity in a clockwise sense (Figures 4.4, 4.5). Shear sense, as shown by S-C fabrics and bookshelf structures, is dextral strike-slip. The sample has a U-Pb age of  $9.9 \pm 0.1$  Ma obtained from a braided zircon fraction (Schermer et al. 1996) which is believed to be the age of plutonic emplacement. Available single-grain total fusion  $^{40}\text{Ar}$ - $^{39}\text{Ar}$  dates are in the range of 9 to 13 Ma for hornblende and 3 to 6 Ma for biotite (Cembrano, 1990; Drake et al. 1991).

## **4.2 Microstructure and possible deformation mechanisms**

Quartz occurs as ribbons with serrated boundaries and fine-grained aggregates around the edges. Plagioclase is brittlely fractured, usually forming bookshelf microstructures surrounded by ductilely deformed quartz. This overall microstructure is commonly interpreted to reflect high strain deformation of granitic rocks under low greenschist facies conditions (e.g. Simpson, 1985).

Aggregates of relic hornblende and biotite fish are commonly developed close to shear bands. Shear bands occur as anastomosing dark-colored sharp discontinuities in the rock, close to which the grain size of quartz and mica aggregates decrease significantly (Figure 4.5). These microstructures are usually interpreted as dynamically recrystallized grains, however without detailed TEM analysis is impossible to assess the relative



**Figure 4.4** (a) Polished slab (~10 by 5 cm) of the heterogeneously deformed granodiorite. Shear bands are represented by discontinuous dark-colored seams oblique to the schistosity. Fish-shaped biotite-amphibole crystal aggregates are common between contiguous shear bands. Section cut parallel to lineation and perpendicular to foliation. Inset shows the area from which a 2 by 2-cm polished thick section was taken for Ar-Ar laser dates (figure 4.b). Target numbers are labeled on the polished thick section.

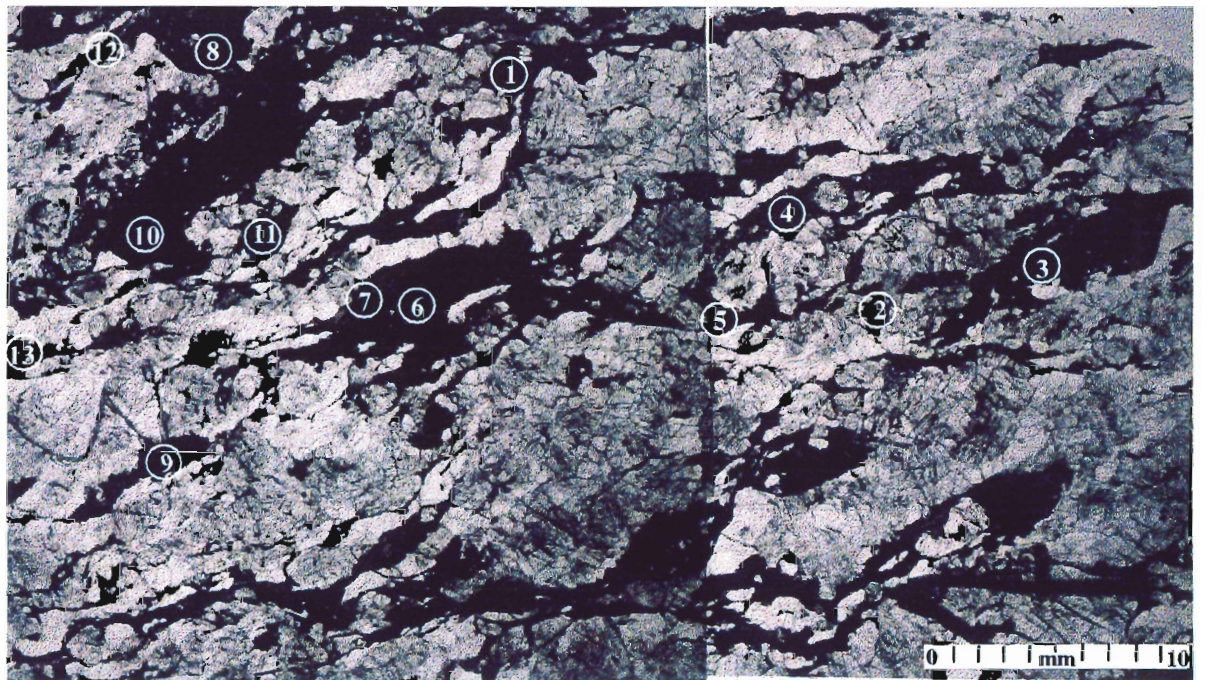
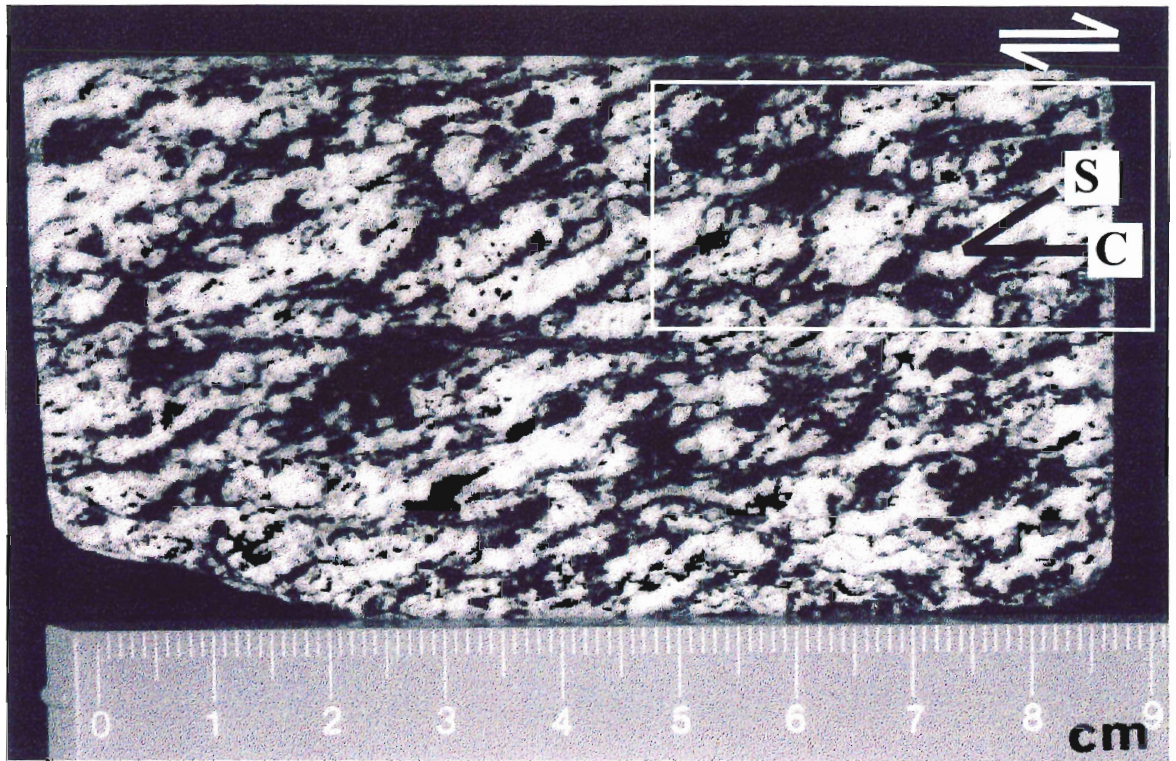
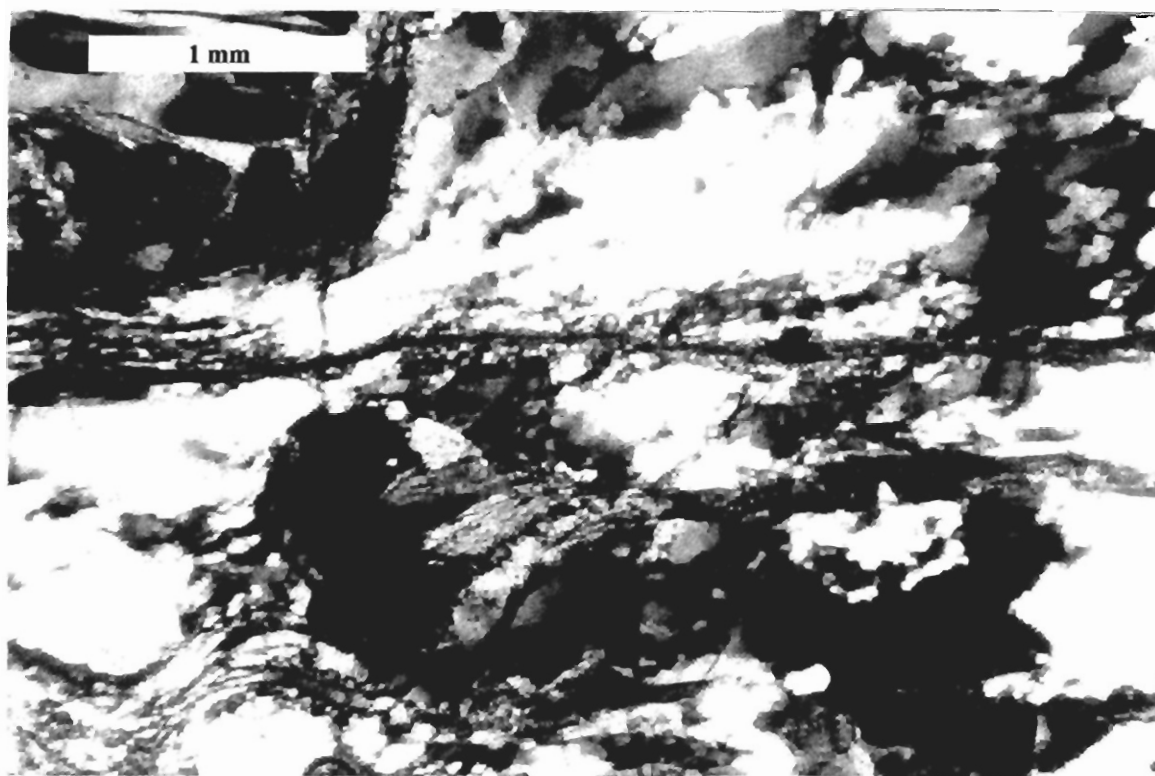


Figure 4.4

**Figure 4.5** Photomicrograph of S-C fabrics. Schistosity is defined by quartz ribbons, which curve asymptotically near the shear bands. Quartz and mica grain size diminishes significantly in the vicinities of the shear bands, interpreted as extensive, high strain dynamic recrystallization took place close to the shear bands.



**Figure 4.5**

**Figure 4.6** Plot of the  $^{37}\text{Ar}/^{39}\text{Ar}$  ratio against apparent age of the different spots selected for laser dates. Data follow a positive slope straight line that intercepts the ordinate axis at around 4.2 Ma. The intercept of the line with the y axis represents the age of a calcium free phase.



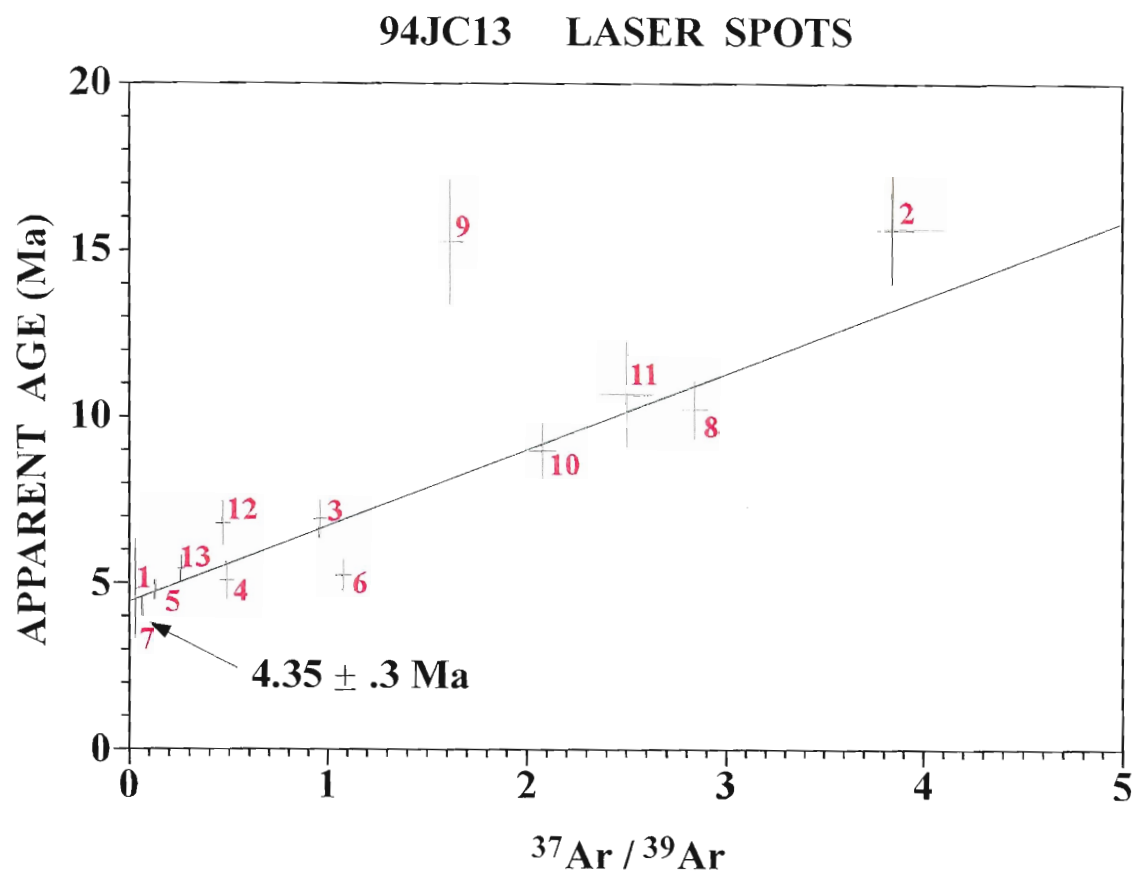


Figure 4.6

importance of other deformation processes such as cataclasis, particularly around biotite grains. In the literature, mica fish are believed to result from combined slip on the basal plane, rigid body rotation, boudinage and recrystallization at the edges (Lister and Snoke, 1984).

### **4.3 Laser dating: technique and targets**

A 2 by 2-cm slab, 100 microns thick, was cut from the upper right side of the sample shown in Figure 4.4a (inset, Figure 4.4b). The thick sections were irradiated in several separate canisters, each containing aliquots of the flux monitor. The packages were shielded with Cd and irradiated in the McMaster University nuclear reactor. Laserprobe analyses were made with a Nd-YAG system operated in the pulse mode (repetition rate = 1kHz) at a wavelength of 1064 nm. The time required to fuse a selected area in a given section was 1-10 s. All isotopic analyses were made on a VG 3600 mass spectrometer using both Faraday and electron multiplier collectors.

The mineral selected to date deformation was biotite because of its high potassium content (better age resolution for very young rocks) and because of its microstructural significance as a highly strained mineral within the rock. Biotite fish along shear bands very likely record the age of deformation as biotite probably underwent intracrystalline deformation and localized microfracturing consistent with the overall low greenschist facies microstructure of the rock. This deformational event probably took place at temperatures slightly below the Ar closure temperature of biotite, thus resetting the isotopic system.

Targets selected for total fusion analyses are shown as correlative numbers on Figure 4.4b. These were plotted in a diagram of  $^{37}\text{Ar}/^{39}\text{Ar}$  ratios against apparent ages; the target number can track each analysis back to the polished section.

#### 4.4 Results

Laser dating on several biotite grains and biotite-hornblende intergrowths gave total fusion dates in the range of 4.3 and 15.5 Ma (Figure 4.6, plot of  $^{37}\text{Ar}/^{39}\text{Ar}$  against apparent ages). Figure 4.6 shows that targets with decreasing amounts of calcium contamination (low  $^{37}\text{Ar}/^{39}\text{Ar}$  ratios) yielded consistently younger apparent ages, which we interpret as dates dominated by biotite. In fact, a target with a virtually zero  $^{37}\text{Ar}/^{39}\text{Ar}$  ratio corresponds to the center of a biotite fish. This spot gave an apparent age of  $4.35 \pm 0.3$  Ma. We interpret this date as the age of a low greenschist facies ductile deformational event that took place in the Patagonian Batholith during Pliocene times.

Recent efforts to date high strain solid-state deformation along the Patagonian Batholith between 42 and 47 degrees south have shown a predominance of  $^{40}\text{Ar}/^{39}\text{Ar}$  ages (bulk mineral separates) in the range of 3 to 6 Ma (Schermer et al. 1996). These have been interpreted by Cembrano et al (1998) as the age of a Pliocene transpressional deformation event along the magmatic arc related to the subduction of consecutive segments of the Chile Ridge during the last 6 Ma.



## **4.5 Discussion**

### **4.5.1 Limitations and advantages of the laser method in dating deformation of young plutonic rocks deformed under low greenschist facies conditions**

The high spatial resolution laser technique applied to the dating of deformed rocks is indeed a useful method and have been successfully used in the past recent years (i.e. Reddy et al. 1996). However, for deformed rocks in young orogenic belts, there is a critical limit to the laser method because measurable amounts of daughter Ar are needed. Thus, although there is a need to resolve at the few microns level to date small recrystallized grains, a minimum threshold has to be overcome to ensure that the amount of gas is at least two orders of magnitude greater than the blank. For a K-rich mineral such as biotite, overcoming the threshold requires targets in excess of 50 microns in diameter. This implies that the use of infrared laser allows a resolution that is good enough for the purpose of dating young rocks, because eventual targets smaller than ~ 50 microns will not yield measurable amounts of daughter Ar.

### **4.5.2 Significance of the ages for the tectonic evolution of the southern Andes**

High-resolution laser dating on one deformed sample from the Patagonian Batholith at the Southern Andes plate boundary zone allowed us to better constrain the age of a regional deformation event that took place between 6 and  $4.3 \pm 0.3$  Ma. This age suggests a strong causal link between subduction of consecutive segments of the Chile Ridge and the tectonics of the overriding South American plate. Ridge collision may have caused dextral transpressional deformation at the leading edge of South America by an indenter mechanism analogous to the collision of India with Asia (e.g. Taponnier and

Molnar, 1976). Collision of a positive bathymetric element is known to produce shortening concomitant with oblique-slip and strike-slip escape faults toward both sides of the indenter. Prominent lineaments observed to the north and south of the Chile-Ridge collision zone strongly suggest the above tectonic model applies to the southern Chile margin at least for the last 6 Ma.

## Chapter 5. Discussion and conclusions

### 5.1 Discussion

Many authors have speculated that the southern Andes plate boundary zone records a protracted history of bulk transpressional deformation during most of the Cenozoic (e.g. Forsythe and Nelson, 1985; Dewey and Lamb, 1992; Hervé et al. 1994; Nelson and Arit, 1994; Cembrano et al. 1996). However, there have been no systematic field and thermochronological studies to document those speculative ideas. Previous studies have also suggested that Cenozoic deformation of the overriding South American plate has concentrated mainly along the magmatic arc (e.g. Hervé, 1994). Although this seems to be reasonably well supported, the actual nature, style and timing of magmatic arc deformation appear to change significantly along and across the strike of the orogen (Cembrano et al. 1996). Furthermore, in contrast to the Central Andes, no foreland fold and thrust belt has developed in the Patagonian region north of 47°S (Ramos and Kay, 1992; Hervé, 1994).

The present study was undertaken to address along and across-strike variations in the nature and timing of plate-boundary deformation to better understand the Cenozoic kinematics of the southern Andes plate boundary zone. A broader objective was to gain insights into the nature of continental transpressional deformation at obliquely convergent margins.

The northernmost segment of the southern Andes main Cordillera shows predominantly ductile deformation of pre-Late Cretaceous age (e.g. Liquiñe, 39°S) with

little, if any evidence of overprinting brittle deformation. In contrast, Late Cenozoic brittle faulting of Cretaceous and Miocene plutons is very well developed at Reloncaví (41°S). Analysis of fault slip data documents Late Cenozoic contractional to strike-slip deformation regimes for this area.

Further to the south, at Hornopirén (42°S), Late Cenozoic ductile to brittle dextral strike-slip deformation appears to be continuous from ca. 10 Ma, at the time of pluton emplacement, to nearly 4 Ma when low temperature, solid-state deformation took place. Brittle kinematic analysis of fault-slip data indicates dextral strike-slip deformation remained active after 3 Ma.

In the Puyuhuapi and Aysén transects (44-46°S), there is a remarkable increase in the contractional component of both ductile and brittle deformation in closer proximity to the Nazca-South America-Antarctica triple junction. In the Puyuhuapi transect (44°S), north-south trending, high-angle contractional ductile shear zones that developed from plutons and wallrocks, coexist with moderately dipping dextral-oblique shear zones. Ductile shear zones from the Aysén transect show variable kinematics. Top to the southeast, oblique thrusting predominates to the west of the Cenozoic magmatic arc, whereas dextral strike-slip shear zones develop within it.

New thermochronological data from undeformed and deformed rocks of the mapped ductile shear zones of southern Chile, suggest that dextral strike-slip and contractional deformation occurred at the same time but within different structural domains along and across the southern Andes. For instance,  $^{40}\text{Ar}$ - $^{39}\text{Ar}$  laser dating on highly strained (recrystallized?) synkinematic biotite from plutonic rocks with S-C fabrics at 42°S documents an event of dextral ductile shear at 4.3 Ma. Similar ages were

obtained on both high strain pelitic schists with dextral strike-slip kinematics (4.4 Ma, laser on muscovite-biotite aggregates, Aysén transect, 45°S) and on mylonitic plutonic rocks (3.8 to 4.2 Ma, fine-grained, recrystallized biotite, Puyuhuapi transect).

Oblique-slip, dextral reverse kinematics, is also documented in several high strain zones such as the Canal Costa shear zone at 45°S and the Queulat shear zone at 44°S. There are, however, no available absolute dates of deformation for these shear zones. Because plutonic rocks close of Canal Costa are Miocene (Bartholomew, 1984), deformation of these rocks is likely to be Late Miocene or Pliocene, probably coeval with that of the dated shear zones. Similarly, deformation on the Queulat shear zone must also be Late Tertiary, since it affects rocks of the mid-Tertiary Traiguén Formation.

The apparently contemporaneous character of the strike-slip and contractional deformation on several ductile shear zones in the southern Andes suggests high degrees of along- and across-strike deformation partitioning of bulk transpressional deformation resulting from long-term oblique subduction of the Nazca plate beneath South America. The southward increase in the contractional component of deformation may result from the collision of successive segments of the Chile Ridge at the 6 to 3 Ma time interval.

The existence of very young, ductile shear zones cropping out exclusively within the Miocene belt of the Patagonian Batholith suggests differential exhumation rates of the Cenozoic magmatic arc with respect to the adjacent forearc and foreland regions that completely lack young, ductile shear zones.

The spatial distribution of north-south trending geologic units at the regional-scale also indicates that deeper structural levels are consistently exposed within the Cenozoic plutonic belt, which is flanked by major crustal lineaments of the LOFZ (Figure 3.2).

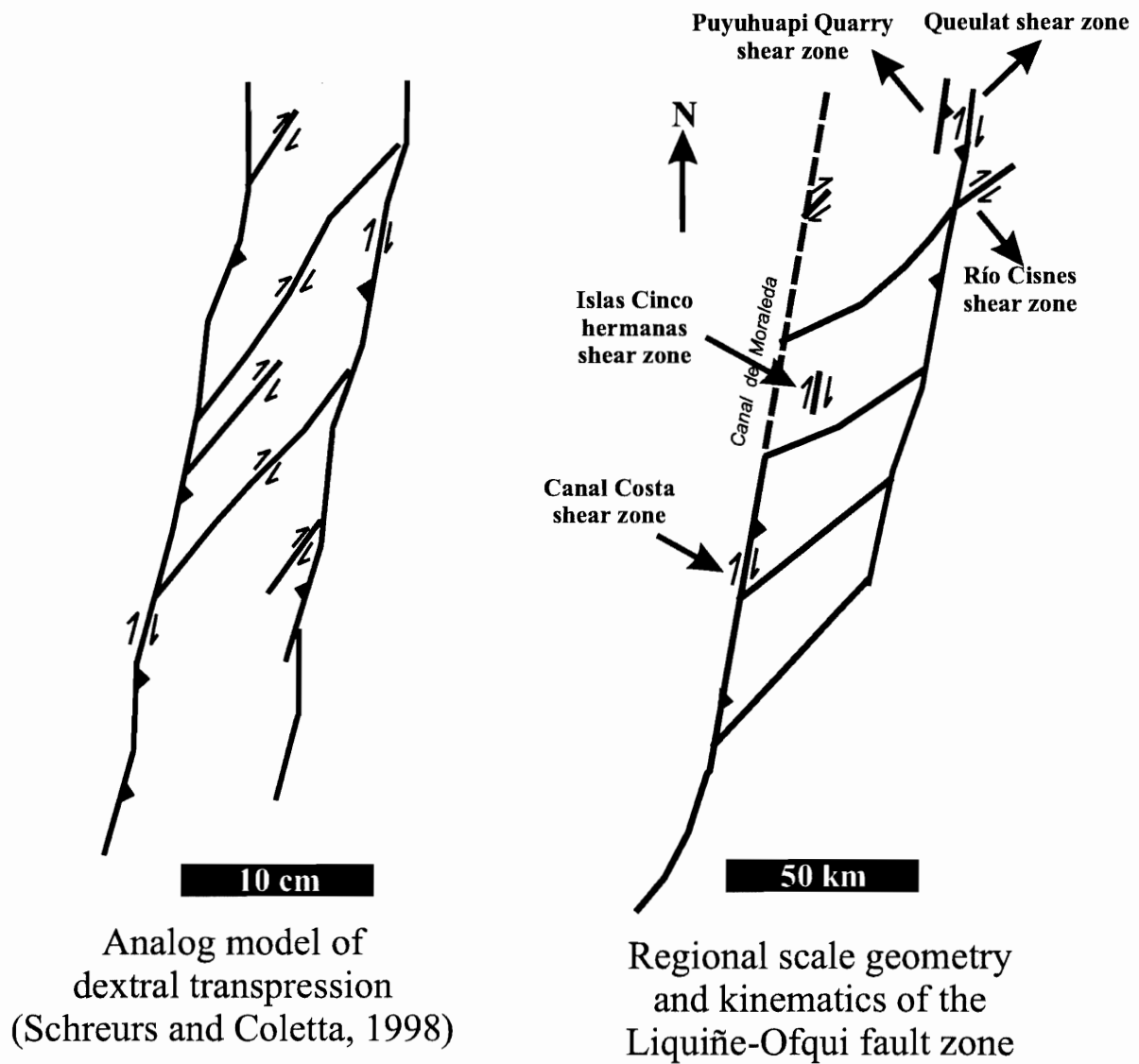
The exposure of deeper structural levels to the east of the Canal de Moraleda is consistent with east-dipping regional ductile shear zones showing top-to-the-west sense of shear. The nature of the eastern boundary of the Cenozoic plutonic belt is less well defined. However, limited data indicates that both east- and west-dipping ductile shear zones mark this boundary. Sense of shear is generally dextral reverse and overall tectonic transport is commonly to the northeast.

In summary, the present-day spatial distribution of geologic units along with the mostly contractional nature of their boundaries strongly suggest the development of a half-flower or flower structure (Figure 1.10, Figure 3.15). The Cenozoic magmatic arc rocks are thrust westwards over the basement/Traiguén Formation and appear to be thrust eastward over the Cretaceous belt of the Patagonian batholith. This pop-up like structure, at a colossal scale, is very similar to that obtained through three-dimensional numerical dynamic modeling of transpressional deformation at obliquely convergent plate margins (Braun and Beaumont, 1995). Recent experimental analog modeling of transpressional deformation by Schreurs and Colletta (1998) also shows striking similarities with the field data. Furthermore, the series of en echelon structures joining the two main boundaries of the Cenozoic plutonic belt in southern Chile resembles the duplex-like structure observed in the same analog models (Figure 5.1)

Structural and thermochronological work in the southern Andes has shown that bulk transpressional deformation at convergent plate boundaries is accommodated in a very complex manner in space and time. Dip-slip contractional, oblique-slip and strike-slip deformation can coexist at different scales along and across convergent plate margins. Therefore, bulk transpression arising from the combination of oblique

**Figure 5.1** Comparison between the geometry and kinematics of transpressional shear zones in experiments and nature. (a) Geometry and kinematics obtained from recent analog models of transpression (Schreurs and Coletta, 1998); (b) Geometry and kinematics of ductile shear zones in the Cenozoic magmatic arc of the southern Andes (Liquiñe-Ofqui fault zone).

Figure 5.1





subduction and ridge collision is accommodated heterogeneously at the regional scale, with the contraction component being absorbed not only by vertical extrusion but also through oblique displacement along shear zones. Currently accepted models of monoclinic transpression (e.g. Tikoff and Greene, 1997) do not account for oblique-slip components of motion. The structural and kinematic data from the southern Andes plate boundary zone supports the more complex, triclinic models of transpression (e.g. Robin and Cruden, 1994; Lin et al. 1998). Further insight into the question of why and how triclinic transpressional deformation is accommodated in nature requires extensive mapping of geological structures in the field and detailed dating of kinematically significant high strain rocks.

## 5.2 Conclusions

- The Southern Andes plate boundary zone, north of the Nazca-South America-Antractica triple junction, has undergone a complex history of heterogeneously distributed transpressional deformation during Cenozoic times. The nature, style and timing of deformation varies along and across strike, as suggested by structural mapping and detailed  $^{40}\text{Ar}$ - $^{39}\text{Ar}$  thermochronology carried out on five transects along the Cenozoic magmatic arc. These data were integrated with structural information from previously published tectonic studies undertaken in the forearc and foreland regions. From this analysis, I have shown that the magmatic arc has accommodated most of the bulk transpressional deformation; the forearc and foreland regions have remained nearly undeformed.

- A one-kilometer wide mylonitic zone at Liquiñe (39°S) records sinistral-oblique deformation with a strong component of orogen-orthogonal shortening. An undeformed porphyritic dyke crosscuts the mylonites and yields a well-defined mean  $^{39}\text{Ar}$ - $^{40}\text{Ar}$  age on hornblende of  $100\pm 2$  Ma. Therefore, sinistral ductile deformation is pre-mid Cretaceous in age.
- A north-northeast trending regional zone of brittle faults is exposed along the main lineaments of the LOFZ at Reloncavi (41°S). These faults cut both Cretaceous and Miocene plutonic rocks of the Patagonian Batholith that show little evidence of ductile deformation. Inversion of the fault-slip data for the stress tensor yields east-west compressional and north-south dextral strike-slip stress regimes. Both compression and strike-slip deformation are post-Miocene in age.
- At the Hornopiren transect (42°S), a 3-4 km wide, northeast-trending deformation zone affects plutonic rocks of the Patagonian Batholith and metamorphic wallrocks. The geometry and kinematics of magmatic and solid-state fabrics indicate dextral shear was active during emplacement and cooling of plutons. Fine-grained aggregates of biotite and biotite fish microstructure along shear bands on a 9.9 Ma (U-Pb, zircon) plutonic unit were selectively dated using the  $^{40}\text{Ar}$ - $^{39}\text{Ar}$  spot laser technique. A well-defined date of  $4.3\pm 0.2$  Ma on biotite fish was interpreted to be the age of a low greenschist facies event of dextral ductile high-strain deformation. Brittle faults affect the mylonites and document a dextral-strike slip deformational event of post 3.3 Ma.

- The Puyuhuapi transect (44°S) shows several centimeter- to- hundreds-of-meters wide north-east-trending ductile shear zones that affect Paleozoic metamorphic rocks, mid-Tertiary stratified rocks and Miocene plutonic rocks. Some of these shear zones, e.g. the Puyuhuapi and Queulat shear zones, roughly define the eastern boundary of the Miocene belt of the North Patagonian Batholith. Steeply-dipping meter-wide mylonite zones display dextral oblique reverse sense of shear in the plutons whereas wider, lower strain shear zones, show top-to-the-east ductile shear kinematics. Several  $^{40}\text{Ar}$ - $^{39}\text{Ar}$  step-heating analyses on fine-grained biotite separates from mylonitic zones within Miocene plutons yielded well-defined mean ages between  $3.8\pm 0.2$  and  $4.2\pm 0.2$  Ma. These were interpreted as the timing of a Pliocene dextral transpressional deformation event of regional character.
- The Aysen transect shows northeast-trending ductile shear zones developed within Paleozoic metamorphic rocks, Miocene plutons and mid-Tertiary metasedimentary-metavolcanic rocks. Dextral, high-strain shear zones developed from the Paleozoic basement at Islas Cinco Hermanas. One  $^{40}\text{Ar}$ - $^{39}\text{Ar}$  step-heating staircase spectrum from 10 to 4 Ma was obtained from muscovite bulk mineral separates suggesting a mixed signature of relic grains and recrystallized grains. This behavior was confirmed on one laserspot analysis on bands of fine-grained mica, which showed a range of apparent ages between 4.6 and 9.4 Ma. A laser spot analysis performed on another companion sample with good kinematic control showed analitically significant dates around 4.3 Ma. The staircase spectra of the bulk muscovite separate, and the spatially-resolved laser-spot analyses support a complex history of cooling and high-strain deformation constrained at around 4.3-4.6 Ma.

- The similar  $^{40}\text{Ar}$ - $^{39}\text{Ar}$  dates, in the range of 4 to 6 Ma, obtained from ductile shear zones of different kinematics (ranging from pure strike-slip to pure contractional) strongly suggest bulk transpressional deformation has been partitioned in a complex way along and across the southern Andes magmatic arc during Pliocene times.
- The increased contractional component of overall transpressional deformation in the southern transects, close to the Pliocene and present-day position of the triple junction, suggest a strong causal link between consecutive episodes of Pliocene ridge collision and continental margin tectonics. Oblique subduction, a process that has taken place since 48 Ma, has been a driving mechanism for long-term dextral transpression along the continental margin and cannot be causally separated from ridge collision. Both ridge collision and oblique subduction produce bulk transpressional deformation along the leading edge of the continent.
- The contractional/dextral-oblique kinematics of regional scale shear zones at both the western and eastern boundaries of the Miocene plutonic belt of the Patagonian Batholith, suggest Pliocene bulk transpressional continental deformation has been accommodated through coeval thrusting, oblique-slip and strike-slip deformation. These orogen-parallel crustal shear zones have produce differential exhumation of Miocene plutons and wallrocks with respect to relatively undeformed forearc and foreland regions. The scale, geometry and kinematics of these shear zones are very similar to those predicted by numerical three-dimensional experiment (e.g. Braun and Beaumont 1995) and by recent analog models of transpressional deformation (e.g. Schreurs and Coletta, 1998).

## **APPENDIX 1.**

**$^{40}\text{Ar}$ - $^{39}\text{Ar}$  analytical data and release spectra from  
bulk mineral separates dated by furnace step-  
heating and/or total laser fusion techniques.**

SPOT#	CODE#	mV 39	AGE (Ma) $\pm 2\sigma$	% ATM	37/39	36/40	39/40	% IIC
1	Y12-2	2.1	4.8 $\pm$ 1.5	45.4	.02	.001532	.040366	.01
2	Y12-3	5.6	15.2 $\pm$ 1.9	53.2	1.61	.001802	.01094	.38
3	Y12-4	13.2	6.9 $\pm$ .6	55.1	.95	.001866	.02312	.42
4	Y12-5	7.1	5 $\pm$ .6	44	.48	.00149	.039356	.28
5	Y12-6	29.2	4.7 $\pm$ .3	49.7	.12	.001684	.03746	.07
6	Y12-7	10.5	5.2 $\pm$ .5	55.2	1.07	.001867	.030624	.61
7	Y12-8	42.7	4.3 $\pm$ .3	54.3	.06	.00184	.037864	.04
8	Y11-1	9.5	10.2 $\pm$ .9	48.3	2.83	.001635	.018085	.92
9	Y11-2	2.3	15.6 $\pm$ 3.2	47.2	3.84	.001598	.012032	.9
10	Y11-3	8.7	8.9 $\pm$ .9	50.7	2.07	.001715	.019614	.74
11	Y11-4	3.7	10.6 $\pm$ 1.6	44.3	2.49	.001497	.018646	.78
12	Y11-5	9	6.7 $\pm$ .7	54.6	.46	.001848	.023859	.21
13	Y11-6	12.7	5.4 $\pm$ .4	50.8	.25	.001719	.032398	.14

**UNCERTAINTIES AT 2 $\sigma$  LEVEL INCLUDING ERROR IN J**

J = .000197  $\pm$  9E-06 ( 4.6 %)

37/39, 36/40 AND 39/40 Ar RATIOS ARE CORRECTED FOR MASS SPECTROMETER DISCRIMINATION, INTERFERING ISOTOPES AND SYSTEM BLANKS

% IIC - INTERFERING ISOTOPES CORRECTION

## 94JC54 HORNBLLENDE ARGON SUMMARY

TøC	mV 39	% 39	AGE (Ma)±1å	% ATM	37/39	36/40	39/40	% IIC
600	3	2.6	58.8 ± 10.1	55.6	2.09	.001869	.032696	1.29
700	5.9	5.1	27.2 ± 7.4	83.1	2.56	.002804	.027179	3.25
800	7.6	6.6	25.8 ± 4.7	73.5	2.61	.002479	.044844	3.48
900	7.6	6.6	40.2 ± 3.6	47.1	5.24	.001597	.057247	4.59
1000	46.6	40.5	102.5 ± 1	12	8.71	.000415	.036985	3.29
1100	17	14.8	86.5 ± 2.2	26	7.74	.000889	.036927	3.39
1200	23.3	20.3	103.8 ± 1.9	28.7	9.6	.000976	.029572	3.59
1300	1.7	1.4	126.7 ± 20.6	52.5	13.53	.001775	.015944	4.29
1450	1.9	1.6	107.9 ± 51.2	84.4	12.11	.00285	.006209	4.39

**TOTAL GAS AGE = 86.8 ± 2.6 Ma**

MEAN AGE(1000øC-1200øC)= 99.7 ± 1.8 Ma (2å UNCERTAINTY, INCLUDING ERROR IN J)

J = .002443 ± .000017 ( .6 %)

37/39,36/40 AND 39/40 Ar RATIOS ARE CORRECTED FOR MASS SPECTROMETER DISCRIMINATION, INTERFERING ISOTOPES AND SYSTEM BLANKS

% IIC - INTERFERING ISOTOPES CORRECTION

□

95-JC-1 BIOTITE ARGON SUMMARY

TøC	mV 39	% 39	AGE (Ma) ±1σ	% ATM	37/39	36/40	39/40	% IIC
550	41.5	3	-128.3 ±-3.8	960	67.57	.031041	.276388	12.75
600	33.8	2.4	-56.9 ±-4.7	308	32.82	.010247	.151868	16.28
650	41.4	2.9	-25.9 ±-2.7	167	15.91	.005628	.108746	18.44
700	79.5	5.7	-5.8 ±-1.3	124	5.8	.004197	.17893	31.51
750	89.9	6.5	-2.1 ±-1	115	3.88	.003871	.308042	59.86
800	77.6	5.6	-1.3 ±-1	110	3.37	.003713	.337276	81.72
850	82.9	6	.4 ± .7	95	2.4	.003192	.474628	177.89
900	84.1	6	1.2 ± .7	84.5	1.91	.002839	.494858	47.3
950	136.1	9.8	3.1 ± .4	57.1	.94	.001926	.560082	9.43
975	140.8	10.1	3.2 ± .3	46.1	.72	.001561	.687272	7.13
1000	160.2	11.5	3.6 ± .2	33.2	.53	.001131	.748429	4.57
1025	132.8	9.6	3.5 ± .3	31.8	.55	.001091	.791464	4.97
1050	105.2	7.6	3.5 ± .3	30.9	.61	.001068	.79696	5.52
1100	156.8	11.3	3.9 ± .2	28.8	.39	.000978	.742279	3.13
1200	17.5	1.2	-1.4 ±-3.2	105	2.39	.003493	.170124	55.31
1450	1.6	.1	-104.4 ±-225.2	103	33.92	.003492	.001414	8.3

**TOTAL GAS AGE = 3 ± .2 Ma**

MEAN AGE(950øC-1100øC)= 3.5 ± .2 Ma (2σ UNCERTAINTY, INCLUDING ERROR IN J)

J = .00232 ± .0000162 ( .6 %)

37/39,36/40 AND 39/40 Ar RATIOS ARE CORRECTED FOR MASS SPECTROMETER DISCRIMINATION, INTERFERING ISOTOPES AND SYSTEM BLANKS

% IIC - INTERFERING ISOTOPES CORRECTION

□



95-JC-1 HORNBLLENDE ARGON SUMMARY

TøC	mV 39	± 39	AGE (Ma)±1å	± ATM	37/39	36/40	39/40	% IIC
650	10.1	3.3	62.5 ± 10.8	88.5	2.83	.002999	.007472	1.58
750	12.3	4	15.2 ± 7.6	94.7	2.19	.003209	.014273	4.63
850	13.4	4.4	2.9 ± 4.8	97	2.88	.003293	.041459	30.37
950	42.6	14.1	19.5 ± 2.1	80.2	9.99	.002721	.041731	16.61
975	44	14.5	21.7 ± 1.5	64.3	12.98	.002194	.067549	19.48
1000	49	16.2	17.5 ± 1.3	60.8	13.18	.002087	.092011	24.39
1025	19.1	6.3	14 ± 2.7	66.8	11.38	.002315	.0967	26.1
1050	8.2	2.7	14.2 ± 5.3	75.3	10.24	.002603	.071129	23.16
1075	6.3	2	10 ± 9	91.2	13.15	.003115	.03598	41.87
1100	7.3	2.4	15 ± 9.2	90.9	15.88	.003095	.024792	34.08
1125	12.4	4.1	18.4 ± 6.2	88.8	15.9	.003017	.02495	28
1150	12	3.9	27 ± 5.8	84.1	15.8	.002856	.024254	19.24
1200	33.9	11.2	31.5 ± 2.7	73.7	15.71	.002503	.034221	16.5
1250	11.8	3.9	21.9 ± 6.4	88	15.88	.002989	.022421	23.58
1350	13.7	4.5	12.7 ± 8.3	96.7	15.88	.003275	.010697	40.15
1450	5	1.6	-53.4 ±-35.2	103	14.03	.003498	.002643	7.46

**TOTAL GAS AGE = 20.7 ± 2 Ma**

MEAN AGE(950øC-1350øC)= 20.2 ± 2 Ma (2å UNCERTAINTY, INCLUDING ERROR IN J)

J = .00232 ± .0000232 ( 1 %)

37/39,36/40 AND 39/40 Ar RATIOS ARE CORRECTED FOR MASS SPECTROMETER DISCRIMINATION, INTERFERING ISOTOPES AND SYSTEM BLANKS

% IIC - INTERFERING ISOTOPES CORRECTION

□

95-JC-2 BIOTITE ARGON SUMMARY

TøC	mV 39	% 39	AGE (Ma)±1á	% ATM	37/39	36/40	39/40	% IIC
550	19.6	1.5	-132.6 ±-8.2	1634	71	.043443	.387645	12.82
600	10	.7	-116.6 ±-11.8	1634	60.12	.036556	.364203	12.81
650	12.9	1	-56.2 ±-8.2	289	31.42	.009248	.132213	15.8
700	32.4	2.5	-11 ±-3.2	137	7.72	.004587	.140649	21.76
750	106.8	8.3	-.3 ±-.8	103	1.66	.003469	.593526	192.52
800	273.9	21.3	1.7 ± .2	39.8	.43	.001367	1.39478	7.76
850	268.2	20.9	1.7 ± .1	24.1	.32	.000865	1.719379	5.82
900	157	12.2	1.3 ± .2	39.7	.47	.001381	1.747207	10.91
950	60.6	4.7	-.5 ±-.6	124	1.27	.003841	1.877213	88.76
975	35.7	2.7	-1.5 ±-.6	374	1.97	.006809	3.500425	42.98
1000	48.9	3.8	-.1 ±-.4	100	1.22	.003034	2.374611	
12370.68								
1025	56.8	4.4	.7 ± .3	62.3	.89	.002059	1.846029	39.47
1050	52.6	4.1	.5 ± .3	69.5	.83	.002234	1.83787	44.83
1100	109	8.5	1.8 ± .2	39.8	.2	.00131	1.315038	3.51
1200	37.1	2.8	1.7 ± 1.6	87.8	.28	.002891	.289009	5.22
1450	.9	0	-66.2 ±-463.1	101	36.56	.003419	.000922	15.31

**TOTAL GAS AGE = 1.5 ± .2 Ma**

MEAN AGE(800øC-900øC)= 1.6 ± .2 Ma (2á UNCERTAINTY, INCLUDING ERROR IN J)

J = .00232 ± .0000232 ( 1 %)

37/39,36/40 AND 39/40 Ar RATIOS ARE CORRECTED FOR MASS SPECTROMETER DISCRIMINATION, INTERFERING ISOTOPES AND SYSTEM BLANKS

% IIC - INTERFERING ISOTOPES CORRECTION

□

## 95-JC-4 BIOTITE ARGON SUMMARY

T°C	mV 39	% 39	AGE (Ma) ± 1σ	% ATM	37/39	36/40	39/40	% IIC
550	31.7	2.2	-98 ± -6.8	417	61.95	.013616	.132815	16.38
600	22.3	1.5	-52.2 ± -7.4	240	32.65	.007926	.109694	17.81
650	28.9	2	-17 ± -5.6	126	13.11	.004261	.065689	23.51
700	56.6	4	-1 ± -3	101	3.82	.003426	.080565	132.82
750	84	5.9	2.4 ± 1.7	88.4	2.1	.002972	.196596	27.22
800	69.3	4.9	2 ± 1.9	89.5	2.43	.003004	.214004	38.11
850	84.5	6	3.6 ± 1.2	69.5	1.72	.002334	.345849	15.06
900	77.2	5.5	3.9 ± 1.1	59	1.43	.001988	.427411	11.66
950	102.7	7.3	4.9 ± .8	48.1	.91	.001621	.432076	5.9
975	125.7	8.9	5.1 ± .5	29.9	.71	.001028	.558256	4.41
1000	204.8	14.6	5.3 ± .3	18.1	.34	.000624	.62939	2.05
1025	225.6	16.1	5.6 ± .2	11	.24	.000386	.644185	1.36
1050	150.2	10.7	5.4 ± .2	15.1	.31	.000525	.637975	1.84
1100	95.8	6.8	5.1 ± .5	28.5	.46	.000965	.561897	2.85
1200	35.8	2.5	3.5 ± 2.4	77.8	1.27	.002574	.256589	11.42
1450	4.7	.3	-30 ± -46.9	104	14.31	.003515	.006162	14.21

**TOTAL GAS AGE = 4.7 ± .4 Ma**

MEAN AGE(950°C-1100°C) = 5.3 ± .3 Ma (2σ UNCERTAINTY, INCLUDING ERROR IN J)

J = .00232 ± .0000232 ( 1 %)

37/39, 36/40 AND 39/40 Ar RATIOS ARE CORRECTED FOR MASS SPECTROMETER  
DISCRIMINATION, INTERFERING ISOTOPES AND SYSTEM BLANKS

% IIC - INTERFERING ISOTOPES CORRECTION

□

95-JC-4 HORNBLLENDE ARGON SUMMARY

TøC	mV 39	± 39	AGE (Ma) ± 1σ	% ATM	37/39	36/40	39/40	% IIC
650	18.1	5.8	-49.9 ± -8	124	37.38	.004218	.021157	21.42
750	15.2	4.8	-29.4 ± -9.8	109	25.49	.003707	.014044	25.81
850	14.1	4.5	-16.5 ± -7.6	107	20.37	.003633	.019659	37.64
950	14.8	4.7	-14 ± -6	110	18.72	.003713	.030779	41.23
975	9.7	3.1	-13.5 ± -7.7	110	25.13	.003716	.032562	57.31
1000	13.4	4.3	-1.7 ± -5.7	101	25.99	.003413	.033072	
504.01								
1025	30.5	9.7	13.5 ± 2.7	85.6	24.43	.002894	.04387	57.8
1050	59.7	19	25.7 ± 1.9	76.3	19.54	.002582	.038096	24.98
1100	18.6	5.9	25.2 ± 3.3	64.8	18.46	.0022	.05706	23.96
1125	4.6	1.4	18.3 ± 10.7	81	24.55	.002718	.04182	43.3
1150	6.2	1.9	26.5 ± 8.3	74.2	25.56	.002503	.039426	31.63
1175	12.9	4.1	34.7 ± 4.8	68.1	22.51	.002304	.037658	21.64
1200	11.9	3.8	38.4 ± 5.2	65.9	22.33	.002229	.036261	19.48
1250	38.5	12.3	37.5 ± 2.1	63.5	21.07	.00215	.040068	18.81
1350	34.1	10.8	37.2 ± 2.4	63.7	21.83	.002158	.040106	19.62
1450	10.1	3.2	58 ± 7.3	69.3	23.52	.002335	.021646	14.05

**TOTAL GAS AGE = 30.3 ± 2.1 Ma**

MEAN AGE(1250øC-1350øC)= 37.4 ± 3.2 Ma (2σ UNCERTAINTY, INCLUDING ERROR IN J)

J = .00232 ± .0000232 ( 1 %)

37/39, 36/40 AND 39/40 Ar RATIOS ARE CORRECTED FOR MASS SPECTROMETER DISCRIMINATION, INTERFERING ISOTOPES AND SYSTEM BLANKS

% IIC - INTERFERING ISOTOPES CORRECTION

□

TøC	mV 39	± 39	AGE (Ma)±1á	± ATM	37/39	36/40	39/40	± IIC
550	1.3	0	18.2 ± 41.6	86.5	36.29	.002733	.027781	64.46
600	7.1	.3	15.9 ± 12.4	78.1	6.47	.002558	.055596	13.08
650	36.4	1.9	15.5 ± 3.3	63.6	1.34	.00212	.096896	2.79
700	108	5.8	14.8 ± .9	41.5	.47	.00139	.163844	1.03
750	204.6	11.1	14.6 ± .3	16.7	.23	.000558	.236413	.5
800	310.8	16.9	14.3 ± .2	7.5	.14	.000252	.267607	.31
850	196.9	10.7	14.4 ± .2	7.8	.26	.000265	.264022	.58
900	102.9	5.6	14.2 ± .4	15.3	.71	.000518	.244703	1.6
950	107.3	5.8	14.3 ± .6	20.7	.7	.000695	.228504	1.59
1000	104.9	5.7	14.2 ± .5	17.2	.77	.000582	.240189	1.75
1050	209.7	11.4	14.2 ± .4	11.2	.43	.00038	.258885	.97
1100	287.1	15.6	14.3 ± .2	8.4	.37	.000286	.265203	.84
1200	150.3	8.2	14.3 ± .3	14.1	.78	.000482	.247193	1.76
1450	3	.1	250.4 ± 47.7	53.7	454.86			
						.001918	.0071	82.78

**TOTAL GAS AGE = 14.8 ± .3 Ma**

MEAN AGE(650øC-1200øC)= 14.4 ± .3 Ma (2å UNCERTAINTY, INCLUDING ERROR IN J)

J = .00232 ± .0000232 ( 1 %)

37/39,36/40 AND 39/40 Ar RATIOS ARE CORRECTED FOR MASS SPECTROMETER DISCRIMINATION, INTERFERING ISOTOPES AND SYSTEM BLANKS

% IIC - INTERFERING ISOTOPES CORRECTION

□

95-JC-6 HORNLENDE ARGON SUMMARY

T°C	mV 39	± 39	AGE (Ma)±1σ	± ATM	37/39	36/40	39/40	% IIC
650	18	2.1	16 ± 3.9	79.1	.68	.002686	.054145	1.38
750	61.6	7.3	11.3 ± 1	54.8	.23	.001862	.166933	.65
850	61.5	7.3	10.9 ± .9	47.1	.46	.001606	.201649	1.36
900	29.5	3.5	12.7 ± 1.6	50.3	1.6	.00173	.162285	4.04
950	33	3.9	15.5 ± 2	61.7	5.19	.002115	.102282	10.81
975	51.1	6	17.5 ± 1.4	56.3	8.24	.001936	.102916	15.24
1000	225.6	26.8	15.2 ± .4	47	9.23	.001609	.144158	19.55
1025	152.1	18	14.3 ± .5	28.2	9.07	.00103	.204592	20.37
1050	59.9	7.1	14.3 ± .8	23.3	6.49	.000926	.215059	14.55
1075	40.1	4.7	12.9 ± 1	32.2	3.65	.001172	.213963	9.04
1100	42.2	5	12.9 ± 1.3	47.5	5.63	.001668	.166737	13.99
1125	23.9	2.8	12.9 ± 2.6	66.9	9.81	.002314	.104947	24.31
1150	7.9	.9	7.8 ± 8	91.9	12.08	.00314	.042667	49.06
1200	6.5	.7	.4 ± 11.9	99	12.65	.00339	.023506	840.2
1250	4.3	.5	-5.7 ±-19.4	102	12.56	.003467	.015287	69.57
1350	13.4	1.5	1.2 ± 8.7	99	11.29	.003373	.015062	
290.56								
1450	10	1.1	8.5 ± 15.8	98.6	2.44	.003342	.006368	9.12

TOTAL GAS AGE = 13.7 ± .7 Ma

MEAN AGE(1000°C-1125°C)= 14.4 ± .6 Ma (2σ UNCERTAINTY, INCLUDING ERROR IN J)

J = .00232 ± .0000232 ( 1 %)

37/39,36/40 AND 39/40 Ar RATIOS ARE CORRECTED FOR MASS SPECTROMETER DISCRIMINATION, INTERFERING ISOTOPES AND SYSTEM BLANKS

% IIC - INTERFERING ISOTOPES CORRECTION

□

95-JC-14 BIOTITE ARGON SUMMARY

TøC	mV 39	% 39	AGE (Ma)±1σ	% ATM	37/39	36/40	39/40	% IIC
550	11.2	.6	-67.8 ±-6.8	356	39.55	.011387	.150647	16.09
600	43.8	2.5	-4.6 ±-1.8	111	6.14	.003754	.10971	42.33
650	149.8	8.7	4.3 ± .5	78.2	1.21	.002629	.206765	8.77
700	297.2	17.3	5.8 ± .2	42.6	.44	.00143	.408531	2.41
750	366.1	21.3	6.2 ± .1	24.6	.29	.000825	.503958	1.5
800	200.6	11.7	5.9 ± .2	42.6	.44	.001424	.400065	2.36
850	87.4	5.1	4.7 ± .4	40.3	.95	.001342	.509703	6.28
900	67.1	3.9	4.5 ± .5	47.2	1.13	.001561	.477224	7.97
950	84.7	4.9	5.2 ± .5	51	.72	.001688	.387755	4.43
975	70.5	4.1	4.9 ± .7	66.7	.68	.002213	.27884	4.35
1000	76	4.4	5.3 ± .4	38	.66	.001251	.478727	3.99
1025	70.9	4.1	6 ± .4	35.4	.22	.001146	.443894	1.2
1050	56.8	3.3	6.4 ± .5	38.6	-.02	.00124	.394752	.07
1100	92	5.3	6.3 ± .5	43.6	.06	.00143	.36744	.32
1200	35.8	2	4.6 ± 1.3	73.2	.72	.002397	.237803	4.92
1450	1.4	0	-106.8 ±-202.5	103	27.84	.003495	.001509	6.62

TOTAL GAS AGE = 5.6 ± .2 Ma

MEAN AGE(700øC-1200øC)= 5.7 ± .2 Ma (2σ UNCERTAINTY, INCLUDING ERROR IN J)

J = .00232 ± .0000232 ( 1 %)

37/39,36/40 AND 39/40 Ar RATIOS ARE CORRECTED FOR MASS SPECTROMETER DISCRIMINATION, INTERFERING ISOTOPES AND SYSTEM BLANKS

% IIC - INTERFERING ISOTOPES CORRECTION

□

96GA01 BIOTITE ARGON SUMMARY

T°C	mV 39	ε 39	AGE (Ma)±1σ	ε ATM	37/39	36/40	39/40	ε
IIC								
AA								
Å								
550	3.9	.3	32.7 ± 20.6	92	.07	.003107	.010591	.08
600	12.2	1	17.9 ± 9.1	94.4	.01	.003193	.013627	.03
650	30.1	2.5	11.6 ± 4	93.6	.02	.003168	.023884	.07
700	49.2	4.2	6.8 ± 2.2	92.7	.11	.003134	.04707	.57
750	49.3	4.2	6.6 ± 1.8	92	.02	.003113	.052252	.13
800	48.1	4.1	9.7 ± 2.6	92.9	0	.003144	.03196	.02
850	81.2	6.9	7.3 ± 1.6	91.6	.03	.003099	.04999	.15
900	88	7.5	6.3 ± .8	79.5	.03	.002686	.142186	.16
950	170.6	14.6	5 ± .4	74.4	.01	.002514	.224959	.12
1000	263.8	22.6	4.1 ± .2	51.6	.02	.001742	.517498	.21
1050	213.1	18.3	4.2 ± .1	29.5	.07	.000997	.737535	.59
1100	143.1	12.3	4.4 ± .2	24.9	.01	.00084	.738192	.12
1150	8.7	.7	12.9 ± 1.3	24.5	.28	.000818	.251538	.73
1200	1.3	.1	60.6 ± 24.6	64.4	2.32	.002145	.025223	1.39
1450	.7	0	206.6 ± 163	87.9	2.27	.002965	.002438	.49
AA								
Å								

TOTAL GAS AGE = 5.8 ± .6 Ma

MEAN AGE(1000°C-1100°C) = 4.2 ± .2 Ma (2σ UNCERTAINTY, INCLUDING ERROR IN J)

J = .002438 ± .000017 ( .6 %)

37/39, 36/40 AND 39/40 Ar RATIOS ARE CORRECTED FOR MASS SPECTROMETER DISCRIMINATION, INTERFERING ISOTOPES AND SYSTEM BLANKS

ε IIC - INTERFERING ISOTOPES CORRECTION

□



96GA03 BIOTITE ARGON SUMMARY

TøC	mV 39	% 39	AGE (Ma)±1å	% ATM	37/39	36/40	39/40	% IIC
600	12.1	1.3	9.6 ± 6.3	95.5	.21	.003231	.020206	.74
700	56.8	6.5	6.7 ± 2.2	94.6	.31	.003203	.034677	1.55
750	38.2	4.4	5.1 ± 1.9	94.2	.26	.003186	.049883	1.74
800	42.7	4.9	6.9 ± 2	92.9	.26	.003144	.044537	1.24
850	65.8	7.5	9.2 ± 1.6	90.3	.16	.003054	.046354	.59
900	60.8	7	8.9 ± .8	71.4	.12	.002415	.140129	.45
950	99.3	11.4	4.4 ± .5	74.6	.1	.002524	.249257	.76
1000	187.4	21.5	3.9 ± .2	49.4	.07	.001672	.564888	.64
1050	176.8	20.3	3.8 ± .2	40.6	.36	.001384	.685682	3.18
1100	103.9	11.9	3.5 ± .3	58.1	.39	.00197	.526781	3.75
1150	18	2	5 ± 1.8	79.5	1.19	.00269	.176981	7.78
1200	3	.3	5.5 ± 14.6	96.1	5.33	.003246	.030504	32.26
1450	2.9	.3	13.4 ± 34.5	97.9	6.78	.003311	.006756	17.01

**TOTAL GAS AGE = 5.2 ± .6 Ma**

MEAN AGE(1000øC-1100øC)= 3.8 ± .2 Ma (2å UNCERTAINTY, INCLUDING ERROR IN J)

J = .002434 ± .000017 ( .6 %)

37/39,36/40 AND 39/40 Ar RATIOS ARE CORRECTED FOR MASS SPECTROMETER DISCRIMINATION, INTERFERING ISOTOPES AND SYSTEM BLANKS

% IIC - INTERFERING ISOTOPES CORRECTION

□

95GA04 BIOTITE ARGON SUMMARY

TøC	mV 39	% 39	AGE (Ma)±1σ	% ATM	37/39	36/40	39/40	% IIC
550	2.4	.2	14.4 ± 13.8	89.3	.49	.00299	.032244	1.15
600	13.4	1.1	4.5 ± 2.9	93	.2	.003137	.06677	1.45
650	30.1	2.5	6.1 ± 1.5	88.2	.12	.00298	.084613	.65
700	52.7	4.5	5.6 ± .8	82.5	.11	.002786	.136143	.69
750	59.2	5	5.9 ± .7	79.7	.06	.002694	.149934	.36
800	54.6	4.6	6.3 ± 1.3	89.8	.11	.003038	.070011	.58
850	81.8	7	6.2 ± .7	83.2	.06	.002813	.118801	.35
900	80.7	6.9	4.9 ± .4	67.7	.07	.002286	.285148	.52
950	136.4	11.6	4.6 ± .2	53.6	.05	.001811	.437423	.38
1000	275.4	23.5	4 ± .1	33.2	.04	.001124	.718569	.35
1050	235.7	20.1	4.1 ± .1	28.8	.18	.000978	.750052	1.45
1100	131	11.2	4.3 ± .1	27	.08	.000914	.739727	.61
1200	10.3	.8	3.6 ± 2.7	87.1	1.2	.00292	.15493	11.08
1450	4.2	.3	23 ± 14.5	92.3	1.07	.003117	.014502	1.59

**TOTAL GAS AGE = 4.8 ± .2 Ma**

MEAN AGE(950øC-1050øC)= 4.2 ± .1 Ma (2σ UNCERTAINTY, INCLUDING ERROR IN J)

J = .002432 ± .000017 ( .6 %)

37/39,36/40 AND 39/40 Ar RATIOS ARE CORRECTED FOR MASS SPECTROMETER DISCRIMINATION, INTERFERING ISOTOPES AND SYSTEM BLANKS

% IIC - INTERFERING ISOTOPES CORRECTION  
□

95GA17 MUSCOVITE ARGON SUMMARY

T°C	mV 39	± 39	AGE (Ma) ± 1σ	% ATM	37/39	36/40	39/40	% IIC
600	11	21.8	15.1 ± 4.5	78.7	1.71	.002657	.061747	3.82
700	15	29.7	15.9 ± 3	67.1	1.59	.00227	.090155	3.37
750	4.8	9.5	3 ± 4.8	87.7	.87	.00292	.175907	9.5
800	2.4	4.8	9.9 ± 12	82.9	1.65	.002766	.07436	5.55
850	2.9	5.8	-2.5 ± 8.9	106	1.96	.003551	.122357	26.36
900	2.4	4.9	12.7 ± 6.9	62.3	1.28	.002068	.127723	3.39
950	2.6	5.2	24.6 ± 9.2	55.2	1.87	.001852	.078697	2.61
1000	2.7	5.4	50.5 ± 5.2	12	2.63	.00044	.074789	1.86
1050	2.2	4.5	95.2 ± 13.7	28.4	7.01	.000984	.032085	2.81
1100	1	2.1	220.2 ± 42	26	12.91	.000899	.013888	2.65
1150	1.3	2.5	329.1 ± 51.9	26.6	39.17	.000931	.009008	6.12
1200	.4	.9	391.9 ± 107	26.9	51.7	.000956	.007435	7.25
1450	1.1	2.3	97.2 ± 254	94.2	13.33	.003184	.002561	5.26

**TOTAL GAS AGE = 40.7 ± 14.4 Ma**

J = .002433 ± 1.7031E-05 ( .7 %)

37/39,36/40 AND 39/40 Ar RATIOS ARE CORRECTED FOR MASS SPECTROMETER DISCRIMINATION, INTERFERING ISOTOPES AND SYSTEM BLANKS

% IIC - INTERFERING ISOTOPES CORRECTION

□

## 95GA19 POLISHED SLAB ARGON SUMMARY

SPOT#	CODE#	mV	39	AGE (Ma) ± 2σ	J	ATM	37/39	36/40	39/40	IIC
AA										
1	Y7-2	2		7.4 ± 6.4	75.1	.38	.002541	.011933	.16	
2	Y7-3	1.9		4.9 ± 4.7	74.8	.34	.00253	.018112	.2	
3	Y7-4	3.7		4.7 ± 1.9	63	.23	.00213	.028076	.14	
4	Y7-6	21.3		4.6 ± .3	43.7	.06	.00148	.042928	.04	
5	Y7-7	20.1		4.2 ± .7	74.6	.13	.002525	.021457	.09	
6	Y8-1	19.2		4 ± .5	63.1	.01	.002136	.032585	.01	
7	Y8-2	11.12		4.9 ± .9	67.2	.01	.002273	.023852	0	
8	Y8-3	10.5		4.4 ± .9	68.8	.01	.002327	.025172	0	
9	Y10-1	5.4		5.9 ± 7.1	91.4	.17	.003093	.00515	.08	
10	Y10-2	2.9		4.2 ± 5.2	85.4	.42	.002891	.012108	.29	
11	Y9-1	1.3		13.9 ± 64.2	93.9	2.34	.003179	.001546	.6	
12	Y9-2	9.5		5.3 ± 1.8	79.6	.21	.002696	.01361	.11	
AA										

**MEAN AGE (SPOT 4 - SPOT 8) = 4.4 ± .3 Ma**

UNCERTAINTIES AT 2σ LEVEL INCLUDING ERROR IN J

$J = .000197 \pm 9E-06$  ( 4.6 %)

37/39, 36/40 AND 39/40 Ar RATIOS ARE CORRECTED FOR MASS SPECTROMETER  
DISCRIMINATION, INTERFERING ISOTOPES AND SYSTEM BLANKS

% IIC - INTERFERING ISOTOPES CORRECTION

96-GA-26 MUSCOVITE ARGON SUMMARY

TøC	mV 39	± 39	AGE (Ma)±1å	± ATM	37/39	36/40	39/40	±
IIC								
AA								
Å								
550	2.4	.1	7.8 ± 6.2	76.9	0	.002385	.111454	0
600	5.6	.3	8.6 ± 1.7	44.8	.11	.001571	.272863	.44
650	14	.7	7.3 ± 1.2	44.7	0	.001536	.318981	.02
675	17.2	.9	6.9 ± 1.1	44.8	.03	.001538	.338126	.18
700	21.7	1.2	5.1 ± 1.5	66.2	.03	.002259	.278627	.2
725	31.8	1.7	5.9 ± 1	52.4	.02	.001786	.335482	.11
750	43	2.3	5.6 ± .7	48.6	.01	.001658	.384821	.08
775	67.2	3.7	5.8 ± .7	61.9	0	.002101	.273282	.01
800	242.4	13.4	6.2 ± .2	51.5	0	.001745	.324493	.01
825	323.1	17.8	6.3 ± .1	25.6	0	.000869	.489688	0
850	223.4	12.3	6.3 ± .1	18.5	0	.000627	.535572	0
900	275.6	15.2	6.3 ± .1	25	0	.000848	.496512	0
950	158.7	8.7	6.2 ± .3	37.3	0	.001266	.421508	0
1000	92.6	5.1	6.1 ± .5	46.4	0	.001575	.362133	.04
1100	209	11.5	6.1 ± .3	43.5	0	.001474	.381153	.02
1200	74.3	4.1	5.9 ± .7	63	.01	.002139	.258096	.06
1450	5.9	.3	-64.8 ±-32.5	104	.23	.003525	.002732	.1
AA								
Å								

**TOTAL GAS AGE = 6.2 ± .2 Ma**

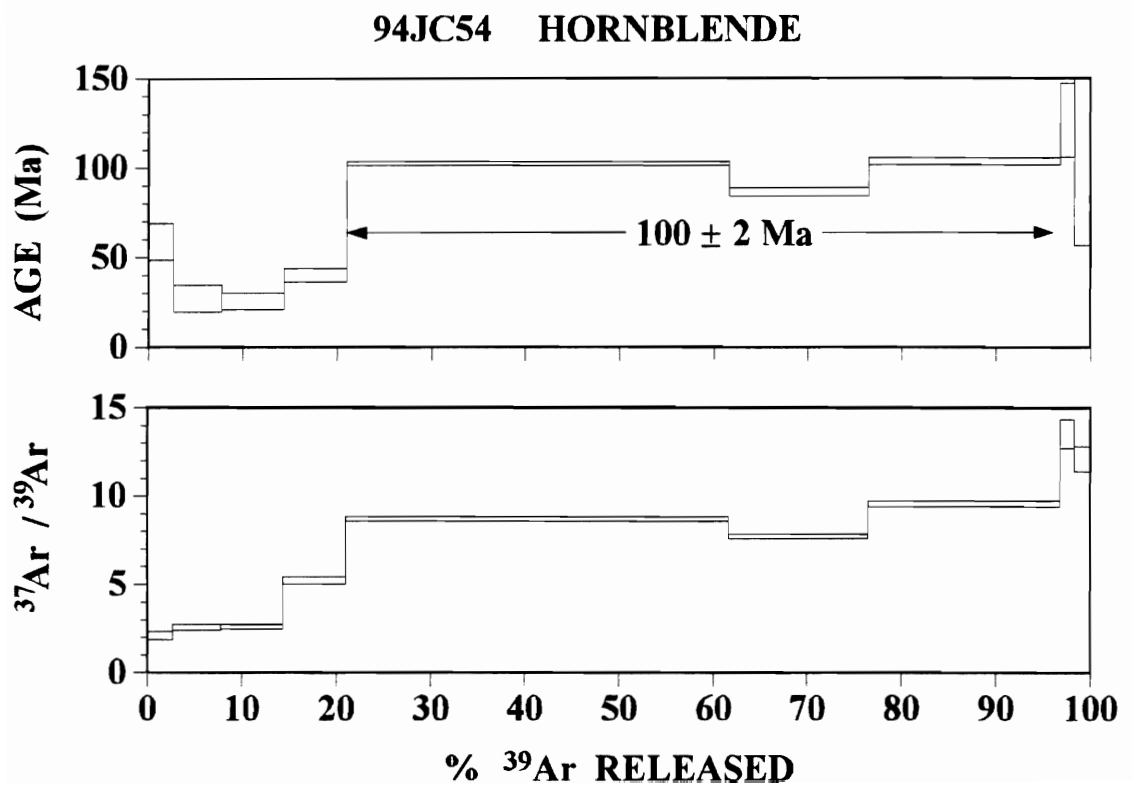
MEAN AGE(750øC-1100øC)= 6.2 ± .2 Ma (2å UNCERTAINTY, INCLUDING ERROR IN J)

J = .00232 ± .0000232 ( 1 %)

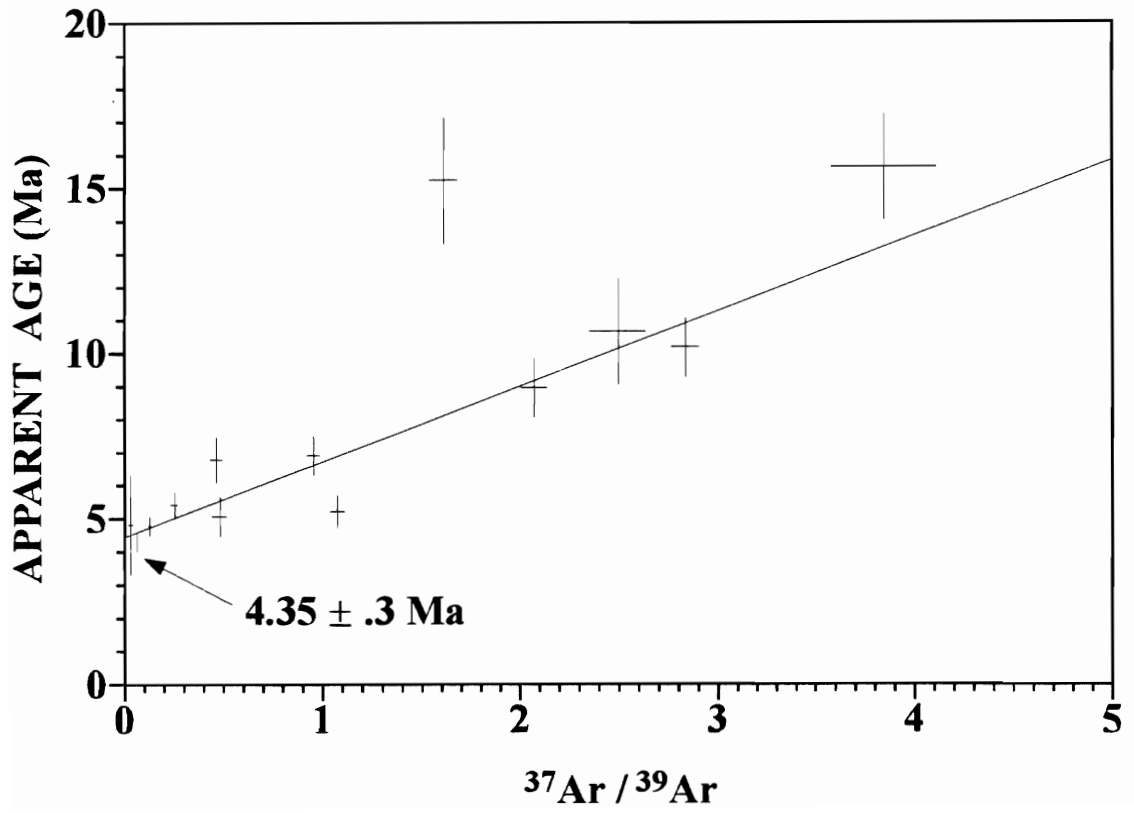
37/39,36/40 AND 39/40 Ar RATIOS ARE CORRECTED FOR MASS SPECTROMETER DISCRIMINATION, INTERFERING ISOTOPES AND SYSTEM BLANKS

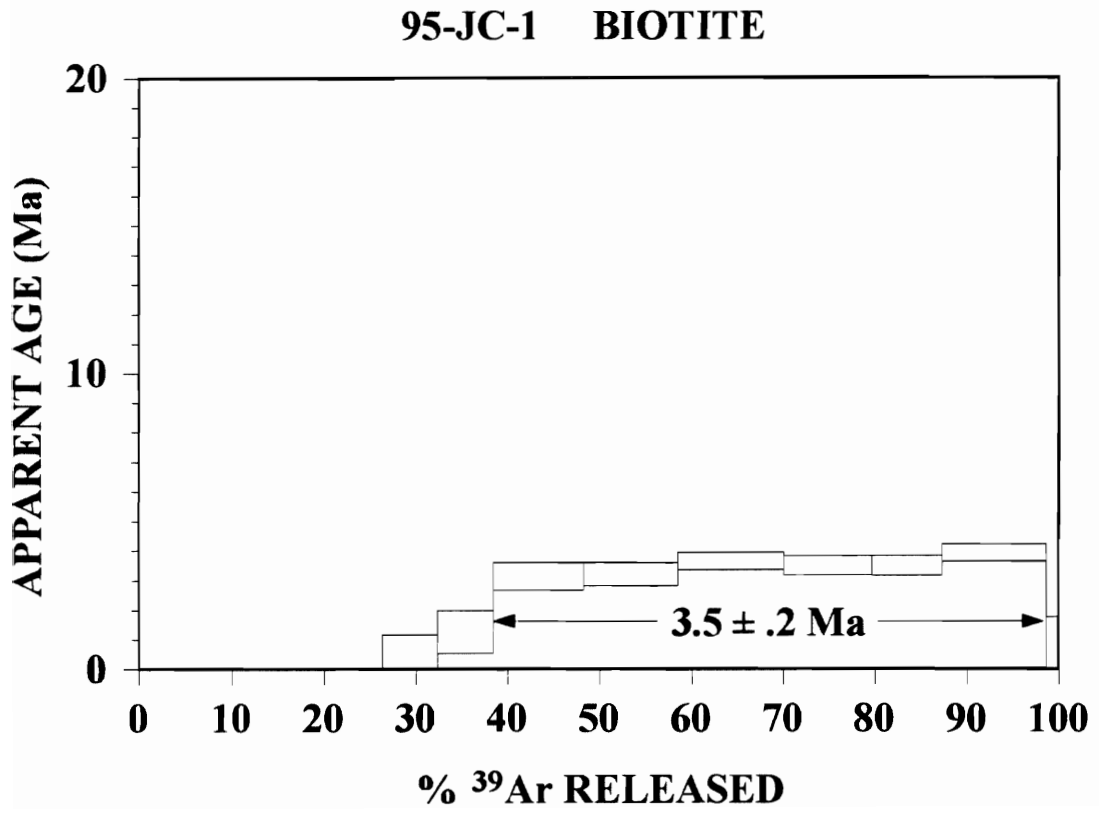
± IIC - INTERFERING ISOTOPES CORRECTION

□



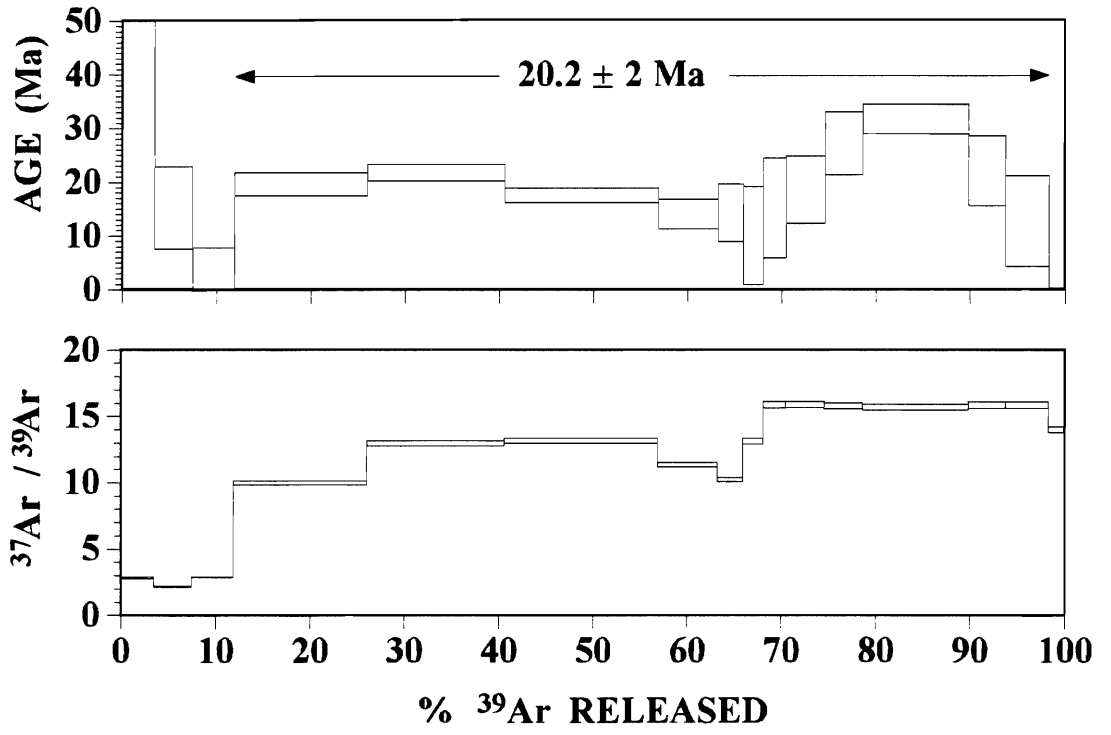
### 94JC13 LASER SPOTS

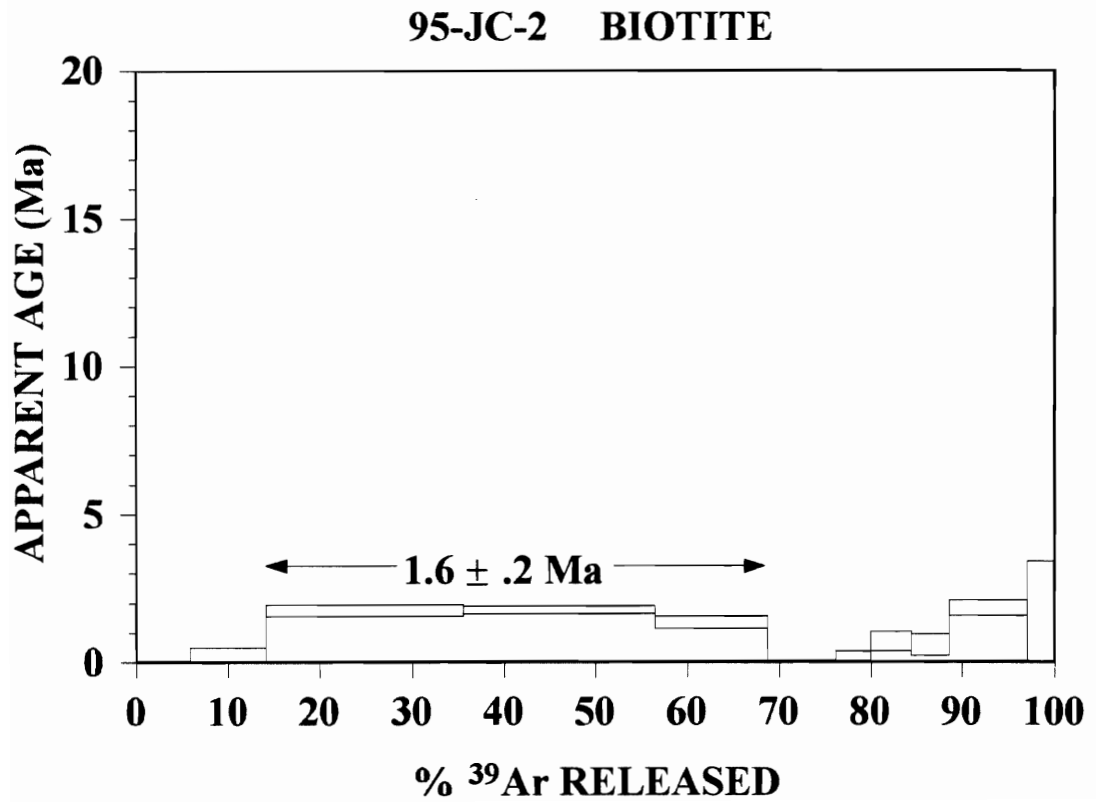


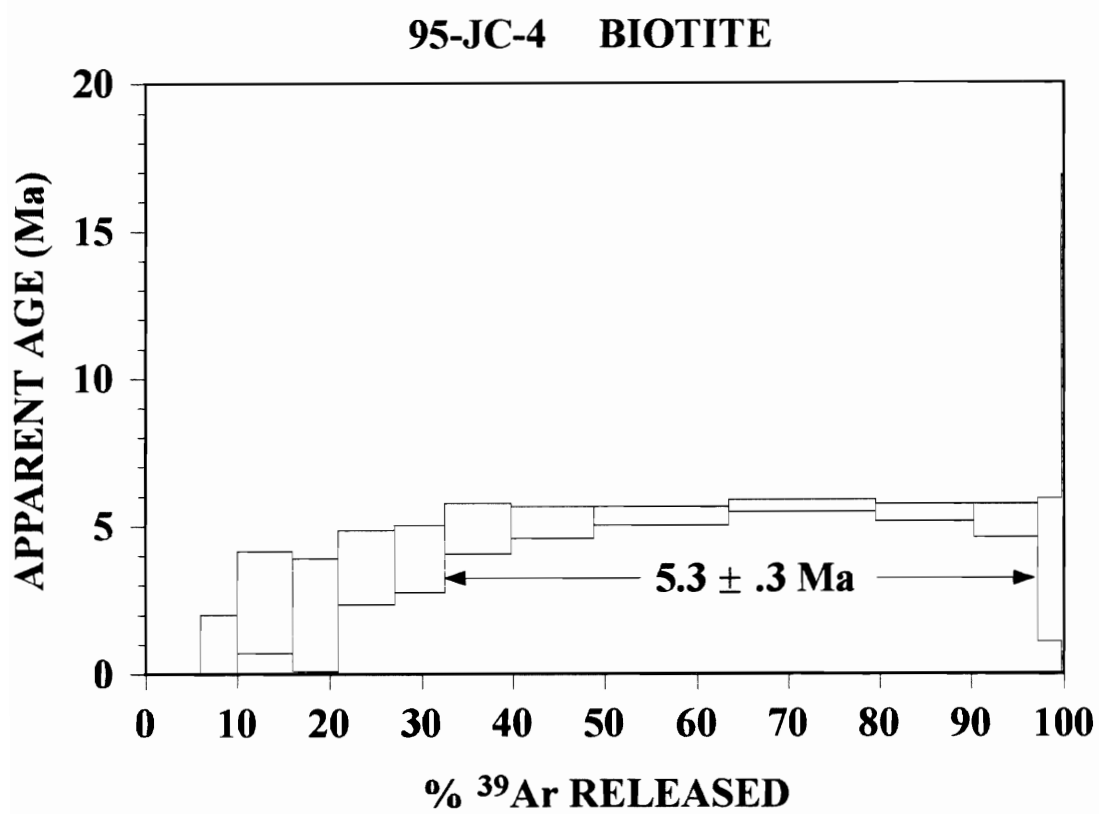


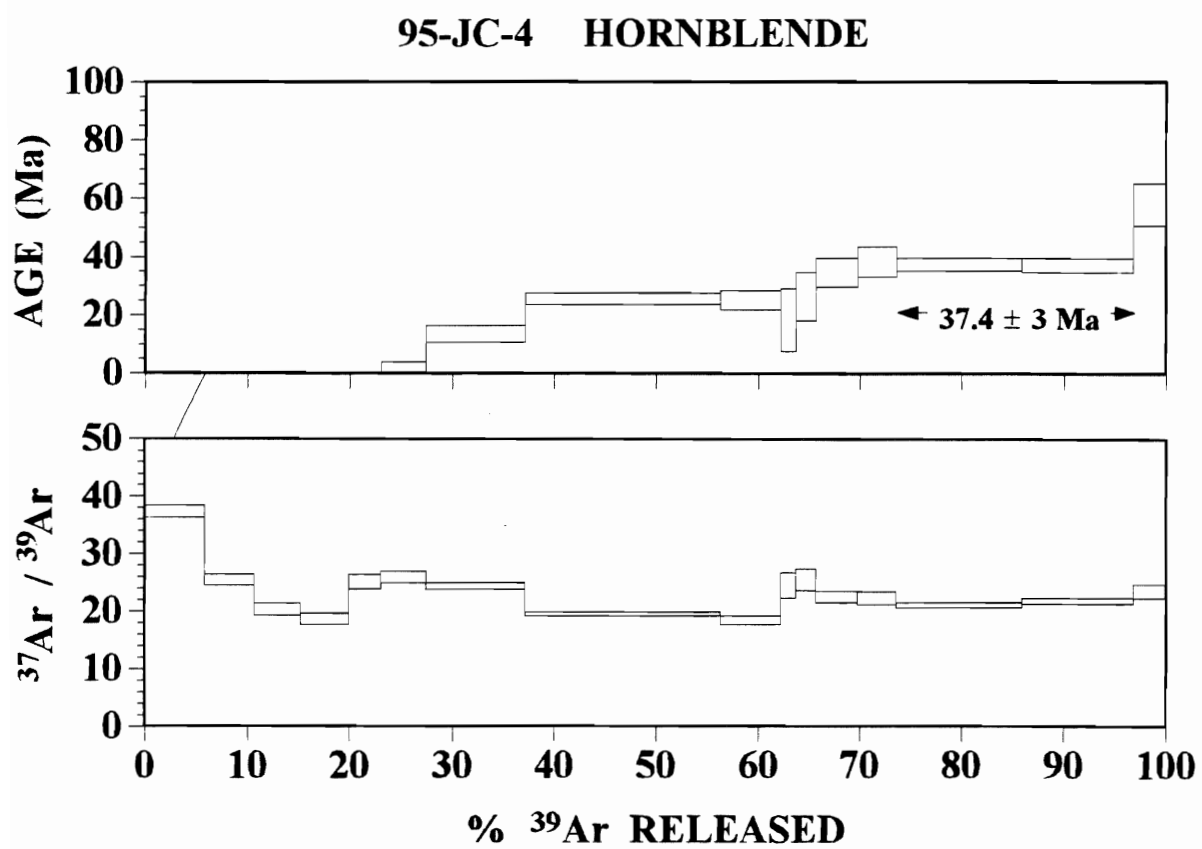


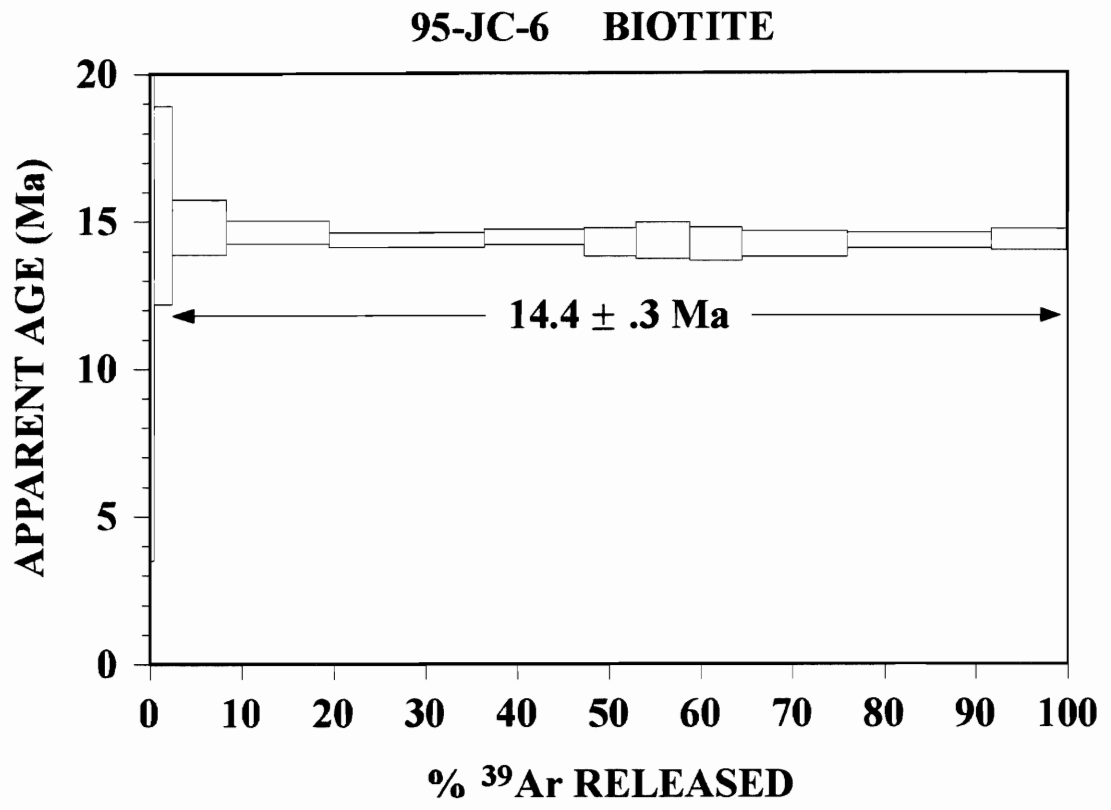
95-JC-1 HORNBLLENDE



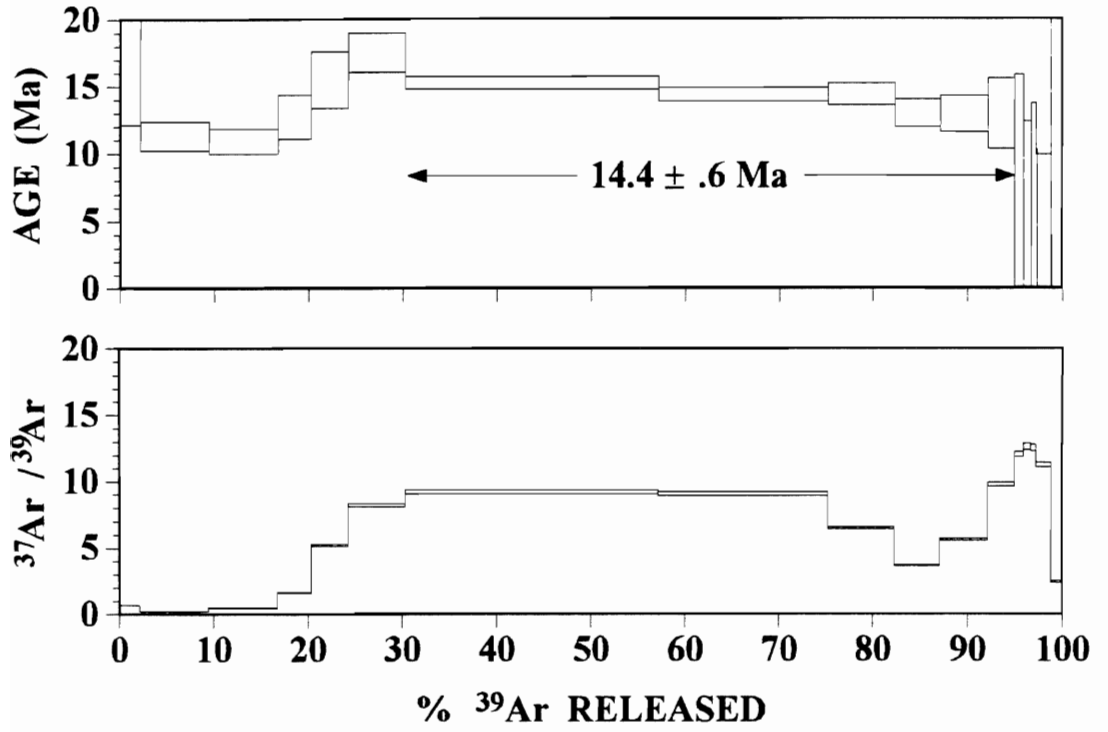




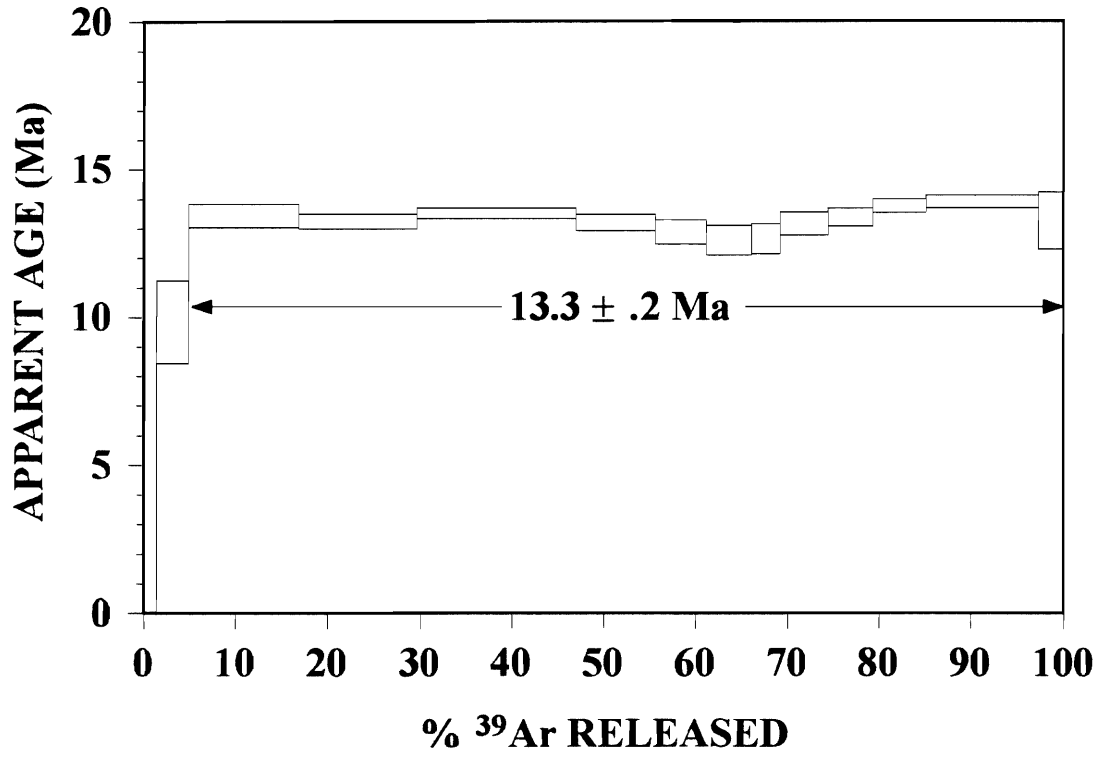




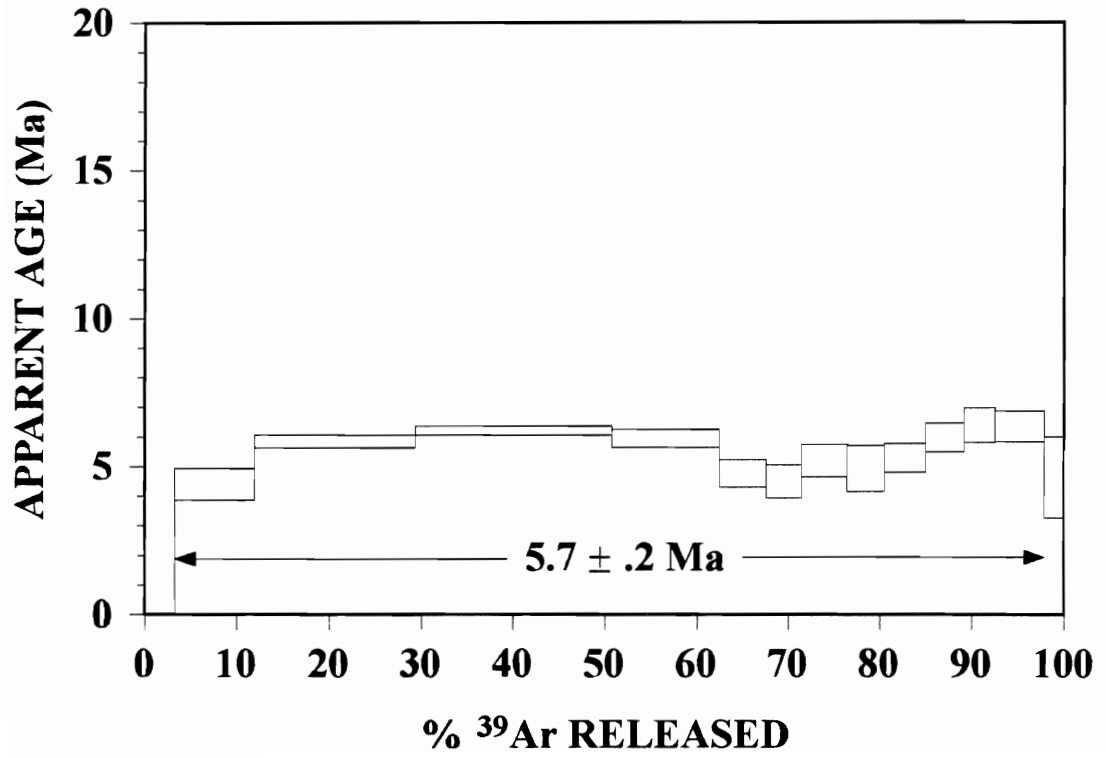
95-JC-6 HORNBLLENDE



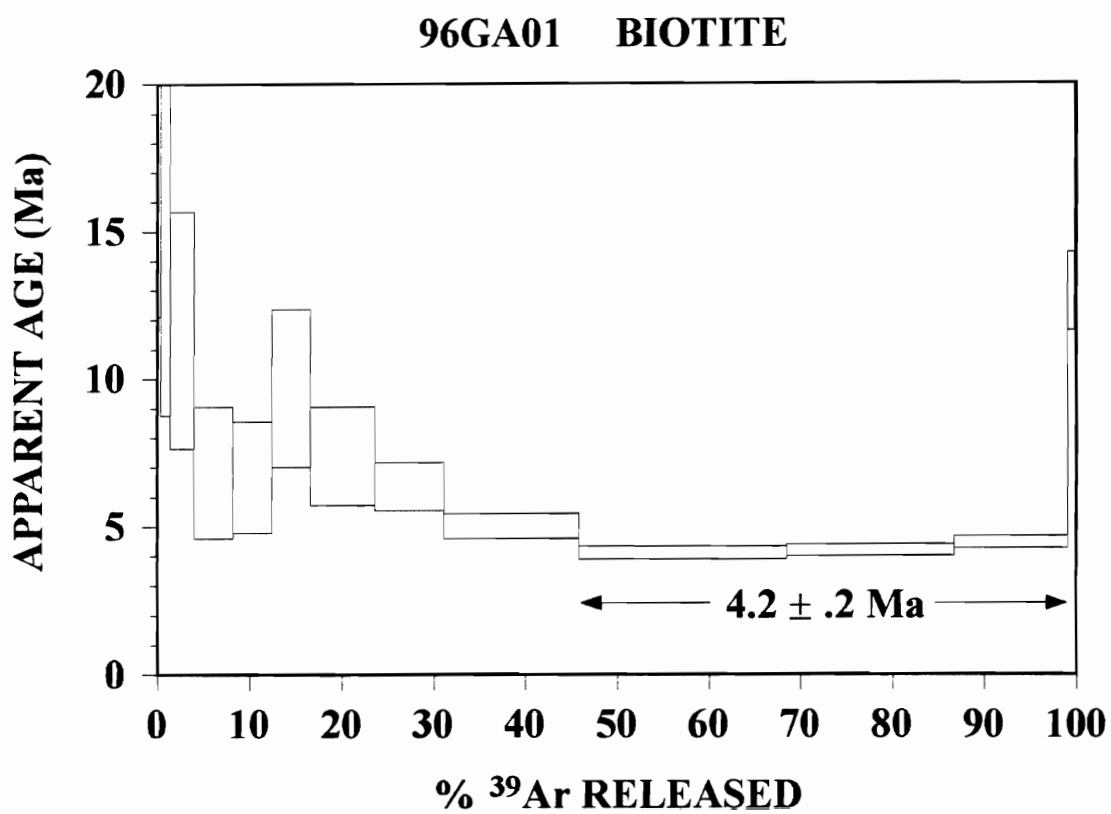
**95-JC-12 BIOTITE**

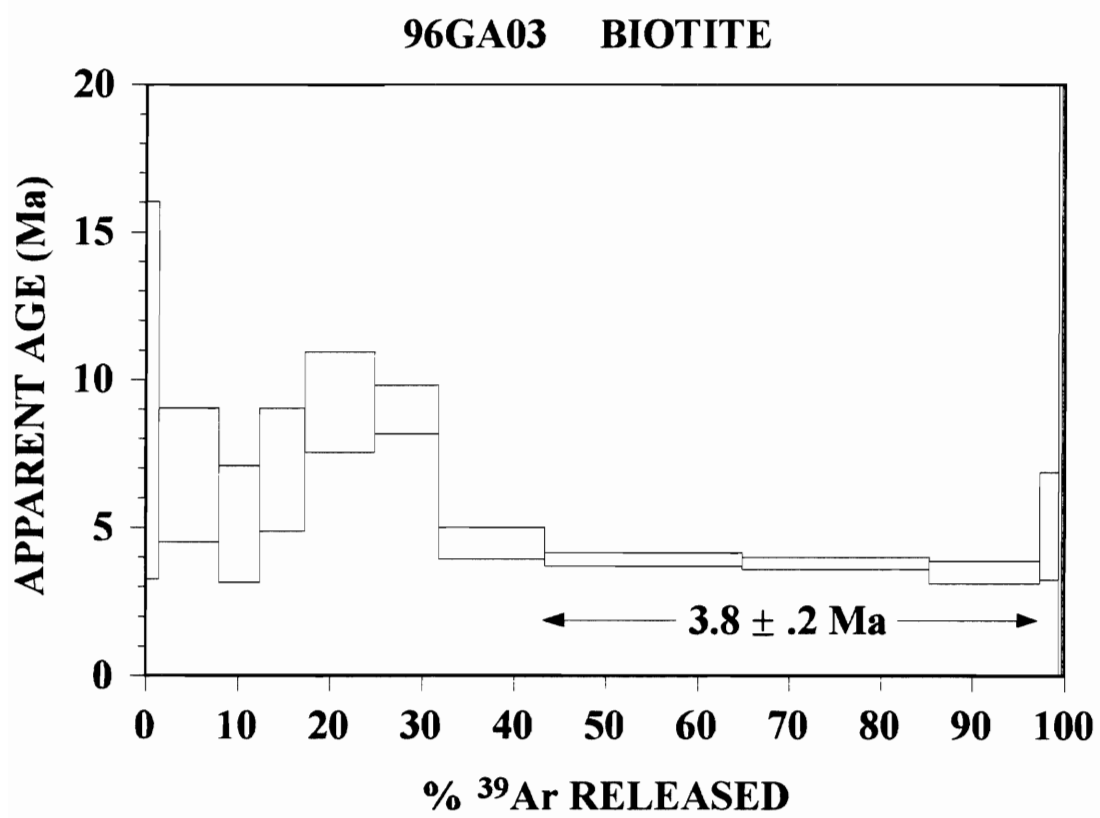


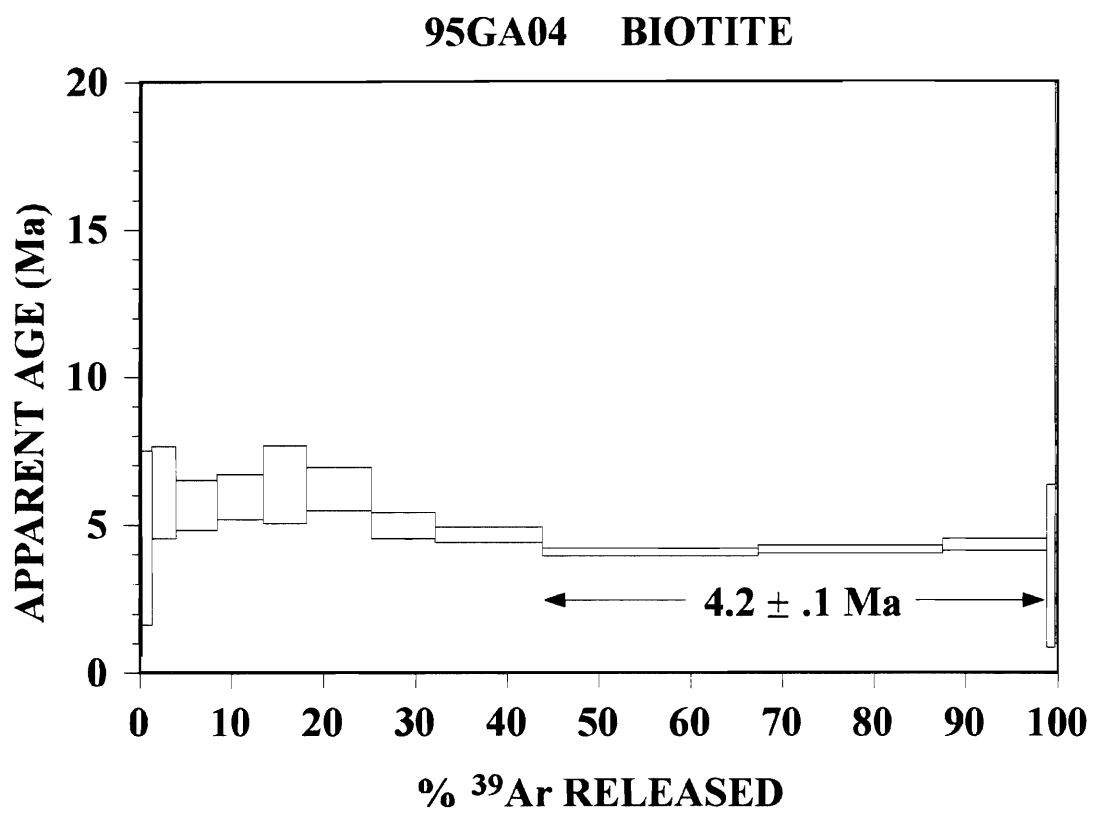
**95-JC-14 BIOTITE**



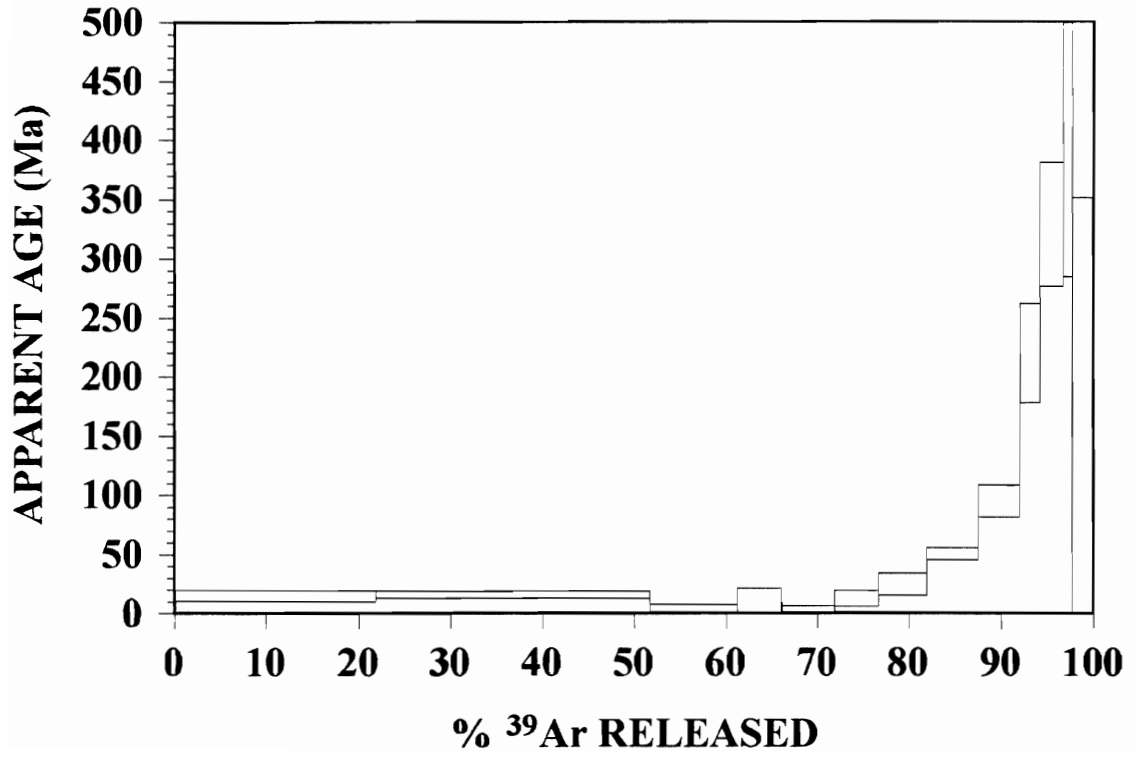


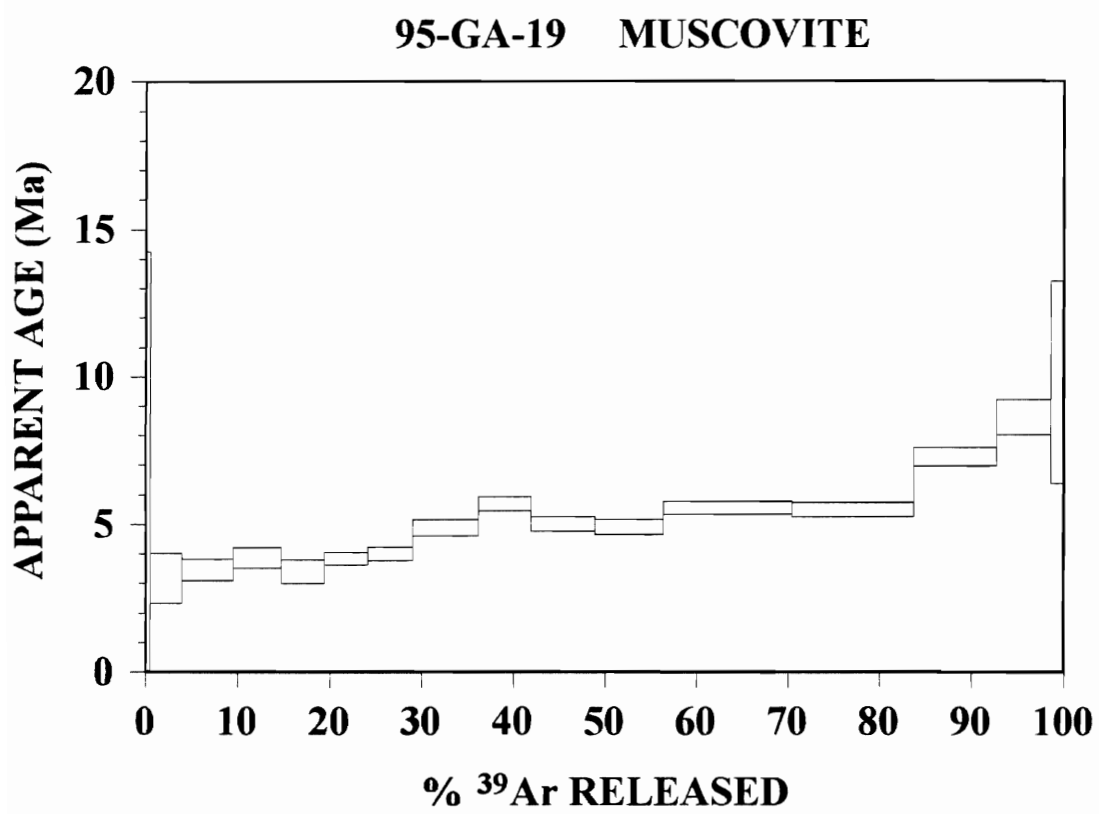


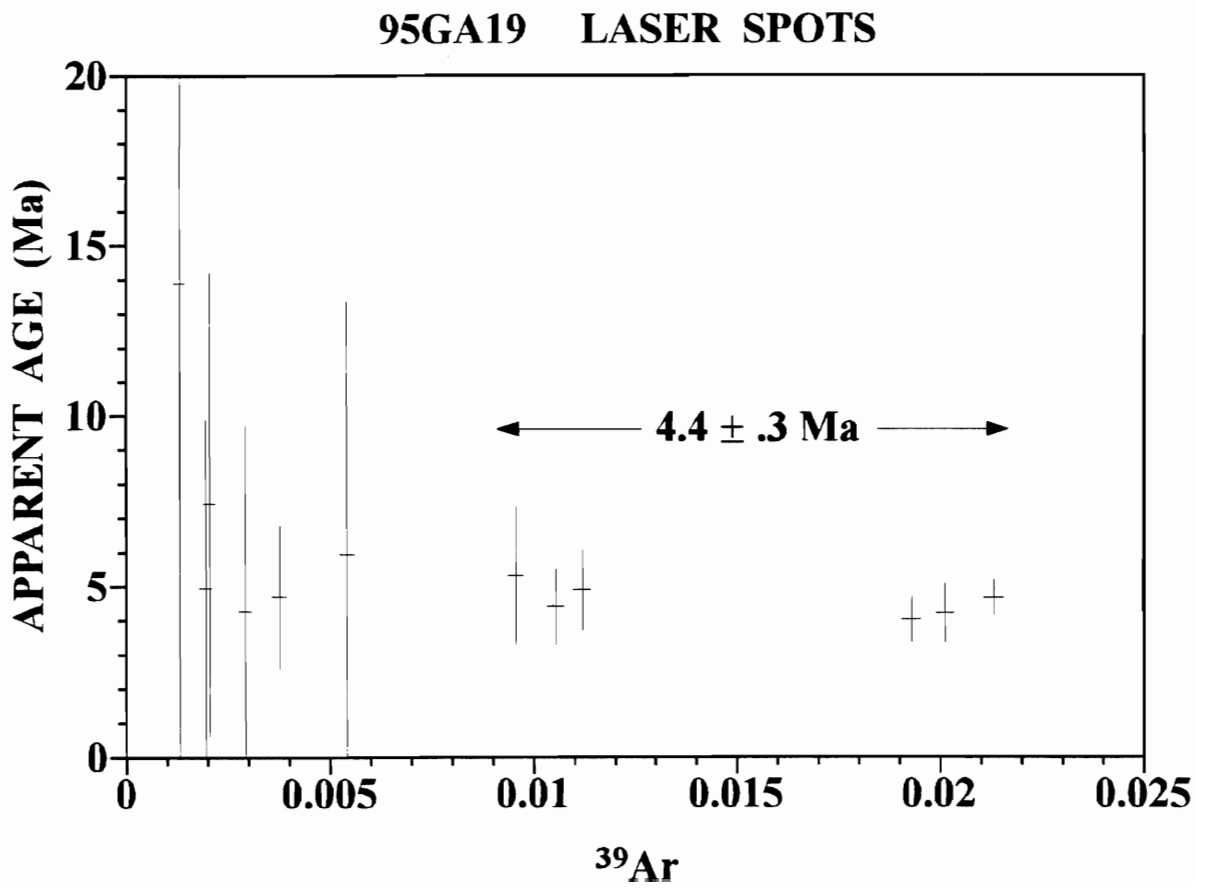


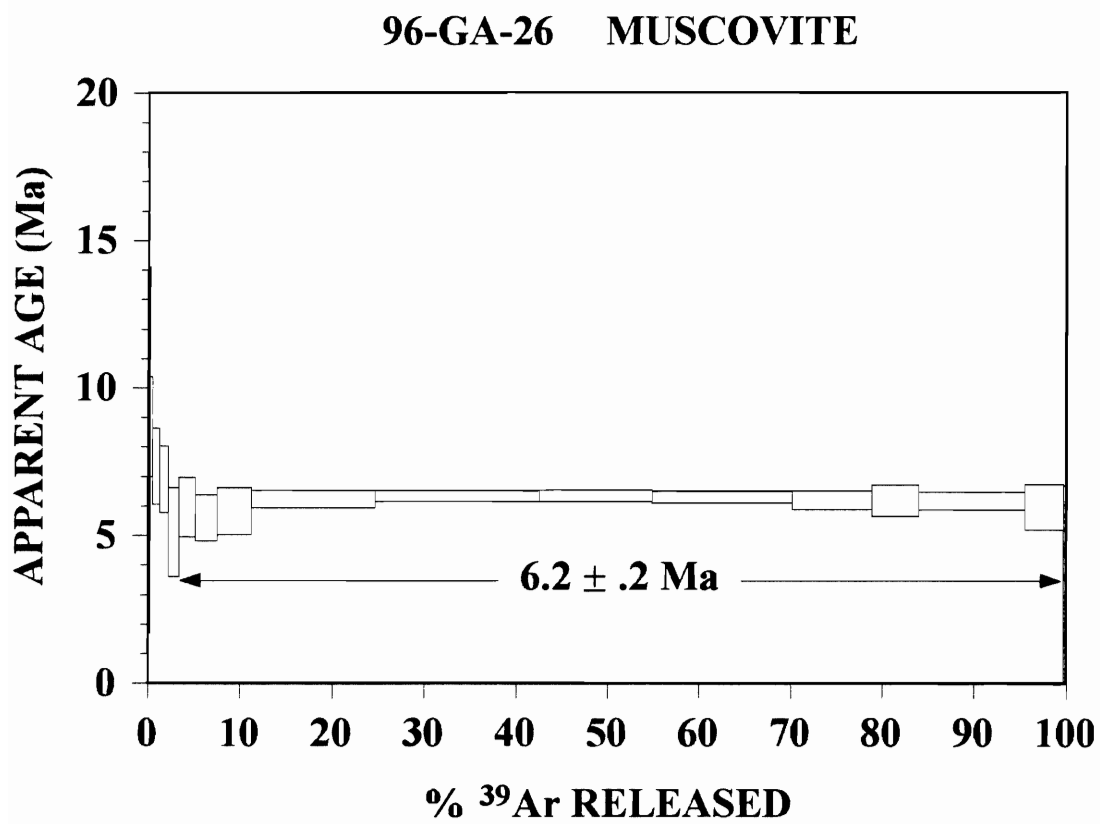


**95GA17 MUSCOVITE**









## **REFERENCES**



**REFERENCES**

- Barrientos, S.E. and Ward, S.N. 1990. The 1960 Chile earthquake: inversion for slip distribution from surface deformation. *Geophysical Journal International*, **103**: 589-598.
- Barrientos, S.E. and Acevedo, P. 1992. Seismological aspects of the 1988-1989 Lonquimay (Chile) volcanic eruption. *Journal of Volcanology and Geothermal Research*, **53**: 73-87.
- Bartholomew, D.S. 1984. Geology and geochemistry of the Patagonian Batholith (45°-46°S), Chile. Unpublished PhD thesis, Leicester University, United Kingdom. 196 p.
- Bartholomew, D.S. and Tarney, J. 1984. Crustal extension in the southern Andes (45°-46° S). *In* B.P. Kokelaar, M.F. Howells and R.A. Roach (editors). *Volcanic processes in marginal basins*. Special Publication, Geological Society of London, 195-205.
- Beck, M. 1983. On the mechanism of tectonic transport in zones of oblique subduction. *Tectonophysics*, **93**: 1-11.
- Beck, M.E. 1988. Analysis of Late Jurassic-Recent paleomagnetic data from active plate margins of South America. *Journal of South American Earth Sciences*, **1**: 39-52.
- Beck, M.E. 1991. Coastwise transport reconsidered: lateral displacements in oblique subduction zones, and tectonic consequences. *Physics of the Earth Planetary Interiors*, **68**: 1-8.
- Beck, M.E., Rojas, C. and Cembrano, J. 1993. On the nature of buttressing in margin-parallel strike-fault systems. *Geology*, **21**: 755-758.
- Behrmann, J.H., Lewis, S., Musgrave, R. and Shipboard Party, 1992. Proceedings of the Ocean Drilling Program, initial results, Volume 141: College Station, Texas, Ocean Drilling Program.
- Bell, T.H. 1981. Foliation development - the contribution, geometry and significance of progressive, bulk, inhomogeneous shortening. *Tectonophysics*, **75**: 273-296.
- Bell, T.H., Rubenach, M.J. and Fleming, P.D. 1986. Porphyroblast nucleation, growth and dissolution in regional metamorphic rocks as a function of deformation partitioning during foliation development. *Journal of Metamorphic Geology*, **4**: 37-67.

- Berthe, D., Choukroune, P. and Jegouzo, P. (1979). Ortogneiss, mylonite and non-coaxial deformation of granites: the example of the South Armorican shear zone. *Journal of Structural Geology*, **1**: 31-42.
- Bobenrieth, L., Díaz, F., Davidson, J., Portigliati, C. 1983. Mapa metalogénico XI región, Sector Norte Continental, comprendido entre 45° lat. S y el límite con la X región. Informe inédito 3931, SERNAGEOMIN.
- Bott, M.H.P. 1959. The mechanisms of oblique slip faulting. *Geological Magazine*, **96**: 109-117.
- Boullier, A.-M. and Bouchez, J.-L. 1978. Le quartz en rubans dans les mylonites. *Société géologique de France, Bulletin*, **7**: 253-262.
- Bourgois, J., Martin, H., Lagabrielle, Y., Le Moigne, J. and Frutos Jara, J. 1996. Subduction erosion related to spreading-ridge subduction: Taitao peninsula (Chile margin triple junction area). *Geology*, **24**: 723-726.
- Braun, J. and Beaumont, C. 1995. Three-dimensional numerical experiments of strain partitioning at oblique plate boundaries: Implications for contrasting tectonic styles in the southern Coast Ranges, California, and central South Island, New Zeland. *Journal of Geophysical Research*, **100**: 18,059-18,074.
- Brown, M., Díaz, F. and Grocott, J. 1993. Displacement history of the Atacama fault system, 25°00'S-27°00'S, northern Chile. *Geological Society of America Bulletin*, **105**: 1165-1174.
- Busby-Spera, C.J., and Saleeby, J.B. 1990. Intra-arc strike-slip fault exposed at batholithic levels in the southern Sierra Nevada, California. *Geology*, **18**: 255-259.
- Cande, S.C. and Leslie, R.B. 1986. Late Cenozoic tectonics of the Southern Chile Trench. *Journal of Geophysical Research*, **91**: 471-496.
- Carey, E.. 1979. Recherche des directions principales de contraintes associées au jeu d'une population de failles. *Revue de Géographie Physique et Géologie Dynamique*, **21**(1):57-66.
- Carey, E. and Brunier, B. 1974. Analyse théorique d'un modèle mécanique élémentaire appliqué à l'étude d'une population de failles. *Comptes Rendus de l'Académie des Sciences, Paris*, **279**: 891-894.
- Carrasco, V. 1995. Geología y geoquímica del Batolito Norpatagónico y rocas volcánicas asociadas a la zona de falla Liquiñe-Ofqui (41°05'-41°40'L.S.), X Región. Unpublished thesis,. Departamento de Geología, Univ. de Chile, Santiago.

- Cembrano, J. 1990. Geología del Batolito Norpatagónico y de las rocas metamórficas de su margen occidental: 41°50'S-42°10'S. Unpublished thesis,. Departamento de Geología, Universidad de Chile, Santiago.
- Cembrano, J. 1992. Geologic and paleomagnetic reconnaissance of the Liquine-Ofqui fault zone in the province of Palena, Chile (42°-44°S). Master's thesis, Bellingham, Western Washington University.
- Cembrano, J., Beck, M.E., Burmester, R.F., Rojas, C., García, A. and Hervé, F. 1992. Paleomagnetism of Lower Cretaceous rocks from east of the Liquiñe-Ofqui fault zone, southern Chile: evidence of small in-situ clockwise rotations. *Earth and Planet. Science Letters*, **113**: 539-551.
- Cembrano, J. and Hervé, F. 1993. The Liquiñe-Ofqui fault zone: a major Cenozoic strike slip duplex in the Southern Andes. *Proceedings Second Symposium International "Géodynamique Andine"*, Oxford (UK), pp. 175-178. ORSTOM editions.
- Cembrano, J. and Moreno, H., 1994. Geometria y naturaleza contrastante del volcanismo cuaternario entre los 38° y 46°S, Dominios compresionales y tensionales en un regimen transcurrente?. In *Septimo Congreso Geologico Chileno*, **1**: 240-244.
- Cembrano, J., Hervé, F. and Lavenu, A. 1996. The Liquine-Ofqui fault zone : a long-lived intra-arc fault system in southern Chile. *Tectonophysics*, **259** (special issue on Andean Geodynamics):55-66.
- Cembrano, J., Lavenu, A., Arancibia, G., Sanhueza, A. and Reynolds, P. 1998. Coeval transpressional and transtensional magmatic arc tectonics in the southern Andes. *Proceedings Simposio Final Proyecto IGCP 345, Evolucion Litosferica de los Andes*, vol III, pp. 1613-1616.
- Chinn, D.S. and Isacks, B.L. 1983. Accurate source depths and focal mechanisms of shallow earthquakes in western South America and in the New Hebrides island arc. *Tectonics*, **2**:529-563.
- Choukroune, P., Gapais, D. and Merle, O. 1987. Shear criteria and structural symmetry. *Journal of Structural Geology*, **9**:525-530.
- Cifuentes, I.L. 1989. The 1960 Chilean Earthquakes. *Journal of Geophysical Research*, **94**, B1, pp. 665-680.
- Curtis, M.L. Development of kinematic partitioning within a pure-shear dominated dextral transpression zone: the southern Ellsworth Mountains, Antarctica. *In*: Holdsworth, R.E., Strachan, R.A. and Dewey, J.F. (eds.) 1998. *Continental Transpressional and Transtensional Tectonics*. Geological Society, London, Special Publication, **135**:289-306.

- De Saint Blanquat, M., Tikoff, B., Teyssier, C and Vigneresse, J.L. 1998. Transpressional kinematics and magmatic arcs. *In: Holdsworth, R.E., Strachan, R.A. and Dewey, J.F. (eds) Continental transpressional and transtensional tectonics. Geological Society of London Special Publication 135: 327-340.*
- Dewey, J.F. 1980. Episodicity, sequence, and style at convergent plate boundaries. *Geological Association Canadian, Special Paper, 20:553-573.*
- Dewey, J.F. and Lamb, S.H. 1992. Active tectonics of the Andes. *Tectonophysics, 205: 79-95.*
- Dewey, J.F., Holdsworth, R.E. and R.A. Strachan. 1998. Transpression and transtension zones. *In: Holdsworth, R.E., Strachan, R.A. and Dewey, J.F. (eds.) 1998. Continental Transpressional and Transtensional Tectonics. Geological Society, London, Special Publication, 135:1-14.*
- Dodson, M.H. 1973. Closure temperatures in cooling geochronological and Petrological systems. *Contributions to mineralogy and Petrology 40: 259-274.*
- Dodson, M.H., 1976. Kinetic processes and thermal history of slowly cooling solids. *Nature 259: 551-553.*
- Drake, R., Hervé, F., Munizaga, F. and Pankhurst, R. 1990. Radioisotopic ages of the North Patagonian batholith and their relation to the Liquiñe-Ofqui Fault Zone, Chile (40°-42°S Lat.), ICOG-7, Canberra, Geological Society of Australia Abs. pp. 27-29.
- Drake, R., Hervé, F., Munizaga, F. and Beck, M. 1991. Magmatism and the Liquiñe-Ofqui Fault Zone, Chile Sur (40°-46°S. Lat.). *Comunicaciones, 42:69-74, Departamento de Geología, Universidad de Chile, Santiago, Chile.*
- Dunlap, J.W., Teyssier, C., McDougall, I. and Baldwin, S. 1991. Ages of deformation from K/Ar and  $^{40}\text{Ar}/^{39}\text{Ar}$  dating of white micas. *Geology, 19:1213-1216.*
- Ebert, H.D. and Hasui, Y. 1998. Transpressional tectonics and strain partitioning during oblique collision between three plates in the Precambrian of southeast Brazil. *In: Holdsworth, R.E., Strachan, R.A. and Dewey, J.F. (eds.) 1998. Continental Transpressional and Transtensional Tectonics. Geological Society, London, Special Publication, 135:231-252.*
- Fitch, T.J. 1972. Plate convergence, transcurrent faults, and internal deformation adjacent to southeast Asia and the western Pacific. *Journal of Geophysical Research, 77:4432-4460.*

- Fitz-Gerald, J.D. and Stunitz, H. 1993. Deformation of granitoids at low metamorphic grade. I. Reactions and grain size reduction. *Tectonophysics*, **221**:269-297.
- Flint, S.S., Prior, D.J., Agar, S.M. and Turner, P. 1994. Stratigraphic and structural evolution of the Tertiary Cosmelli Basin and its relationship to the Chile triple junction. *Journal of the Geological Society, London*, **151**:251-268.
- Forsythe, R.D. and Nelson, E. 1985. Geological manifestation of ridge collision: Evidence for the Golfo de Penas, Taitao basin, southern Chile. *Tectonics*, **4**:477-495.
- Fossen, H., Tikoff, B., and Teysier, C. 1994. Strain modelling of transpressional and transtensional deformation. *Norsk Geologisk Tidsskrift*, **74**:134-145.
- Fossen, H. and Tikoff, B. 1998. Extended models of transpression and transtension, and application to tectonic settings. *In: Holdsworth, R.E., Strachan, R.A. and Dewey, J.F. (eds.) 1998. Continental Transpressional and Transtensional Tectonics. Geological Society, London, Special Publication, 135*:15-33.
- Fuenzalida, R. and Echart, H., 1975. Geología del territorio de Aysen comprendido entre los 43 45 y los 45 latitud sur. Instituto de Investigaciones Geológicas, Santiago, Chile, 99p.
- García, A., Beck, M.E., Burmester, R.F., Hervé, F. and Munizaga, F. 1988. Paleomagnetic reconnaissance of the region de los Lagos, southern Chile, and its tectonic implications. *Revista Geológica de Chile*, **15**:13-30.
- Godoy, E., Davidson, J., Hervé, F., Mpodozis, C. and Kawashita, K. 1984. Deformación sobrepuesta y metamorfismo progresivo en un prisma de acreción paleozoico: Archipiélago de los Chonos, Aysén, Chile. *Actas IX Congr. Geológico Argentino, Bariloche*, **IV**:211-232.
- Harding, T.P. 1974. Petroleum traps associated with wrench faults. *Bulletin, American Association of Petroleum Geologists*, **58**: 1290-1304.
- Harland, W.B. 1971. Tectonic transpression in Caledonian Spitzbergen. *Geological Magazine* **108**, 27-42.
- Harrison, T.M. 1983. Some observations on the interpretation of  $^{40}\text{Ar}$ - $^{39}\text{Ar}$  spectra. *Isotopic Geoscience*, **1**, 319-338.
- Harrison, T.M., Duncan, I. and McDougall, I. 1985. Diffusion of  $^{40}\text{Ar}$  in biotite: Temperature, pressure and compositional effects. *Geochimica Cosmochimica Acta*, **49**:2461-2468.

- Herron, E.M., Cande, S.C. and Hall, B.R. 1981. An active spreading center collides with a subduction zone; a geophysical survey of the Chile margin triple junction. *Geological Society of America, Memoir*, **154**: 683-701.
- Hervé, F. 1988. Late Paleozoic subduction and accretion in southern Chile. *Episodes*, **11**:183-188.
- Hervé, F. 1994. The southern Andes between 39° and 44°S latitude: the geological signature of a transpressive tectonic regime related to a magmatic arc. *In*: K.-J. Reutter, E. Scheuber and P.J. Wigger (Editors), *Tectonics of the Southern Central Andes*, pp. 243-248.
- Hervé, F., Araya, E., Fuenzalida, J.L. and Solano, A. 1979. Edades radiométricas y tectónica neógena en el sector costero de Chiloé continental, X Región. II Congreso Geológico Chileno, *Actas*, **1**:F1-F8.
- Hervé, F., Moreno, H. and Parada, M.A. 1974. Granitoids of the Andean Range of Valdivia Province, Chile. *Pacific Geology*, **8**:39-45.
- Hervé, F. and Thiele, R. 1987. Estado de conocimiento de las megafallas en Chile y su significado tectónico. *Comunicaciones*, **38**:67-91, Departamento de Geología, Universidad de Chile, Santiago, Chile.
- Hervé, F., Pankhurst R.J., Drake, R., Beck, M. and Mpodozis, C. 1993. Granite generation and rapid unroofing related to strike-slip faulting, Aysen, Chile. *Earth and Planet. Science Letters*, **120**:375-386.
- Hervé, F., Pankhurst, R.J., Drake, R. and Beck, M. 1995. Pillow metabasalts in a mid-Tertiary extensional basin adjacent to the Liquiñe-Ofqui fault zone: the Isla Magdalena area, Aysén, Chile, *Journal of South American Earth Sciences*, **8**, nº1, pp. 33-46.
- Hervé, M. 1976. Estudio geológico de la falla Liquiñe-Reloncaví en el área de Liquiñe; antecedentes de un movimiento transcurrente (Provincia de Valdivia). I Congreso Geológico Chileno, *Actas*, **1**:B39-B56.
- Hervé, M. 1977. Geología del área al este de Liquiñe, Provincia de Valdivia, X Región. Unpublished thesis, Depto. de Geología, Univ. de Chile.
- Hudleston, P.J., Schulz-Ela, D. and Southwick, D.L. 1988. Transpression in the Archean greenstone belt, northern Minnesota. *Canadian Journal of Earth Science*, **25**: 1060-1068.
- Jarrard, R.D. 1986. Relations among subduction parameters. *Reviews of Geophysics*, **24**: 217-284.

- Jiang, D. and Williams, P.F. 1998. High-strain zones: a unified model. *Journal of Structural Geology*, **20**: 1105-1120.
- Jones R.R. and Tanner, P.W.G. 1995. Strain partitioning in transpression zones. *Journal of Structural Geology*, **17**: 793-802.
- Jones, R.R. and Holdsworth, R.E. 1998. Oblique simple shear in transpression zones. *In*: Holdsworth, R.E., Strachan, R.A. and Dewey, J.F. (eds.) 1998. *Continental Transpressional and Transtensional Tectonics*. Geological Society, London, Special Publication, **135**: 35-40.
- Jordan, T.E., Isacks, B.L., Allmendinger, R.W., Brewer, J.A., Ramos, V.A. and Ando, C.J. 1983. Andean tectonics related to geometry of subducted Nazca plate. *Geological Study of America Bulletin*, **94**:341-361.
- Kligfield, D.L. Hunziker, J., Dallmeyer, R.D. and Schmid, S. 1986. Dating of deformation phases using K-Ar and Ar-Ar techniques: results from the northern Apennines. *Journal of Structural Geology*, **8**:781-798.
- Krantz, R.W. 1995. The transpressional strain model applied to strike-slip, oblique-convergent and oblique-divergent deformation. *Journal of Structural Geology*, **17**: 1125-1137.
- Lavenu, A., Noblet, C. and Winter, T. 1995. Neogene ongoing tectonics in the Southern Ecuadorian Andes: Analysis of the evolution of the stress field. *Journal of Structural Geology*, **17** (1), pp. 47-58.
- Lee, J.K.W., Onstott, T.C., Cashman, K.V., Cumbest, R.J., and Johnson, D. 1991. Incremental heating of hornblende in vacuo: implications for  $^{40}\text{Ar}/^{39}\text{Ar}$  geochronology and the interpretation of thermal histories. *Geology*, **19**: 872-876.
- Lee, J.K.W., 1995. Multipath diffusion in geochronology. *Contribution of Mineralogy and Petrology*, **120**:60-822.
- Lin, S. and Williams, P.F. 1992. The origin of ridge-in-groove slickenside striae and associated steps in an S-C mylonite. *Journal of Structural Geology*, **14**, n°3, pp. 315-321.
- Lin, S., Jiang, D. and Williams, P.F. 1998. Transpression (or transtension) zones of triclinic symmetry: natural example and theoretical modelling. *In*: Holdsworth, R.E., Strachan, R.A. and Dewey, J.F. (eds.) 1998. *Continental Transpressional and Transtensional Tectonics*. Geological Society, London, Special Publication, **135**:41-57.

- Lister, G.S. and Snoke, A.W. 1984. S-C mylonites. *Journal of Structural Geology*, **6**:617-638.
- Lopez-Escobar, L; Cembrano, J and Moreno, H., 1995. Geochemistry and tectonics of the Chilean southern Andes Quaternary volcanism (37-46S). *Revista Geologica de Chile* **22**: 219-234.
- McCaffrey, R. 1992. Oblique plate convergence, slip vectors, and forearc deformation. *Journal of Geophysical Research*, **97**(6), pp. 8905-8915.
- McDougall, I. and Harrison, T.M. 1988. *Geochronology and Thermochronology by the 40Ar/39Ar Method*, Oxford University Press. 212 p.
- McKenzie, D. and Jackson, J. 1993. The relationship between strain rates, crustal thickening, paleomagnetism, finite strain and fault movements within a deforming zone. *Earth and Planetary Science Letters* **65**: 182-202.
- Means, W.D. 1990. Kinematics, stress, deformation and material behavior. *Journal of Structural Geology* **12**: 953-971.
- Moreno, H. and Parada, M.A.. 1976. Esquema geológico de la Cordillera de los Andes entre los paralelos 39° y 41°30'S. *Actas I° Congreso geológico chileno (Santiago)*, pp. A213-A226.
- Munizaga, F., Hervé, F., Drake, R., Pankhurst, R., Brook, M. and Snelling, N. 1988. Geochronology of the lake region of south central Chile (39°-42°S): Preliminary results. *Journal of South American Earth Sciences*, **1**:309-316.
- Murdie, R.E., Prior, D.J., Styles, P., Flint, S.S., Pearce, R.G., and Agar, S.M., 1993. Seismic responses to ridge-transform subduction: Chile triple junction. *Geology*, **21**: 1095-1098.
- Murdie, R.E. 1994. Seismicity and Neotectonics associated with the subduction of an active ocean ridge transform system Southern Chile. PhD. Thesis University of Liverpool.
- Nelson, E., Forsythe R. and Arit, I. 1994. Ridge collision tectonics in terrane development. *Journal of South American Earth Sciences*, **7**, n° 3/4, pp. 271-278.
- Pankhurst, R.J. and Hervé, F. 1994. Granitoid age distribution and emplacement control in the North Patagonian batholith in Aysen (44°-47°S). *7° Congreso geológico chileno*, **II**:1409-1413.
- Pankhurst, R., Hervé, F., Rojas, L. and Cembrano, J. 1992. Magmatism and tectonics in continental Chiloé, Chile (42° and 42°30'S). *Tectonophysics*, **205**:283-294.



- Parada, M.A., Godoy, E., Hervé, F. and Thiele, R. 1987. Miocene calc-alkaline plutonism in the Chilean southern Andes. *Revista Brasileira de Geociencias*, **17**:450-455.
- Parada, M.A., Palacios, C. and Lahsen, A. 1996. Magmatic evolution of the eastern part of the Chilean Patagonia (Aysen region): Geochronological and geochemical constraints. Proceedings Third Symposium International "Géodynamique Andine", St. Malo, France, pp. 617-629.
- Pardo-Casas, F. and Molnar, P. 1987. Relative motion of the Nazca (Farallon) and South American plates since Late Cretaceous times. *Tectonics*, **6**:233-248.
- Passchier, C.W. 1998. Monoclinic model shear zones. *Journal of Structural Geology*, **20**, N°8, pp. 1121-1137.
- Passchier, C.W. and Simpson, C. 1986. Porphyroclast systems as kinematic indicators. *Journal of Structural Geology*, **8**:831-843.
- Petit, J.P. 1987. Criteria for the sense of movement on fault surfaces in brittle rocks. *Journal of Structural Geology*, **9**(5/6), pp. 597-608.
- Plafker, G. and Savage, J.C. 1970. Mechanism of the Chilean earthquakes of May 21 and 22, 1960. *Geological Society of American Bulletin*, **81**:1001-1030.
- Platt, J.P. 1984. Secondary cleavages in ductile shear zones. *Journal of Structural Geology* **6**, 439-442.
- Ramos, V.A. 1989. Foothills structure in Northern Magallanes Basin, Argentina. *Am. Assoc. Pet. Geol.* **73**:887-903.
- Ramos, V.A. and Kay, S.M. 1992. Southern Patagonian plateau basalts and deformation: backarc testimony of ridge collisions. *Tectonophysics*, **205**:261-282.
- Ramsay, J. G., 1980. Shear zone geometry: a review. *Journal of Structural Geology* **2**: 83-99.
- Reddy, S.M., Kelley, S.P. and Wheeler, J. 1996. A  $^{40}\text{Ar}/^{39}\text{Ar}$  laser probe study of micas from the Sesia Zone, Italian Alps; implications for metamorphic and deformation histories. *Journal of Metamorphic Geology*, **14**: 493-508.
- Reddy, S.M., Kelley, S.P. and Magennis, L. 1997. A microstructural and argon laserprobe study of shear zone development at the western margin of the Nanga Parbat-Haramosh Massif, western Himalaya. *Contribution to Mineralogy and Petrology* **128**:16-29.

- Reus, J. and McClay, K. 1998. Salar Grande pull-apart basin, Atacama Fault System, northern Chile. *In: Holdsworth, R.E., Strachan, R.A. and Dewey, J.F. (eds.) 1998. Continental Transpressional and Transtensional Tectonics. Geological Society, London. Special Publication, 135:127-141.*
- Robin, P.-Y.F. and Cruden, A.R. 1994. Strain and vorticity patterns in ideally ductile transpression zones. *Journal of Structural Geology, 16, N°4, pp. 447-466.*
- Rojas, C., Beck, M.E., Burmester, R.F., Cembrano, J. and Hervé, F. 1994. Paleomagnetism of the Mid-Tertiary Ayacara Formation, southern Chile: counterclockwise rotation in a dextral shear zone. *Journal of South American Earth Sciences, 7:45-56.*
- Saint Blanquat, M., Tikoff, B., Teyssier, C. and Vigneresse, J.L. 1998. Transpressional kinematics and magmatic arcs. *In: Holdsworth, R.E., Strachan, R.A. and Dewey, J.F. (eds.) 1998. Continental Transpressional and Transtensional Tectonics. Geological Society, London. Special Publication, 135:327-340.*
- Sanderson, D. and Marchini, R.D. 1984. Transpression. *Journal of Structural Geology, 6:449-458.*
- Schermer E.R., Cembrano, J. and Sanhueza, A. 1995. Kinematics and timing of intra-arc shear, southern Chile. *Geological Society of America Abstracts with Programs, pp. A409.*
- Schermer E.R., Cembrano, J., Sanhueza, A. and McClelland, W.C. 1996. Geometry, kinematics and timing of intra-arc shear, southern Chile. *International Geological Congress Proceedings, Beijing, China, 1, pp. 214.*
- Scheuber, E. and Andriessen, P.A.M. 1990. The kinematic and geodynamic significance of the Atacama Fault Zone, northern Chile. *Journal of Structural Geology, 12:243-257.*
- Scheuber, E. and Reutter, K.-J. 1992. Magmatic arc tectonics in the Central Andes between 21° and 25°S. *Tectonophysics, 205:127-140.*
- Scheuber, E., Hammerschmidt, K. and Friedrichsen, H. 1995. <sup>40</sup>Ar-<sup>39</sup>Ar and Rb-Sr analyses from ductile shear zones from the Atacama fault zone, northern Chile: the age of deformation. *Tectonophysics, 250:61-87.*
- Schreurs, G. and Colletta, B. 1998. Analogue modelling of faulting in zones of continental transpression and transtension. *In: Holdsworth, R.E., Strachan, R.A. and Dewey, J.F. (eds.) 1998. Continental Transpressional and Transtensional Tectonics. Geological Society, London. Special Publications, 135:59-79.*

- Sébrier, M., Mercier, J.L., Mégard, F., Laubacher, G. and Carey-Gailhardis, E. 1985. Quaternary normal and reverse faulting and the state of stress in the central Andes. *Tectonics*, **4** (7), pp. 739-780.
- Shimamoto, T. 1989. The origin of S-C mylonites and a new fault zone model. *Journal of Structural Geology*, **11**, N°1/2, pp. 51-64.
- Simpson, C. and Schmid, S.H. 1983. An evaluation of criteria to deduce the sense of movement in sheared rocks. *Bulletin of the Geological Society of America* **94**: 1281-1288.
- Simpson, C. 1985. Deformation of granitic rocks across the brittle-ductile transition. *Journal of Structural Geology*, **5**: 503-511.
- Tapponier, P. and Molnar, P. 1976. Slip-line theory and large-scale continental tectonics. *Nature* **264**:319-324.
- Tchalenko, J.S. 1970. Similarities between shear zones of different magnitudes. *Geological Society of America Bulletin*, **81**: 1625-1640.
- Teyssier, C., Tikoff, B and Markley, M. 1995. Oblique plate motions and continental tectonics. *Geology*, **23**:447-450.
- Teyssier, C. and Tikoff, B. 1998. Strike-slip partitioned transpression of the San Andreas fault system: a lithospheric-scale approach. *In*: Holdsworth, R.E. Strachan, R.A and Dewey, J.F. (eds.) 1998. *Continental Transpressional and Transtensional Tectonics*. Geological Society, London. Special Publications, **135**:143-158.
- Thiele, R., Hervé, F., Parada, M.A. and Godoy, E. 1986. La megafalla Liquiñe-Ofqui en fiordo Reloncaví (41°30'12"S), Chile, *Comunicaciones*, **37**:31-44. Departamento de Geología, Universidad de Chile.
- Tikoff, B. and Teyssier, C. 1992. Crustal-scale, en échelon "P-Shear" tensional bridges: A possible solution to the batholithic room problem: *Geology*, **20**: 927-930.
- Tikoff, B. and Teyssier, C. 1994. Strain modelling of displacement field partitioning in transpressional orogens. *Journal of Structural Geology* **16**: 1575-1588.
- Tikoff, B. and Saint Blanquadt, M. 1997. Transpressional shearing and strike-slip partitioning in the Late Cretaceous Sierra Nevada magmatic arc, California. *Tectonics*, **16**, 442-459.
- Tikoff, B. and Greene, D. 1997. Stretching lineation in transpressional shear zones: an example from the Sierra Nevada Batholith, California. *Journal of Structural Geology*, **19**:29-39.

- Tobisch O.T., Saleeby, J., Renne, P.R. McNulty, B., Tong, W. 1995. Variations in deformation fields during development of a large-volume magmatic arc, central Sierra Nevada, California. *Geological Society of America Bulletin*, **2**:148-166.
- Trimby, P.W., Prior, D.J. and Wheeler, J. 1998. Grain boundary hierarchy development in a quartz mylonite. *Journal of Structural Geology*, **20**, N°7, pp. 917-935.
- Tullis, J. and Yund, R.A. 1987. Transition from cataclastic flow to dislocation creep of feldspar: Mechanisms and microstructures. *Geology*, **15**:606-609.
- Wartho, J. 1995. Apparent argon diffusive loss  $^{40}\text{Ar}$ - $^{39}\text{Ar}$  spectra in amphiboles. *Earth and Planetary science Letters*, **134**:393-407.
- West, D.P. and Lux, D.R., 1993. Dating mylonitic deformation by the Ar-Ar method: An example from the Norumbega Fault Zone, Maine. *Earth and Planetary Science Letters*, **120**:221-237.
- White, S.H. 1975. Tectonic deformation and recrystallization of oligoclase. *Contributions to Mineralogy and Petrology*, **50**: 287-34
- White, S.H., Burrows, S.E., Carreras, J., Shaw, N.D. and Humpreys, F.J. 1980. On mylonites in ductile shear zones. *Journal of Structural Geology*, **2**:175-187.
- White, S.H., Bretan, P.G. and Rutter, E.H. 1986. Fault-zone reactivation: kinematics and mechanisms. *Philosophical Transactions, Royal Society of London*, **A317**:81-97.
- Woodcock, N.H. and Fisher, M. 1986. Strike-slip duplexes. *Journal of Structural Geology*, **8**(7), pp. 725-735.